

UNIVERSITÉ DE SHERBROOKE
Faculté de génie
Département de génie mécanique

Effet de l'angle de flèche sur le bruit à large
bande de ventilateur

Effect of blade sweep on low-speed fan broadband noise

Thèse de doctorat
Specialité: génie mécanique

Dipali Ghodake

Sherbrooke (Québec) Canada

July 2022

JURY MEMBERS

Stéphane Moreau

Supervisor

Mathieu Picard

Examiner

Marlène Sanjose

Examiner

Manuel Henner

Examiner

Adrien Mann

Examiner

RÉSUMÉ

Le bruit produit par le ventilateur de radiateur devient une préoccupation croissante. En effet, les véhicules électriques modernes ne produisent pas le bruit engendré par les groupes motopropulseurs et moteurs traditionnels. Fondé sur une revue de littérature, nous avons classé les différentes sources de bruit ainsi que leur contribution sur le spectre acoustique. Les concepts de dévers de pale avant et arrière ont démontré un potentiel avantage de réduction de bruit large bande aux détriments du rendement aérodynamique. Par conséquent, cette approche est très peu utilisée dans l'industrie. Cette étude vise à comprendre la mécanique de réduction de bruit afin de mitiger le bruit large bande en utilisant l'angle de flèche tout en préservant le rendement aérodynamique. Nous avons choisi des modèles et outils de calculs afin de comprendre le comportement aérodynamique ainsi que le bruit généré par l'angle de flèche. En premier lieu, une simulation Reynolds Averaged Navier Stokes (RANS) est utilisée afin d'évaluer le champ d'écoulement. Ensuite, une méthode Lattice Boltzmann (LBM) haute-fidélité est utilisée afin de prédire la radiation sonore. LBM nous permet de déterminer la source des bruits combinés. Finalement, afin de séparer le bruit large bande généré par les turbulences, nous avons adapté le modèle d'Amiet's leading-edge afin de représenter l'angle de flèche d'un ventilateur axial. Nos résultats indiquent que le dévers de pale avant surpasse le dévers de pale arrière pour la région décrochage, la radiation sonore et la consommation énergétique lorsque les performances aérodynamique est restaurée. Nous recommandons le dévers de pale avant afin de réduire le bruit de large bande émis par le ventilateur du radiateur. Cependant, des recherches additionnelles seront nécessaires afin d'évaluer le bruit tonal. Ces recherches pourront renforcer l'utilisation de l'angle de flèche dans la conception de pales.

Mots-clés : Véhicules électriques, bruit de ventilateur axial, flèche des pales, RANS, LBM, modèle d'Amiet

ABSTRACT

The radiator fan noise is becoming a growing concern since other noise sources radiated from traditional powertrains and combustion engines are omitted in modern electric vehicles. Based on a literature review, we classified the noise sources and their contribution in noise spectra. The forward sweep and backward sweep showed a strong potential in broadband noise reduction but at the cost of loss in aerodynamic efficiency. Hence, this skepticism restrained from its wide usage in fan design. Therefore, this study aims at understanding the noise reduction mechanism so that to mitigate broadband noise using blade sweep by preserving its aerodynamic performance. The various computational tools are used to investigate the aerodynamic behavior and its associated noise in swept blades. First, an industry-friendly steady Reynolds Averaged Navier Stokes (RANS) simulation technique is assessed to investigate the flow field and later a high-fidelity, unsteady Lattice Boltzmann method (LBM) is evaluated to predict the noise radiation. LBM provides the combined knowledge of all noise sources. So, finally, to segregate broadband noise generated due to turbulence interaction, we adapted Amiet's leading-edge noise prediction tool to the swept blade of an axial fan. The results indicate that forward sweep has improved pressure rise by almost 25% than backward sweep and unswept blade when designed for similar loadings. In addition, the forward sweep has reduced noise levels by 12 dB than unswept blade. We recommend using a forward sweep to reduce broadband noise emitted by the radiator fan based on our findings. However, further research is needed to investigate tonal noise that could strengthen the usage of sweep in blade design.

Keywords: Electric vehicles, axial fan noise, blade sweep, RANS, LBM, Amiet's model

to the pleasant earth planet

ACKNOWLEDGEMENTS

In 2015, when team of engineers were asked to solve fan noise problem in ERC, Tata Motors, I was involved as a CFD engineer. I could establish a correlation with physical test but understanding its sources was a challenge. Therefore, I decided to join PhD and thankfully Prof. Stephane Moreau offered me the same problem from Valeo to work up on it. I thank Tata Motors for introducing me to such practical problem.

I am incredibly grateful to the funding received towards my Ph.D. from the industrial chair of aeroacoustics sponsored by Valeo, France, Dassault Systemes for providing Powerflow software and Compute Canada for offering their massive computational services and relentless support.

I behold extreme gratitude towards my supervisors, Prof. Stephane Moreau and Dr. Marlene Sanjose, for their invaluable advice, continuous support, and patience during my Ph.D. study. Their immense knowledge and ample experience have encouraged me in all the time of my academic research. I would also like to thank Dr. Manuel Henner and Adrien Mann for their technical support of my study. Certainly, I would like to thank all the members of my lab. Their kind help and support have made my study and life in Sherbrooke a wonderful time.

Finally, I would like to express my gratitude to my parents, brother, and sister-in-law. Without their tremendous understanding and encouragement in the past few years, it would be impossible for me to complete my study. I'll never forget my friends for their support and kindness in my difficult time. I express my deep gratitude towards everyone who is part of my life directly and indirectly.

TABLE OF CONTENTS

| | | |
|----------|--|-----------|
| 1 | Introduction | 1 |
| 2 | Literature Review | 5 |
| 2.1 | Background | 5 |
| 2.2 | Selection of fans | 5 |
| 2.3 | Noise source mechanisms | 7 |
| 2.3.1 | Broadband noise source mechanisms | 8 |
| 2.3.2 | Discrete noise | 15 |
| 2.3.3 | Tip vortex noise | 18 |
| 2.4 | Blade sweep and aerodynamic behaviour | 24 |
| 2.4.1 | Effect of blade sweep on aerodynamic behaviour | 26 |
| 2.5 | Effect of blade sweep on noise source mechanisms | 29 |
| 2.5.1 | Forward sweep | 29 |
| 2.5.2 | Backward sweep | 30 |
| 2.6 | Summary | 31 |
| 3 | Noise Prediction Tools | 33 |
| 3.1 | Lattice Boltzmann Method (LBM) | 33 |
| 3.1.1 | Modelling rotating domain | 35 |
| 3.1.2 | Linking LBM to NSE | 36 |
| 3.1.3 | Boundary conditions | 37 |
| 3.2 | Navier Stokes Solver | 38 |
| 3.2.1 | Governing equations of fluid flow | 38 |
| 3.2.2 | Energy cascade in turbulence flows | 39 |
| 3.2.3 | Direct Numerical Simulation (DNS) | 40 |
| 3.2.4 | Large Eddy Simulation (LES) | 40 |
| 3.2.5 | Reynolds Averaged Navier Stokes (RANS) | 41 |
| 3.2.6 | Near wall treatment | 42 |
| 3.3 | Computational Aeroacoustics | 43 |
| 3.3.1 | Direct Acoustics | 43 |
| 3.3.2 | Hybrid approach | 44 |
| 3.4 | Analytical modelling for LE noise | 46 |
| 3.5 | Validation | 53 |
| 3.6 | Conclusion | 55 |
| 4 | Test Configurations | 57 |
| 4.1 | Testing at Valeo and MSU | 58 |
| 4.2 | Testing at FAU | 59 |
| 4.2.1 | Numerical modelling approach | 60 |
| 4.2.2 | Uniform vs experimental inlet configurations | 62 |
| 4.2.3 | Investigation of inflow distortion | 63 |

| | | |
|----------|--|------------|
| 4.3 | Extracting turbulence characteristics using statistical analysis | 66 |
| 4.3.1 | Detrending non-stationary signal | 71 |
| 4.3.2 | Extraction of turbulent characteristics | 73 |
| 4.4 | Conclusion | 75 |
| 5 | Aerodynamics Analysis | 77 |
| 5.1 | RANS for Ring fan | 77 |
| 5.1.1 | Numerical configuration | 77 |
| 5.1.2 | Validation | 80 |
| 5.1.3 | Performance and flow field analysis | 82 |
| 5.2 | Ducted fans | 94 |
| 5.2.1 | Numerical configuration for RANS | 94 |
| 5.2.2 | Validation and flow field analysis | 94 |
| 5.3 | LBM for ducted fan | 113 |
| 5.3.1 | Numerical configuration | 113 |
| 5.3.2 | Flow field analysis and validation | 116 |
| 5.4 | Conclusion | 135 |
| 6 | Aeroacoustic and Noise Sources Investigations | 137 |
| 6.1 | Validation of noise spectra | 137 |
| 6.2 | Noise sources identification | 149 |
| 6.2.1 | dB maps of wall-pressure fluctuations | 149 |
| 6.2.2 | Dilatation fields | 150 |
| 6.2.3 | Tip modal structure | 154 |
| 6.2.4 | Broadband noise prediction | 158 |
| 6.3 | Conclusion | 171 |
| 7 | Conclusion Français | 175 |
| 7.1 | Recommandations et perspectives d'avenir | 177 |
| 8 | Conclusion-English | 179 |
| 8.1 | Recommendations and future perspective | 181 |
| | LIST OF REFERENCES | 183 |

LIST OF FIGURES

| | | |
|------|--|----|
| 1.1 | Representative model of automotive noise (source: internet) | 1 |
| 2.1 | Cordier diagram adapted from [55] (left), A typical coolpack arrangement in a vehicle (right) | 6 |
| 2.2 | Classification of noise source mechanisms | 8 |
| 2.3 | Flow conditions producing airfoil self noise adapted from [12] | 10 |
| 2.4 | Far field and wall spectra for vortex shedding case adapted from [73] | 11 |
| 2.5 | A schematic of acoustic feedback loop and noise spectrum adapted from [67, 73] | 12 |
| 2.6 | Coherence plot for three different cases adapted from [73] | 13 |
| 2.7 | Noise radiation and wall spectra adapted from [73] | 13 |
| 2.8 | Noise spectra and contours of vorticity for NACA0012 adapted from [54] | 13 |
| 2.9 | Sketch showing incoming turbulence eddies adapted from [40] | 16 |
| 2.10 | Noise spectrum of lift of fan adapted from [40] | 17 |
| 2.11 | Smoke visualization of contracting flow adapted from [103] | 17 |
| 2.12 | Tip flow representation adapted from [61] | 18 |
| 2.13 | Test set up adapted from [61, 127] | 19 |
| 2.14 | Noise measured for different tip clearance adapted from [61, 127] | 19 |
| 2.15 | Tip vortex behaviour with decreased flow rate (increased loading) simulated by Magne <i>et al.</i> [63] | 21 |
| 2.16 | Effect of tip gap and flow rate on tip leakage vortex size [30] | 21 |
| 2.17 | PSD of fluctuating velocity at 0.96span [30] | 22 |
| 2.18 | Cross correlation of signal recorded on fixed frame [30] | 22 |
| 2.19 | Relation between peak of velocity fluctuation frequency spectra and fan RPM [30] | 23 |
| 2.20 | Noise source mechanisms in a low speed fan | 24 |
| 2.21 | Sweep in wings | 25 |
| 2.22 | Definition of sweep angle by Kimball and Gray [37, 48] | 25 |
| 2.23 | Axial (left) and radial (right) velocity by Zenger and respective sketch by Vad <i>et al.</i> [108, 125] | 27 |
| 2.24 | Representation of boundary layer on a swept blade [124] | 28 |
| 2.25 | Noise spectrum for forward (S1F),backward(S1B) and unswept(S1U) blade fan under free inflow condition [124] | 29 |
| 2.26 | Noise source localization with beamforming under free inflow for forward sweep fan [124] | 30 |
| 2.27 | Noise source localization with beamforming under free inflow for backward sweep [124] | 31 |
| 3.1 | Three ways to Lattice Boltzmann Equation (LBE) [94] | 33 |
| 3.2 | Steps to define of coordinate system, sweep angle and strip for the axial fan | 51 |
| 3.3 | Calculation of far field PSD of noise radiated by an axial fan | 52 |

| | | |
|------|--|----|
| 3.4 | Experimental setup in the ECL large open-jet anechoic wind tunnel adapted from [34](left), Far-field noise spectrum of turbulence-impingement noise (right) | 54 |
| 3.5 | Far-field noise spectrum calculated for different turbulence length scales interactions in presence of no sweep-solid line, dashed line-35°, solid line with plus symbols-45° and dotted line- 55° | 54 |
| 4.1 | Test cases used in this study | 57 |
| 4.2 | Axial fan testing facility at ACFRD, MSU (left) and Reverberant acoustic setup at Valeo (right) | 58 |
| 4.3 | Axial fan testing facility at FAU, Germany adapted from [124] | 60 |
| 4.4 | Microphone arrangement to record fan noise; schematic (left) and photograph (right) adapted from [124] | 61 |
| 4.5 | Discretization performed in Powerflow for Exp setup (top); UI setup(bottom) | 62 |
| 4.6 | Contours of a. mean static pressure, b. mean velocity magnitude; Top: Exp setup and Bottom: UI setup | 64 |
| 4.7 | Contours of mean velocity magnitude (left) and 2D plot of mean axial velocity (right) | 64 |
| 4.8 | Contours of mean radial (left) and mean tangential (right) velocity with overlapped 2D streamlines | 65 |
| 4.9 | Isosurface of mean vorticity field | 65 |
| 4.10 | Mean velocity streamlines in z-plane | 65 |
| 4.11 | Data recording using radially distributed probes | 67 |
| 4.12 | Plot of axial velocity recorded using probes near hub, mid of the duct, near diffuser casing respectively (left to right) | 67 |
| 4.13 | Mean velocity convergence | 69 |
| 4.14 | Normalized autocorrelation function plotted for mid-probe | 70 |
| 4.15 | Detrending of non-stationary data | 72 |
| 4.16 | Autocorrelation function after de-trending of non-stationary data | 72 |
| 4.17 | Axial velocity (left); Turbulent length scale (right) | 74 |
| 4.18 | Turbulence intensity in % (left) and zoomed view (right) | 74 |
| 5.1 | H380EC01 radiator cooling fan | 78 |
| 5.2 | Numerical domain modelling approach for a single blade passage | 78 |
| 5.3 | Prism layer near blades, localized refinement at LE and TE | 79 |
| 5.4 | Tetrahedral elements in the bulk fluid | 79 |
| 5.5 | Fan performance validated with previous studies | 80 |
| 5.6 | Azimuthally averaged velocity components (u_x, u_r, u_t) measured near TE (RANS tet -present, URANS, LBM- previous study, EXP- MSU) | 80 |
| 5.7 | Velocity profiles measured near TE, Top-axial velocity, middle-radial velocity, bottom-tangential velocity | 81 |
| 5.8 | Velocity contours at iso-radial cut-section i.e. near hub, midspan and tip | 82 |
| 5.9 | Isosurface of Q-criteria compared with other simulations | 83 |
| 5.10 | Streaklines on blade surface | 83 |
| 5.11 | Aerodynamic performance of swept blades of ring fans from Valeo | 84 |

| | | |
|------|---|-----|
| 5.12 | Static pressure contours and C_p plot; near hub (left), mid span (middle) and near tip (right) | 85 |
| 5.13 | Azimuthally averaged velocity in relative frame extracted 10mm before LE and plotted along the span normalized with tip radius; left (axial velocity, U_x), middle(tangential velocity, U_t), right(radial velocity U_r) | 86 |
| 5.14 | Blade geometrical extractions; left (chord), middle (stagger angle, λ), right (inlet flow angle, β_i and incidence angle (i)) for ring fans | 86 |
| 5.15 | Simplified velocity triangle and angle definition for low speed axial fan | 86 |
| 5.16 | Streaklines for swept blades | 88 |
| 5.17 | Isosurface of radial cut section colored with total pressure in relative frame | 89 |
| 5.18 | Axial velocity profiles in stationary frame taken before LE and after TE for EC01, EC02 and EC03 | 89 |
| 5.19 | Radial velocity profiles in stationary frame taken before LE and after TE for EC01, EC02 and EC03 | 90 |
| 5.20 | Tangential velocity profiles in stationary frame taken before LE and after TE for EC01, EC02 and EC03 | 90 |
| 5.21 | Azimuthally averaged profiles in stationary frame at LE for EC01, EC02 and EC03 | 91 |
| 5.22 | Azimuthally averaged profiles in stationary frame at TE for EC01, EC02 and EC03 | 91 |
| 5.23 | Isosurface of Q criteria at 100k | 91 |
| 5.24 | Boundary layer parameters extracted at 85% of chord length | 92 |
| 5.25 | The fan performance tested at Valeo for 2200 RPM | 93 |
| 5.26 | Computational domain for RANS simulation of ducted fans (left) and snapshot of meshing (right) | 95 |
| 5.27 | Aerodynamic performance of ducted fan for unswept, forward sweep and backward sweep fan | 96 |
| 5.28 | Pressure coefficient distribution along the normalized chord length at 20%, 50%, 77% and 95% radial locations plotted from left to right, respectively | 96 |
| 5.29 | Azimuthally averaged velocity in relative frame extracted 10mm before LE and plotted along the span normalized with tip radius; left (axial velocity, w_x), middle (tangential velocity, w_t), right (radial velocity w_r) for ducted fans | 97 |
| 5.30 | Blade geometrical extractions; left (chord), middle (stagger angle, λ), right (inlet flow angle, β_i and incidence angle (α)) for ducted fans | 97 |
| 5.31 | Contours of azimuthally averaged mean axial velocity extracted 10mm before and along LE extracted using LDA in experiment and compared with RANS and LBM | 99 |
| 5.32 | Contours of azimuthally averaged mean radial velocity extracted 10mm before and along LE extracted using LDA in experiment and compared with RANS and LBM | 100 |
| 5.33 | Contours of azimuthally averaged mean tangential velocity extracted 10mm before and along LE extracted using LDA in experiment and compared with RANS and LBM | 101 |

| | | |
|------|--|-----|
| 5.34 | Contours of azimuthally averaged mean turbulent kinetic energy extracted 10mm before and along LE extracted using LDA in experiment and compared with RANS and LBM | 102 |
| 5.35 | Contours of azimuthally averaged mean axial velocity extracted 10mm before and along TE extracted using LDA in experiment and compared with RANS and LBM | 103 |
| 5.36 | Contours of azimuthally averaged mean radial velocity extracted 10mm before and along TE extracted using LDA in experiment and compared with RANS and LBM | 104 |
| 5.37 | Contours of azimuthally averaged mean tangential velocity extracted 10mm before and along TE extracted using LDA in experiment and compared with RANS and LBM | 105 |
| 5.38 | Contours of azimuthally averaged mean turbulent kinetic energy extracted 10mm before and along TE extracted using LDA in experiment and compared with RANS and LBM | 106 |
| 5.39 | Azimuthally averaged mean velocity profiles at LE | 107 |
| 5.40 | Azimuthally averaged mean velocity profiles at TE | 108 |
| 5.41 | Demonstration of radial flow with vector diagram in stationary frame . . . | 109 |
| 5.42 | Isosurface of λ_{ci} at 100 colored by helicity varies from blue to red (-1 to +1) left-S1F, middle-S1U, right-S1B | 109 |
| 5.43 | Isosurface of λ_{ci} at 315 colored by helicity varies from blue to red (-1 to +1) left-S1F, middle-S1U, right-S1B | 110 |
| 5.44 | Contours of velocity in rel. frame taken near hub (10% of span), near mid (50% of span) and near tip(99% of span) | 111 |
| 5.45 | Boundary layer parameters extracted suction side at 85% of chord length . | 112 |
| 5.46 | LBM set up | 113 |
| 5.47 | LRF creation using volume of revolution confined to blades and hub, sliding mesh setting and simulation parameter in Powercase | 114 |
| 5.48 | Meshing strategy executed in Powerflow discretizer | 114 |
| 5.49 | The voxels and surfels distribution in different VR regions in Powerflow discretizer | 115 |
| 5.50 | Static pressure convergence plot monitored inside plenum for fine cases . . | 117 |
| 5.51 | Mean flow field averaged over each fan revolution | 117 |
| 5.52 | Static pressure contours from LBM simulations plotted for FS (left); US(middle), BS(right) | 118 |
| 5.53 | Pressure coefficient calculated from Eq. 5.1 and compared at 20%, 50%, 77%, 95% of span length from left to right respectively | 118 |
| 5.54 | Static pressure contours from RANS simulations plotted for FS (left); US(middle), BS(right) | 119 |
| 5.55 | LBM Azimuthally averaged mean velocity profiles at LE | 120 |
| 5.56 | LBM Azimuthally averaged mean velocity profiles at TE | 121 |
| 5.57 | Contours of instantaneous velocity from LBM simulation taken near hub (10% of span), near mid (50% of span) and near tip (99% of span) | 123 |
| 5.58 | FS tip vortex plotted using isosurface of $\lambda_2 = -2e7$ calculated from instantaneous flow field | 125 |

| | | |
|------|--|-----|
| 5.59 | BS tip vortex plotted using isosurface of $\lambda_2 = -2e7$ calculated from instantaneous flow field | 126 |
| 5.60 | US tip vortex plotted using isosurface of $\lambda_2 = -2e7$ calculated from instantaneous flow field | 127 |
| 5.61 | Time evolution of FS tip vortex plotted using isosurface of $\lambda_2 = -2e7$ calculated from instantaneous flow field | 128 |
| 5.62 | Time evolution of US tip vortex plotted using isosurface of $\lambda_2 = -2e7$ calculated from instantaneous flow field | 129 |
| 5.63 | Time evolution of US tip vortex plotted using isosurface of $\lambda_2 = -2e7$ calculated from instantaneous flow field | 130 |
| 5.64 | Top view of $\lambda_2 = -2e5$ isosurface from mean flow field of LBM simulations plotted for FS (left); US(middle), BS(right) | 131 |
| 5.65 | Top view of $\lambda_2 = -2e5$ isosurface from RANS simulations plotted for FS (left); US(middle), BS(right) | 131 |
| 5.66 | Front view of $\lambda_2 = -1e5$ isosurface from mean flow field of LBM simulations plotted for FS (left); US(middle), BS(right) | 132 |
| 5.67 | Front view of $\lambda_2 = -0.7e5$ isosurface from RANS simulations plotted for FS (left); US(middle), BS(right) | 132 |
| 5.68 | Probes provided in the casing to record pressure | 132 |
| 5.69 | Probes provided in the casing to record pressure | 133 |
| 5.70 | Time trace of wall-pressure fluctuations on the duct in the tip gap for FS | 133 |
| 5.71 | PSD of wall-pressure fluctuations on the duct in the tip gap for FS | 133 |
| 5.72 | Time trace of wall-pressure fluctuations on the duct in the tip gap for BS | 133 |
| 5.73 | PSD of wall-pressure fluctuations on the duct in the tip gap for BS | 134 |
| 5.74 | Time trace of wall-pressure fluctuations on the duct in the tip gap for US | 134 |
| 5.75 | PSD of wall-pressure fluctuations on the duct in the tip gap for US | 134 |
| 6.1 | Comparison of noise spectra of FS fan for coarse and fine mesh | 138 |
| 6.2 | Contours of x-vorticity varying from (-5,5) and projected streamlines showing casing flow field generated before the fan | 138 |
| 6.3 | Comparison of sound pressure level at different microphones for US | 141 |
| 6.4 | Directivity plot for US | 142 |
| 6.5 | Comparison of sound pressure level at different microphones for FS | 143 |
| 6.6 | Directivity plot for FS | 144 |
| 6.7 | Comparison of sound pressure level at different microphones for BS | 145 |
| 6.8 | Directivity plot for BS | 146 |
| 6.9 | Comparison of noise spectra at different microphones for all fans | 147 |
| 6.10 | Directivity plot for compared for fans from LBM | 148 |
| 6.11 | Contours of PSD of filtered wall pressure top -front view, bottom- rear view | 151 |
| 6.12 | Contours of PSD of filtered wall pressure top -front view, bottom- rear view | 152 |
| 6.13 | Contours of PSD of filtered wall pressure top -front view, bottom- rear view | 153 |
| 6.14 | Band pass filtered time derivative of density fluctuations (-0.001 to 0.001 Kg/m ³ s) | 155 |
| 6.15 | Contours of band pass filtered [900-1100 Hz] pressure fluctuations | 156 |
| 6.16 | Contours of band pass filtered [1700-2300 Hz] pressure fluctuations | 156 |

| | | |
|------|--|-----|
| 6.17 | Isosurface of instantaneous $\lambda_2 = -2e7$ colored by relative velocity | 156 |
| 6.18 | Histogram of relative velocity take from isosurface of λ_2 | 157 |
| 6.19 | Interaction frequency calculated for CV of S1F | 158 |
| 6.20 | Histogram of isosurface of λ_2 from RANS | 158 |
| 6.21 | Histogram of relative velocity take from isosurface of λ_2 | 159 |
| 6.22 | Sweep angle (left) and extraction planes (right) for ducted fans | 159 |
| 6.23 | Parameters for Amiet's model and von Kármán spectrum extracted for ducted fans | 161 |
| 6.24 | Stripwise distribution of turbulence spectrum and sound power prediction using Amiet's model | 163 |
| 6.25 | Sound maps for S1U from beamforming method used in experiment by Zenger [124] | 164 |
| 6.27 | Validation of ducted fan noise spectra with experiments represented with EXP-dot/dash linestyle, LE Amiet extended-line with markers, TE Amiet classical-markers | 165 |
| 6.28 | Comparison of classical vs extended Amiet's model prediction for free-tip fans | 165 |
| 6.29 | Integrated octave band spectra [124] | 166 |
| 6.30 | Sweep angle (left) and extraction planes (right) for ring fans | 167 |
| 6.31 | Parameters for Amiet's model and von Kármán spectrum extracted for ring fans | 168 |
| 6.32 | Stripwise distribution of turbulence spectrum and sound power prediction using Amiet's model for ring fans | 169 |
| 6.33 | RPM scalability check using LBM | 170 |
| 6.34 | Validation of ring fans noise spectra with experiments represented with EXP-dot/dash linestyle, LE Amiet extended-line with markers, TE Amiet classical-markers | 170 |
| 6.35 | Comparison of Amiet's model prediction for ring fans | 171 |

CHAPTER 1

Introduction

Quintessential chase of comfort and luxury put humans into a brassy environment produced by machines. Studies published in the British medical bulletin ratify that these ear-splitting noises cause threats to human health in the form of permanent hearing loss, distress, hypertension, and risk of cardiovascular diseases [86, 107, 112]. Over more than two decades, developing and highly populated countries are facing disrupted life quality despite their economic boom because increasing trading demands are resulting in a surge in transport vehicles [97]. In fact, on average, humans are exposed to shrilling noise levels between 55 dB to 67 dB during the daytime; however, only a typical automotive alone radiates noise in the range of 60-80 dB. Figure 1.1 represents different potential noise sources that a vehicle comprises. All of these sources contribute to the vehicle overall noise levels. They are mainly divided into structure-borne and air-induced noise. Decennaries of technical advancements were muffling structural noise sources while human ears would be exposed more and more to air-induced whizzing and whistling sounds. Although many potential air-induced noises influence the sound quality, automotive OEMs are mainly concerned with a radiator fan noise because it directly impacts vehicle pass-by noise certification. Secondly, it restrains customer satisfaction/comfort. Generally, a

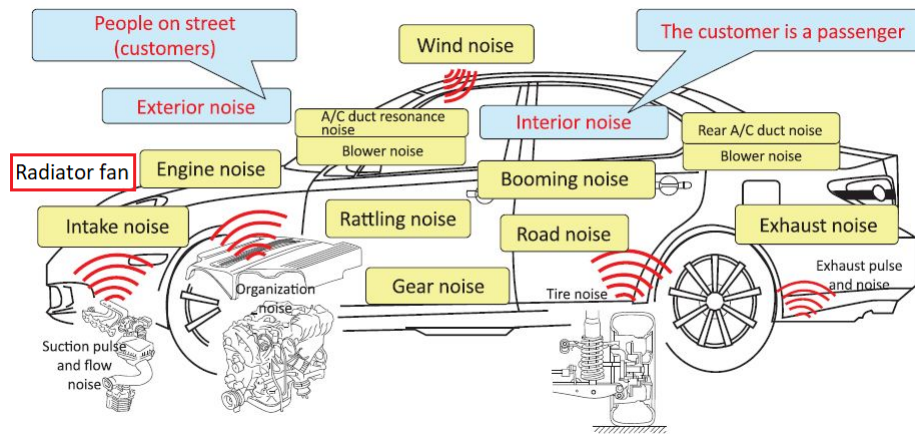


Figure 1.1 Representative model of automotive noise (source: internet)

pass-by test resembles a car operating under heavy city traffic conditions where customers sitting inside and outside the vehicle will be exposed to the noise. In such a condition, engine load is high, and the vehicle either moves with less than 40 km/hr or idle at times.

In a second scenario, while the car is parked, the engine is supposed to cool down rapidly. Hence, the fan rotates at its maximum speed, resulting in annoying noise radiation in the parking zone. Moreover, scenarios of fast electrical vehicle charging at high load conditions may cause hurdles in meeting certification standards (72 dBA) or compromise customer comfort, and further, defame not only the product but also deteriorate human life quality.

Hence, we must address a fan noise problem by understanding the various root causes of noise generations. Chapter 2- state of the art explains the physical sense of fan noise source mechanisms. It is broadly classified into 1. tonal 2. broadband noise. Tonal noise is a discrete peak at the fundamental frequency of a rotation and its harmonics rising above broadband noise. Broadband noise is usually random in nature and spreads all over the frequency range; it provides shape to the spectra; it significantly contributes to the overall noise levels too. It is further divided into the leading edge (LE) and trailing edge (TE) noise. In the absence of any other perturbations, a minimal noise produced by the fan is due to its turbulent boundary layer scattering at the trailing edge— called self-noise. LE noise is due to incoming small-scale turbulence interactions that closely resemble the fan operating condition described above. A fan rotating at high speed pulls air from the front grille (imagine a general passenger car here). The components present before the fan creates large-scale turbulent structures, which are then sucked through series of heat exchangers. The tightly spaced fins in the heat exchanger break down big eddies into small-scale turbulence. These small-scale turbulence impacts blade LE, producing broadband noise. Therefore, as a primary concern to address LE broadband noise, blade sweep is selected. It creates non-linear interactions along a span, forming the interference patterns among the radiated acoustics waves such that either it arrests or slows their far-field propagation. However, sweep divides an incoming flow and forms crossflow at LE, resulting in the reduced spanwise lift. Hence, despite the ability to reduce noise, reduced aerodynamic efficiency challenges designers to use sweep in blade design.

This challenge motivates us to study blade sweep without losing its aerodynamic performance and gain knowledge of associated noise source mechanisms, which will help us reduce fan noise emission levels. In saving development time and prototype cost, we have chosen the digital method over experiments. We surveyed numerous computational tools in Chapter 3 and chose the most suitable Lattice Boltzmann method (LBM) CFD solution for our study. Although LBM provides highly accurate results and a detailed flow field, it is a relatively expensive and time-consuming tool during an early product development cycle. Hence, we investigate analytical tools that can suffice the initial design phase, demanding quick and cheap design recommendations with fairly less accuracy. We have

selected easy and already proven Amiet’s analytical model for low speed fans. At the end of Chapter 3, we discuss Amiet’s models and their extension to account for blade sweep. Also, to gain confidence in the level of model accuracy, it is validated with an experiment conducted in the large open-jet anechoic wind tunnel at Ecole Centrale de Lyon on a thin, loaded, and isolated airfoil with and without sweep.

The initial idea was to prove the method on the H380 fan- designed and developed at Valeo, France, and its sweep variants. However, industrial test case supplies limited data for validation, and fortunately, we found the experimental study performed at Erlangen universitat in Germany by Zenger [124] as part of his Ph.D. thesis. He recorded flow field with advanced techniques such as laser doppler anemometry (LDA) and fan pressure characteristics, casing pressure measurements, and noise recordings on simple fans design meant for academic investigations. Therefore, in Chapter 4, we illustrate the fan matrix picked from Valeo and Erlangen’s study, experimental setup, and measurement details used in our research. Then, the usual practice of simplifying the domain is analyzed against the actual experimental setup. The results pointed to inflow distortion that needs to be properly captured in order to 1. provide accurate noise prediction and 2. establish a high level of correlation with aerodynamic results. Therefore, the computational domain used in our analysis mimics the actual test configuration.

Aerodynamic analysis conducted with RANS using ANSYS CFX and LBM method implemented in the commercial software Powerflow (PF) is presented in Chapter 5. Three fans from Valeo and three selected academic test cases are validated with experimental results. The detailed post-processing of CFD results illustrated the blade to blade flow, LDA measurements, pressure contours, tip vortex visualization with λ_2 plot, etc. At the end, findings on aerodynamic behavior for forward/backward sweep and ducted/ring fans are highlighted. The reasons behind the loss of efficiency due to sweep are discussed at the end.

In chapter 5, the noise radiated from all sources predicted from LBM simulation is compared with experimental recording. As a part of our core objective of this study, noise sources are investigated by conducting Fourier analysis on blade wall pressure, modal analysis in tip gap flow, and dilatation field. The noise sources for unswept, forward and backward swept fans are compared with beamforming results performed on experimental data. In addition, the analytical tool developed for the swept blade is used to calculate LE broadband noise. The required statistical inputs are extracted from RANS simulations. Finally, noise levels are compared for all six fans and validated with experimental results.

In summary, this study introduces effect of sweep in presence of controlled design parameters for ring and free tip fans. Firstly, the loading variations and noise radiation are studied by adding forward sweep to the design. Secondly, aero and noise performance are investigated by adding forward and backward sweep by maintaining loading. For the first time, LBM simulation is performed using the full experimental set up and achieved excellent correlation with far field noise spectra from the test. The noise source localization methods contribute to the research by showcasing the sweep role in the noise sources. The investigations revealed that in absence of any external disturbances, tip noise dominates the noise spectra from low frequency to high frequency. The free tip forward and backward sweep show different tip flow behavior than unswept blade, tracing their importance in the noise spectra. Finally, simulations have generated a wide database that agrees very well with experimental data and is also used to validate analytical models for LE noise extended for the sweep in low-speed axial fans.

CHAPTER 2

Literature Review

2.1 Background

The axial fans are widely used in cooling units of cars, trucks and locomotives due to their high volumetric flow rate and low pressure rise characteristics. These fans are essential to maintain the correct temperature of the engine coolant, which in turn determines the fuel efficiency and emission levels of a vehicle. Therefore, in order to meet vehicle emission standards, the right fan is likely to be selected in the early vehicle development stages. However, fan noise was never accounted for then. On the other hand, even though conventional IC engines will be replaced by electrically powered vehicles, the fan will remain a primary source to cool condensers and liquid-cooled batteries. This eventually will lead to augmented noise contribution in surrounding by a fan in the near future. Moreover, the most recent Ford motors and Canadian government joint investment of two billion dollars in future electrical vehicle manufacturing has pressing hard to address the fan noise issue beforehand. Therefore, after contemplating advancement and environmental protection, Valeo has decided to attenuate noise levels by optimizing the fan blade design with the sweep. Thus, the focus of this study is to gain additional knowledge on sweep and its associated noise source mechanisms. Before diving directly into the swept blade, a brief overview of the fan selection and its noise source mechanisms are deduced in the following section. Then, the swept blade fans and their implications on the aerodynamic performance and noise emission are discussed.

2.2 Selection of fans

Turbomachines are rotating devices that either extract energy from fluid in dynamic motion or supplies the power to a rotating shaft to raise the pressure of a fluid in contact with them. Generally, the classification of turbomachines is based upon a meridional airflow path. In axial turbomachinery, the air flows axially, and in centrifugal turbomachinery, air enters axially and leaves radially, whereas a mixed flow turbine is viewed as a cross design between a radial and an axial turbine [87]. Axial turbomachines are used in multiple applications such as,

- power consuming machines e.g. propeller, radiator fan, cooling fan in electronic equipment ...
- power generation e.g. axial turbines, wind turbines ..

As noticed from applications, the diameter of these machines varies from a few centimeters to meters. For pumps and fans, Cordier has organized these machines under one curve based on their specific diameter and specific speed, as shown by Fig. 2.1. The curve exhibits the optimal machines in the specific speed versus specific diameter plot of (N_s, D_s) and thus, proves to be useful while designing the machines for different applications. The parameters used in the plot are defined in Eq. (2.1) and Eq. (2.2).

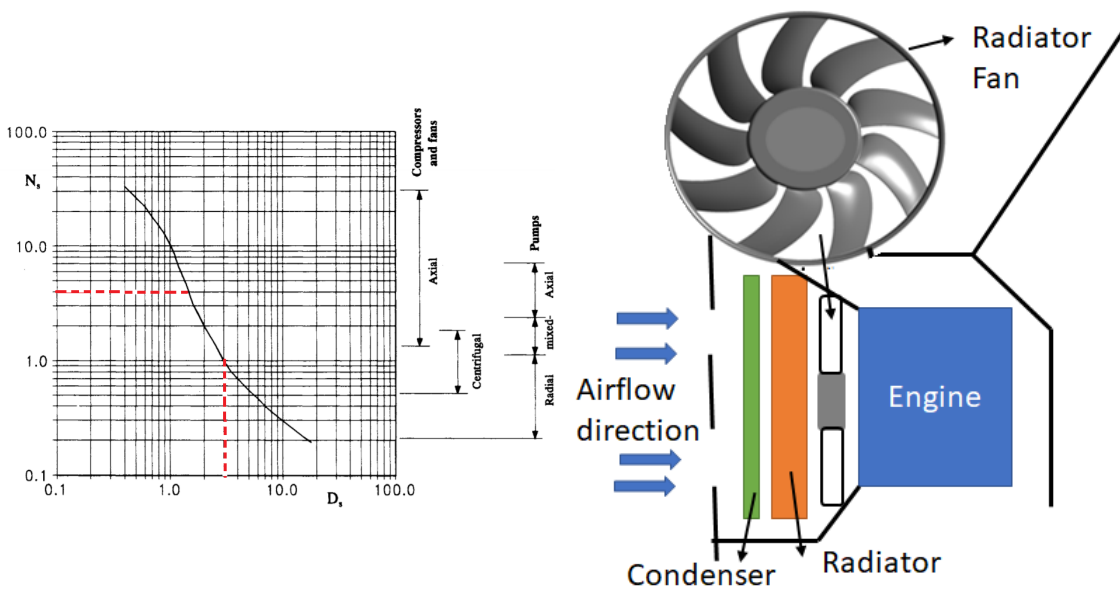


Figure 2.1 Cordier diagram adapted from [55] (left), A typical coolpack arrangement in a vehicle (right)

$$N_s = \frac{\phi^{\frac{1}{2}}}{\psi^{\frac{3}{4}}} \quad \text{and} \quad D_s = \frac{\psi^{\frac{1}{4}}}{\phi^{\frac{1}{2}}} \quad (2.1)$$

$$\psi = \frac{\Delta P}{N^2 D^2} \quad \text{and} \quad \phi = \frac{Q}{N D^3} \quad (2.2)$$

The IC engine is a primary energy source to propel an automotive vehicle and drive the accessories such as engine mounted fan, pumps and alternator, etc... Therefore, it is essential to minimize the power consumption of accessories to increase vehicle fuel mileage and reduce pollutant emission. It implies that a fan indirectly contributes to environmental pollution. Therefore, to meet power consumption and emission standards, small diameter

and low speed fans are targeted. Moreover, a radiator cooling fan is designed such that it should supply a high flow rate against increasing resistance. An axial fan meets the above requirements, and out of its large operating range, i.e., $1.5 < N_s < 20$, often a fan specific speed N_s below four and its corresponding specific diameter D_s less than two is selected — shown by the dotted line in Fig. 2.1. Consequently, it is ascertained that the outcome of the present study can be directly applied to the low solidity fans, operating in low subsonic flows and in high Reynolds number flows in turbulent regime— e.g., cooling fans in electronic equipment, marine propellers and wind turbines [16].

Automotive cooling fan displayed in Fig. 2.1 is relatively large in diameter and rotates at a slow speed where the tip Mach number is always less than 0.3. This subsonic flow implies that we can treat the flow field around a fan blade as incompressible. These low speed fans also have low solidity (< 0.7). The solidity, (σ) – defined as the ratio between the chord of a blade and pitch ($\frac{2\pi r}{N_b}$), where r is the radius and N_b is number of blades. A designer optimizes all other design parameters like blade shape and blade installation to meet a fan aerodynamic performance. However, these optimized blade shapes don't withstand updated, more stringent noise emission norms (72 dBA) that are difficult to meet. Moreover, for instance, none can avoid the problem by playing with the position of a single microphone. Hence, it is necessary to ameliorate shrilling fan noise. How can we resolve this noise problem? The short answer is by gathering knowledge of noise sources' origin.

2.3 Noise source mechanisms

Sharland in 1964 [98] demonstrated a link between the aerodynamic behavior of a fan to its aeroacoustic performance. He inferred that the overall noise level radiated by a fan was essentially dipole in nature and originated due to fluctuating forces exerted by a blade surface on a fluid passing over it. This logical inference is strictly in coherence with Curle's analogy [25]. Curle regarded the influence of fixed solid surfaces in aerodynamically generated noise by extending Lighthill's general theory [57]. For rotating blades, Ffowcs Williams and Hawkings in free field analogy derived from Curle's approach became the fundamental basis of fan noise prediction models. While studying a fan noise spectrum, Sharland classified it broadly into broadband and discrete noise [98]. The broadband noise is nothing but random distribution of noise over all frequency range. In contrast, discrete noise is identified as the peaks regarded at fundamental blade passing frequency, and its harmonics are referred to as tonal noise. Furthermore, noise source mechanisms are classified as given by Fig. 2.2 Each of these noise sources are discussed briefly in following

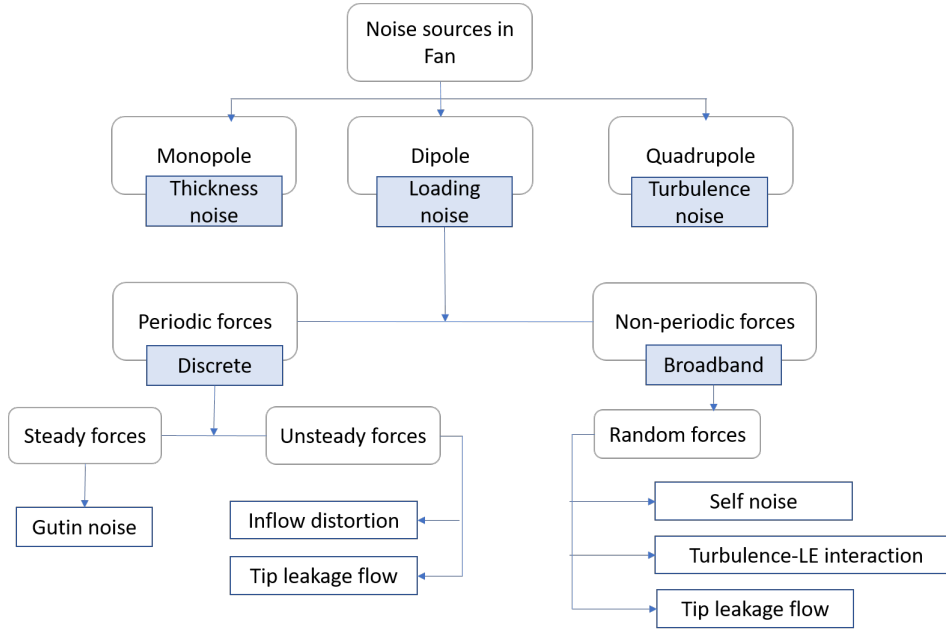


Figure 2.2 Classification of noise source mechanisms

sections.

2.3.1 Broadband noise source mechanisms

At low speed, broadband noise is of dipolar nature and is caused by random fluctuations of forces over a blade surface that also yields random lift variations. These random wall-pressure fluctuations trigger two main noise mechanisms:

1. Trailing edge noise — scattering of turbulent eddies formed in a boundary layer near the trailing edge
2. Leading edge noise — Turbulent eddies impacting the blade leading edge

Now, the challenge is to identify contribution from each noise source in the fan noise spectra. Therefore, in order to simplify rotor noise problem, Schlinker and Amiet [6, 95] followed by Sinayoko *et al.* [101] regarded rotating fan blades as a stacking of profiles seen as equivalent dipoles in local translation. Noise power spectral density (PSD) generated by a fan (S_{pp}^F) is calculated by multiplying instantaneous PSD radiated from a blade (S_{pp}^γ) by first keeping it at fixed azimuthal angle and then averaging power spectra around the azimuth with number of blades, illustrated by Eq. (2.3). The vectors \vec{X} , $\vec{\Sigma}$ are local coordinate systems where observer and source are defined, respectively. The aerodynamic response of a blade can be predicted by integrating over a lift produced by an individual isolated airfoil when placed in a turbulent flow field. The frequency change due to moving sources — commonly known as Doppler effect, is accounted in the following expression,

where, rotating source radiate noise at ω' but it is heard at ω at fixed observer location in far field.

$$S_{pp}^F(\vec{X}, \omega) = \frac{B}{2\pi} \int_0^{2\pi} \left(\frac{\omega(\theta')}{\omega'} \right)^2 S_{pp}^\gamma(\vec{\Sigma}, \omega') d\theta' \quad (2.3)$$

The environment in which a blade operates identifies its respective source contribution in the spectra. Trailing edge noise is generally recorded by placing an isolated airfoil in a low subsonic ($M < 0.1$) uniform flow. Conversely, the LE noise is measured by placing the airfoil in an incoming mean flow, convecting small-scale turbulence.

A. Self noise of isolated airfoil in uniform flow

The solidity condition plays a significant role in identifying the aerodynamic interactions between the fan blades. For a low speed, low pressure fan, solidity is less than 0.7 [114, 124], thus provides an opportunity to model each blade as segments of isolated airfoils. The eddies developed in a boundary layer on either side of the airfoil are scattered near the trailing edge. Sharland [98] stated that these instantaneous eddy separations near the trailing edge differ from the upper and lower surface of the airfoil, are responsible for vortex shedding noise. Yet, he did not account for additional flow conditions on chord-based Reynolds number (Re_c) and various angles of attack (α) that can influence noise generating mechanisms. Consequently, Brooks *et al.* [12] demonstrated them by conducting a series of systematic experiments on NACA0012 airfoils of different sizes and shapes shown in Fig. 2.3.

Turbulent boundary layer trailing edge noise:

Prior to Brooks *et al.*, Yu and Joshi [122] also experimentally visualized eddies behavior near trailing edge using 2D isolated airfoil in order to establish the physical sense of noise generation mechanism. The cross-correlation between far-field and near-field microphones helps identify local broadband noise sources that resided at the trailing edge. Powell [83] showed that the radiated noise scales with the velocity to a power 4. Hence, they selected two free stream velocities i.e. $U_\infty = 29.7m/s$ and $53.9m/s$ and their corresponding Reynolds numbers being $Re_c = 1.22 \times 10^6$ and 2.21×10^6 respectively. The magnitude of correlation peaks identified the degree of coherence. Surprisingly, the coherence was decreased with the increasing U_∞ and increased with boundary layer tripping. Similar behavior was also observed on a NACA0012 airfoil, mainly because the tripping aids the uniform turbulence distribution in a boundary layer with the increasing velocity [11]. When the angle of attack (α) was changed from 0° to 10° , the coherence was reduced. Hence, these experiments led us to two traces of course:

1. Dependence of radiated noise on free stream velocity and boundary layer thickness

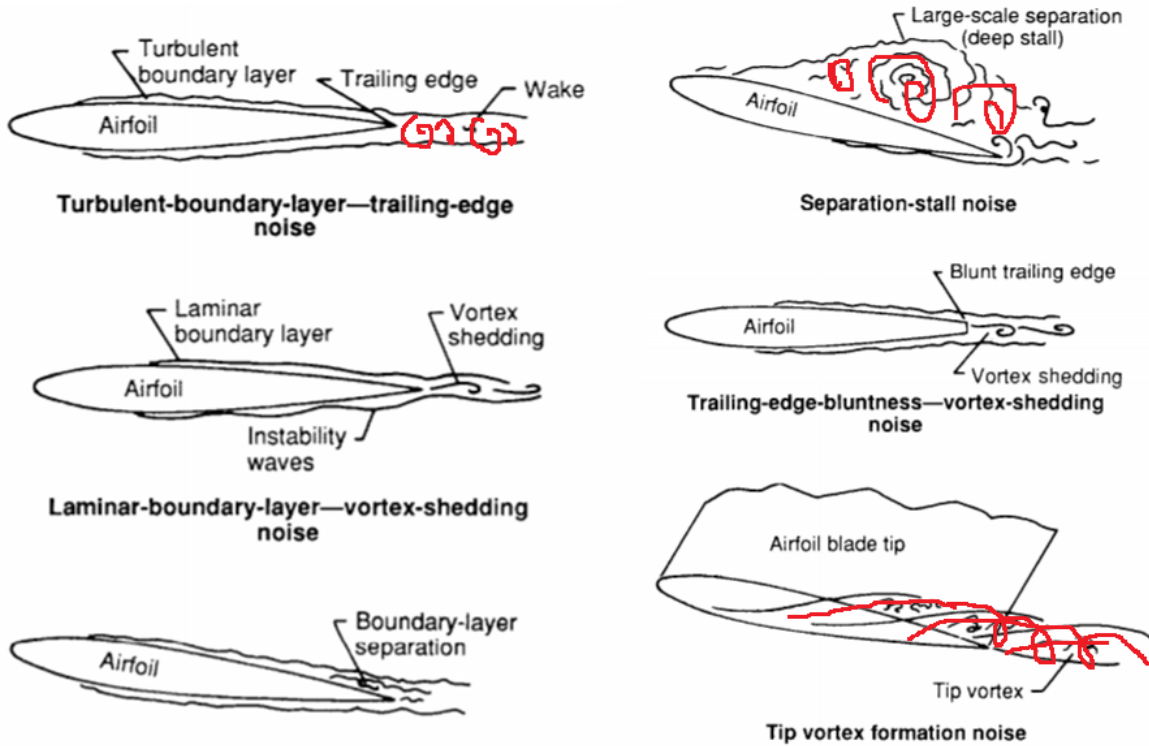


Figure 2.3 Flow conditions producing airfoil self noise adapted from [12]

2. Relation between radiated noise and spatial and temporal resolution of an eddy

This indicates that trailing edge noise radiation depends on mean velocity and eddy size in the boundary layer and boundary layer thickness. The correlation between boundary layer and noise can be accurately predicted by measuring wall-pressure spectra.

Therefore, in the case of $\alpha = 0^\circ$, Yu and Joshi measured the wall-pressure spectra and interestingly observed that the suction side contributed mainly to the low frequency components, whereas the pressure side dominated mostly high frequency region of the wall-pressure spectra. This observation hints at the possibility of instantaneous vortex shedding from the upper and lower surface as suggested by Sharland [98]. In addition, they also observed that the correlation between far-field noise and surface pressure measured on the suction side is in the opposite phase with that measured on the pressure side. However, when noise and surface pressure are measured on the same side of an airfoil, the surface pressure and the radiated noise is in phase. This analysis proved to be the first evidence of dipolar source in trailing edge noise radiation. Yu and Joshi further concluded series of events that occur in a trailing edge noise generation that are as described below:

1. In zero pressure gradient flow, the sub-laminar bubble burst to produce a turbulent boundary layer and forms large scale coherent motion centered in the outer layer

2. These large scale eddies convect downstream with mean flow U_∞ and exert pressure variations near the trailing edge
3. Pressure variations are causing dipole-like noise radiation.

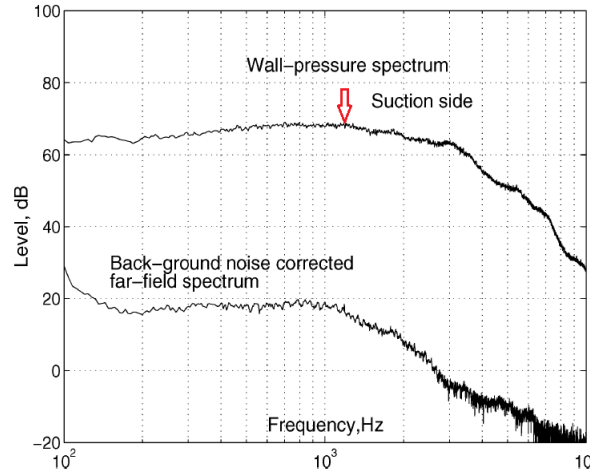


Figure 2.4 Far field and wall spectra for vortex shedding case adapted from [73]

The turbulent boundary layer behavior on a Controlled-Diffusion (CD) airfoil under flow velocity 16 – 30 m/s and high angle of attack 8 – 13° was studied by Moreau and Roger [73]. They noticed a similar formation of laminar separation bubble near the leading edge, followed by a fully developed boundary layer near the trailing edge. The radiated noise was dominated over particularly 400 Hz-10 kHz frequency range as shown in Fig. 2.4.

Hutcheson and Brooks [43] showed that trailing edge noise spectra depends upon Mach number, boundary layer displacement thickness and effect of Reynolds number on both pressure and suction sides. When an angle of attack is increased, the peak frequency of a noise spectra shifts to the lower frequency and the amplitude increases with increasing angle of attack.

Laminar boundary layer instability noise:

This is a particular case of low Reynolds number flow, in which the boundary layer at least on one side of the airfoil stays laminar. On the suction side, instabilities originate at a point and propagate downstream. If the chord length is not sufficient for these instabilities to transit from laminar to turbulent boundary layer, these instability waves experience diffraction at geometric singularity generating acoustic waves. These acoustic waves travel upstream towards the point of instability, forming an acoustic feedback loop. If proper phasing happens with this feedback loop, a resonance occurs, which is visualized

in noise radiation spectra as a strong tonal peak on a broadband hump as shown in Fig. 2.5.

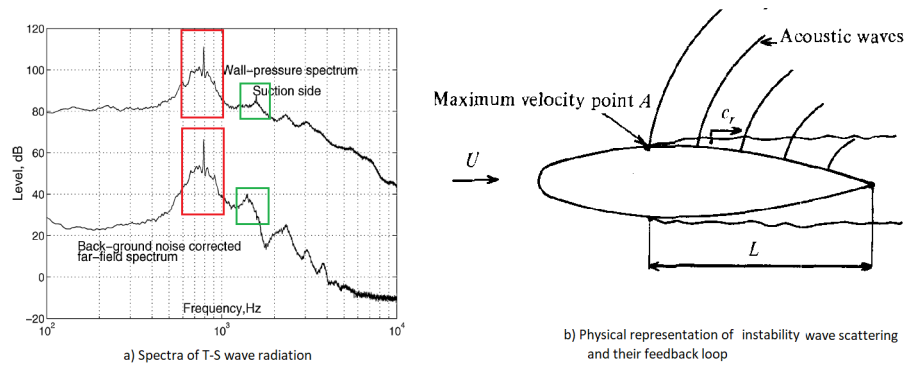


Figure 2.5 A schematic of acoustic feedback loop and noise spectrum adapted from [67, 73]

Indeed, if the favorable phase lock-in of the acoustic feedback loop occurs, at least one sharp tone is heard. Hence it is either tonal or broadband noise source based on acoustic feedback coupling mechanism [22, 67, 78, 84]. This mechanism can occur in fan [60] but at very specific conditions as demonstrated by Moreau and Roger [73] and Yakina and Roger *et al.* [119]. In practical cases, described phenomena are less dominant and rare to occur because of approaching turbulence in the presence of heat exchangers. Therefore, this mechanism is briefly reviewed but is not included in this study.

Turbulent boundary layer vortex shedding :

Generally, fan blades operate under fully grown turbulent boundary layer without any flow separation. This operating condition was studied using a CD airfoil [73]. Despite differences in shape of the wall spectra and the noise spectra, coherence plot showed a bump at high frequency. As flow velocity increased, the bump moved towards high frequency. This interprets that vortex shedding is coherent at some dominant frequencies and its location depends upon flow velocity (refer Fig. 2.6). The influence of operating conditions on noise spectra is as shown in Fig. 2.7

Trailing edge bluntness also shows vortex shedding phenomena [11, 43]. The spectral shape and peak frequency depends upon the trailing-edge shape and its thickness. With the help of spectral scaling, Brooks *et al.* [11] predicted far field noise and inferred that when trailing-edge bluntness height is smaller than the boundary layer thickness, its contribution to noise radiation is minimal.

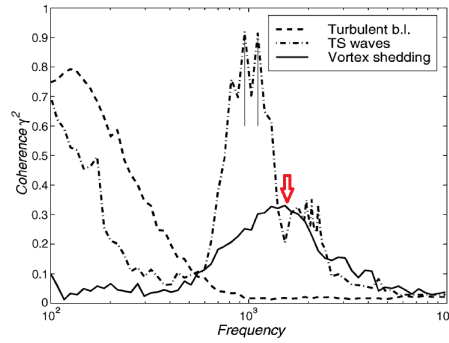


Figure 2.6 Coherence plot for three different cases adapted from [73]

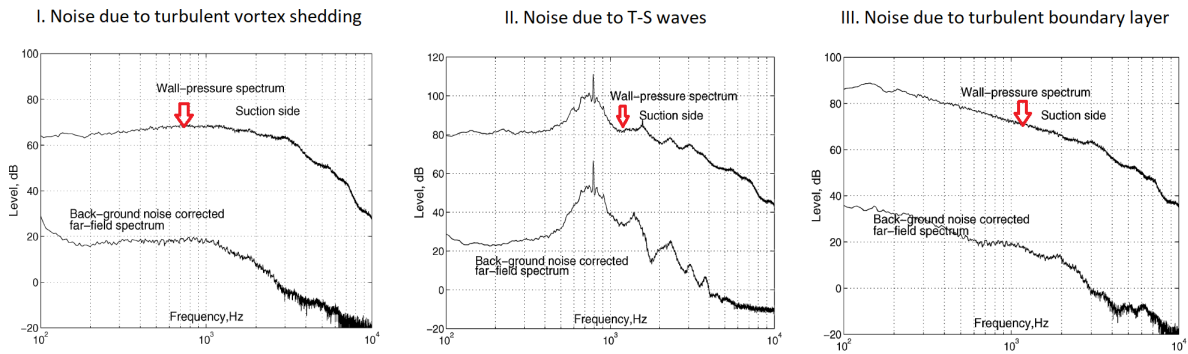


Figure 2.7 Noise radiation and wall spectra adapted from [73]

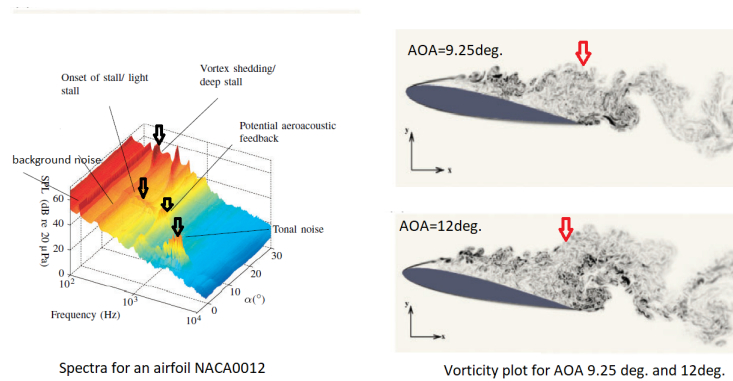


Figure 2.8 Noise spectra and contours of vorticity for NACA0012 adapted from [54]

Noise radiation due to stall :

As the angle of attack increases, noise levels start rising over background noise from the test setup. Paterson *et al.* [77] linked this noise generating mechanism to trailing edge noise that is mainly broadband in nature. However, in the case of light and deep stall where flow separates at the leading edge, a low frequency tonal peak is observed [75]. The occurrence of tonal peaks are due to

- Kelvin-Helmholtz instability
- Vortex-shedding

Chord-based Strouhal number agrees with the Strouhal number of the bluff body operating under vortex shedding region [54]. We intend to study fan noise at the design point where generally fan doesn't stall. Hence this noise source mechanism is reviewed briefly.

Noise due to tip flow :

In a wing, the flow locally separates near the tip forming a vortex. However, a tip flow noise is due to tip leakage formed between the casing and rotor for the turbomachines. This behavior is quite complex and will be studied in section 'Tip flow noise.'

The noise generated by an isolated airfoil placed under uniform flow and operated with a different geometric and aerodynamic loading, as discussed above, are likely addressed as "Self-noise mechanisms" [12].

B. Isolated airfoil in turbulent flow

In an automotive radiator fan, prominently three things can source turbulence on blades viz.

- presence of front grille and accessory components like horn, pedestrian safety beam, impact bar, etc. which may generate viscous wakes
- breaking down large incoming eddies by heat exchanger into small scale turbulence
- boundary layer turbulence formed in shroud gap or on walls of sealing- interacting with blade tips [40]

The turbulent patterns generated are such that either they impart random or periodic loads. Random loads produce broadband noise and periodic loads create discrete peaks in noise spectrum [28]. Therefore, to separate the effect of loads, noise generated by an airfoil in a turbulent flow is studied.

An airfoil scatters turbulent eddies convected by mean flow at a leading edge, generating broadband noise. Incident turbulence is composed of different length scales, which scatter in different manner at the leading edge. The random scattering produces unsteady lift forces or equivalent dipoles, which act as potential noise sources [76, 98]. The time-dependent velocity components normal to a leading edge cause variations in local lift fluctuations [40, 100]. The lift fluctuations scaling with increasing velocity lead to an increase in noise levels. However, fluctuations in angle of attack do not influence leading edge turbulence interaction noise [73, 76]. Moreau and Roger [73] observed that the CD

airfoil and the flat plate have almost similar radiation patterns despite slight asymmetry for the CD airfoil on the suction and pressure sides. Although the difference in radiation pattern is due to the camber effect, its influence on the noise spectrum is minimal. Changing the thickness of an airfoil reduced noise levels significantly, as observed in the NACA0012 case. Sharland [98] showed that leading-edge turbulence-interaction noise is higher than trailing-edge noise. Moreover, these random fluctuations interact with the span and adds up to the overall noise levels. Does it allude to us to introduce phase shift to create interference patterns? It is answered in the following section on the impact of sweep on noise source mechanisms.

The experimental techniques and published studies provide helpful insight into noise-generating mechanisms. However, isolating airfoil noise radiation from background noise is a challenging task. The uncertainty and difficulty associated with segregating aerodynamic parameters and their impact on radiated noise seek a simple analytical modeling approach. Therefore, a cost-effective, quick and reliable broadband noise prediction models have already been built using the knowledge of performed experiments [4, 6, 76, 89] which is discussed later in Chapter 3.

2.3.2 Discrete noise

Until now, the discussion is focussed on a random nature of forces acting on the surface. However, there are other mechanisms in which periodic forces impart on rotor blades that give rise to discrete frequency peaks in the noise spectrum. According to Gutin [39], a rotating propeller in a steady medium produces periodic disturbances by displacing the fluid around the blade. The so-called thickness noise contributes far less significantly than the periodic unsteady loads introduced by inflow distortion and incident atmospheric turbulence in a low speed fan [98]. Sharland [98] described discrete noise generating mechanism as an interaction of the elemental air pockets with a rotating blade or its associated pressure field. A blade experiences periodic fluctuations of mean forces that ultimately result in noise production. The fundamental frequency of excitation at which the blade passes through the elemental disturbances, i.e., rotational frequency times number of blades, is referred to as blade passing frequency (BPF). BPF and its harmonics depend upon the shape of a disturbance and a period compared to one periodic cycle of a blade. For a rotating fan, the recurring disturbances generally originate from–

1. Inflow distortion
 2. Tip flow interaction with blades
 3. Potential rotor stator interaction
-

The stator or struts can be placed before or after the fan. Based on their position, viscous wake either from strut or from rotor generate unsteady and spatially non-uniform disturbances causing force variations either on the rotor or on strut [28]. These force fluctuations produce tonal and broadband noise. Since this study is focused on noise due to rotor only, the rotor-stator interaction noise mechanism is not discussed here.

Inflow distortion

While the fan rotates in an unsteady, non-uniform and/or inhomogeneous inflow, blades experience periodic and random forces. Blade interaction with periodic disturbances produce discrete peaks and random interactions generate broadband noise [40, 100]. Tonal or BPF peaks are present under non-uniform inflow conditions while in steady and uniform flow, discrete peaks are absent [28, 64, 106]. In experiments, turbulence is produced by placings grids. These grids produce uniform and isotropic turbulence [8, 41], ergo, we intend to model it with isotropic turbulence. However, the importance of anisotropic turbulence is demonstrated first by Hanson [40] and then by Signor [100]. The eddies passing through a blade passage are stretched in an axial direction (refer Fig. 2.9). As a result, the blade experience more velocity fluctuations in the transverse direction than in the streamwise direction. This is because a stretching eddy preserves an angular momentum by amplifying its transverse velocity fluctuations. In fact, the size of an eddy decides the discrete peak shape. If eddy is smaller than rotor diameter, a sharp peak is noticed. In the case of bigger eddies, they are chopped multiple times by blades and as a result of that noise spectrum traces heap at the fundamental frequency and its harmonics instead of sharp peaks as shown in Fig. 2.10. If blade loads are perfectly coherent, the loads unite to form a tonal peak. However, for partially coherent loads, the heap in a spectrum can be witnessed [40].

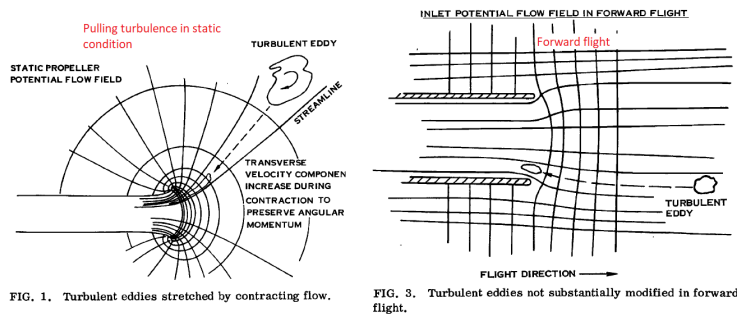


Figure 2.9 Sketch showing incoming turbulence eddies adapted from [40]

During experiments in an anechoic chamber, even if the steady and uniform flow is assumed, due to suction created by a fan in a room can generate large-scale eddies [104].

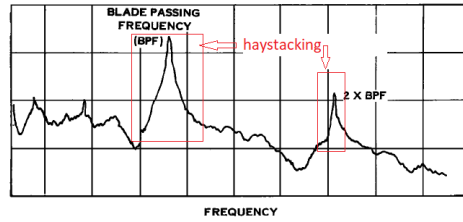


FIG. 2. Noise spectrum of lift fan (Ref. 4).

Figure 2.10 Noise spectrum of lift of fan adapted from [40]

Alike Hanson's observation of an eddy stretching [40], Sturm and Carolus also visualized a helical vortex stretching while entering into a fan impeller using smoke as shown in Fig. 2.11. The only apparent difference in their studies seems to be in the source of inflow distortion. Eddies in atmospheric turbulence were replaced by quasi-steady, self-induced, coherent structures in an incoming flow. The presence of coherent vortices and their interaction with the blade were reinforced by performing modal analysis. They assumed that finite azimuthal peaks (modes) in circumferential wave patterns exist, which interacts with a blade periodically to generate BPF. Investigating further, they analyzed recorded pressure on the surface of a blade using the cross-correlation technique, which confirmed a more vital interaction between the leading edge of a blade and the modes. However, they did not explain the reason behind the origin of modal structures, their analysis points towards tip leakage vortex formation instead of indicated inflow distortion. This observation is confirmed after 45 years by Zhu *et al.* [127] in their tip vortex interactions by conducting similar modal analysis in their study. The above scrutinizing discussion points that tonal noise is due to correlated blade responses with coherent vortices.

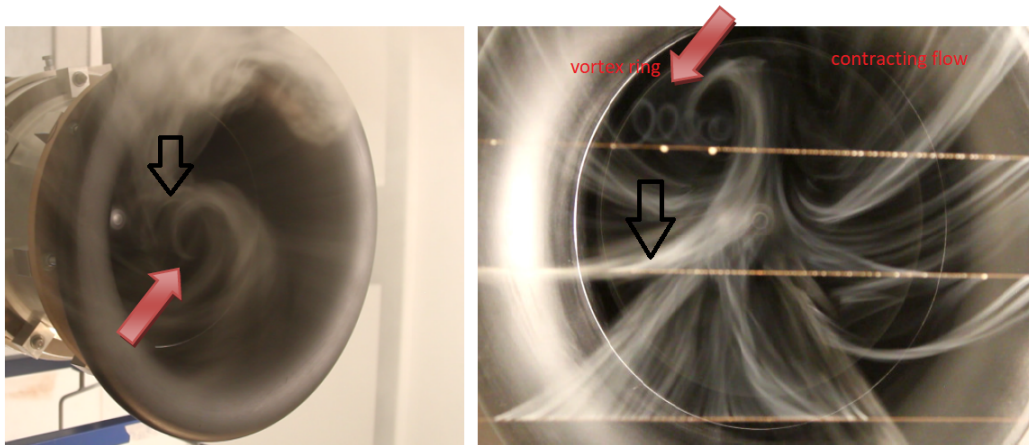


Figure 2.11 Smoke visualization of contracting flow adapted from [103]

2.3.3 Tip vortex noise

Longhouse(1978) performed experiments on an axial flow fan to visualize tip flow using the smoke visualization technique. During the test high degree of turbulence was observed near the tip region of a suction side. He apprehended it as a tip recirculation which is exemplified by Fig. 2.12. The further discussion illustrates that tip vortex formed under favorable pressure gradient conditions interacts with the trailing edge and impacts the leading edge (pressure side) of the adjacent blade near the tip region. Hence to justify the presence of tip vortex, he varied tip clearance from 1.33%C (0.76mm) to 0.09%C (0.05mm) (C-blade chord) and ran similar tests to measure emitted noise level. The aerodynamic efficiency of a fan is dropped with increasing tip gap and overall noise is significantly reduced for lower tip clearance [10, 30, 32, 52, 61]. Compellingly, tonal peaks present at BPF for 0.09%C clearance at blade passing frequency are shifted for 1.33%C case. Higher clearance reinforces the presence of more broadband energy in the low frequency region. Recently, a similar finding has also been reported by Zhu *et al.* [127] who first experimentally and later numerically investigated tip flow noise source with more advanced test setup and surface pressure measurements. Despite different fan design and experimental setup (Fig. 2.13), Zhu *et al.* and Longhouse had indeed the same observation regarding shifting of tonal peaks away from BPF when tip clearance was increased. In addition Zhu *et al.* had pinpointed the presence of those subharmonic peaks, which are equal to 0.74BPF (blade passing frequency) and its harmonics.

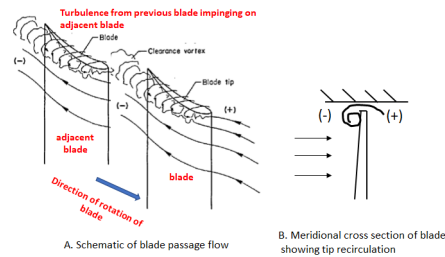


Figure 2.12 Tip flow representation adapted from [61]

Longhouse further added that flow in front of a blade is highly unsteady and monopole type for the heavily loaded blade. Hence dominant noise source was present due to mass fluctuation possibility in front of the blade. He also mentioned that non-rotating instability was responsible for tip leakage noise. But this contradicts with Zhu *et al.*[127] modal analysis. Their study showed that rotating instability(RI) was responsible for tip noise generation. The term rotating instability was first introduced by Kameier and Neise in 1997 [45] while performing experiments on a low speed high pressure axial fan. In the noise

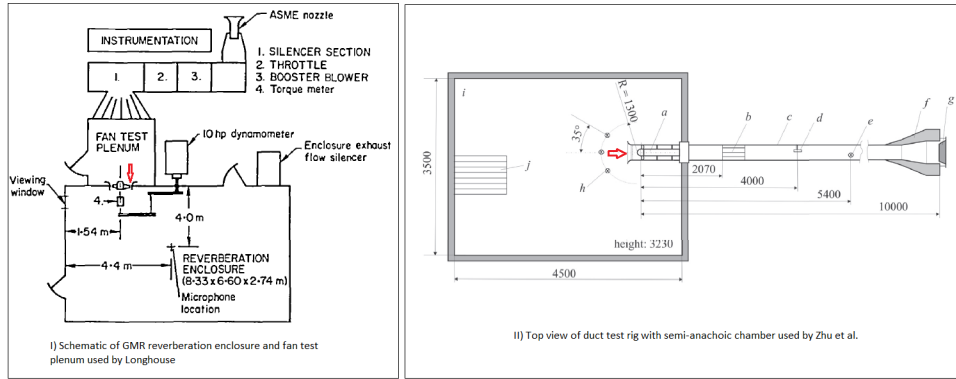


Figure 2.13 Test set up adapted from [61, 127]

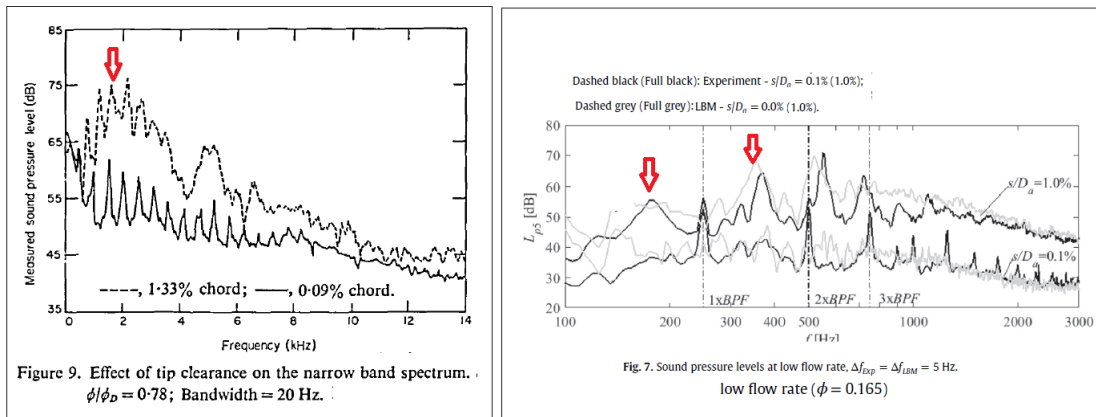


Figure 2.14 Noise measured for different tip clearance adapted from [61, 127]

spectrum, they mentioned that blade passing frequency peaks were observed because non-uniformities of intake flow or inflow turbulence were present and tip clearance noise is independent of inflow turbulence. Rotating instability is either due to fluctuating flow disturbance or because fluctuating source mechanisms rotate relative to the blade. It is interesting to note that RI moved to a low frequency region when throttling is increased. Another head-turning point is for smaller tip clearance rotating instability component appears in wall spectra only. This means that RI noise is either masked under other frequencies or not strong enough to account when noise spectra are measured at observer location. In addition, hotwire measurements performed in the blade tip region and within tip clearance showed that RI was observed under reverse flow conditions in the tip gap region. Circumferential tip vortex separation occurred under a situation when the reverse flow was strong enough to eradicate the absolute component of axial velocity of tip gap flow [44]. Powerful interaction of vortex separation with individual blade happened when the azimuthal wavelength of shed vortices is equal to blade spacing which produced significant

tip noise [44, 63]. When flow rate was reduced, the flow separation region was extended over the entire radius along the blade span [44, 45], which was also witnessed in smoke experiment [61].

Longhouse [61] had scrutinized smoke turbulence behavior traveling spanwise extent when fan throttling increased (lower flow rate and high pressure rise). With acenaphthene patterns on the blade, he stated that increased turbulence is due to tip leakage vortex causing high turbulence on the pressure side of an adjacent blade for the highest loading. The genesis of increasing tip vortex size with reducing flow rate is engaging with results of Magne *et al.* [63] URANS simulation, which demonstrated tip behavior for increased loading shown by Fig. 2.15. Fukano *et al.* [30] also confirms this observation with experiments conducted at design and off-design conditions. The tip vortex extends along the span as the flow rate is reduced to a lower flow coefficient. Fig. 2.16 demonstrates two effects: i.e., 1. As the tip gap is changed from 2 mm to 4.5 mm for $\Phi = 0.31$, the vortex region extended more along the span (see a and b); 2. In the case of a 2 mm tip gap and increased flow coefficient ($\Phi = 0.39$), the vorticity region has reduced than $\Phi = 0.31$ (see a and c). To further analyze the investigated spectrum of velocity fluctuations, refer to Fig. 2.17. They found that for $\Phi = 0.39$ and 2 mm tip gap, velocity fluctuations appeared approximately at 400 Hz. However, for $\Phi = 0.31$ and the same tip gap, the peak moved to the lower frequency. When the tip gap was increased to 4.5 mm, the peak moved further towards the lower frequency. This explains that as the flow rate is reduced, tip vortex size increases and velocity fluctuations move towards lower frequency. The increasing tip vortex size explains its dominance in the form of the subharmonic hump in the noise spectrum as shown in Fig. 2.17 [30]. For higher flow rates, tip leakage is significantly low and fluctuations caused by tip flow interactions are contributing to broadband noise [66]. In addition, Fukano *et al.* [30] studied the evolution of spectral peak by taking the cross-correlation between two signals recorded by two hot wires sensors (i.e. one fixed and other rotating). Delayed time was calculated using peak correlation. Delayed time represents the peak of spectra of velocity fluctuations (for tip gap 2/4.5 mm, delay time 0.004/0.006 s corresponds to 250/160 Hz). Fig. 2.18 exhibits the same correlation at different span positions for 2 mm (a) and 4 mm (b) tip gaps and their corresponding tip vortices rotating anticlockwise represented by contours of relative velocity, respectively. Fukano tried to explain the tip flow noise mechanism using these observations. The velocity fluctuations scale with fan rotational speed and with flow coefficient (refer to Fig. 2.19). As observed by Longhouse [59], Zhu [127], Marsan [66], Fukano [32] also stated that the tip vortex interacts with the blade tip producing noise. Despite the fact that three different tip vortex noise sources illustrated by You *et al.* [120], Fukano addressed unambiguously only

the noise formed due to a tip leakage flow in a free tip ducted fan and traced it on the noise spectra in the form of peaks.

On the other hand, is it logical to compare tip vortex behavior of fixed shroud fan with ring fan?

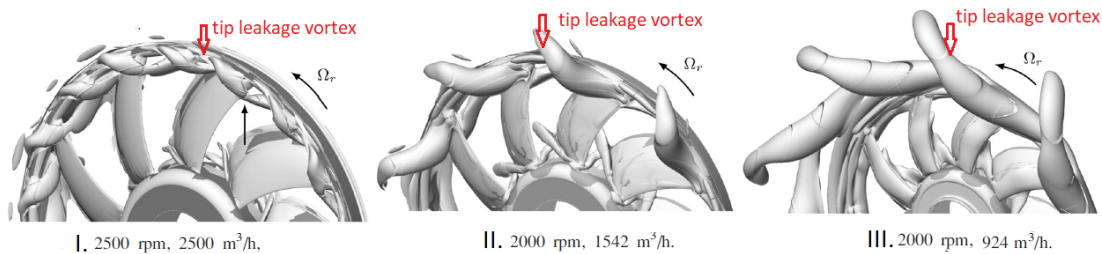


Figure 2.15 Tip vortex behaviour with decreased flow rate (increased loading) simulated by Magne *et al.* [63]

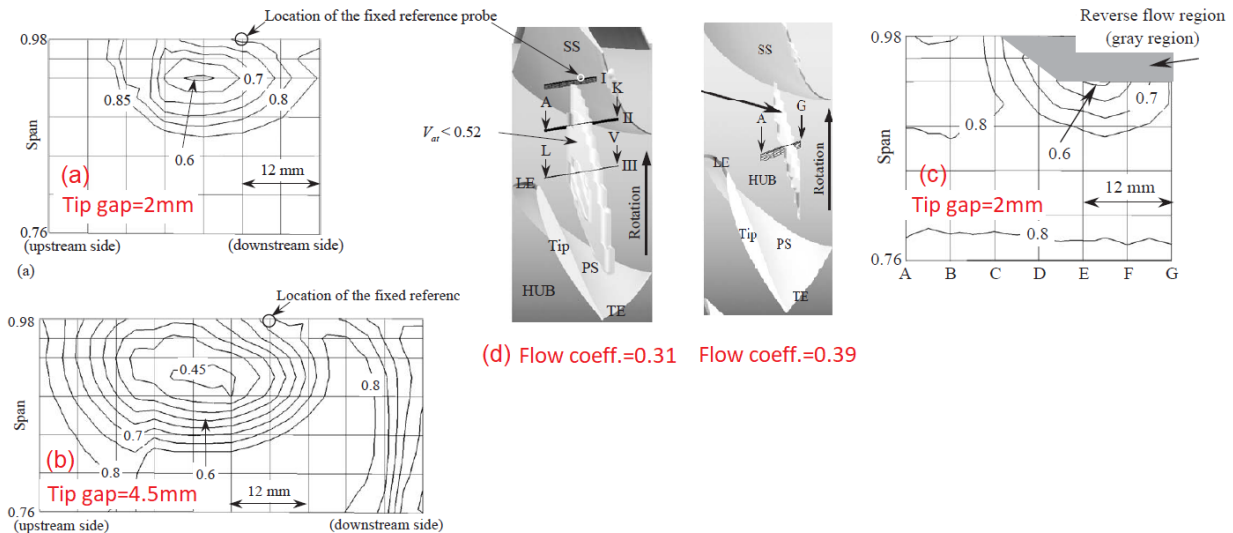


Figure 2.16 Effect of tip gap and flow rate on tip leakage vortex size [30]

Longhouse [61] anticipated accurately that noise augmentation because of the increase in tip clearance was due to tip vortex interaction with the blade. Therefore he hypothesized that coherent tip vortices were responsible for noise generation. Hence he put serration on the tip to disturb the flow, but it increased the noise instead of reducing it. Another configuration is tested by providing multiple slots on the outer portion of the span in the flow direction by hoping that it could reduce the tip vortex interaction with the blade trailing edge in the presence of bleeding flow through multiple slots. Nonetheless, the noise did not change. In the third configuration, to move the tip vortex away from the blade, a suction side shroud was used, which resulted in a slight increase in noise. He

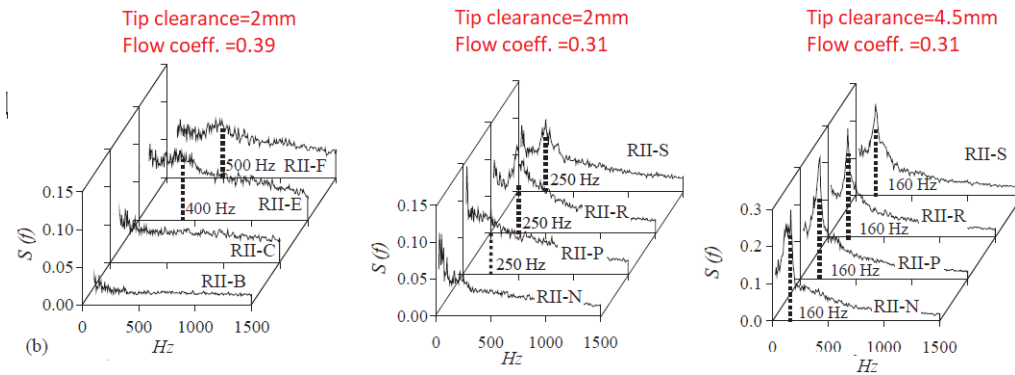


Figure 2.17 PSD of fluctuating velocity at 0.96span [30]

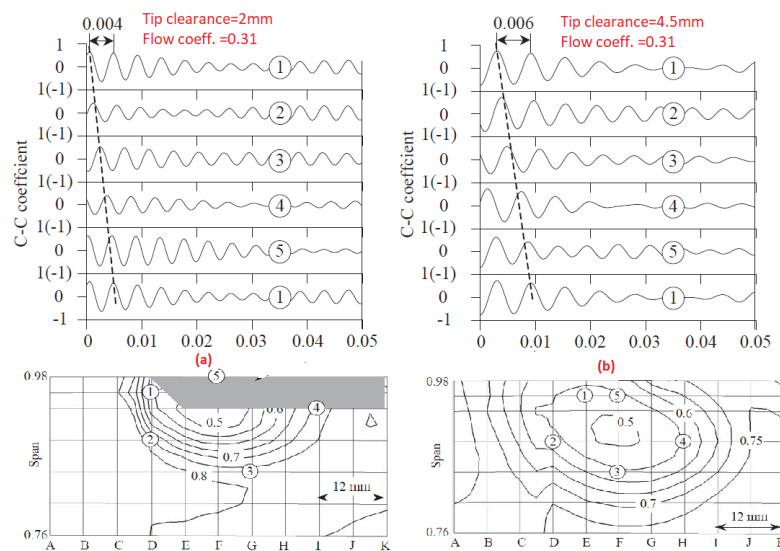


Figure 2.18 Cross correlation of signal recorded on fixed frame [30]

discerned that control of blade tip flow is essential to reduce tip noise, which will prevent tip vortex interaction with the adjacent blade. The only method was to use "zero clearance." Therefore he installed a rotating shroud on blade tips which is known as a fan ring these days. The ring did not forbid flow leakage through clearance, but it could escape direct interaction of blade. Rotating ring shroud was already used in screw propellers to create slip between blade tips and surrounding water [85]. However, the addition of ring surface introduced potent noise sources due to leakage flow unsteady interaction with the incoming flow or by flow separation at the inlet of the rotating ring, which can be controlled by properly designing ring shape. Therefore Longhouse [61] designed a ring inlet contour with a larger radius. While avoiding flow separation on ring surface, increased surface contact with an incoming flow formed boundary layers which rotate with ring and resulted in built-

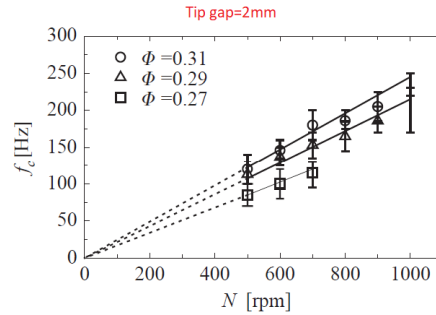


Figure 2.19 Relation between peak of velocity fluctuation frequency spectra and fan RPM [30]

up of viscous drag [42, 61]. This modification resulted in fan efficiency loss and an increase in power demand to overcome extra drag force; ergo short ring was designed [61]. He had shown that a fan with a ring increased fan efficiency and reduced noise level compared with a fixed shroud fan (no ring). We can comment that tip leakage vortex is present for both fans (fixed shroud and ring) with this discussion. They behave similarly with increased throttling as mentioned by Magne *et al.* [63], Fukano *et al.* [30] and Longhouse.

In fact Magne *et al.* observation about tip vortex is arresting. His numerical analysis on a blade passage flow shows that the coherent tip vortices impact the blade surface slower than the fan rotational speed and backflow angular velocity. Piellard *et al.* [81] analyzed further on sub-harmonic humps and calculated speed of tip vortex rotation followed by calculating its interaction frequency. They used isosurface of λ_2 structures colored with tangential velocity and calculated its histogram. Zhu *et al.* [127] used modal analysis to calculate the interaction frequency of a tip vortex using cross power spectral density of wall pressure recorded on a blade surface. These described methods help identify interaction frequency that corresponds to humps in the noise spectra.

The above discussion manifests the presence of tip vortex and noise caused by its interaction with blades. However, tip vortex formation and its destruction mechanism are still unknown. Tip noise seeks further flowfield insight in tip gap and blade passage. The limited data recording capability of experiments inhibits the exploration of tip flow noise mechanisms. In this case, analysis with computational fluid dynamics is a beneficial tool that provides a platform to discern flow fields in a detailed manner.

Based on the above discussion, generalized noise sources are indicated on a blade as shown in Fig. 2.20. However, these sources are impossible to segregate in a noise spectrum. Therefore, in the absence of tip flow and inflow distortion, Moreau and Roger [74] used Amiet's model to compare broadband noise contribution from trailing edge and leading

edge. Wall fluctuations measured from experiments supplied to Amiet’s model. The study ignores turbulent boundary layer separation at the leading edge, vortex shedding in the boundary layer, laminar boundary layer instabilities since those conditions rarely occur in a fan mounted on the vehicle. The small-scale turbulence is generated when air passes through series of heat exchangers present just before the fan. It causes a turbulent boundary layer on the blade surface that separates at the trailing edge. Sanjose and Moreau [90] showed the behavior of two noise mechanisms varying with a flow rate in such operating conditions. They inferred that the leading edge noise dominates when the flow rate is reduced from the design point, while for higher flow rates trailing edge noise governs the spectra. In this study, the fan is operated at the design point. Hence, we are more concerned about the leading edge broadband noise mechanism over others.

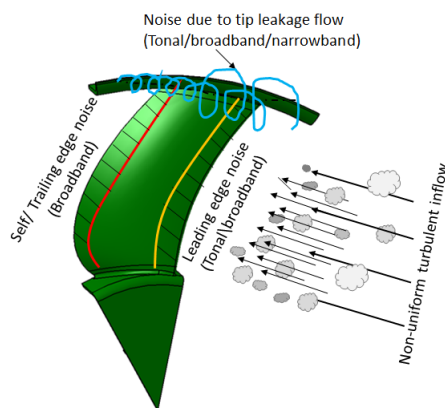


Figure 2.20 Noise source mechanisms in a low speed fan

In general, incident turbulent eddies in phase over the span are chopped simultaneously to produce raucous LE noise. The fundamental physics principle of wave interference can address this noise problem by creating the de-phasing effect. It is achieved by providing non-linear interfaces with LE, called– sweep. Sweep creates primarily phase-shift effects causing a delay in wave propagation. Secondly, it changes the angle of propagation since acoustics waves radiate parallel to LE. Although swept blades contribute to subside noise, the process isn’t very direct because sweep modifies the aerodynamic loading, which influences the noise sources. Therefore, the next section is focused more on flow behavior in the presence of sweep and its ability to handle different noise source mechanisms.

2.4 Blade sweep and aerodynamic behaviour

The first appearance of sweep is observed in airplane wings (Fig. 2.21). Swept wings helped in improving the lift-drag ratio. Although earlier in turbomachines, sweep and

dihedral were an accidental by-product of a manufacturing process, later applied purposely to enhance aerodynamic performance. Nonetheless, in the turbo-machines definition of sweep or lean varies according to its applications. In this case, we have considered low speed axial machines only.

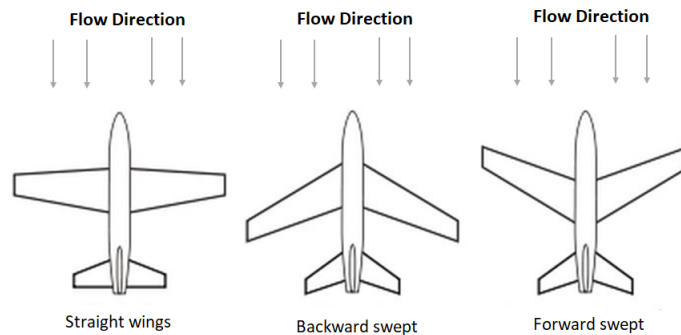


Figure 2.21 Sweep in wings

Sweep applied for wings, identifies as the movement of wings towards or away from flow direction (Fig. 2.21) which is adapted for the first time by Smith and Yeh [102] for axial turbomachinery. Let's consider a simple definition on a broad level. While a blade moves along a chord towards the direction of rotation, it is called 'Forward sweep.' On the contrary, when a blade moves opposite to the direction of rotation, it is called 'Backward sweep.' An international patent published by Kimball [48] defines forward blade sweep angle concerning leading-edge, and a US patent published by Gray [37] also measure sweep angle at the leading edge for the backward skewed fan. However, angle definition is not elaborated. They did not mention it in their article, but are they trying to link the leading edge to its respective noise mechanism?

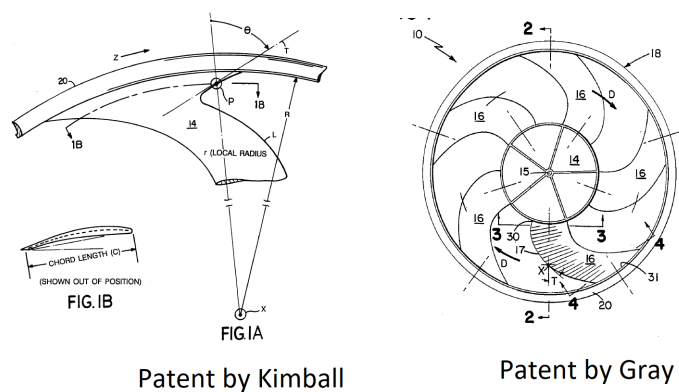


Figure 2.22 Definition of sweep angle by Kimball and Gray [37, 48]

In the literature, the geometrical definition of the sweep varies with respect to choice of references such as blade stacking line, leading edge line ... [9, 24, 31, 69, 108, 109, 111, 116, 124]. The ambiguity in sweep angle definition found in literature and noticeably in patents demands properly explained and meaningful sweep angle definition. Hence, we made an effort to address it in Chapter 3.

The non-linear leading edge induces a spanwise/radial flow component, resulting in modifying aerodynamic load along the blade span. The following section describes altered loading and its link to change in - 1. meridional flow 2. blade to blade flow and 3. boundary layer growth on a blade surface [116].

2.4.1 Effect of blade sweep on aerodynamic behaviour

Forward sweep

Vad *et al.* [108, 109, 111] studied different applications of axial rotors and impact of forward sweep on their performances. For axial pump and fan, for partial loads (below design flow rate), the total-to-static efficiency and pressure rise increased [9, 68, 69]. The contrary, according to Zenger's study [124] fan efficiency and pressure rise has increased for higher flow rate and reduced for lower flow rate. Although the efficiency and pressure rise behaviour is sensitive to the design method, extension of stall region to further lower flow rate is unanimously accepted by Corsini *et al.* [23, 24], Beiller [9] along with Vad *et al.* [108] and Zenger [124].

Zenger recorded azimuthal phase-locked ensemble-averaged distribution of meridional and radial velocity during experiments. For forward sweep blade (FS), axial velocity near the tip is significantly increased and slightly reduced near the hub on the suction side and remains same as of unswept blade (US) on the pressure side Fig. 2.23 . This measurement correlates with the sketch presented by Vad *et al.* [108]. Forward sweeping of a blade causes earlier near tip incoming flow interaction than close to the hub, reflecting non-uniform axial velocity distribution along the span at a leading edge. Although Zenger designed FS and US blade for a similar angle of attack, axial velocity variation hints deviation in the angle of attack from its design value for FS. It can also be understood from velocity triangles and can be agreed with the observation by Vad *et al.* [108]. Previously Corsini *et al.*, Beiller and Carolus measured velocity components near the trailing edge. However, it seems that measurements at the leading edge also supply helpful information about flow and blade sweep behaviors.

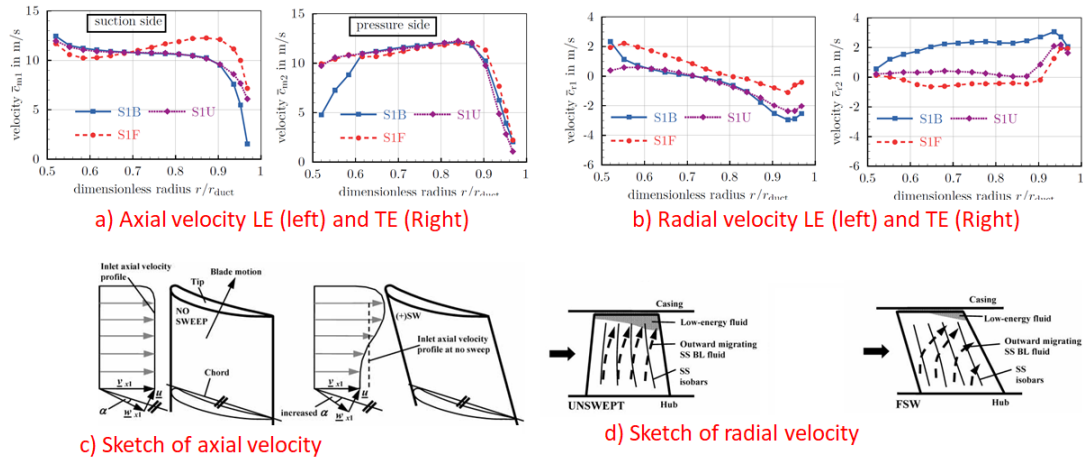


Figure 2.23 Axial (left) and radial (right) velocity by Zenger and respective sketch by Vad *et al.* [108, 125]

Negative radial flow due to forward sweep (C_{r2}) agrees with sketch given by Vad *et al.* as shown in Fig. 2.23. According to free vortex theory, linear distribution of a radial velocity suggests design accuracy, but inflection near hub and tip indicates secondary flow dominance, observed in radial velocity plots at LE in Fig. 2.23. Similar flow behavior is also observed in our study illustrated in Chapter 5.

When the radial equilibrium of the unswept fan is modified after the addition of the forward sweep, it reduces boundary layer thickness. It helps in uniform pressure distribution over the span. Reduced pressure gradient along the span prohibited radial migration of boundary layer that results into minimized total pressure loss [23, 24, 110, 116]. This not only helps in extending the stall region to a lower flow rate but also increases the efficiency [23, 24, 110]. The near tip boundary layer fluid accelerates which also can be accounted for extended stall region [23, 24, 110]. However, we can confirm these conclusions by extracting boundary layer thickness for FS and US cases. Conversely, if forward sweep is applied to perfectly achieved radial equilibrium for unswept fan, it rather deteriorates aerodynamic performance. Because relative velocity makes an angle $(90 - \lambda)$ with the span, in this case, λ is sweep angle, and incident streamwise component becomes $\sin(90 - \lambda) = \cos \lambda$ resulting in the reduction of the lift by $\cos \lambda$ times per unit span. This phenomenon is generally known as the $\cos \lambda$ effect. However through simulations, Beiler and Carolus [9] showed that pressure rise reduces by a factor $(\cos \lambda)^{0.62}$ instead of $(\cos \lambda)$ [102, 116], which is a deviation from theoretical analysis. The change in exponent factor can be linked to reduced secondary flow losses. Therefore, we intend to verify this exponent factor in our study.

Wright and Simmons [116] talked about boundary layer migration over a blade which is very well schematically explained by Zenger [124] as shown in Fig. 2.24. Wright and Simmons commented that the boundary layer thickness could be increased or decreased depending upon the sweep angle and shape of a blade planform. Due to blade rotation, a centrifugal force acts on the boundary layer, which triggers radial flow movement. Forward sweep limits radial migration of the boundary layer. Zenger tried to link travel of the boundary layer and velocity components with a trailing edge noise mechanism, explained later.

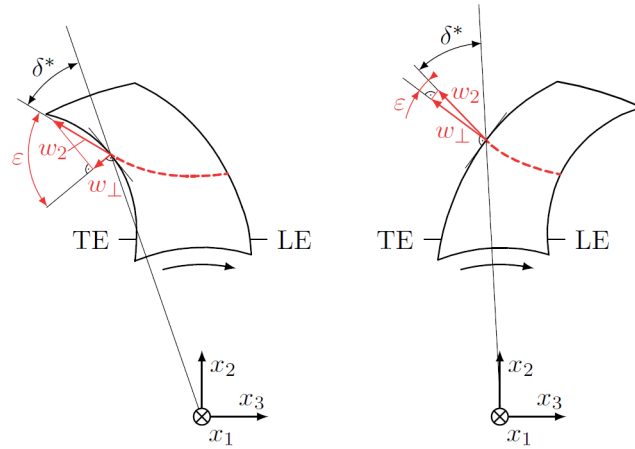


Figure 2.24 Representation of boundary layer on a swept blade [124]

Moreover, the above observations don't confirm the aerodynamic benefit of the forward sweep. Therefore, this study has selected two different families of fan designs to address the ambiguity i.e one with forward sweep and other with forward sweep but its design corrected for aerodynamic losses.

Backward sweep

Zenger showcased thicker wake with axial velocity and turbulent kinetic energy (k_2) contour plots near TE. It suggest thicker boundary layer formation in backward sweep fan than forward or unswept fans. Higher TKE (k_1) at the leading edge near the tip indicates larger local shear and turbulence formation. The radial migration of fluid is more severe in backward sweep than in forward sweep and is evidenced by the increase in radial velocity as observed in Fig. 2.23. These flow features trigger loss in a pressure rise and a decrease in efficiency. However, the discrepancy in behavior is observed in backward sweep performance. Although backward sweep performs better from design point to higher flow rate, [9, 124], we will investigate the causes at design point only in this study.

2.5 Effect of blade sweep on noise source mechanisms

US patent by Gray [36] refers to forward sweep fans as low noise fans. He designed a swept blade fan to tackle high turbulence generated due to radiator and managed to reduce fan noise from 72 dBA to 64 dBA. However, he didn't illustrate the link between noise reduction and the aerodynamic behavior of source mechanisms.

2.5.1 Forward sweep

Forward sweep reduces boundary layer thickness [108, 116, 124], which will directly reduce broadband noise [11, 31, 31, 98, 116]. Nevertheless, based on Curle's analogy [25], Zenger [124] relate trailing edge noise to radial migration of boundary layer fluid and angle between outlet relative velocity (w_2) and velocity perpendicular to trailing edge (w_\perp) (refer to Fig. 2.24). For forward-skewed blade, w_\perp is higher than for backward-skewed blade, which can cause increased broadband noise levels. This is clearly observed in far-field noise spectra of forward skewed fan (S2) above 2 kHz, but a slight difference is observed for forward swept S1 fan as given by Fig. 2.25. He used the beamforming method to trace the sources on the blade and the source is visualized with the central frequency of the third-octave spectrum. As observed in Fig. 2.26, noise sources shifted to the trailing edge as frequency is increased from 2 KHz to 6.3 KHz however, most of the noise sources are concentrated in the tip region. This indicates strong tip vortex interaction with adjacent blades or a blade itself. The beamforming method indicates noise source location, but doesn't provide any

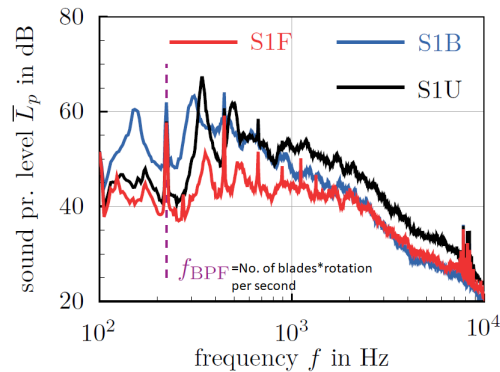


Figure 2.25 Noise spectrum for forward (S1F), backward (S1B) and unswept (S1U) blade fan under free inflow condition [124]

information on its origin.

For free inflow conditions, the noise emitted from the forward swept blade is far below up to 2 kHz than the unswept or backward swept blade. However, the broadband noise level

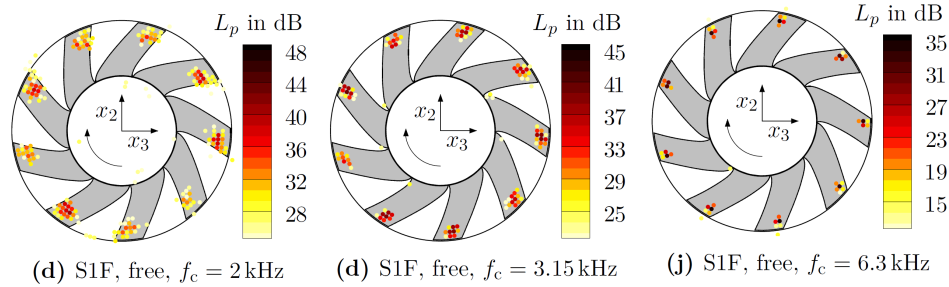


Figure 2.26 Noise source localization with beamforming under free inflow for forward sweep fan [124]

in the higher frequency range matches for backward and forward sweep [124]. Despite their disagreement below the low-frequency regime, they agree on the overall sound power level. In general, the sound power level is lowest for the forward swept blade than the backward swept blade and unswept blade. The critical observation is that for the forward sweep, high frequency (above 2 kHz) sources are localized near tip at leading edge; however, for the backward swept rotor, source distributions along span changed concerning the frequency (refer to pages 240, 241 from [124]). The cause of the increase in noise levels is still unknown. Hence, it demands further exploration of multiple designs with different sweep angles. The study published by Beiler and Carolus [9], Bamberger and Carolus [7] also agreed on significant noise reduction by forward swept blade fan compared with backward swept blade fan.

2.5.2 Backward sweep

Fukano *et al.* [31] commented that the backward swept impeller did not show any noise reduction when compared with the forward swept blade. However, Gray [37] showed noise reduction with the backward skewed fan by 6 dBA. However, the sources are located slightly at lower radius than in forward sweep. In backward sweep also most of the sources are traced near the tip region as shown in Fig. 2.27 Wright and Simmons [116] stated that high-frequency broadband noise associated with a trailing edge might increase. His observation does not agree with experiments by Zenger [124]. According to Zenger, reduced noise levels are due to smaller w_{\perp} fluctuations for the backward skewed than for the forward skewed blade (Fig. 2.24). Therefore, extracting boundary layer thickness and edge velocity will act as added proof.

In conclusion, there are evidences present in literature about ability to reduce noise by using sweep. However, previous studies don't show how sweep aerodynamics is linked to noise. Most of the studies are performed on different fan designs where design parameters

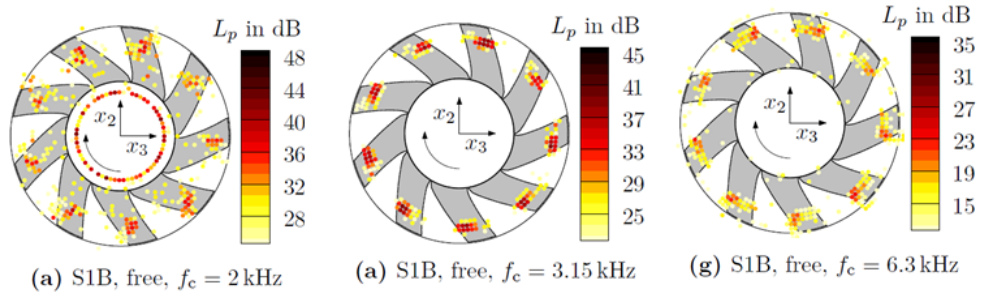


Figure 2.27 Noise source localization with beamforming under free inflow for backward sweep [124]

vary widely from one to another. The LE sweep is supposed to influence leading edge noise mechanisms but no study confirm the benefit of using sweep on LE broadband noise. Moreover TE noise is assumed to be least important in automotive fans based on previous discussion but it seems sweep drastically modifies its sources. Nevertheless, observation of variation boundary layer thickness in presence of sweep and its sole impact on noise isn't confirmed yet. In addition, the recent development showed that sub-harmonic humps are generated due to tip flow interaction with blades. The previous studies have completely unaware of tip flow noise mechanism and lacks the understanding on how sweep can influence tip flow noise.

2.6 Summary

Automotive engine cooling fans are low-speed axial machines that operate in the range of transitional to turbulent and subsonic flow. They generate both tonal and broadband noise. Tonal noise is a result of non-uniform flow or periodic interaction with surrounding elements. Tip flow interactions can emit noise in the form of broadband, tonal and/or sub-harmonic humps. All noise source mechanisms and their indicative presence are marked over fan using Fig. 2.2 and Fig. 2.20 respectively. From Fig. 2.20, it is understood that non-orthogonal interaction of turbulence with leading edge causes de-phasing of disturbances which results in weak acoustic wave propagation. This de-phasing is achieved with LE blade sweep. Until now, the blade sweep angle is defined using a blade stacking line but the noise radiation is directly influenced by the angle made by blade LE with incoming turbulence. Therefore, the efforts are focussed to define sweep angle by taking LE and incoming flow in the relative reference frame.

Aeroacoustic is always linked with the aerodynamic behavior of an axial fan. Therefore, in section 2.4.2, sweep influence on blade aerodynamic performance is explained. Theory

shows that in presence of sweep the spanwise lift reduces by " $\cos \lambda$ " times and therefore sweep deteriorates the pressure rise of a fan. Beiller and Carolus [9] suggested a correction factor of $\cos \lambda^{0.67}$ based on their studies. However, the re-usability of the exponent factor isn't validated for other designs. The previous studies were conducted on multiple designs where design parameters vary along with sweep. Moreover, the research is susceptible in usage of forward and backward sweep for noise reduction since it is observed that noise benefit pertains to the design and operating condition of the fan. Therefore, it is very difficult to draw definite conclusions that are caused by sweep alone.

This thesis aims to gain knowledge of fan noise behavior in presence of sweep. Therefore, two fan families are selected where only sweep-related parameters are modified. The first family is ring fans designed with a controlled vortex theory. In these fans, only forward sweep angle is added to the base design and the remaining parameters are kept the same. The objective of this selection is to verify $\cos \lambda$ and its exponent factor on pressure rise at the design point and forward sweep influence on LE noise.

The second family is free tip fans designed with free vortex theory by applying $\cos \lambda^{0.67}$ factor to recover pressure losses caused due to sweep. It consists of unswept, backward and forward swept fans. The main objective of this study is to identify which noise mechanisms are altered in presence of free inflow conditions. How forward and backward sweep affects LE noise mechanism and tip flow noise. How to trace each noise mechanism in the spectra and how sweep modifies their levels or location in the noise spectra. Which fan i.e backward or forward sweep performs better in terms of aerodynamic performance and noise and how?

In the end, confusion in the literature about the boundary layer thickness, momentum thickness and edge velocity for forward and backward sweep will be addressed by extracting those parameters from simulations and their influence on trailing edge noise is assessed using analytical model. Besides, this study will also illustrate tip flow vortex and blade sweep interaction which is missing from the literature.

To summarize, the literature review conducted in this chapter establishes a firm background to analyze sweep influence on noise source mechanisms emphasizing LE broadband noise and tip vortex interaction in detail.

CHAPTER 3

Noise Prediction Tools

State of the art exhibits various physical processes in any low speed axial fan responsible for noise generations. The evidence from literature also reveal that the acoustic sources link to the aerodynamic flow field developed around the fan blades. Hence, to capture those intricate details using high fidelity computations, sections 3.1 and 3.2 are dedicated to explaining methods suited for low Mach number and moderate Reynolds number flows. Computational aeroacoustics (CAA) elaborates on direct and hybrid approaches in section 3.3. Once we secured profound knowledge of noise source modeling and noise radiation analogies in the far-field, we used them to build a simple analytical model for the swept blade in section 3.4. Finally, the tool is validated using an academic test case in section 3.5.

3.1 Lattice Boltzmann Method (LBM)

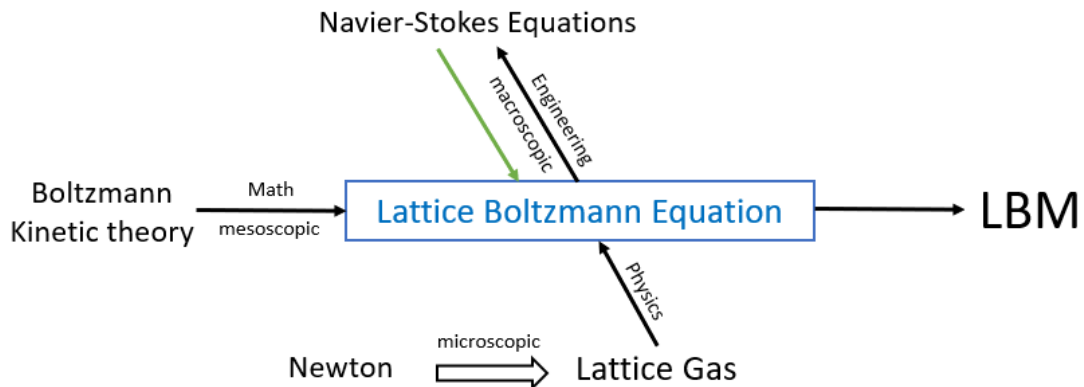


Figure 3.1 Three ways to Lattice Boltzmann Equation (LBE) [94]

Historically, Lattice Boltzmann Equation (LBE) can be derived using three different ways, as shown in Fig. 3.1. Generally, Navier Stokes Equations (NSE) are used in engineering applications. They are basically derived from Lattice Boltzmann equations using Chapman-Enskog expansion with Lattice Gas Automaton (LGA) as its precursor. LGA is derived from governing equations based on Newton's dynamic using a microscopic approach based

on molecular interactions. In principle, one can directly use Boltzmann kinetic theory of gases to describe fluid behavior using conservative interactions of molecules. The mesoscopic (scale between macroscopic to microscopic) kinetic theory comprises the distribution of particles in a gas that evolves on time scales around mean collision time. We can write a continuous Boltzmann equation as follows:

$$\frac{\partial f}{\partial t} + \xi_\beta \frac{\partial f}{\partial x_\beta} + \frac{F_\beta}{\rho} \frac{\partial f}{\partial \xi_\beta} = \Omega_c(f) \quad (3.1)$$

where $f(x, \xi, t)$ is the particle distribution function in the velocity space ξ . The first two terms on the left hand side (LHS) represent the distribution function being advected with the velocity ξ . The third term represents forces affecting velocity. $\Omega_c(f)$ is the source term representing local redistribution of f as a result of particle collisions, known as collision operator. This original collision operator is a bit complicated and cumbersome, calculated by taking double integral over velocity space. While one can solve the advection term in Eq. (3.1) in the absence of external force in a linear manner, the advection term $(u \cdot \nabla)u$ in NSE makes the equation non-linear. LBM uses discretized version of Eq.(3.1) where f is replaced by discrete velocity distribution function f_i , and velocity with $\xi_i = (\xi_{ix}, \xi_{iy}, \xi_{iz})$ on physical space x and time t . By discretizing the Boltzmann equation in velocity space, physical space, and time, we find the lattice Boltzmann equation as

$$f_i(\vec{x} + \xi_i \Delta t, t + \Delta t) = f_i(\vec{x}, t) + \Omega_i(\vec{x}, t) \quad (3.2)$$

It means that particle $f_i(x, t)$ travels with velocity ξ_i ; collides on its way determined by Ω_i ; redistributes to new state at later time Δt that streams in neighbouring i^{th} direction-represented by LHS. The Boltzmann equation that is discretized in space and time forms the Lattice Boltzmann Method. This approach is fundamentally simple and easy to solve. The simplified collision operator (Ω_i) developed by Bhatnagar-Gross-Krook, commonly known as BGK, is a widely used operator for any hydrodynamic problem.

$$\Omega_i(f) = -\frac{1}{\tau}(f_i - f_i^{eq})\Delta t \quad (3.3)$$

It relaxes the populations towards an equilibrium f_i^{eq} at a rate determined by the relaxation time τ . The collision term satisfies the mass, momentum and energy conservation laws. The macroscopic properties of a fluid such as density, momentum can be restored by simply

summing distribution function over velocity spaces, commonly referred to as moments.

$$\rho(\vec{x}, t) = \sum_i f_i(\vec{x}, \vec{\xi}_i, t) \quad (3.4)$$

Eq. (3.4) calculates the contribution to the density of particles from all possible velocities at position x and time t for a macroscopic fluid. Again considering all possible velocities, we find the macroscopic momentum density as below

$$\rho(\vec{x}, t)u(\vec{x}, t) = \sum_i \xi_i f_i(\vec{x}, \vec{\xi}_i, t) \quad (3.5)$$

Similarly, we can find the macroscopic total energy density as

$$\rho(\vec{x}, t)E(\vec{x}, t) = \frac{1}{2} \sum_i |\xi_i|^2 f_i(\vec{x}, \vec{\xi}_i, t) \quad (3.6)$$

This contains two types of energy; the energy $\frac{1}{2}\rho|u|^2$ due to the bulk motion of the fluid and the internal energy due to the random thermal motion of the gas particles [50].

3.1.1 Modelling rotating domain

Note that Eq. (3.2) is written in absence of any external force. In case of a rotating fan, the inertial forces act on the fan blades, which needs to be modelled in Eq. (3.2)

$$f(\vec{x} + \xi_i \Delta t, t + \Delta t) = f_i(\vec{x}, t) + \Omega_i(\vec{x}, t) + \underbrace{F_i(\vec{x}, t)}_{\text{external force}} \quad (3.7)$$

where F_i indicates the external force term. The forcing term can be written using power series as

$$F_i = \omega_i \left[A + \frac{B \cdot \xi_i}{c_s^2} + \frac{C : (\xi_i \xi_i - c_s^2)}{2c_s^4} \right] \quad (3.8)$$

where A, B and C are functions of F determined with the condition that moments of F_i should be consistent with hydrodynamic equations. One can obtain the zeroth and second order moment as below [38]

$$\sum_i F_i = A, \quad \sum_i \xi_i F_i = B, \quad \sum_i \xi_i \xi_i F_i = c_s^2 A I + \frac{1}{2} [C + C^T] \quad (3.9)$$

The component A of an external body force is equated to the inertial forces, introduced by non-inertial local rotating regions [79]. The rotating fan region is modeled with a non-inertial local reference frame (LRF) that communicates with a global fixed frame through

interfaces. The total inertial forces acting on fan blades combine centrifugal force, Coriolis force and Euler force.

$$A = \underbrace{\left[-\Omega(t) \times \Omega(t) \times r(\vec{x}, t) \right]}_{\text{centrifugal force}} + \underbrace{\left[-2\Omega(t) \times u(\vec{x}, t) \right]}_{\text{Coriolis}} + \underbrace{\left[-\frac{d\Omega(t)}{dt} \times r(\vec{x}, t) \right]}_{\text{Euler}} \quad (3.10)$$

Note that $\Omega(t)$ represents an angular speed of a fan and should not be confused with the collision operator. $r(\vec{x}, t)$ is the distance vector from a centre of rotation and $u(\vec{x}, t)$ is a local fluid velocity vector. In fact, the Euler force is formed due to variation of an angular speed of a fan and in our simulation, we always consider a fixed speed of rotation. Hence, the Euler force term is not modeled in this study. The half-force velocity correction is given as

$$u'(\vec{x}, t) = \frac{1}{\rho} \left[u(\vec{x}, t) + \frac{A(\vec{x}, t)}{2} \Delta t \right] \quad (3.11)$$

This velocity, u' enters in the equilibrium distributions and is also the macroscopic fluid velocity solving the NSE. Using only $u(\vec{x}, t)$ leads to first order rather than second order space-time accuracy. The velocity u' can be interpreted as an average velocity during a time step, i.e. an average of pre- and post-collision values [50]. Finally, the external force term has the following form

$$F_i = \left(1 - \frac{1}{2\tau} \right) \omega_i \left[\frac{\xi_i - u'}{c_s^2} + \frac{\xi_i \cdot u'}{c_s^4} \xi_i \right] \cdot A \quad (3.12)$$

Further details on the external force component of B and C can be found in Guo *et al.* [38].

3.1.2 Linking LBM to NSE

Now the challenge is to derive macroscopic properties from LBM so that fluid behavior can be understood outside equilibrium. Here, Chapman-Enskog analysis plays an important role. Their derivation on continuous Boltzmann equations can be directly applied to discrete LBM. It shows that in any inviscid and adiabatic condition $f_i \cong f_i^{eq}$ that is well represented with Euler equation and any perturbations beyond Euler equation must be equated to non-equilibrium part of f_i i.e. $f_i^{neq} = f_i - f_i^{eq}$. The perturbation expansion of f_i around f_i^{eq} is given in terms of the Knudsen number. The Knudsen number is a dimensionless quantity that is defined as a ratio of the molecular mean free path to the characteristic length scale (or physical distance) $Kn = \frac{\lambda}{L}$. We can write the expansion of

f_i using label ϵ^n to indicate terms of order Kn^n as

$$f_i = f_i^{eq} + \epsilon f_i^{(1)} + \epsilon^2 f_i^{(2)} + \dots \quad (3.13)$$

The purpose of this section is to provide relevant background to the reader. For a more detailed derivation of moments of perturbed functions, one can refer to the book by S. Chapman and T.G Cowling [17] and by Kruger *et al.* [50]. Similar to equations (3.4) - (3.6), the mesoscopic properties of the fluid are recovered by summing over distribution functions. The kinematic viscosity is given by

$$\nu = \left(\tau - \frac{\Delta t}{2}\right)T \quad (3.14)$$

where T is the fluid temperature. Chen *et al.* [18] redefined the Knudsen number as a ratio of two time scales instead of length scales. The Knudsen number is used to replace a relaxation time (τ) by the characteristics collision time (τ_{turb}) associated with the turbulent eddy interactions and a flow advection time scale due to turbulent flow, in Eq. (3.3). The turbulent scales below $Kn \ll 1$ are recovered with eddy viscosity models. Using the systematic renormalization group theory, they established a link between τ_{turb} and turbulent fluctuations that covers a wide range of turbulent flows as follows:

$$\tau_{turb} = \tau_0 + C_\mu \frac{k^2/\epsilon}{T(1 + \eta^2)^{1/2}} \quad (3.15)$$

where τ_0 is the bare molecular relaxation time, $\eta = Sk/\epsilon$, S^{-1} is the characteristic turbulent time scale, k is the turbulent kinetic energy, ϵ is the turbulence dissipation rate. Chen *et al.* [19] expanded the analogy of LBM-turbulence and demonstrated the turbulent viscosity derivation. More interested readers are directed to [19]. In this study, very Large Eddy Simulation (VLES) is used to solve for larger eddies and smaller eddies are modelled using τ_{turb} formulation.

3.1.3 Boundary conditions

Li *et al.* [56] explained the wall boundary condition. The no-slip boundary condition is achieved by simply reversing all the particle velocities, called a bounce-back process. On the other hand, the specular reflection process reverses normal velocity components and preserves tangential velocity to satisfy free boundary conditions. In the case of rotating walls, the standard bouncing back process is extended. The bouncing is first calculated in the moving wall reference frame and then transformed to the inertial frame. The open

boundary condition such as inlet and outlet where fluid enters or leaves the domain are treated with velocity profiles, density and pressure. For detailed understanding, one can refer to the chapter on boundary conditions from Kruger *et al.* [50]

LBM forms a different approach from the Navier Stokes equations that are explained below.

3.2 Navier Stokes Solver

The classical Navier Stokes(NS) solver is a favorite choice of any CFD engineer, not because it is simple but widely studied in the literature. We believe that the reader is too familiar to present a detailed discussion here. From figure 3.1, we can say that even though NS equations are based on a macroscopic approach, fundamentally, they are derived from LBE. The governing equations for NS solver are stemmed from conservations laws of physics i.e.

- Mass is conserved
- Newton’s second law of motion-rate of change of momentum equals the sum of forces on a fluid particle
- First law of thermodynamics– the rate of change of energy is equal to the sum of the rate of heat added to and the rate of work done on a fluid particle

The principle difference between LBM and NS solver is that the fluid is treated as a continuum instead of a discrete particle distribution and governing equations are directly solved for macroscopic properties of a fluid such as density, pressure, velocity and energy.

3.2.1 Governing equations of fluid flow

For 3D, unsteady, compressible fluid, the continuity equation is

$$\frac{\partial \rho}{\partial t} + \frac{\partial(\rho v_i)}{\partial x_i} = 0 \quad (3.16)$$

Where ρ is fluid density, v fluid velocity vector and its components represented with $i = 1, 2, 3$ in 3D space. For incompressible flows, the continuity equation becomes

$$\nabla \cdot v = 0 \quad (3.17)$$

Momentum equation for viscous and Newtonian fluid in presence of external force is written as

$$\frac{\partial \rho v_i}{\partial t} + v_j \cdot \nabla(\rho v_i) = -\frac{\partial p}{\partial x_i} + \frac{\partial \tau_{ij}}{\partial x_j} + F \quad (3.18)$$

The first term on RHS is hydrostatic stress, normal stress acting due to static pressure p exerted by a fluid, F is an external body force and τ_{ij} is a viscous stress tensor. In many fluid flows τ_{ij} can be represented as a local deformation rate or strain rate function, which is further split into linear and volumetric deformation rate for 3D flows.

$$\tau_{ij} = \mu \left(\frac{\partial v_i}{\partial x_j} + \frac{\partial v_j}{\partial x_i} \right) + \lambda \nabla \cdot v \quad (3.19)$$

where the first term on RHS represents the rate of linear deformation linked to the shear stress by viscosity using Newton's law of viscosity. In practice, although λ , a volumetric dilation coefficient is considered to be insignificant, for the gases using Stoke's hypothesis it is written as $\lambda = -\frac{2}{3}\mu$. The liquid that is assumed to be incompressible becomes zero since $\nabla \cdot v = 0$. Finally, the energy equation is written as

$$\frac{\partial \rho E}{\partial t} + \nabla \cdot \rho E v = -p \nabla \cdot v + \frac{\partial \tau_{ij} v}{\partial x_j} - \frac{\partial q_i}{\partial x_i} \quad (3.20)$$

where E is the total energy of the fluid and q_i is the heat flux. The set of equations from (3.16) to (3.20) are called the 'Navier-Stokes equations'. Explicit analytical solutions don't exist for these equations except in straightforward cases. Therefore, spatial and temporal computations are essential to converge towards a stable solution. Even though spatial discretization can be achieved with structured and/or unstructured mesh in many applications, unstructured mesh proves to be easier and quicker for industrial complex fan geometries.

3.2.2 Energy cascade in turbulence flows

In 1883, Reynolds exhibited experimentally that the instabilities introduced into the regularly layered viscous, so-called laminar flows generate random chaotic motions-resulting into rapid mixing- referred to as turbulent flows. However, the process is decomposed into the series of events- shearing mean flow forms the larger eddies as a result of linear deformation. They extract turbulent kinetic energy from the mean flow itself, then undergo further breakdown to produce smaller and smaller structures. This energy cascade process continues until dissipation happens at a condition where the inertial forces equal the viscous stresses (where $Re_\eta = 1$). These dissipative scales are named after Russian scientist Kolmogorov who deduced his theory in 1841. Dominant viscous stresses in a small scale transform their associated energy into thermal energy. Thus the vigorous mixing in turbulent motions comes at the expense of mean flow energy loss. The turbulence

modeling approach based on these energetic length scales' resolution is summarised in the next section.

3.2.3 Direct Numerical Simulation (DNS)

This method solves NSE for the whole range of turbulent scales, i.e., from larger eddies to the dissipative scales on a numerical grid. Therefore, the mesh size requirement is extremely small to capture dissipative scales that result in a huge computational time and power. Moin and Choin [20] published a study in which Kolmogorov scales are resolved on the grid where total mesh count scaled with $Re_{L_x}^{37/14}$, L_x is the length of a flat plate. Typically for an axial fan that always operates in a turbulent regime which has Reynolds number in the range of 2×10^5 , calculated based upon chord length and velocity near the tip. It results in more than 10^{14} grid points to resolve such a complex flow field for one blade span. Imagine the number when these grid points are scaled by the number of blades. Hence, albeit with its high accuracy, this method is also inconvenient for any industrial usage. Nonetheless, DNS helps in comprehending turbulent structures solved for simple cases that can be used to build turbulence models. For example, the DNS conducted on a Controlled-Diffusion (CD) airfoil by Moreau *et al.* [93] revealed turbulent boundary layer formation physics under installation effects which later helped to understand trailing edge noise mechanism.

3.2.4 Large Eddy Simulation (LES)

DNS difficulty is handled by solving only for more prominent structures only where dissipative scales are modeled using subgrid-scale models. However, the size of large eddies is simply driven by spatial filter where the flow variable ϕ is convoluted with G spatial filter over a computational domain \mathcal{D} , given as

$$\bar{\phi} = \int_{\mathcal{D}} \phi(x')G(x, x')dx' \quad (3.21)$$

According to Moin and Choin [20], wall resolved grid requirement is typically $N \sim Re^{13/7}$. However, for the wall modeled case, the grid requirement drastically reduces to $N \sim Re_{L_x}$. For a typical axial fan blade case, the near-wall grid requirement reduces from 7×10^9 to 2×10^5 when the wall resolved case is computed using wall modeled solver. Although coarser grid requirement enhances its usage for complex geometry and relatively low computational cost, the use of LES in the industry is still limited. The turnaround time for any design feedback is still higher, so relatively simple and quick estimation with fair accuracy is always welcomed in any industrial application.

3.2.5 Reynolds Averaged Navier Stokes (RANS)

The simpler approach is to directly model all the turbulent length scales and obtain a steady-state simulation instead. Reynolds statistically decomposed the flow variables (ϕ) into mean ($\bar{\phi}$) and fluctuating components (ϕ') as

$$\phi = \bar{\phi} + \phi' \quad \text{where} \quad \bar{\phi} = \lim_{T \rightarrow \infty} \frac{1}{T} \int_0^T \phi dt \quad (3.22)$$

He re-derived NSE using Eq. (3.22), to form Reynolds Averaged Navier Stokes equations (RANS). For the sake of simplicity, RANS equations are written for incompressible flows

$$\frac{\partial \bar{v}_i}{\partial x_i} = 0 \quad (3.23)$$

$$\left(\frac{\partial \bar{v}_i}{\partial t} + \bar{v}_j \frac{\partial \bar{v}_i}{\partial x_j} \right) = - \frac{\partial \bar{p}}{\partial x_i} + \frac{\partial}{\partial x_j} [\bar{\tau}_{ij} - \overline{\rho v'_i v'_j}] + \bar{F} \quad (3.24)$$

Equations (3.23) and (3.24) form the RANS equations for continuity and momentum respectively. However, the additional term in momentum equation $\overline{\rho v'_i v'_j}$ is referred to as Reynolds Stress tensor, which introduces nine terms, i.e., three normal stress and six shear stress terms. Now, the total variables become 14 and the total number of the available equation is four. Therefore, a closure equation is needed. The objective of this closure is to study the impact of turbulence on the mean flow properties using the classical turbulence models that are defined based on the number of scalar transport equations that need to be solved along with the above RANS flow equations [113].

In the statistical description of turbulent flow, the variance (σ) of fluctuating velocity component is related to the turbulent kinetic energy (k), also referred to as TKE.

$$k = \frac{1}{2} (u'^2 + v'^2 + w'^2) \quad (3.25)$$

Like viscous stress, using Boussinesq's assumption, the turbulent stresses are equated to a linear rate of deformation through turbulent viscosity.

$$\tau_{ij} = -\rho v'_i v'_j = \mu_t \left(\frac{\partial v_i}{\partial x_j} + \frac{\partial v_j}{\partial x_i} \right) - \frac{2}{3} \rho k \delta_{ij} \quad (3.26)$$

μ_t and k need to be determined and it can be done with more or less complex models involving 1, 2, or more equations. An evolution equation for an additional turbulent parameter is needed in the two equations models, which can be epsilon or omega. However, the $k - \epsilon$ model calculates production and dissipation rates by solving two transport

equations. Yet, the problem with ϵ is the wrong asymptotic behavior and the stiffness of the equation at the wall. This is why Wilcox introduced the $k - \omega$ equations. The $k - \omega$ model accurately captures the near-wall effects, but fails to damp the dissipation rate in free stream flows in the absence of any turbulent kinetic energy. Therefore, in 1992, Menter introduced a model by combining $k - \epsilon$ in the mean flow and transformed $k - \omega$ near the wall. He also used blending functions to set a smooth transition outside the boundary layer between the two models. The model is called 'SST $k - \omega$ model'. This model is suitable for our application and used from the available ANSYS CFX code to capture wall boundary layer transition in high Re flows over a curved airfoil (CD airfoil). These models appear less accurate than DNS and LES, but they meet most engineering applications requiring mean flow estimation. They also reduce grid prerequisite by 10^9 times and cutback computational time drastically. Hence, they are widely used in almost all automotive industries.

3.2.6 Near wall treatment

The turbulent flow behavior is different near the wall than in free shear flows. The fully grown turbulent boundary layer (TBL) on a solid surface can be divided into three layers: the viscous sublayer, the buffer layer and the log layer. The mean flow and turbulence interaction happen in the last layer, where eddies extract the energy from the mean flow. Before wall all the turbulence are damped due to viscous actions when $\tau = \tau_w$ and a linear relation is established as $V = \frac{\tau_w y}{\mu}$ and $u^+ = y^+$, where V mean velocity, $y^+ = \frac{y u_\tau}{\nu}$ dimensionless distance from the wall, $u_\tau = \sqrt{\frac{\tau_w}{\rho}}$ friction velocity. Therefore, the first grid point away from the wall plays an important role in identifying the mean velocity of the flow. However, resolving the boundary layer down to the viscous sub-layers on complex geometries becomes tedious and results in a bigger mesh count. Therefore, log law is formulated. The stricter requirement of $1 < y^+ < 5$ is moderated such that the first grid point can be placed in a TBL within $30 < y^+ < 300$. The log law is given by

$$u^+ = \frac{V}{u_\tau} = \frac{1}{\kappa} \log(Ey^+) \quad k = \frac{u_\tau^2}{\sqrt{C_\mu}} \quad \epsilon = \frac{u_\tau^3}{\kappa y} \quad (3.27)$$

where κ is von Kármán constant, $\kappa = 0.41$ and the smooth wall roughness parameter is $E = 9.8$. Putting the first grid point in the region between $5 < y^+ < 15$ is not advised because it is identified as a buffer zone where the velocity profile distribution is uncertain. A similar wall function approach is followed in LBM, where VLES is used in the bulk flow and near-wall turbulence is modeled with wall functions.

These methods model the aerodynamic field efficiently. However, the accuracy of a predicted flow field depends upon the choice of method. DNS is the best but less practical approach for the industry. LES is feasible but still 25 times more expensive than RANS. RANS is a relatively cheaper and quicker solver for industry.

Compared to NS, LBM is especially suitable for our low Mach simulations because the low speed fan generates a weak compressible flow field that needs to be accurately captured with the less dispersive and dissipative high order schemes. According to the study published by Marie [65] and Bres [13], global 1st order LBM exhibits dispersion properties similar to 2nd and 3rd order finite difference scheme in NS solver and for acoustic dissipation are equivalent to 6th order NS schemes. Bres also evaluated that to propagate 5 kHz acoustic pulse 1 m away requires 12-16 points per wavelength at the cost of 0.068 dB loss per wavelength. LBM then provides a relatively coarser grid outside the source region to propagate the acoustic perturbation. Moreover, LBM proves to be faster in time than any conventional methods [71]. Therefore, the VLES approach in LBM has been chosen using the commercial code Powerflow 5.5c.

The numerical methods are the founding stone for computational aeroacoustics. The source modeling and its different ways of radiating and propagating can be handled in multiple ways explained in the next section.

3.3 Computational Aeroacoustics

The numerical study that deals with noise generation due to flow interaction with solid surfaces or noise originated from turbulent interactions referred to as computational aeroacoustics (CAA). Once the sound source is known, it can be propagated to far-field in multiple approaches using direct and hybrid methods.

3.3.1 Direct Acoustics

In the direct approach, the acoustic source and its propagation are solved for full-time dependant compressible Navier Stokes equations using high precision numerical methods such as DNS preferably. However, LES with high order schemes can also be used in predicting direct acoustics. This method captures the reflection/refraction/diffraction present outside the source region. However, the inclusion of a far-field in the computational domain makes the simulation expensive and lengthy.

3.3.2 Hybrid approach

On the other hand, once the sound source is known, it can be transmitted using different integral methods. Therefore the hybrid approach is formulated where the source and its propagation are treated separately. Lighthill [57, 58] in 1952, indeed noticed the fluid dynamics affair with the acoustics for the first time whence recorded the aerodynamically generated noise in a quiescent medium. Then, he formulated an inhomogeneous wave equation by combining the Navier Stokes equations, assuming an isentropic, uniform far-field at rest

$$\frac{\partial \rho'}{\partial t^2} - c_0^2 \frac{\partial \rho'}{\partial x_i^2} = \frac{\partial^2 T_{ij}}{\partial x_i \partial x_j} \quad (3.28)$$

where $T_{ij} = \rho v_i v_j + (p' - c_0^2 \rho') \delta_{ij} - \sigma_{ij}$ is the Lighthill tensor. The beauty of this method is that the wave equation on LHS meant for propagation in the far-field can be decoupled from the aerodynamically fluctuating source term on RHS. It is solved by taking integration over a volume enclosing the source using Green's theorem. The analogy is limited only to free-flow sources (i.e. turbulence in jet flow). Nevertheless, other wall-bounded sources such as the fluctuating lift forces are accounted by Curle [25] in 1955 by extending Lighthill's analogy for the fixed solid surfaces. This becomes popular and forms the basis for many analytical models discussed in the following section. Yet, Curle's theory can't be used for rotating sources. Thus, Ffowcs Williams and Hawkings [27, 115] have generalized Curle's equation for rotating solid boundaries, which is the versatile extension in the free field of the Lighthill's analogy, commonly referred to as FWH equation. The general solution [14, 35, 47, 70] for FWH equation where source located at \vec{y} radiates noise that is heard at observer placed at \vec{x} , is given as

$$\begin{aligned} c_0^2 \rho'(x, t) = & \frac{\partial^2}{\partial x_i \partial x_j} \int_{+\infty}^{+\infty} \int_{V_e} T_{ij}(\eta, t') \frac{\delta(t' - t + \frac{R_\eta}{c_0})}{4\pi R_\eta} d\eta dt' \\ & + \frac{\partial}{\partial x_i} \int_{-\infty}^{+\infty} \int_{V_\infty} (\sigma'_{ij} \delta(f)) \frac{\partial f}{\partial y_j}(\eta, t') \frac{\delta(t' - t + \frac{R_\eta}{c_0})}{4\pi R_\eta} d\eta dt' \\ & + \frac{\partial}{\partial t} \int_{-\infty}^{+\infty} \int_{v_\infty} \rho_0 (V_{si} \delta(f)) \frac{\partial f}{\partial y_i}(\eta, t') \frac{\delta(t' - t + \frac{R_\eta}{c_0})}{4\pi R_\eta} d\eta dt' \end{aligned} \quad (3.29)$$

where R_η is the distance between source and observer. Finally, the FWH equation becomes

$$c_0^2 \rho'(\vec{x}, t) = \frac{1}{4\pi} \frac{\partial^2}{\partial x_i \partial x_j} \int_{v_e} \left[\frac{T_{ij}}{R|1 - M_r|} \right] d\vec{\eta} - \frac{1}{4\pi} \frac{\partial}{\partial x_i} \int_S \left[\frac{P_i}{R|1 - M_r|} \right] ds_{\vec{\eta}} - \frac{1}{4\pi} \frac{\partial}{\partial t} \int_s \left[\frac{\rho_0 V_n}{R|1 - M_r|} \right] dS_{\vec{\eta}} \quad (3.30)$$

$1 - M_r$ is the Doppler factor related to a projected motion on a line from a source to the observer where $M_r = \mathbf{M} \cdot \mathbf{R} / R$. The square bracket is computed at the retarded time $\tau = t - \frac{R}{c_0}$, where $R = |\mathbf{X} - \mathbf{Y}|$ is the distance between the source and the observer. The first term accounts for noise due to quadrupoles (volume source), the second term for noise due to dipoles (force fluctuations over the surface) and the third term is for noise due to monopoles (thickness noise). For a low speed fan, as the Mach number ($M \sim 0.1$) is very low, the quadrupole term can be neglected. The monopole noise due to blade thickness which is very small and treated as a compact source can be neglected. Therefore, the remaining surface integral term, regarded as dipole- becomes a major contributing noise source for any low speed fan. Apart from these analogies, a far-field noise can also be computed using the following approach.

Linearised Euler Equations (LEE) are formed by decomposing each variable into mean and fluctuating components and keeping only the linear first-order variations. It accounts for the actual background mean flow whereas in the acoustic analogies the background flow is always uniform. The LEE doesn't account for acoustics non-linearities present in high Mach number compressible flows. Although LEE helps save CPU time, the accurate description of acoustics in the far-field is often compromised due to dissipation and dispersion errors. In the case of the axial fan, LE and TE broadband noises are present significantly in the high frequency region (say 500 Hz to 10,000 Hz). Fine mesh is needed to capture such small wavelengths in the far-field. In a way, the benefit of LEE is lost and doesn't seem to be a viable option to compute axial fan noise in the far-field.

Kirchhoff method assumes the simple wave equation governs the sound transmission. Similar to LEE, the source and near field computations are obtained numerically. The controlled surface enclosing non-linear source terms are propagated into the far-field. The sound pressure is obtained by taking normal and time derivatives over a control surface. Although the Kirchhoff method is used in many applications such as jet noise, rotor noise, ducted fan, etc., it is limited to a fixed media. Thus, similar to Goldstein [35], Ghorbaniasl *et al.* [33] extended it to moving medium. Kirchhoff method and FW-H show similarity where a porous surface replaces a control surface. The way of handling non-linearity on the

control surface distinguishes Kirchhoff's method from porous FW-H. Kirchhoff method can work only when a linear wave equation is present on a control surface, limiting the choice of the control surface. Otherwise, the accuracy of a Kirchhoff method highly depends upon the linear acoustics prediction by high-resolution CFD [62].

Since we have acquired the knowledge of source modeling using numerical methods and the different ways of its propagation in a hybrid approach, we propose some quick and easy analytical tools in the following section.

3.4 Analytical modelling for LE noise

We understood that computing fan noise is still an expensive affair for any automotive industry where usually multiple designs are tested and optimized in a limited time frame. Hence, we choose an analytical model— a simple approach. Indeed, it can drive a design optimization process in a quick and much cheaper way. Adamczyk [1] and Amiet [4] used Curle's analogy [25] as a theoretical basis to predict LE noise. The analogy relates aerodynamically generated pressure fluctuations on a stationary solid surface to far-field sound. Adamczyk [1, 2] obtained an approximate solution for unsteady aerodynamic response produced by the infinite swept wing in an oblique gust in a compressible stream. He solved Helmholtz equation derived from linearized Euler equations as a boundary value problem using Wiener-Hopf technique while Amiet [4] solved those equations with Schwarzschild's technique formulated especially to address electromagnetic wave scattering problems. Later, Rozenberg [118] combined their approach and used it for swept blade problem, i.e., formulated equations by placing a rectangular plate in an oblique flow as posed by Adamczyk, but the solution obtained using Schwarzschild's technique. Later noise calculated for a fixed blade is extended to compute low-speed rotating fan noise. Carazo [123] slightly modified Rozenberg's perspective and developed a formulation for swept blade used in high-speed machines. Rozenberg modeled the fan blade as a rectangular flat plate. Instead of LE making an angle with the incoming velocity vector, he rotated the vector itself to make a sweep angle with LE. However, Carazo modeled the blade rather as a flat plate of a parallelogram shape. Moreover, the basic assumption of modeling the blade as a flat plate is feasible because geometrical factors of an airfoil typically used in low speed fans, such as thickness and camber are unimportant for the unsteady lift. While they play a crucial role in inviscid steady lift calculations [46]. Moreover, a low speed fan operating in subsonic flows and with a small angle of attack are suitable conditions to treat the flow over an airfoil as the flow over a flat plate [46]. Hence, the unsteady loading generated by incoming turbulent flow is calculated at each point along the flat plate length

in a streamwise direction. Then these point sources are replaced with fluctuating dipoles that radiate noise in the far-field. The following steps and Figs. 3.2, 3.3 explain how it is applied to the low speed axial fan.

- Step (1)** Let's consider the fan placed in the Cartesian coordinate system (X, Y, Z) and its associated cylindrical coordinate system is (R, θ, Z) as shown in Step 1 of Fig. 3.2. The axial flow is entering from Z -direction and the fan is rotating clockwise along Z -axis.
- Step (2)** Take a point P at the LE at any given radial location. Draw a radial vector passing through the point P and draw a tangent to the LE edge passing through the point P . Project these vectors on the rotational plane and calculate the angle made by these radial and tangent vectors. It is referred as "Sweep angle (ψ) ".
- Step (3)** Now divide the blade span in equal size strips using iso-radial lines and define the sweep angle for each strip as described in Step 2. After unwrapping the strip, it forms a parallelogram shape, yielding $\frac{L}{2b} \sim 0.2$ where L is span of the strip and b is half chord of the blade. In general, based on radial flow evolution, 5 to 10 strips are sufficient to convergent acoustics spectra computed for the LE noise mechanism [90].
- Step (4)** To further simplify the problem, let's define the strip as the parallelogram-shaped flat plate in the unwrapped local coordinate system (ζ, η, z) such that η is following the span of the strip and ζ is along the chord. Define new axis system (x, y) such that it makes angle ψ with ζ and η axes, respectively. The uniform compressible flow with velocity U is entering along ζ -axis.
- Step (5)** Now, project the flat plate in (x, y) plane and projected velocity components become $(u_x = U \cos \psi, u_y = U \sin \psi)$ along x and y axes, respectively. Refer the transformation matrix in Fig. 3.2.
- Step (6)** Now consider a oblique turbulent gust of wavenumber $k(k_x, k_y)$ is convecting with the mean flow and making an angle α with velocity U . The linearised Euler equations are reduced to a canonical wave equation and written for disturbance potential as below

$$(\nabla^2 - \frac{1}{c_0^2} \frac{D^2}{Dt^2})\phi' = 0 \quad (3.31)$$

The above equation can be expanded on (x, y, z) space as

$$\beta_x^2 \frac{\partial^2 \phi'}{\partial x^2} + \beta_y^2 \frac{\partial^2 \phi'}{\partial y^2} + \frac{\partial^2 \phi'}{\partial z^2} - \frac{1}{c_0^2} \frac{\partial^2 \phi'}{\partial t^2} - \frac{2M_x}{c_0} \frac{\partial^2 \phi'}{\partial x \partial t} - \frac{2M_y}{c_0} \frac{\partial^2 \phi'}{\partial y \partial t} - 2M_x M_y \frac{\partial^2 \phi'}{\partial x \partial y} = 0 \quad (3.32)$$

where $\beta_i^2 = 1 - M_i^2$, $M_i = \frac{u_i}{c_0}$ and c_0 is speed of sound in air. We are interested in harmonic solution in frequency space, hence turbulence is decomposed into Fourier modes. Therefore, using Reissner transformation by taking Fourier transform of disturbance potential in space and time, transformed disturbance potential is written as

$$\phi' = \varphi(x, z) e^{i\omega t} e^{-ik_y y} e^{i\frac{M_x^2}{\beta_x^2} k_x x} \quad (3.33)$$

By using further transformation and substituting $k_a = M_x k_x + M_y k_y$, the wave equation (3.32) can be reduced to Helmholtz equation and written in non-dimensional form as

$$\frac{\partial^2 \Phi}{\partial x^{*2}} + \frac{\partial^2 \Phi}{\partial z^{*2}} + \kappa^2 \Phi = 0 \quad (3.34)$$

and the boundary conditions are

I. *Zero potential upstream of the profile*

$$\Phi(x^*, 0) = 0 \quad \text{for } x^* \leq 0$$

II. *Normal velocity is zero on the profile*

$$\frac{\partial \Phi}{\partial z^*}(x, y, 0, t) = -\frac{w_0 b}{\beta_x} e^{-i\bar{k}_x^* x^*} \quad \text{for } 0 < x^* < 2 \quad (3.35)$$

III. *Pressure distribution near TE zero, satisfying Kutta condition*

$$\left[i(\omega b + \frac{u_x M_x}{\beta_x^2} k_x - u_y k_y) + u_x \frac{\partial}{\partial x^*} \right] \Phi = 0 \quad \text{for } x^* > 2$$

where, non-dimensional and reduced frequency terms uses following transformation

$$\begin{aligned} x^* &= \frac{x}{b}, & y^* &= \frac{y}{b}, & z^* &= \frac{z}{b} \beta_x \\ k_x^* &= k_x b, & k_y^* &= k_y b & k_z^* &= k_z b \end{aligned} \quad (3.36)$$

The system of equations is solved using the Schwarzschild technique. The limitation of the method is that it can solve for two boundary conditions at a time. Therefore, unsteady pressure distribution on a profile of finite length is calculated by solving the system of equation iteratively. In the first iteration, the infinite size of the profile is assumed by extending TE to infinity and first and second boundary conditions are used to solve the equation. In the second iteration, the origin of the coordinate is moved to TE. This time LE is extended to infinity and second and third boundary conditions are written in pressure form to solve the equation. The first iteration is referred as LE term and the second iteration as TE term. The procedure to solve this equation is very well explained by J. Christophe in his thesis [21] and also see

appendix of this thesis. The equation solves for unsteady pressure fluctuations over the airfoil, regarded as reduced lift functions that are written as

A. Leading edge term:

$$g_1(x^*, k_x^*, k_y^*) = \frac{e^{-i\pi/4}}{\pi \sqrt{\pi(\bar{k}_x^* + \beta_x^2 \kappa)}(x^* + 1)} e^{-i(\kappa - \bar{k}_x^* M_x^2)(x^* + 1)} \quad (3.37)$$

B. Trailing edge term:

$$g_2(x^*, k_x^*, k_y^*) = -\frac{e^{-i\pi/4}}{\pi \sqrt{2\pi(\bar{k}_x^* + \beta_x^2 \kappa)}} [1 - (1 + i)E^*(2\kappa(1 - x^*))] e^{-i(\kappa - \bar{k}_x^* M_x^2)(x^* + 1)} \quad (3.38)$$

Step (7) The flat plate is transformed back to (ζ, η, z) space. Now the microphone is defined along the z-axis. Lift fluctuations over a flat plate cross-section can be seen as equivalent distribution of dipoles with a phase term associated with them. Dipole strength integrated over the span and radiated far-field using Green's theorem. The far-field acoustics pressure is given by

$$\begin{aligned} \tilde{p}(\vec{X}, \omega) &= \int_{-b\tau}^{b\tau} \int_{-L/2}^{L/2} \frac{i\omega R_3}{4\pi c_0^2 R_s^2} \tilde{l}(x, y, \omega) e^{-i\left(\frac{k_a}{\beta_0^2 S_0} ([S_0 M_x - \beta_y^2 X_1] \zeta / \tau + [S_0 M_y - \beta_x^2 X_2] (\eta + \zeta / \tau))\right)} e^{-ik_y \eta} d\zeta d\eta \\ &= \frac{ik_a X_3 \rho_0 u_x \tilde{w} b L}{2S_0^2 \tau} \mathcal{L}(x, k_x^*, k_y^*) \operatorname{sinc} \left[\frac{L}{2} \left(k_y - \frac{k_a}{\beta_0^2 S_0} (\beta_x^2 X_2 - S_0 M_y) \right) \right] \end{aligned} \quad (3.39)$$

Defining $\zeta^* = \zeta/b$ and non-dimensional aeroacoustic transfer function is

$$\mathcal{L}(x, k_x^*, k_y^*) = \int_{-b\tau}^{b\tau} g(x, k_x^*, k_y^*) e^{\frac{-i\zeta^*}{\tau} \left\{ \frac{k_a}{\beta_0^2 S_0} [\beta_y^2 X_1 - S_0 M_x + \alpha(\beta_x^2 X_2 - S_0 M_y)] \right\}} d\zeta^* \quad (3.40)$$

The total non-dimensional aeroacoustic transfer function is sum of LE scattering and TE backscattering i.e. $\mathcal{L} = \mathcal{L}_1 + \mathcal{L}_2$ and written as below 1. Leading edge scattering term:

$$\mathcal{L}_1((x, k_x^*, k_y^*)) = \frac{\tau}{\pi} e^{-i\theta_2} \sqrt{\frac{2}{\theta_1 (\bar{k}_x^* + \beta_x^2 \kappa)}} E(2\theta_1) \quad (3.41)$$

2. Trailing edge back-scattering term:

$$\mathcal{L}_2((x, k_x^*, k_y^*)) = \frac{\tau}{\pi\theta_1} \frac{e^{-i\theta_2}}{\sqrt{2\pi(\bar{k}_x^* + \beta_x^2\kappa)}} \left\{ i(1 - e^{2i\theta_1}) - (1 + i) \left[E(4\kappa) - \sqrt{\frac{2\kappa}{\theta_3}} e^{-2i\theta_1} E(2\theta_3) \right] \right\} \quad (3.42)$$

where,

$$\begin{aligned} \theta_1 &= \kappa - \bar{k}_x^* M_x^2 - b \left\{ \frac{k_a}{\beta_0^2 S_0} [\beta_y^2 X_1 - S_0 M_x + a(\beta_x^2 X_2 - S_0 M_y)] \right\} \\ \theta_2 &= -\theta_1 + \frac{\pi}{4} + \kappa - \bar{k}_x^* M_x^2 \\ \theta_3 &= 2\kappa - \theta_1 \end{aligned} \quad (3.43)$$

Step (8) Eqn. (3.44) is the final expression to calculate far field noise radiated from a swept blade modelled as a parallelogram.

$$S_{pp}(\vec{\Sigma}, \omega') = \left(\frac{\rho_0 \omega' X_3 b}{c_0 S_0^2} \right)^2 u_x L \pi \int_{-\infty}^{\infty} |\mathcal{L}(x^*, K_x^*, k_y^*)|^2 \text{sinc}^2 \left(k_y - \frac{k_a}{\beta_0^2 S_0} (\beta_x^2 X_2 - S_0 M_y) \right) \Phi_{ww}(K_x, k_y) dk_y \quad (3.44)$$

Step (9) The far-field noise is calculated for the microphone defined in $\vec{\Sigma}(\zeta, \eta, z)$ vector space of the flat plate, but for the fan the microphone is defined in $\vec{X}(X, Y, Z)$ field. Therefore, the transformation matrix is written to account for coordinate change considering the blade sweep angle and stagger angle. The transformation matrix is given in Fig. 3.3.

Step (10) Finally, far field noise generated by the rotating fan, that includes Doppler factor is given by the expression given in Step 10 of Fig. 3.3.

This developed method is tested against experimental results in the following section.

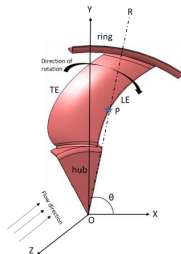
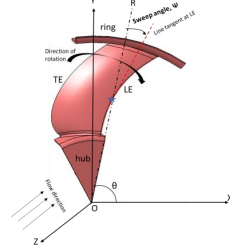
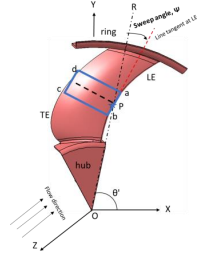
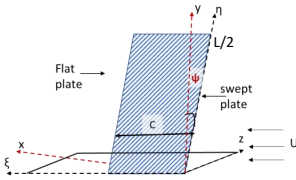
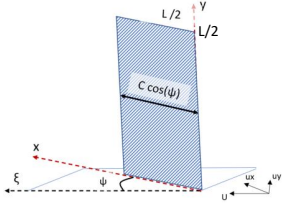
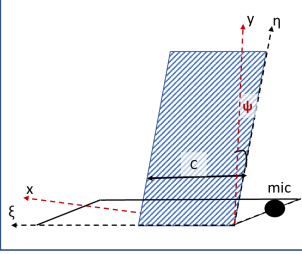
| | | |
|---|---|---|
| <p>Step 1</p> <p>Define coordinate system</p> | <p>Define a global Cartesian orthogonal coordinate system (X,Y,Z) with origin passing from center and its attached cylindrical coordinate system (R,θ,Z). Microphone is defined 1 m away from the origin along Z-axis.</p> |  |
| <p>Step 2</p> <p>Define sweep angle</p> | <p>Consider a point p at LE. Draw a radial vector passing through point p and origin O. Now draw a tangent to LE passing through point P. Project both vectors on a rotational plane. Now, measure the angle made by projected vectors. The measured angle is called as sweep angle (ψ)</p> |  |
| <p>Step 3</p> <p>Strip theory</p> | <p>Divide the blade in at least 10 strips of parallelogram shape along the span. Here, single strip (abcd) is demonstrated for example purpose.</p> |  |
| <p>Step 4</p> <p>Coordinate System for strip</p> | <p>Define a local orthogonal coordinate system for a strip (ξ,η,Z). The flow with velocity U is entering along ξ making a sweep angle (ψ) with LE</p> |  |
| <p>Step 5</p> <p>Transformation matrix</p> | <p>Project the strip on (x,y) plane such that transformation matrix becomes</p> $x = \zeta/\tau \quad a = \tan(\psi) \text{ and } \tau = \sqrt{1 + a^2}$ $y = \eta + a\zeta/\tau \quad \frac{1}{\tau} = \cos(\psi)$ <p>The flow velocity U makes an angle with the LE and its projected velocity components become (u_x,u_y)</p> |  |
| <p>Step 6</p> <p>Reduced lift function</p> | <p>1. Leading edge term:</p> $g_1(x^*, k_x^*, k_y^*) = \frac{e^{-i\pi/4}}{\pi \sqrt{\pi(k_x^{*2} + \beta_x^2 \kappa)}(x^* + 1)} e^{-i(\kappa - \overline{k_x^2} M_0^2)(x^* + 1)}$ <p>2. Trailing edge term:</p> $g_2(x^*, k_x^*, k_y^*) = -\frac{e^{-i\pi/4}}{\pi \sqrt{2\pi(k_x^2 + \beta_x^2 \kappa)}} [1 - (1 + i)E^*(2\kappa(1 - x^*))] e^{-i(\kappa - \overline{k_x^2} M_0^2)(x^* + 1)}$ | |

Figure 3.2 Steps to define of coordinate system, sweep angle and strip for the axial fan

| | | |
|--|--|---|
| <p>Step 7</p> <p>Radiation integral</p> | <p>Rotate back the strip in (ξ, η) plane. Define the microphone 1m away from strip along Z-axis. Using reduced lift function derive the noise radiated at mic. The aeroacoustics transfer function becomes</p> $\mathcal{L}_1((x, k_x^*, k_y^*)) = \frac{\tau}{\pi} e^{-i\theta_2} \sqrt{\frac{2}{\theta_1 (\bar{k}_x^* + \beta_x^2 \kappa)}} E(2\theta_1)$ $\mathcal{L}_2((x, k_x^*, k_y^*)) = \frac{\tau}{\pi \theta_1} \frac{e^{-i\theta_2}}{\sqrt{2\pi (\bar{k}_x^* + \beta_x^2 \kappa)}} \{i(1 - e^{2i\theta_1}) - (1 + i) \left[E(4\kappa) - \sqrt{\frac{2\kappa}{\theta_3}} e^{-2i\theta_1} E(2\theta_3) \right]\}$ <p>where</p> $\theta_1 = \kappa - \bar{k}_x^* M_x^2 - b \left\{ \frac{k_a}{\beta_0^2 S_0} [\beta_y^2 X_1 - S_0 M_x + a(\beta_x^2 X_2 - S_0 M_y)] \right\}$ $\theta_2 = -\theta_1 + \frac{\pi}{4} + \kappa - \bar{k}_x^* M_x^2$ $\theta_3 = 2\kappa - \theta_1$ |  |
| <p>Step 8</p> <p>Far field PSD</p> | <p>Final expression for far field PSD is given by</p> $S_{pp}(\vec{X}, \omega) = \left(\frac{\rho_0 \omega' X_3 b}{c_0 S_0^2} \right)^2 u_x L \pi \int_{-\infty}^{\infty} \mathcal{L}(x^*, K_x^*, k_y^*) ^2 \text{sinc}^2 \left(k_y - \frac{k_a}{\beta_0^2 S_0} (\beta_x^2 X_2 - S_0 M_y) \right) \Phi_{ww}(K_x, k_y) dk_y$ | |

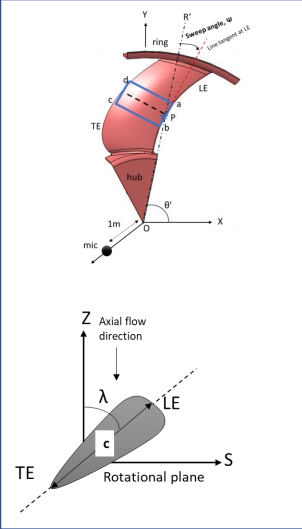
| | | |
|--|--|---|
| <p>Step 9</p> <p>Transformation matrix</p> | <p>Define a microphone 1 m away from the center of the fan in free field (X, Y, Z). The source is defined in a (ξ, η, z). Therefore, a transformation matrix is defined to account for microphone location defined in (X, Y, Z). The mic defined in (ξ, η, z) is transformed to rotational plane (S, R, Z).</p> $\begin{pmatrix} S \\ R \\ Z \end{pmatrix} = \begin{pmatrix} \cos \psi & \sin \psi & 0 \\ -\sin \psi & \cos \psi & 0 \\ 0 & 0 & 1 \end{pmatrix} \begin{pmatrix} \xi \\ \eta \\ z \end{pmatrix}$ <p>Then stagger angle of the blade is accounted while transforming to (X, Y, Z)</p> $\begin{pmatrix} X \\ Y \\ Z \end{pmatrix} = \begin{pmatrix} \cos \lambda & \sin \lambda & 0 \\ 0 & 0 & 1 \\ -\sin \lambda & \cos \lambda & 0 \end{pmatrix} \begin{pmatrix} S \\ R \\ Z \end{pmatrix}$ |  |
| <p>Step 10</p> <p>Reduced lift function</p> | <p>Far field power spectral density is given as</p> $S_{pp}^F(\vec{X}, \omega) = \frac{B}{2\pi} \int_0^{2\pi} \left(\frac{\omega(\theta')}{\omega'} \right)^2 S_{pp}^\gamma(\vec{\Sigma}, \omega') d\theta'$ | |

Figure 3.3 Calculation of far field PSD of noise radiated by an axial fan

3.5 Validation

We have chosen the experiment performed by Giez *et. al* [34] at Ecole Centrale de Lyon (ECL) in an open-jet anechoic wind tunnel facility on a thin swept and loaded airfoil to validate the above broadband noise model. The swept plate with the span of 250 mm and chord 150 mm, is placed in an incoming velocity is 50 m/s such that it makes an angle of 35° with LE of the swept plate. The noise generated by turbulence impingement on the leading edge is recorded by a far-field microphone placed at 90° from the flow direction in the mid-span plane (refer Fig.3.4).

A homogeneous, isotropic turbulence is generated with 4.8% intensity and 16 mm length scale. Von Kármán turbulence spectrum [41] is tuned from hot wire measurements using the following expression:

$$\Phi_{ww}^{VK}(k_x, k_y) = \frac{4}{9\pi} \frac{\bar{u}^2(\hat{k}_x^2 + \hat{k}_y^2)}{k_e^2(1 + \hat{k}_x^2 + \hat{k}_y^2)^{7/3}} \quad (3.45)$$

where \bar{u}^2 mean square of velocity fluctuation, the dimensionless wavenumber $\hat{k}_i = \frac{k_i}{k_e}$, k_e is the wavenumber of most energetic scales, given by $k_e = \frac{\sqrt{\pi} \Gamma(5/6)}{L_e \Gamma(1/3)}$

The prediction made for two cases, i.e., with the actual sweep of 35° and no sweep case. The far-field noise predicted using Eq. (3.44) is compared with experimental results for 35° sweep angle in Fig. 3.4. It is interesting to note that high frequency humps around 3000 Hz and after humps accounted for non-compactness are shifted to higher frequency region for the swept case. The model correlates very well for 1 kHz and above with experimental results but show some under prediction at low frequency.

The infinite span works very well for values $k_x d > 10$ because for high frequencies the k_y contribution over the span reduces. In the swept case, this limitation occurs at 643 Hz. Therefore, noise predicted below 800 Hz is lower than that of experiments. Thus, extended Amiet's model for the swept case can produce overall sound levels in the high frequency region more accurately compared to low frequency for a given length scale.

The above sweep is tested for 16mm lengthscale and 4.3 % of turbulent intensity in presence of 35° sweep angle. Out of curiosity, the sweep angle varied from no sweep to 35°, 45°, 55° and how noise reduction alters with respect to different length scale is understood. The Fig. 3.5 shows the farfield noise contribution by the blade used in above described experiment. This quick exercise shows that maximum noise reduction is possible at larger turbulent length scale and for higher sweep angle. As the size of length scale decreases, the influence

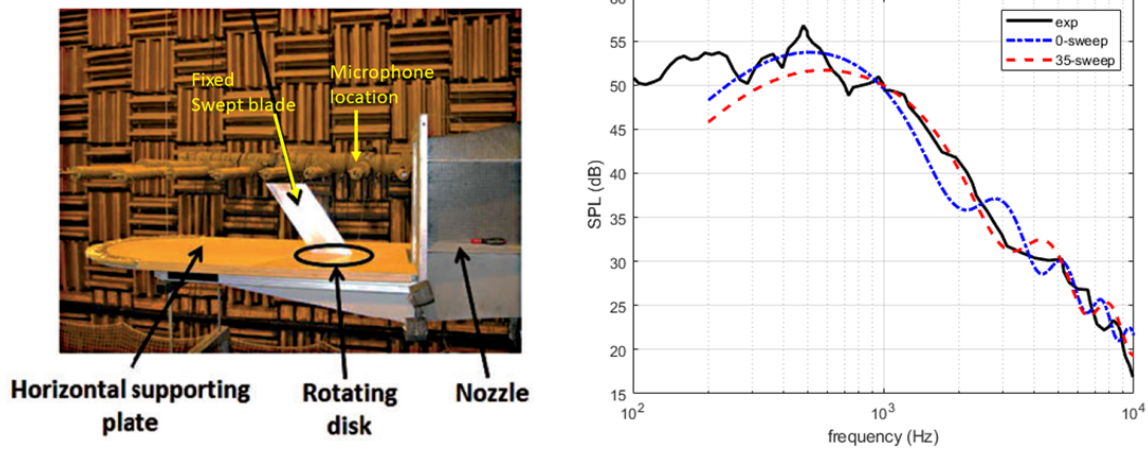


Figure 3.4 Experimental setup in the ECL large open-jet anechoic wind tunnel adapted from [34](left), Far-field noise spectrum of turbulence-impingement noise (right)

of sweep on noise reduction decreases. Therefore, it is important to know the characteristics of turbulence in which fan is operated to identify sweep angle and its contribution to noise emission.

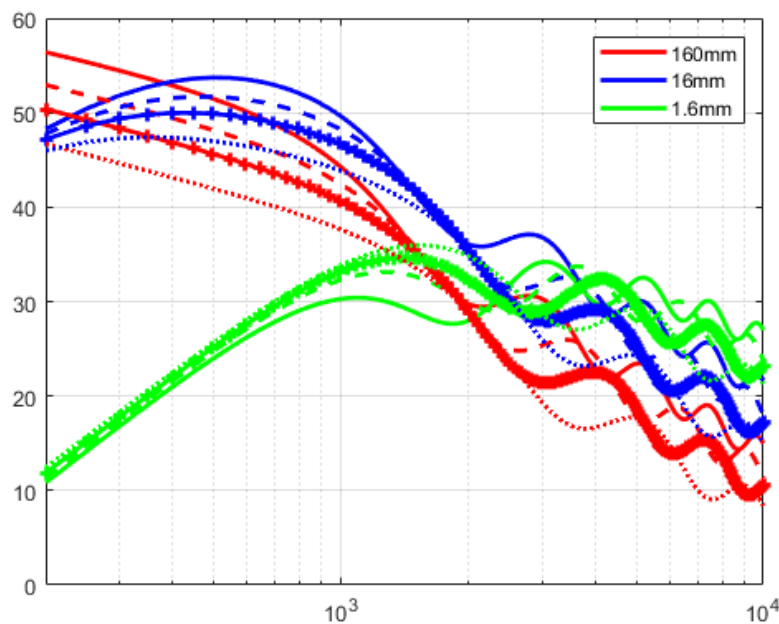


Figure 3.5 Far-field noise spectrum calculated for different turbulence length scales interactions in presence of no sweep-solid line, dashed line-35°, solid line with plus symbols-45° and dotted line- 55°

3.6 Conclusion

This chapter discussed various numerical methods, out of which we chose the RANS and Lattice Boltzmann method (LBM). The steady RANS is helpful to investigate the mean flow, aerodynamic performance and near-wall flow behavior for various sweep angles. In comparison, the LBM provides a deeper understanding of unsteady flow features. Its low dissipative and dispersive schemes are helpful to predict direct acoustics. In addition, our study is focused on handling broadband noise sources due to turbulence impingement on swept blades. Amiet's extended model for the swept case is also used to predict noise levels caused by turbulence interaction. It helps us gain further knowledge about source mechanism and guide us to predict noise levels for variable sweep angles. The necessary data required for these simulations is extracted from steady RANS simulations. The noise predictions and their validations are discussed in Chapter 6.

CHAPTER 4

Test Configurations

This chapter describes short-listed swept blade fans that are tested in an experimental setup versus their numerical modeling. The ducted fans are simulated by mimicing actual experimental set up in the simulation. The idea is to capture any inflow distortions and its affect on noise. The presence of any non-uniformity is tested by modelling uniform inflow against experimental set up. The primary goal is to systematically validate computational methods on a simplified fan meant for academic usage and then apply a fully-proven procedure on a complex, industrial-use fan. This approach provides us a wide set of data recorded in an academic context to compare with the numerical results and facilitates confidence in our process. Therefore, two matrices, i.e., two swept blades and unswept blade designed and tested at Friedrich-Alexander University (FAU), Erlangen-Nurnberg, Germany are taken. Three forward swept radiator fan blades designed by French global automotive supplier Valeo, Paris, France are chosen in this study, as shown in the second row of Fig. 4.1.







| Test cases | Blade 1 | Blade2 | Blade3 |
|----------------|---|--|---|
| Academic fan | US (no sweep) | FS (+45°) | BS (-45°) |
| |  |  |  |
| Industrial fan | FS (+28°) | FS (+30°) | FS (+48°) |
| |  |  |  |
| | | | |

Figure 4.1 Test cases used in this study

Zenger [124] studied a matrix of fan designs based on free vortex and controlled vortex theory. He also varied the sweep angle to measure backward and forward sweep performance in free, and grid generated distorted inflow environment. Out of this vast matrix, we have short-listed unswept fan and its two sweep variants. These fans showcased in Fig. 4.1 (the first row) are tested in a free inflow condition. The experimental setups used for aerodynamic and acoustic testing of these fans are explained in the following section.

4.1 Testing at Valeo and MSU

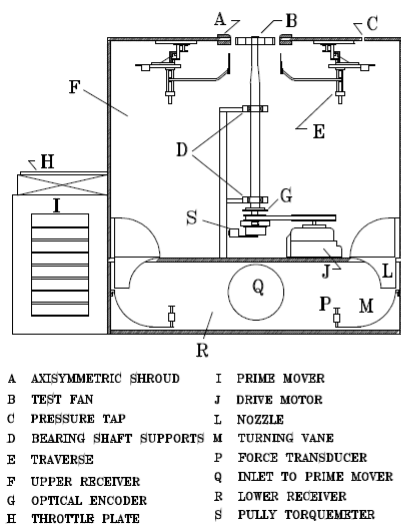


Figure 4.2 Axial fan testing facility at ACFRD, MSU (left) and Reverberant acoustic setup at Valeo (right)

The fan test facility at Valeo Engine cooling, la Verrière (LVR), France, is different from that at Automotive Cooling Fan Research and Development (ACFRD), Michigan state university (MSU). To study the measurement uncertainty, the fan is tested on both setups. The MSU tunnel shown in Fig.4.2 (left) is a vertically mounted suction side tunnel. It uses a momentum flux device to measure the volumetric flow rate. However, the Valeo facility in Fig.4.2 (right) has a pressure side horizontal tunnel, and it uses typical venturi metering nozzles to measure the flow rate. In both facilities, the required flow rate is supplied by an auxiliary fan. In LVR, the pressure rise is measured inside the plenum with the help of three different probes mounted on the plenum walls. The pressure rise is the difference between the averaged pressure and the atmospheric pressure or pressure inside the room. In the ACFRD facility, the pressure rise is the difference between the static pressure measured at ‘F’ i.e. a probe mounted on the top wall, and the total pressure upstream of the fan. The hot wire anemometry available at MSU is used to record three components

of the velocity downstream of the fan, i.e., 33 mm away from TE. It is mounted on an axisymmetric shroud where data is measured at a single azimuthal location. The data is sorted into bins according to the azimuthal angle with the help of an optical encoder. The velocity components are ensemble-averaged for each rotation. Moreover, acoustic measurements are conducted in a reverberant setup at Valeo, indicated in Fig. 4.2. The acoustic power is measured at several flow rates and different rotational speeds using the standard 3-microphone technique. Despite the different test configurations, the fan tested in these setups exhibits good repeatability, and accurate correlation [29]. Hence, we have chosen the MSU setup to model the whole fan in the LBM simulation.

4.2 Testing at FAU

The test facility in Friedrich-Alexander University (FAU) at Erlangen-Nurnberg, Germany is purpose-built to investigate free-tip ducted axial fans. The test setup construction adheres to DIN EN ISO 5801 standards that are primarily used to measure the aerodynamic performance of a fan. It also has sound-absorbing external sandwich walls. It stops any external noise from entering inside the plenum. Additionally, the temporary foam arrangement put forth on the inner walls of the chamber acts as a sound wave absorber and avoids the acoustics reflections from the rigid walls. Hence, this rectangular plenum facilitates aerodynamic testing and serves as the perfect anechoic chamber for aeroacoustics testing.

The test setup is arranged in such a manner that the flow enters from a standardized inlet and passes through multiple bends before entering into the plenum. A butterfly valve installed in the inlet section regulates the flow rate. The rectangular inlet bent duct that connects the inlet section with the plenum allows the flow to enter as a jet, illustrated with a schematic shown in Fig. 4.3. A flow straightener installed inside the plenum breaks the jet and distributes the incoming flow uniformly.

A test fan is installed in a duct with a converging bell-mouth inlet and an enlarging diffuser outlet. The necessary power supply and recording arrangements like motor, driveshaft, and torque meter are installed on a frame outside the plenum. Pressure rise over atmospheric pressure generated by a fan is measured through the pressure tap mounted on the top wall placed 1200 mm away from the inner wall of the plenum as indicated in Fig. 4.3. The auxillary fan mounted at the inlet supplies varying flow, and the desired flow rate is achieved by controlling the butterfly valve. The aeroacoustics recording is conducted for the design point using microphones. They are placed 1 m away from the fan center, and the array of microphones are equispaced 30° apart in a semicircular manner as shown in Fig. 4.4. The Laser Doppler Anemometry is used to record data in an azimuthal plane

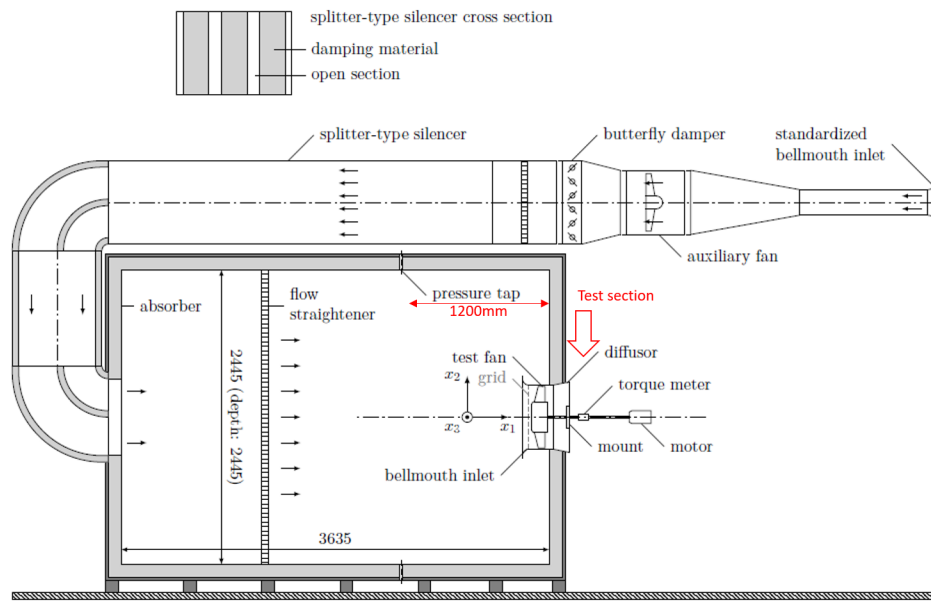


Figure 4.3 Axial fan testing facility at FAU, Germany adapted from [124]

located 10 mm before the leading edge and 10 mm after the trailing edge. These enriched, precise, high-quality flow field recordings provide a unique database to validate simulation results.

Likewise, in the experiment, the probe data is also recorded along the diffuser radius and plotted in fig. 4.7 (right). Further details on recording positions is illustrated in [124].

4.2.1 Numerical modelling approach

Once we gained the knowledge about the test setup and fans, we carefully thought upon modeling it computationally. The flow path in the FAU complex test setup is broken down as :

1. Primarily, the flow enters from the inlet section and passes through a series of bent ducts;
2. Going forward, a jet-like flow enters in the plenum;
3. Then, the honeycomb type flow straightener supposedly stops the jet, redistributes it uniformly, and also kills any incoming flow disturbance;
4. Besides the remaining high frequency turbulence dissipates on the way further downstream before reaching the fan;
5. At the end, the flow enters the inlet duct and passes over the fan blades, and exits from the diffuser section.

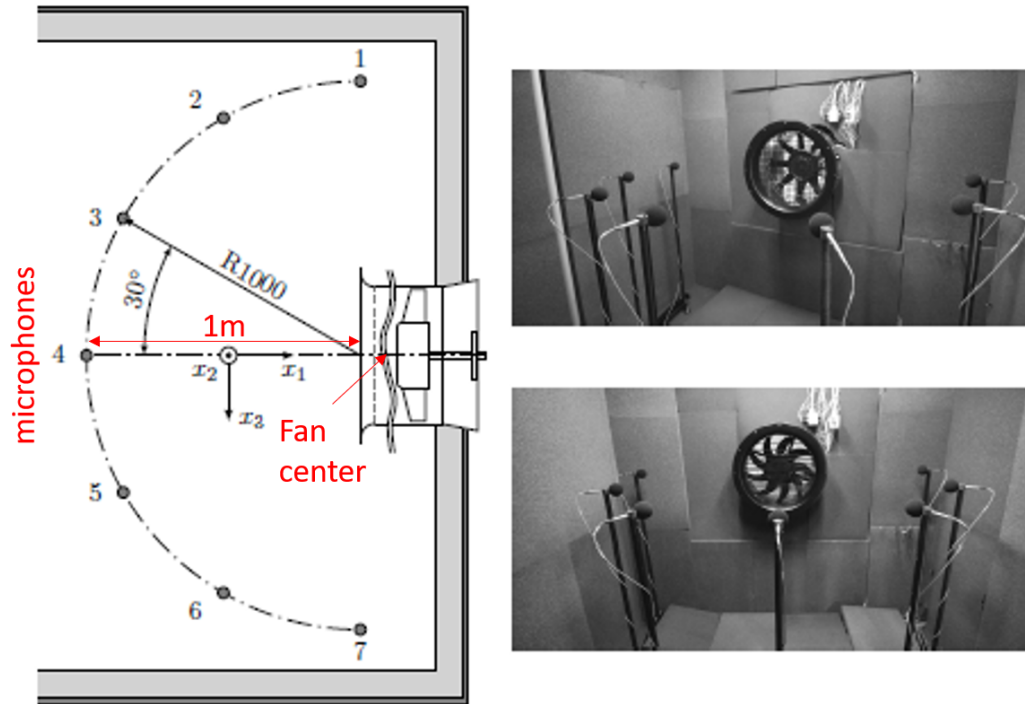


Figure 4.4 Microphone arrangement to record fan noise; schematic (left) and photograph (right) adapted from [124]

Based on this sequence of events, we tested three setups involving complexity in a step-up manner.

- A A single-blade passage modeled by assuming a uniform and perfectly axisymmetric flow around the fan blade
- B The complete fan modeled with the uniform inlet assuming a streamlined, uniform incoming flow from rectangular shape straightener
- C The full experimental setup modeled with the whole plenum and inlet considered from the bent duct, but the complex flow control configuration is ignored

The single blade passage is useful for estimating blade performance with and without sweep in a relatively quick and easy manner in the absence of other disturbances. Therefore, to start with, we evaluated aerodynamic performance with a single blade passage using steady state RANS simulations using option A, described in Chapter 5. To study the effect of either incoming turbulence and inflow distortion as found previously by Sturm et al. at Siegen Universitat [105] or by Pestana et al. [80] on the LP3 test-bed at Ecole Centrale de Lyon [2] two more setups with different inlet configurations, mentioned above in B and C, are modeled.

4.2.2 Uniform vs experimental inlet configurations

Only the hub (no blades) setup is modeled as shown in Fig. 4.5 to keep the analysis simple and computationally affordable. Besides, in the absence of fan blades, a relatively coarser mesh inside the 22 m³ plenum volume helps establish the flow field quickly.

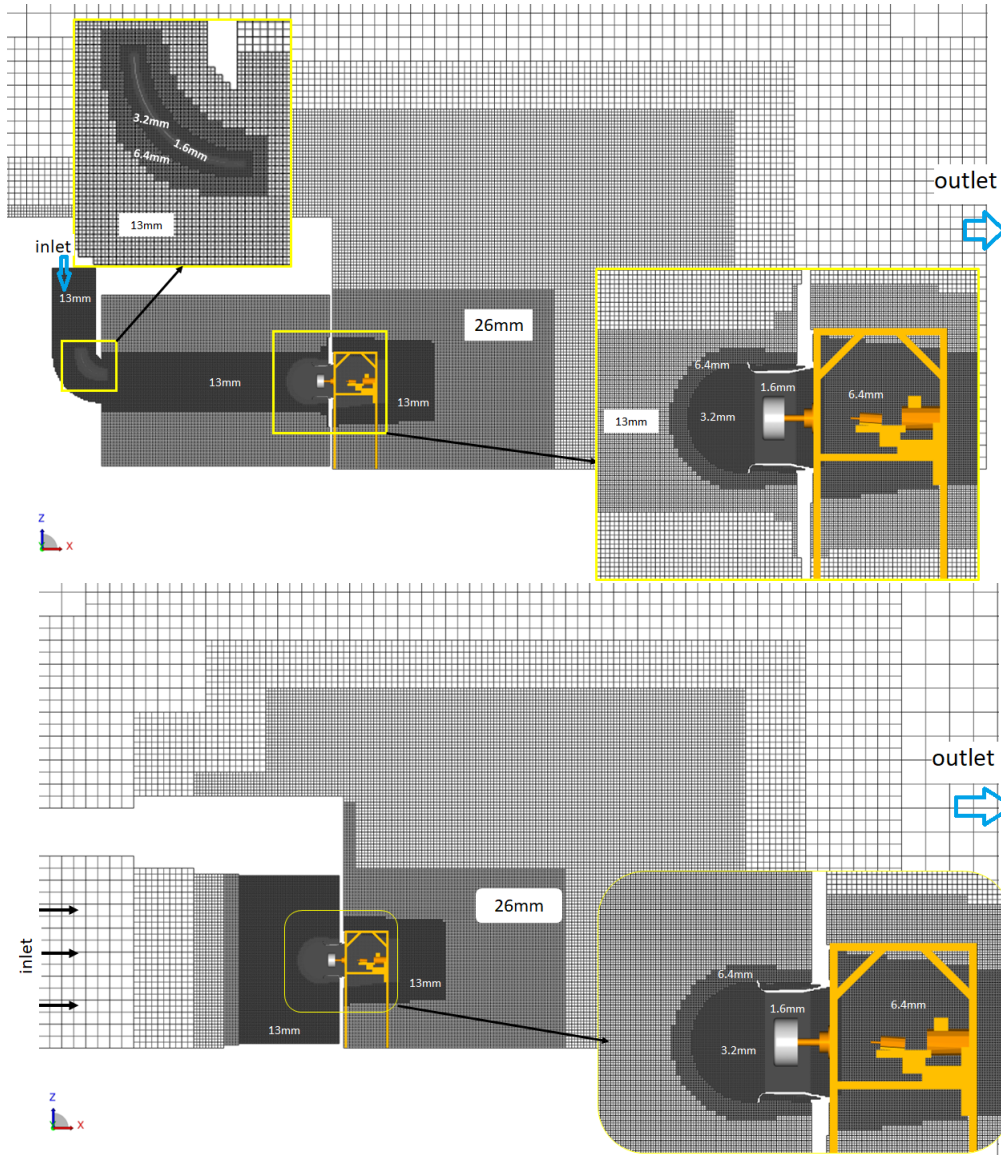


Figure 4.5 Discretization performed in Powerflow for Exp setup (top); UI setup(bottom)

The first computational setup mimics experimental installation precisely. In particular, the dimensions of the rectangular inlet duct, plenum, diffuser, and mounting assembly are identical to the experiment, referred to as 'Experimental (EXP) setup.' The second configuration is built similar to RANS, i.e., uniform-inlet flow except for the rectangular

plenum labeled as 'Uniform-Inlet (UI) setup.' Both plenums are kept in a big room which is at atmospheric pressure.

Fig. 4.5 exhibits similarity in discretization strategy performed in Powerflow on both setups. Except for the plenum volume, different configurations are discretized according to their inlet. The incoming jet in EXP setup is refined with a rectangular virtual region (VR), while for the UI setup, the mesh is refined from the inlet towards the duct in a stepwise manner. The bell-mouth section is refined with spherical and cylindrical VR layers from 6.4 mm to 1.6 mm near the hub. The wake section after the diffuser exit is less important for the upstream flow and noise; hence, it is rapidly coarsened. The RANS simulation is performed with $y^+ = 1$ on hub and blade with 0.1 mm mesh. It is modelled with simplified approach, hence it isn't analyzed for installation effect.

The uniform mass flow is assumed at the inlet while the outlet is modeled as zero static pressure, i.e., at atmospheric. The anechoic walls of the plenum are modeled as porous with infinite resistance. Honeycomb type flow straightener in EXP setup is modeled as porous media to simulate the pressure drop with a resistance curve provided by the supplier. The total volume of the plenum is 22 m³, and the flow enters at 1.4 m³/s, which requires 15.71 s to fill up the chamber completely. Hence, to achieve an established flow field inside the plenum, both configurations are simulated up to 20 s using the LBM.

4.2.3 Investigation of inflow distortion

The mean flow-field analyzed in Fig. 4.6 shows similar uniform static pressure distribution in both setups, though the velocity and vorticity contours are significantly different. Despite these variations, the mean velocity contours, visualized inside the diffuser, confirm an almost identical distribution as seen in Fig.4.7 (left).

In the EXP setup, accelerating flow forms a thin boundary layer over the hub. The flow enters uniformly but at a slightly higher axial velocity in an annular section. The overlapping profiles near the tip indicate similar boundary layer growth on the inner wall of the diffuser in both computations. Notice that these prescribed recordings were performed at one fixed location because perhaps, Zenger [124] might have assumed an axisymmetric flow distribution. Therefore, these comparisons may be biased and demand further investigation of the incoming flow phenomena. Interestingly, 2D streamlines plotted in Fig. 4.8 along with cylindrical velocity components assures non-uniform, asymmetric inflow inside the diffuser. The UI setup shows four counter-rotating recirculation regions uniformly placed at every 90° angular positions. But the radial and the tangential velocities demonstrate nearly axisymmetric flow behavior. However, in the EXP setup, two big counter-rotating

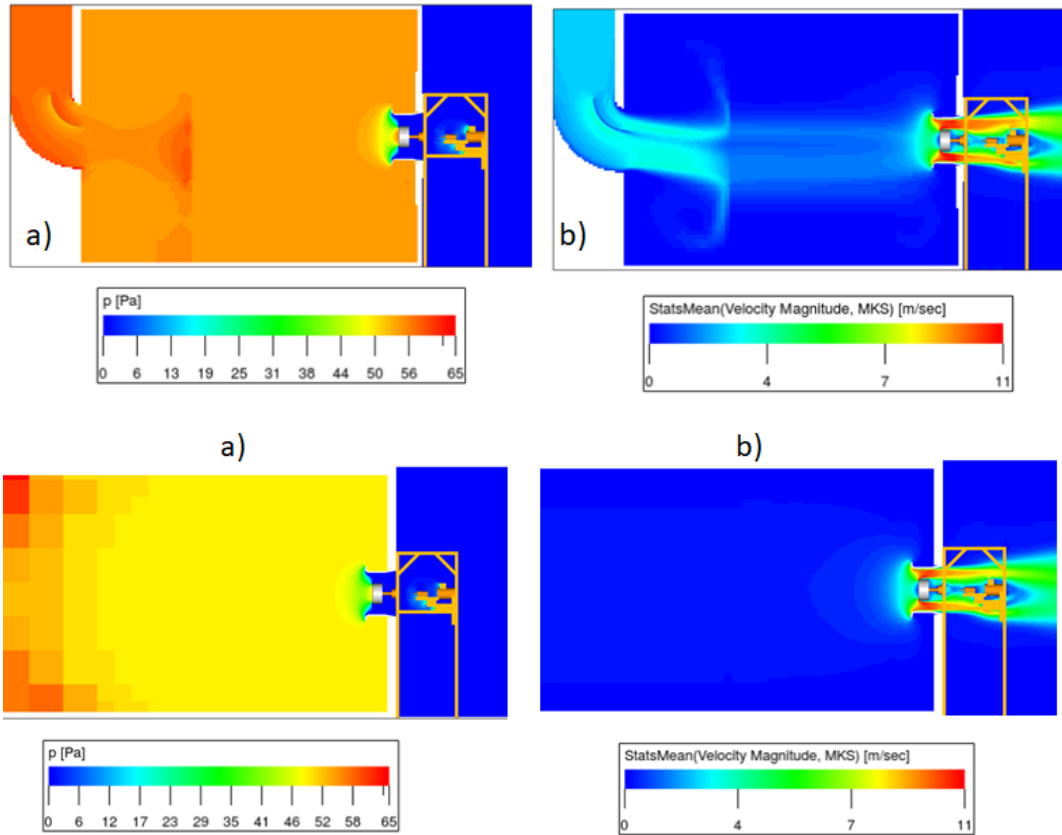


Figure 4.6 Contours of a. mean static pressure, b. mean velocity magnitude; Top: Exp setup and Bottom: UI setup

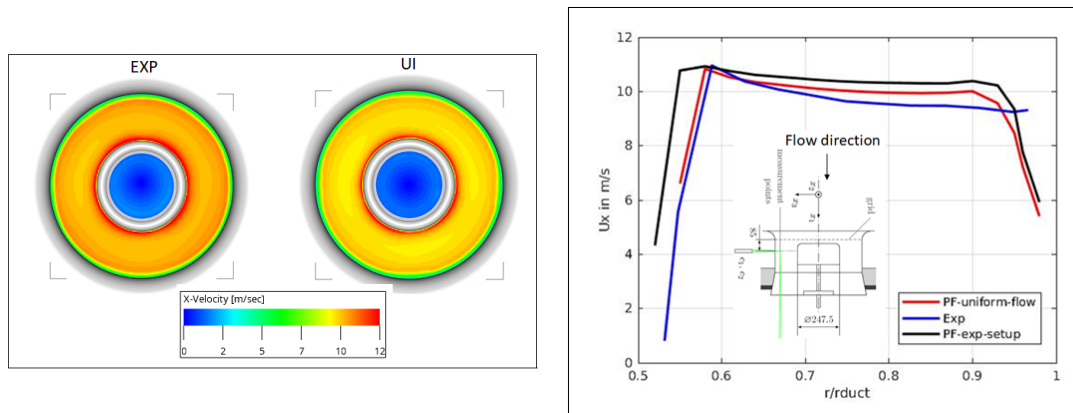


Figure 4.7 Contours of mean velocity magnitude (left) and 2D plot of mean axial velocity (right)

tangential velocity contours and streamlines indicate some non-axisymmetric flow distribution perhaps caused by the development of non-uniform flow field inside the plenum.

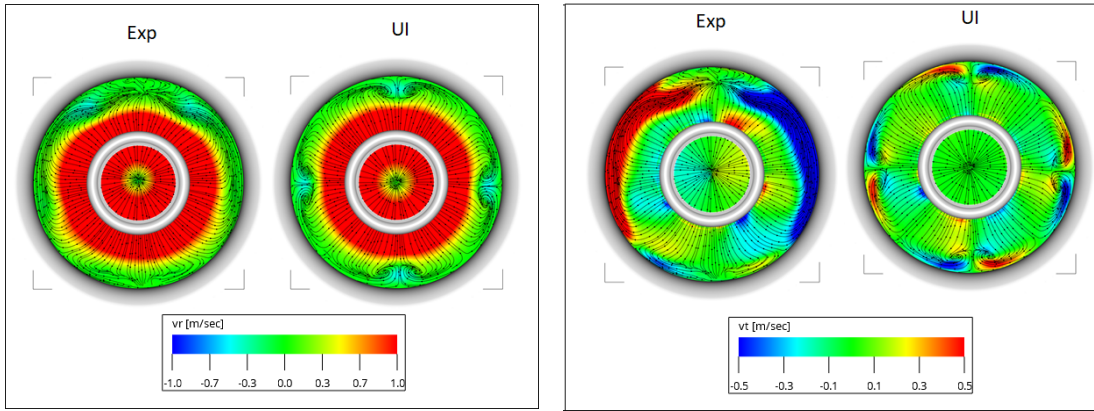


Figure 4.8 Contours of mean radial (left) and mean tangential (right) velocity with overlapped 2D streamlines

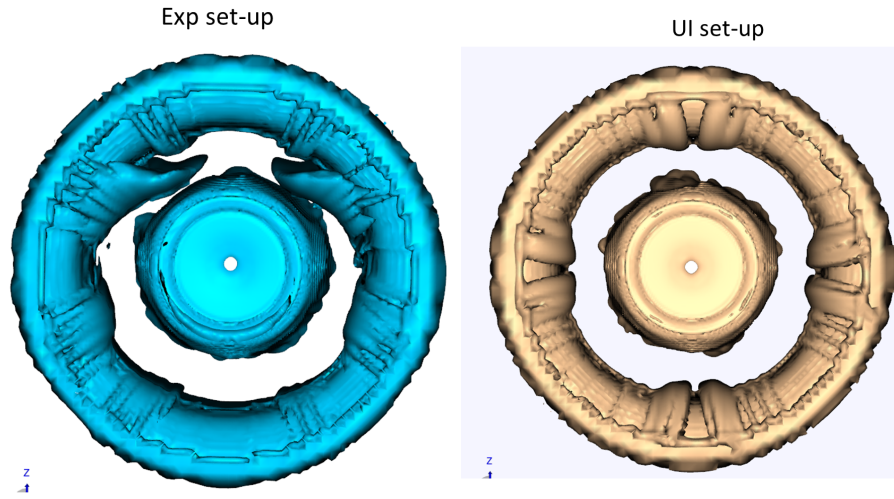


Figure 4.9 Isosurface of mean vorticity field

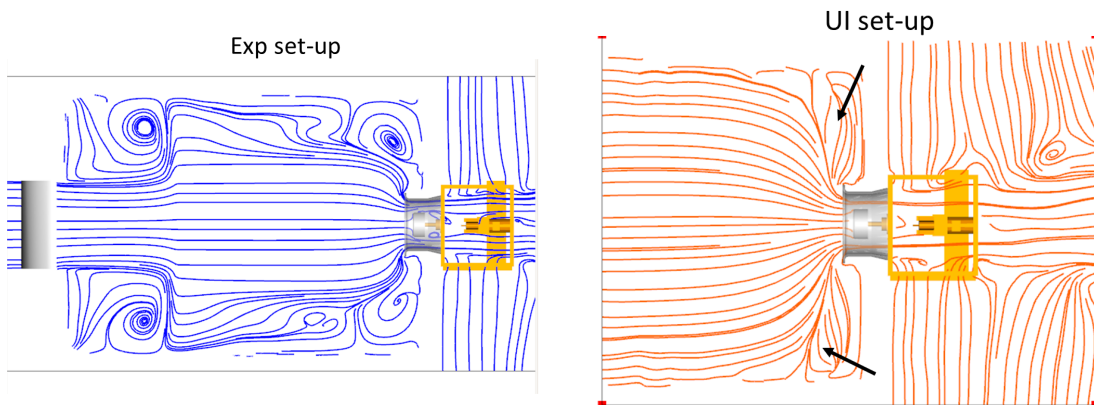


Figure 4.10 Mean velocity streamlines in z-plane

The isosurface of the mean vorticity field shown in Fig. 4.9 provides further insight. The giant tongue of vorticity in the EXP setup coincides with the distribution of streamlines. Hence, we can infer that two counter-rotating flow structures enter inside the diffuser (EXP setup). The streamlines in Fig. 4.10 elucidate the formation of the symmetric recirculation region near the duct (follow black arrows) in UI setup. Moreover, analogous symmetry is also observed in the $y = 0$ plane. Hence, we can confirm that the rectangular inlet forms four symmetric recirculation regions. Recall that the fan at one point suck those recirculating region and produce tonal noise [105]. Contrarily, although EXP setup indicates non-periodic, asymmetric flow distribution inside the plenum, they also cause more pronounced disturbances that will likely interact with fan blades to produce further tonal and higher broadband noise. However, the above mean flow field analysis cannot reveal the source or any dynamic information of turbulence. Hence, to further quantify turbulent parameters, the statistical analysis is performed in the next section.

4.3 Extracting turbulence characteristics using statistical analysis

The aeroacoustic investigations require unsteady simulations and record time-based data. The recorded time series do not provide much information until a statistical analysis is performed. This section is dedicated to illustrating different methods in which the time series can be treated to investigate the stationarity of the data. These methods are also helpful in extracting time-averaged parameters, turbulence characteristics in the flow field, spectral analysis and filtering, etc...

The experimental data recorded over a period of rotation is a mix of random and correlated pieces of information– referred here as time series. Their statistical and mathematical treatments are called time series analysis. These recordings contain coherent structures. These unstable flow elements potentially interact with fan blades to produce noise. We have already solved large-scale turbulence and are interested in comprehending turbulence intensity and length scale using statistical analysis. To confirm traces of turbulence entering inside the diffuser, Zenger has conducted an experiment where he recorded instantaneous velocity in free-flow conditions at radial locations with the help of Laser Doppler Anemometry (LDA) as shown in Fig. 4.11. Similarly, we also placed probes in our simulation and recorded three components of velocity. Here, we discussed axial velocity on three key locations, i.e., two probes near the hub and diffuser wall inside their respective boundary layer and the third one at the mid-height of the annular section. Their time

trace is displayed in Fig. 4.12. Although, we know that 20 s are required to establish a flow field inside the plenum. The time series used from 8 s is just for demonstration purposes. Moreover, sometimes flow establishes earlier in some regions, and we don't have to wait until the whole plenum reaches the equilibrium stage.

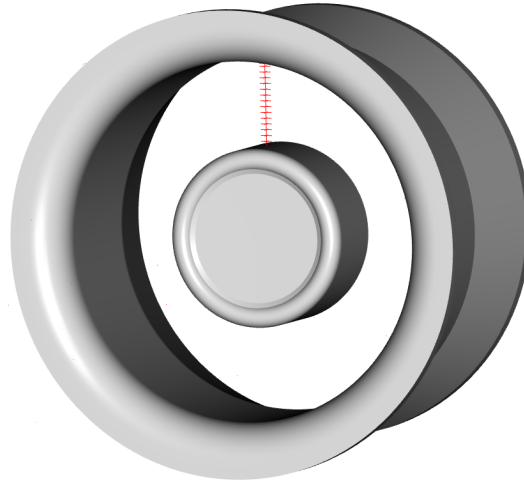


Figure 4.11 Data recording using radially distributed probes

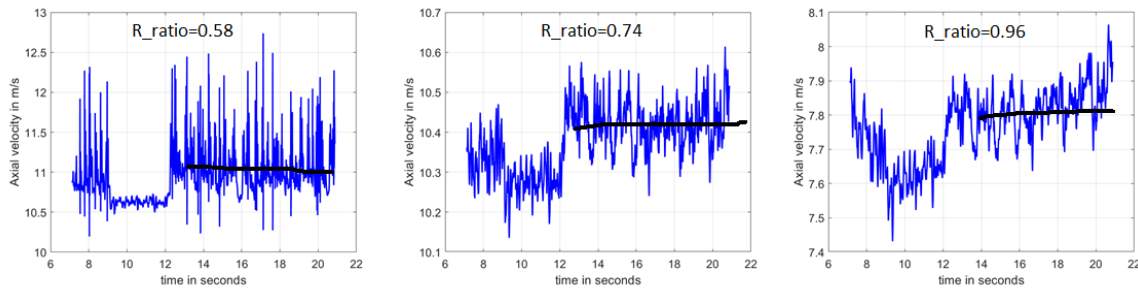


Figure 4.12 Plot of axial velocity recorded using probes near hub, mid of the duct, near diffuser casing respectively (left to right)

Now, the challenge is how to use statistical analysis to extract turbulence characteristics. In order to do any processing on the recorded data referred here as time series, the first and foremost step is to identify the stationarity of a signal. So, we have listed the following four simple criteria out of multiple rules available in the literature.

1. Visual inspection of data
2. Mean convergence test
3. Variance test
4. Autocorrelation function (ACF) test

With mere visual inspection and by selecting the time window from 14 s to 20 s, we can approximately locate the constant value (black line) around which velocity is oscillating from Fig.4.12. However, to quantify the value, mean convergence test is conducted.

Mean convergence test

Before going deep into the analysis, one should also note the sampling frequency with which data is recorded. It is essential because mean and variance at any time window depend upon sampling frequency. To perceive a notion of the sampling frequency, take a classic example of old movies where the car wheel appears to be rotating in the opposite direction while the car is moving forward. The reason is insufficient sampling. The camera with which the scene is recorded has a lower frame rate than the actual rotational frequency of wheels. In our case, the data is recorded with a sufficient sampling frequency of 48 kHz, calculated by taking the inverse of difference of time taken at two consecutive data points in time series ($F_s = \frac{1}{t(2)-t(1)}$). From Fig. 4.12, we quickly figure out that the data is oscillating around a mean value. Therefore, the random variable, in this case, v_x can be decomposed into mean and fluctuating components as given below

$$v_x = \bar{v}_x + v'_x \quad (4.1)$$

In statistical analysis, one can calculate the mean of data using three different ways– 1. Ensemble average 2. The expected value operator 3. Time average, as stated in eqn. (4.2). For strictly stationary data, these three methods should give identical results, but the flow is not always strictly stationary in real life. Hence, we usually treat data as weakly stationary and mean of the short signal recorded from simulation calculated with time average equation.

$$E(v_x) = \int_{-\infty}^{+\infty} v(x) f_x(t) dx \quad (4.2a)$$

$$\hat{v}_x = \lim_{N \rightarrow \infty} \underbrace{\frac{1}{N} \sum_{n=1}^N v(x, n)}_{\text{Ensemble average}} \quad (4.2b)$$

$$\bar{v}_x = \lim_{T \rightarrow \infty} \underbrace{\frac{1}{T} \int_0^T v(x, t) dt}_{\text{Time average}} \quad (4.2c)$$

where v_x is any random variable, here it is axial velocity, and f_x is its probability density function, and E is the expected value operator. We can confirm the stationarity of a

signal when the global mean of a time series matches with the mean calculated at any time window and should not depend on the selection of window size. Let's illustrate the mean convergence test in Fig. 4.13. The part of the plot highlighted with different colors represents the size of a selected window. Visually, we see that the mean should be lower than the global mean when plotted with a 0.5 s scale on the y-axis in the range of from say 10-12 s. However, listed observations in Table 4.1 indicated that the global mean (8-20 s) and the mean calculated for (10-12 s) vary with 1%. Hence, relying only on the mean convergence test may not be sufficient to conclude the stationary nature.

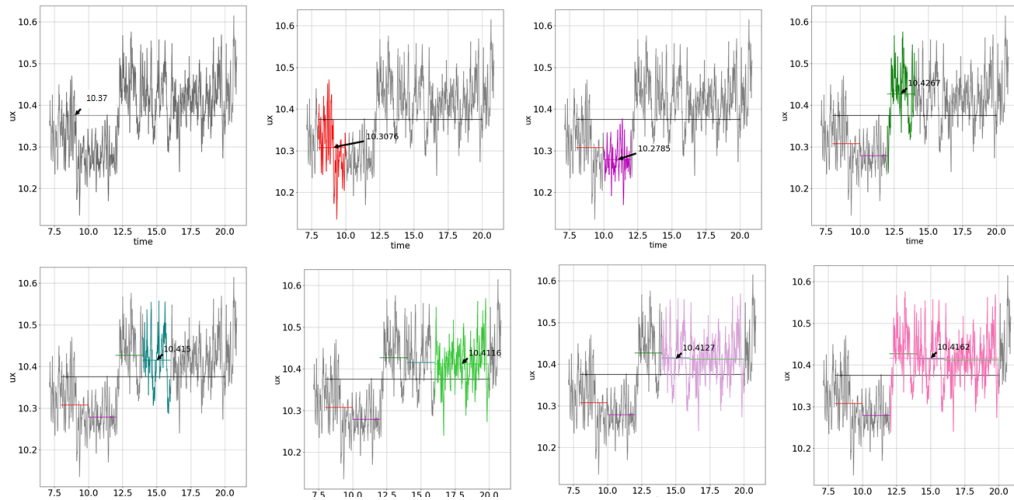


Figure 4.13 Mean velocity convergence

| Time window | Mean in m/s | Variance in m ² /s ² |
|-------------|-------------|--|
| 8-20 s | 10.38 | 0.007 |
| 8-10 s | 10.31 | 0.004 |
| 10-12 s | 10.28 | 0.001 |
| 12-14 s | 10.43 | 0.004 |
| 14-16 s | 10.41 | 0.004 |
| 16-20 s | 10.41 | 0.003 |
| 14-20 s | 10.41 | 0.003 |
| 12-20 s | 10.42 | 0.003 |

Table 4.1 Mean and Variance of mid-probe

Variance test

Variance of a random variable is expected value of squared standard deviation whereas standard deviation is the measure of fluctuation random variable from its mean value, defined as

$$\sigma_w^2 = E[(v_x - \overline{v(x)})^2] = \frac{\sum_{i=1}^n (v_i(x) - \overline{v_i(x)})^2}{n} \quad (4.3)$$

Table 4.1 classifies the variance calculated for the global signal and with different time windows. We recognize the deviation of variance in each time window except for 12-20 s, 14-20 s, and 16-20 s, where the variance remains constant. Although 12-20 s time window passes constant variance criteria, it is too early to comment on stationarity of a signal because autocorrelation function test is yet to be performed.

Autocorrelation test

Autocorrelation function (ρ) is the function of autocovariance (γ) normalized to be one at $\tau = 0$, where τ is the time lag. Autocovariance measures the linear dependence between two points on the same time series observed at different times. Autocorrelation is compelling because it only depends on the time separation or lag.

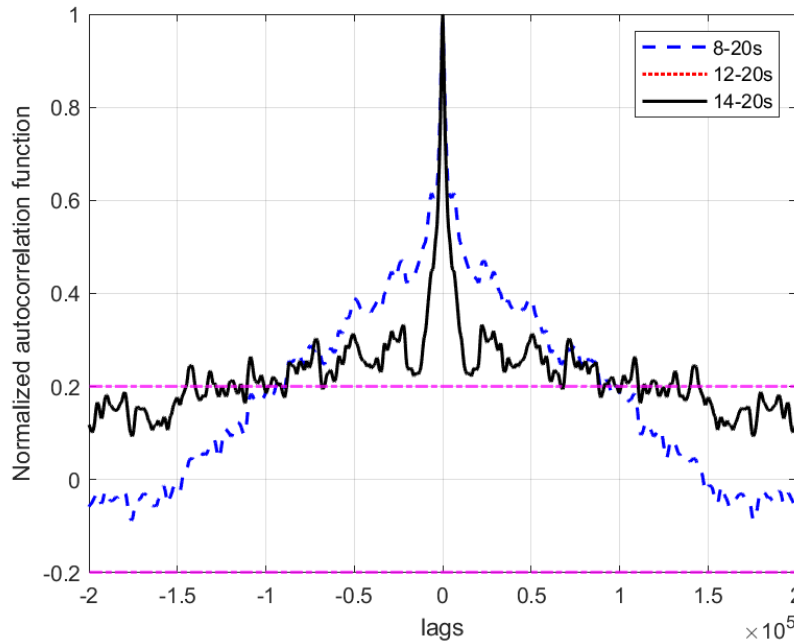


Figure 4.14 Normalized autocorrelation function plotted for mid-probe

Autocorrelation function is defined as

$$\rho(\tau) = \frac{\gamma(t + \tau, t)}{\sqrt{\gamma(t + \tau, t + \tau)\gamma(t, t)}} = \frac{\gamma(\tau)}{\gamma(0)} \quad (4.4)$$

where autocovariance function γ stated below as

$$\gamma(\tau) = \text{Cov}(x_{t+\tau}, x_t) = E[(x_{t+\tau} - \mu)(x_t - \mu)] \quad (4.5)$$

Ideally, the autocorrelation function of white noise is one at lag equal to zero and must drop to zero immediately for increasing lag values. Nonetheless, ACF plotted for global signal spreads over a wide range of lags before reaching zero value, exhibited in Fig. 4.14. In the case of the other two signal lengths, i.e., 12-20 s and 14-20 s, they appear to be quickly decaying to zero but start oscillating later. These oscillations indicate that the signal still contains repeating short signals that reveal the existence of non-stationarity in the time series. So, we can say that despite converged mean velocity and constant variance value, the signal failed its stationarity test.

4.3.1 Detrending non-stationary signal

Instead of calculating time-averaged mean, one can use classical multiple linear regression in time series, generally used to pre-process non-stationary signal. We can express a simple polynomial regression model for any random variable x_t influenced by its independent input z_t as

$$x_t = \beta_0 + \beta_1 z_{t1} + \beta_2 z_{t2} + \beta_3 z_{t3} + \dots \beta_q z_{tq} + w_t \tag{4.6}$$

where β_i is unknown fixed regression coefficients where $i = 1, 2, \dots, q$ w_t is a random error or noise process consisting of independent and identically distributed (iid) normal variables with mean zero and variance σ_w^2 . When the regression coefficients greater than β_1 are zero, then it is referred to as first-order polynomial regression. It suits when data contain continuously increasing or decreasing trends. In our case shown in Fig. 4.15, even if we can say that mean of the signal is showing a non-linear trend that can be fitted with higher-order polynomials, we don't have any clue about the order to which the model best fits the given data. Therefore, the Bayesian information criterion (BIC) is adopted, as shown in Eq. (4.7), to tailor the best model to avoid any under-fitting or over-fitting of the data. The polynomial order is selected at a minimum value of the plot as shown with the red dot in Fig. 4.16 (left).

$$BIC = \overbrace{n}^{\text{data points}} \ln(\epsilon) + \overbrace{k}^{\text{parameters}} \ln(n) \quad \text{where} \tag{4.7a}$$

$$\epsilon = \frac{\sum_{i=1}^n (\overbrace{\hat{v}_i(x)}^{\text{predicted data}} - \overbrace{v_i(x)}^{\text{data}})^2}{n} \tag{4.7b}$$

The autocorrelation function is plotted in Fig. 4.16 after removing the mean by using the polynomial order provided by BIC exhibits better behaviour when compared with

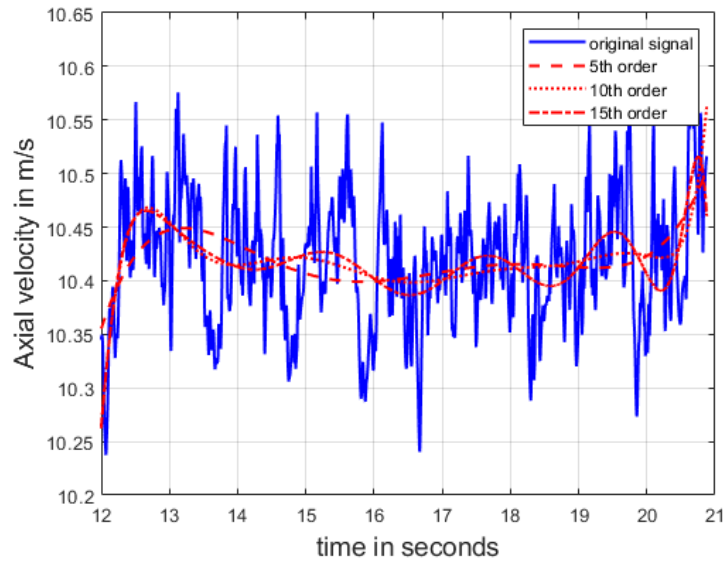


Figure 4.15 Detrending of non-stationary data

autocorrelation function of signal 14-20 s without de-trending the signal. Moreover, it's worthy to note that after removing the trend, the oscillating behavior of autocorrelation still exists. Hence, we have decided selection criteria for the weakly stationary process— if the autocorrelation function oscillates within ± 0.2 after crossing zero, we accept it to extract additional turbulence characteristics as described in our next section. Besides, stationarity can be further checked with other parameters such as the Augmented Dickey-Fuller test, ARIMA models, empirical mode decompositions, etc... Interested readers are directed to any fundamental books on statistical analysis e.g. [99].

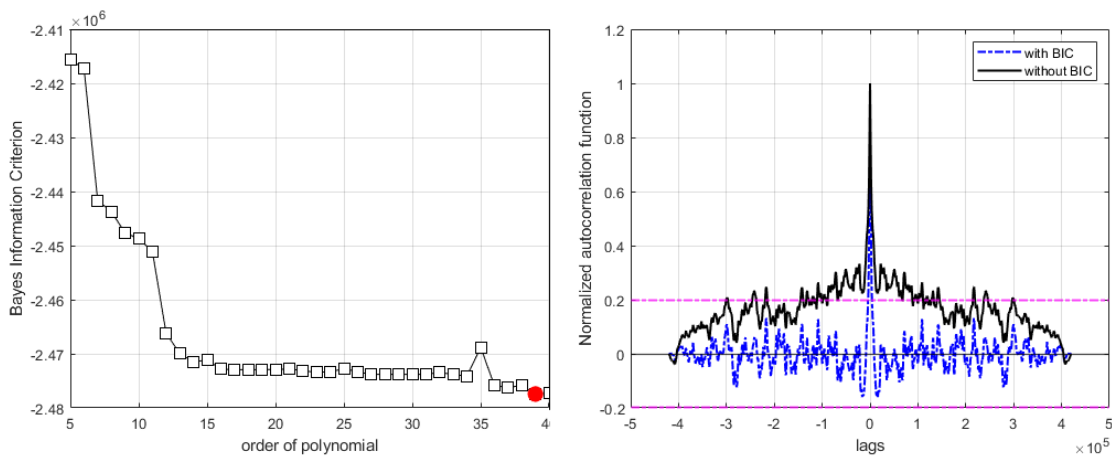


Figure 4.16 Autocorrelation function after de-trending of non-stationary data

4.3.2 Extraction of turbulent characteristics

Eq. (4.1) shows how any recorded quantity can be decomposed into mean and fluctuating quantities. We can use this fluctuating velocity to describe turbulence, such as turbulence intensity and integral length scale. Consider a stationary signal of resultant velocity v has three components (v_x, v_y, v_z) and it is further decomposed into mean and fluctuating quantities as shown below

$$v = \sqrt{v_x^2 + v_y^2 + v_z^2} \quad \text{and} \quad v = \bar{v} + v' \quad (4.8)$$

The mean and fluctuating velocity of these components are $(\bar{v}_x, \bar{v}_y, \bar{v}_z)$ and (v'_x, v'_y, v'_z) , respectively. Turbulence intensity is defined as

$$Tu = \frac{\sqrt{\frac{1}{3}(v'^2_x + v'^2_y + v'^2_z)}}{\bar{v}} \quad (4.9)$$

If the signal is stationary, the mean velocity is computed with the time-averaged equation, else for non-stationary signal, the time-varying mean is calculated by fitting a polynomial. Turbulence intensity is also the measure of mean velocity deviation and signifies the amount of turbulent kinetic energy convected by mean flow. Another turbulence characteristics is the integral time scale of a turbulent motion. It can be calculated using the autocorrelation function. The autocorrelation function measures the similarity of two signals when the second signal is a time-shifted copy of the first signal. At zero time delay, the normalized correlation function value is maximum. It means that signals are perfectly matching as we shift in time. The correlation value reduces to zero. Hence, the integral time scale is calculated over the area under the curve from $\rho_\tau = 1$ to $\rho_\tau = 0$.

$$\mathcal{T} = \int_0^\tau \rho(\tau) d\tau \quad (4.10)$$

The small scale turbulence is convected with the mean flow speed. Hence, the length scale is defined as

$$\Lambda = \bar{v} \int_0^\tau \rho(\tau) d\tau \quad (4.11)$$

Our previous discussion observed that the signal recorded along radially distributed probes is non-stationary in nature, irrespective of its position, whether inside or outside the boundary layer. So, the de-trending process is followed to calculate the mean using polynomial fitting instead of time averaging. Then autocorrelation function is calculated to

predict turbulent length scale by using the BIC criteria discussed above. Following Fig. 4.17 differentiates the mean axial velocity and length scale plotted along radially distributed probes (refer 4.11). The nature of axial velocity (Fig. 4.17 left) distribution is almost similar except that the measurements exp-setup show a thinner boundary layer near the hub than the numerical prediction (no-duct setup), which is also in-line with the smaller eddy size observed in the turbulent length scale plot. Nonetheless, lower turbulence intensity is witnessed in Fig. 4.18. Although near diffuser, mean axial velocity displays similar distribution, we can anticipate large turbulent structure formation in the exp-setup from Fig.4.17 (right). Conversely, we can forecast a slightly higher turbulent boundary layer in the no-duct setup.

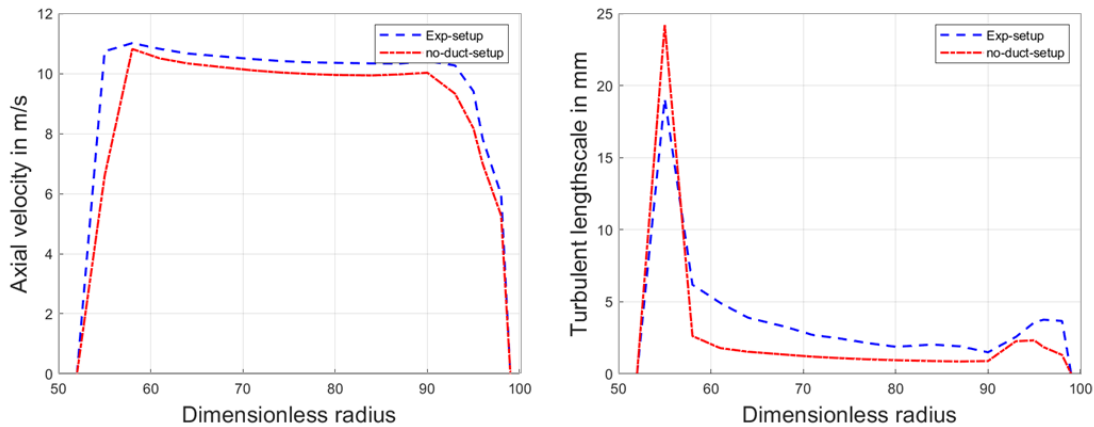


Figure 4.17 Axial velocity (left); Turbulent length scale (right)

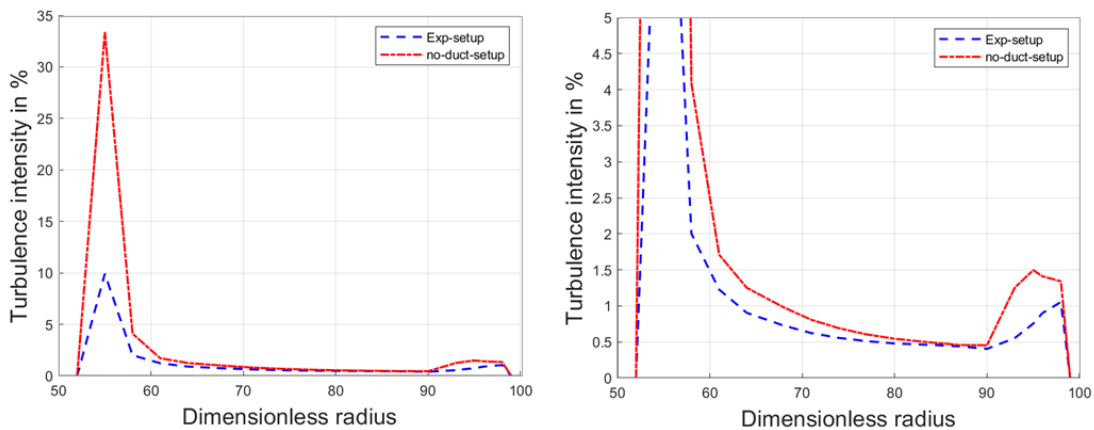


Figure 4.18 Turbulence intensity in % (left) and zoomed view (right)

This study carried on two different setups showcased different boundary layer behavior near walls and the formation of various small-scale turbulence along the radius. Eventhough

the experimental setup seems axisymmetric, non-uniform flow is observed, which should advocate future data extraction around 360 deg.

4.4 Conclusion

In this chapter, the test matrix used in this study is discussed. The experimental configuration and the data recorded for validation are reviewed. The numerical approach and setup are discussed in detail. We argued on modeling the plenum with the actual inlet configuration versus the uniform inlet approach. The analysis is performed using the hub only case for two different inlet configurations. We observed key differences in both approaches. Additionally, the statical methods used in this study are discussed in detail, mainly how to process non-stationary data. The experimental setup contains unique incoming flow features, while the UI setup does not show any such signatures. We understood that we would lose some inherent dynamic characteristics that are important for any acoustics analysis by assuming a uniform inlet. Therefore, the experimental setup is chosen to analyze different fans and capture noise spectra using direct acoustics. The aerodynamics and acoustics findings are discussed in the following chapters.

CHAPTER 5

Aerodynamics Analysis

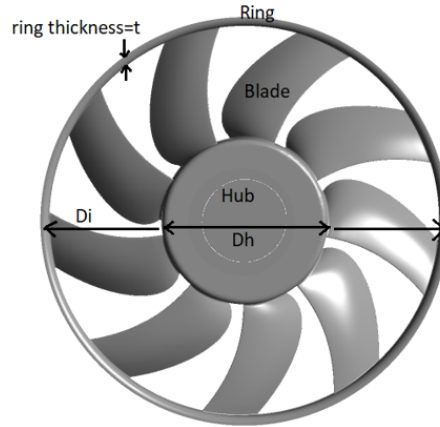
The aerodynamic flow field around a blade is investigated as a two-step process. First, the mean flow field is examined closely by solving the traditional Reynolds-Averaged Navier Stokes (RANS) equations available in the commercial solver ANSYS CFX. The sole objective is to assess an aerodynamic performance on a single blade passage under a mean, steady, uniform, and perfectly periodic flow condition. Second, the installation and other non-periodic, unsteady effects offered by the actual test configuration are simulated with a full fan using the Lattice Boltzmann method (LBM) developed by Powerflow, licensed under 3DS Simulia at Dassault Systemes.

To begin with, the RANS simulation method is established for the Valeo-made ring fan-EC01. Its results are validated with already published data along with the test results. After achieving a satisfactory correlation, a similar method is followed to simulate other swept variants, viz. EC02 and EC03. The key parameters such as performance, the static pressure distribution, the flow field at radial cut sections and the azimuthal planes before LE and TE are investigated. Then, unlike ring fans, ducted fans designed and developed by Zenger [124] are also analyzed. Ultimately, the knowledge gained from these analyses leads to critical conclusions on aerodynamic behaviors. It also provides a solid basis to exchange views on aeroacoustics performance, argued in the next chapter.

5.1 RANS for Ring fan

5.1.1 Numerical configuration

The fan, exhibited in Fig. 5.1, is mainly designed for radiator cooling in a automotive application. The fan outer diameter is 380 mm and has a L-shaped ring that fits inside the shroud with a uniform annular clearance of 2.5 mm. The inner diameter of the fan is 366 mm, the thickness of the ring is 2.5 mm and depth is 65 mm. Nine blades are evenly distributed around the hub of diameter 156 mm, and each blade spans over 105 mm, formed by stacking controlled-diffusion (CD) airfoils. The fan rotates at 2500 rpm to produce 250 Pa of pressure rise at a supplied flow rate of 2500 m³/h. The solidity of the fan is 0.7, which facilitates a single blade passage model to evaluate aerodynamic performance in a uniform incoming flow. The computational domain used in this study



Fan inner dia.: D_i ; Fan outer dia.: $D_o = D_i + 2t$; Hub dia.: D_h

Figure 5.1 H380EC01 radiator cooling fan

is represented in Fig. 5.2. The uniform flow enters the domain with a spherical inlet and leaves through a cylindrical outlet. The sidewalls of the domain are modeled as periodic, and a fan blade in the rotating domain is modeled as multiple reference frame (MRF). The shaft is considered as a frictionless wall with slip boundary condition. This numerical modeling approach is adopted from the published study on the radiator fan modeling by Foss et al. [29], Moreau and Casalino [72] and most recently by Magne et al. [63].

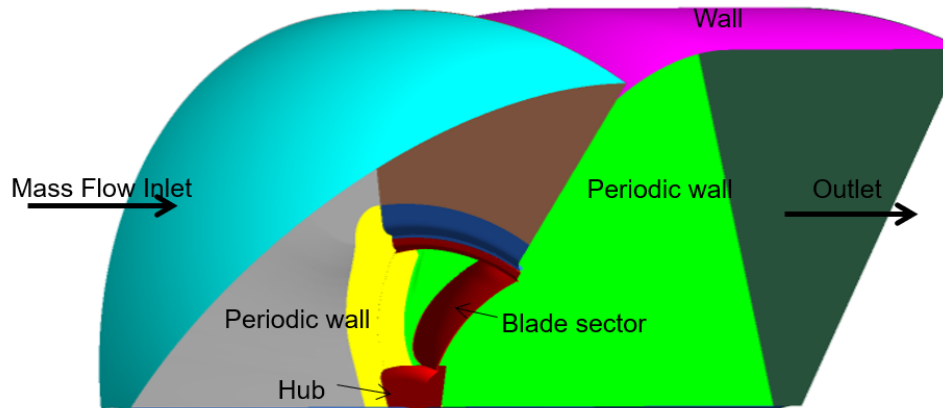


Figure 5.2 Numerical domain modelling approach for a single blade passage

In order to predict the fan performance, the flow rate is varied from $1000 \text{ m}^3/\text{h}$ to $4000 \text{ m}^3/\text{h}$. At the design condition, the Mach number (M) near the tip reaches up to 0.15 and the chord-based Reynolds number (Re_c) is 2×10^5 whereas at mid-span $Re_c = 1 \times 10^5$ and $M=0.07$. This flow velocity implies that the fan generates a low subsonic and turbulent flow field that can be modeled with an incompressible RANS, using $k - \omega$ SST. The first

grid point is placed near-wall such that the dimensionless distance to the wall $y^+ = 1$ and the model can resolve turbulence all the way towards the wall using fine mesh. The dimensionless distance to the wall is defined as $y^+ = \frac{yu_\tau}{\nu}$, where y is the absolute distance from the wall, ν is the kinematic viscosity and friction velocity, $u_\tau = \sqrt{\frac{\tau_w}{\rho}}$, where τ_w, ρ are wall shear stress and the fluid density, respectively. Hence, the first cell is placed 0.1 mm away from the wall, and prisms are grown outwards. The outer layer is discretized with tetrahedra of size 1 mm close to prism and it is slowly grown to the size of 30 mm as evidenced in Fig. 5.3. This meshing strategy helps to capture steep velocity gradients inside the boundary layer with the fine mesh and uniform flow with a bigger mesh size. Special care is given at LE and TE to capture their curvature with the localized refinement zones. The remaining bulk fluid is discretized with tetrahedral elements. The near blade and wake regions are meshed with the fine cell sizes, whereas farther regions are discretized with coarse elements to keep the computational cost low. At first, the $k-\omega$ SST turbulence closure model with RANS is solved with the first-order accuracy. After reaching the converged state, it is switched to the second-order accuracy in momentum and turbulence. In total, 4000 iterations are required to achieve the convergence with $\pm 1\%$ variation, out of which 1500 iterations are used for the first order. Convergence is monitored closely with the pressure rise—the difference between total pressure and static pressure measured at the inlet and outlet of the domain, respectively.

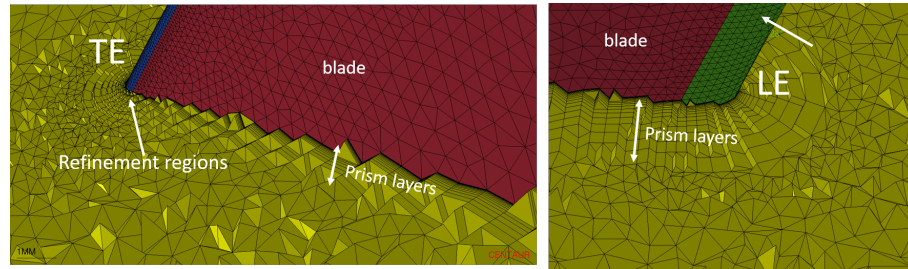


Figure 5.3 Prism layer near blades, localized refinement at LE and TE

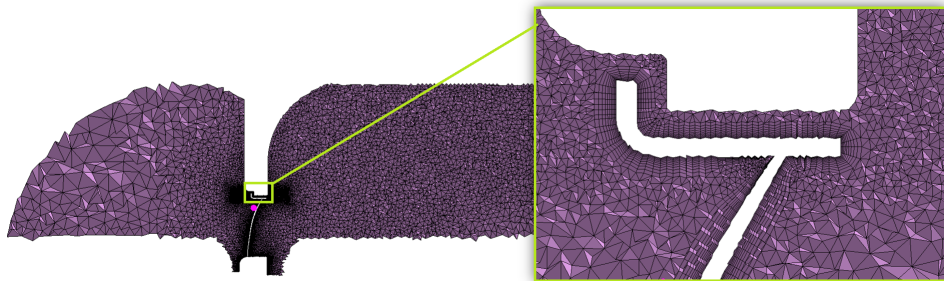


Figure 5.4 Tetrahedral elements in the bulk fluid

5.1.2 Validation

Sanjose et al. [90, 91], Lallier et al. [53], Magne et al. [63] and Foss et al. [29] have studied the H380EC01 fan, and its performances well-documented in the literature are compared in Fig. 5.5. Pressure rise and torque predicted from our simulation correlate with experimental recordings at the design point. However, for lower flow rates, the predictions are slightly higher than the experiments because the secondary flows such as corner vortex, passage vortex, and tip vortex exhibit highly erratic behavior that is difficult to simulate with steady state simulations. Moreover, our studies are concerned with the design point, so we haven't explored outside of it.

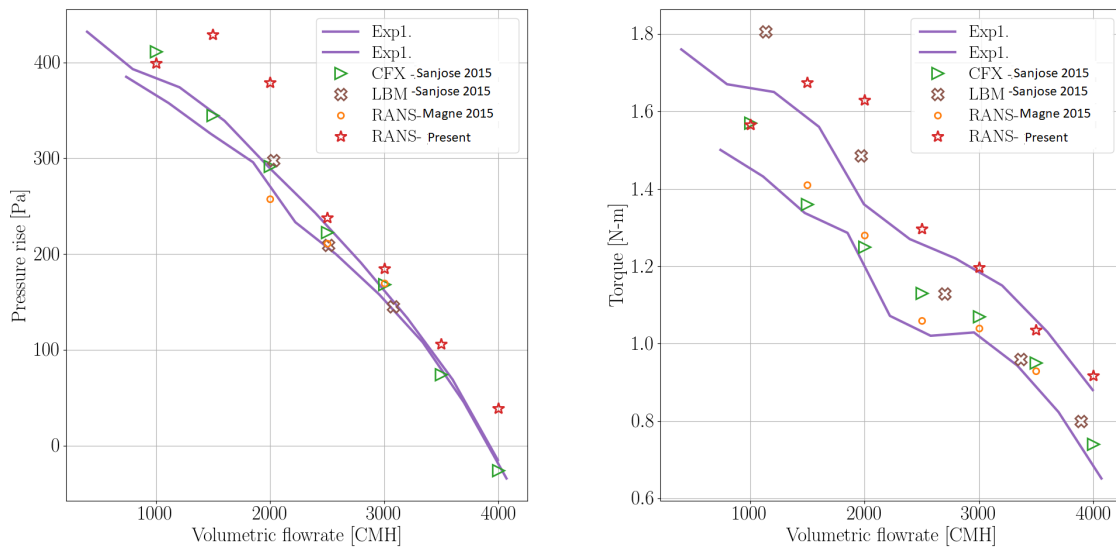


Figure 5.5 Fan performance validated with previous studies

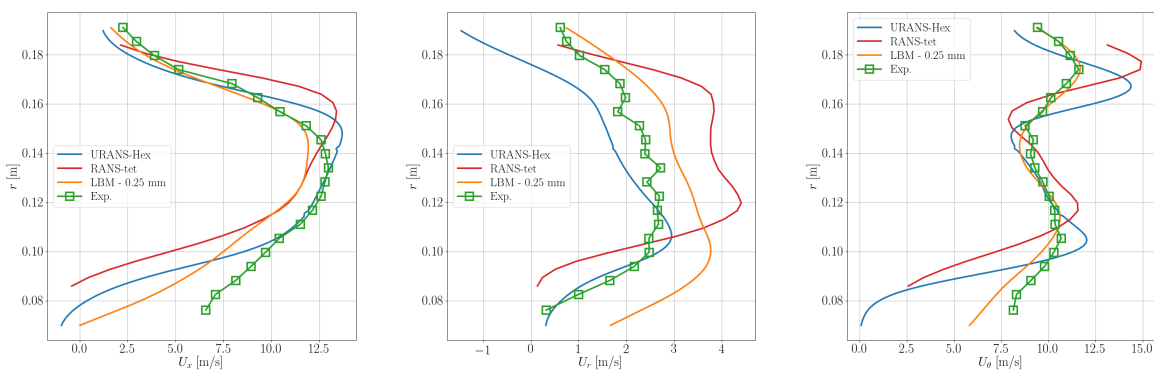


Figure 5.6 Azimuthally averaged velocity components (u_x, u_r, u_t) measured near TE (RANS tet -present, URANS, LBM- previous study, EXP- MSU)

Further validation is performed on the velocity field recorded in a plane 33 mm behind the fan TE, using a hot wire anemometry from the Michigan State University facility. The comparison of the mean azimuthally averaged velocity components is plotted in Fig. 5.6. The axial velocity demonstrates that our simulation results can capture the outgoing flow accurately, as observed in experiments. The radial velocity matches qualitatively except that the amplitudes are slightly higher than in experiments. The velocity contour plots shown in Fig. 5.7 overlays satisfactorily with experiments along the whole blade except for some local deviation near the tip and hub where secondary flow effects are pronounced. The higher tangential velocity denote that tip vortex travels faster in simulation than in the experiment.

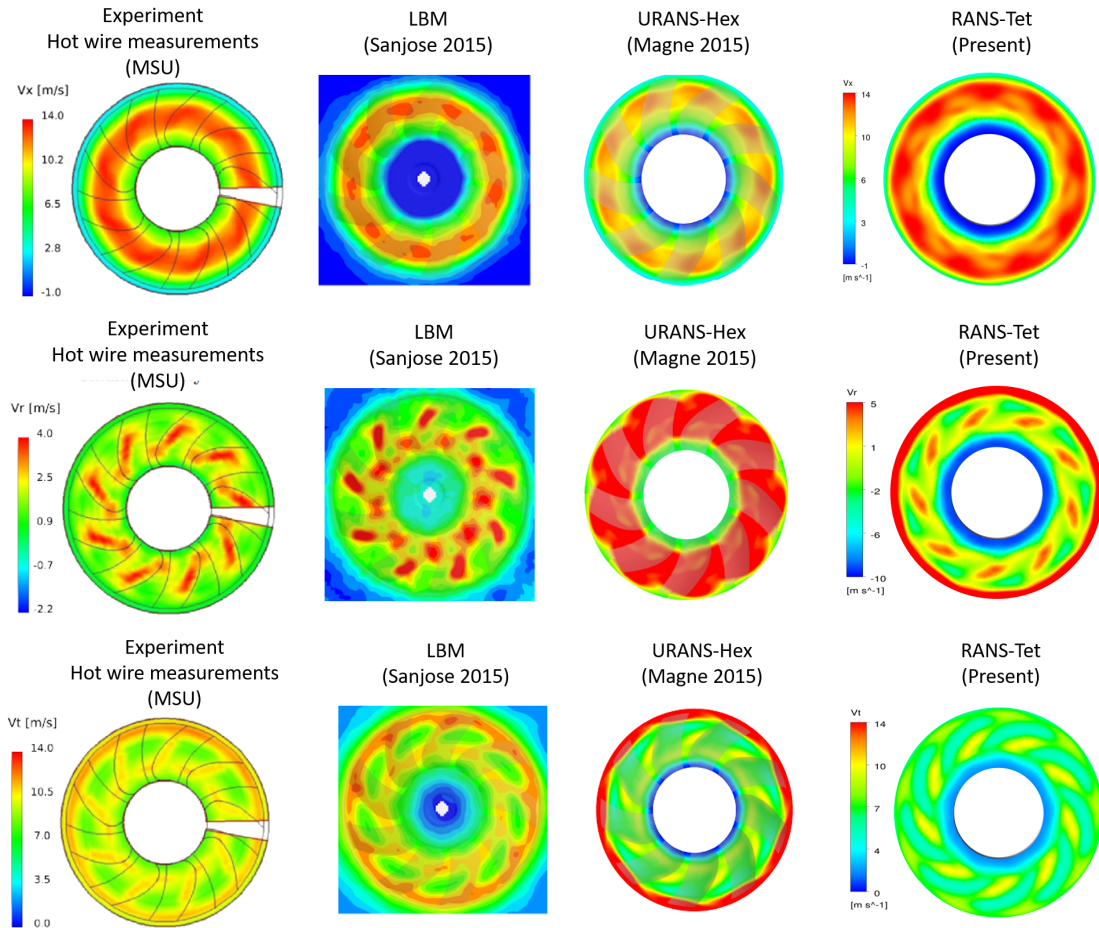


Figure 5.7 Velocity profiles measured near TE, Top-axial velocity, middle-radial velocity, bottom-tangential velocity

Blade-to-blade cut sections at a constant radius reveal flow behavior near the blade. The iso-radial flowfield shown in Fig. 5.8 closely resembles that of the RANS study performed on structured HEX mesh [90] except near the hub. The latter differences come from the

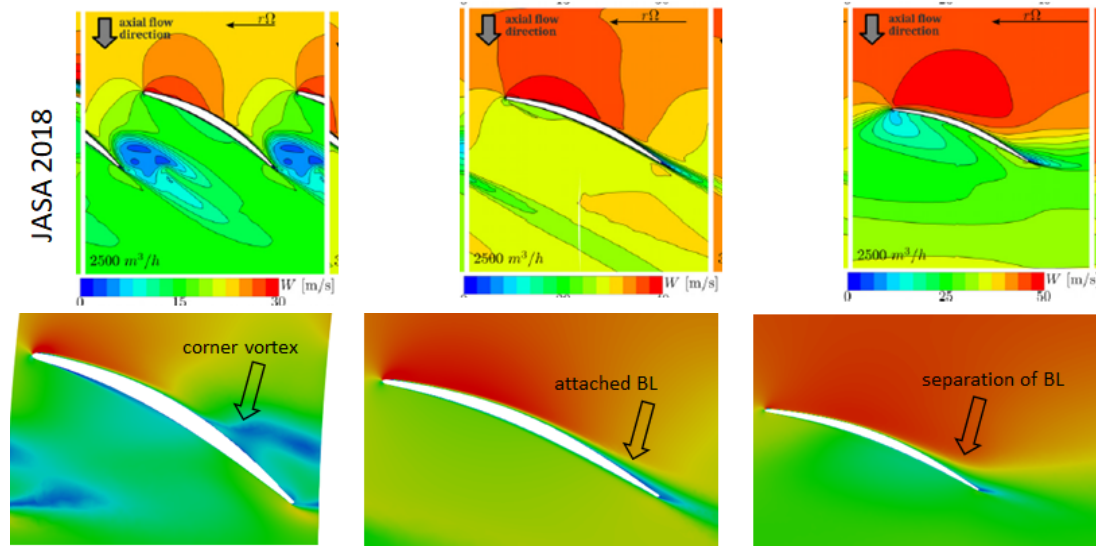


Figure 5.8 Velocity contours at iso-radial cut-section i.e. near hub, midspan and tip

slight modification in the updated geometry received lately. The added small cusp tends to separate the flow earlier and forms a larger corner vortex recirculating region. This is also seen in Fig. 5.9. Streaklines plotted in Fig. 5.10 demonstrate two dominant features: a strong positive radial flow near the cusp, observed in the LBM simulation [91] and a leading edge separation bubble (LSB), noticed in the RANS with structured mesh [90]. The high pressure gradients in the tip gap generate recirculation regions that wrap around the ring— pinpointed by the LBM simulation in Fig. 5.9 and also experimentally noticed by Canepa et al. [15] in their PIV measurement. On the contrary, steady RANS simulation predicts recirculating regions that stay tangential to the ring rather than being sucked by the blade. Surface streaklines shown in Fig. 5.10 demonstrate their tangential behavior over the ring surface.

All these moderate and acceptable validations with previously published studies give us confidence in our meshing strategy and simulation method. Therefore, a similar technique is then used on the other two swept blades, and their results are compared against the EC01 blade in the following section.

5.1.3 Performance and flow field analysis

The two forward sweep variants are developed using the EC01 fan as the base design and are shown in the matrix of the industrial fan as shown in Fig. 4.1. The EC01 fan already has 28° of forward sweep measured near the tip. For low-speed fans, the sweep is commonly evaluated in the plane of rotation as illustrated in Fig. 3.2. The sweep angle

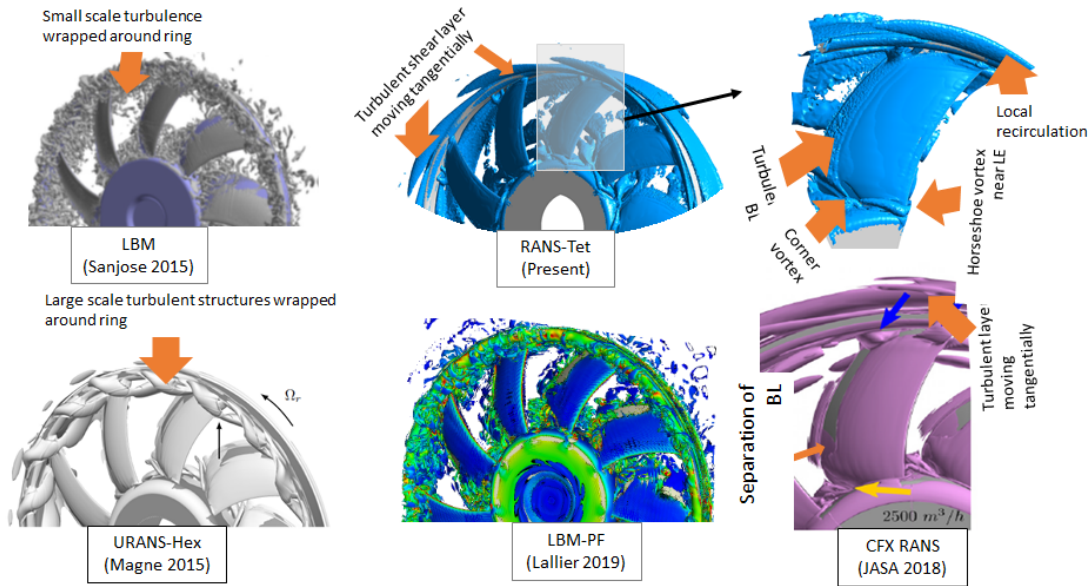


Figure 5.9 Isosurface of Q-criteria compared with other simulations

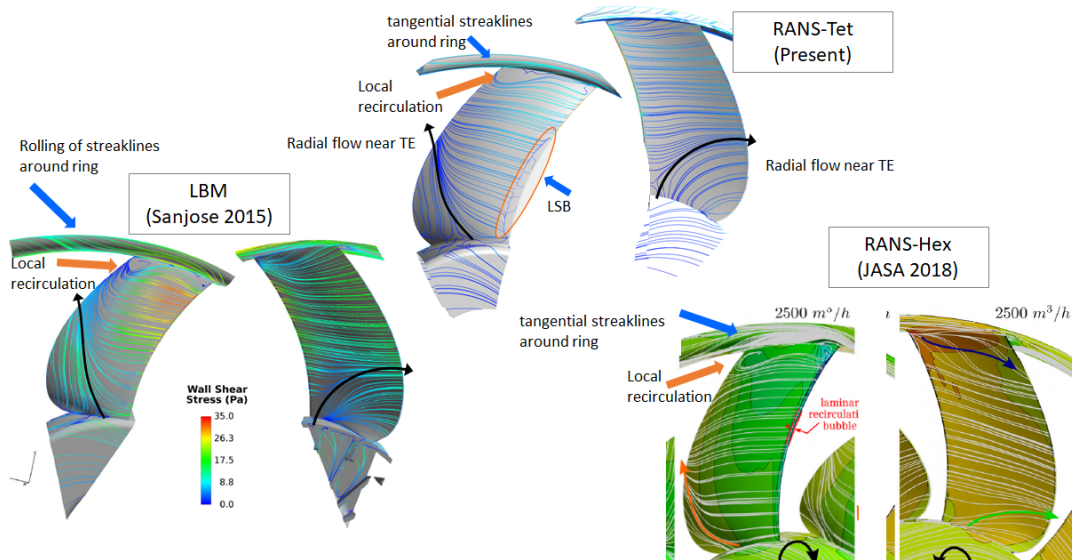


Figure 5.10 Streaklines on blade surface

measured in a similar fashion for forward swept blades EC02 and EC03 is 30° and 48° , respectively. RANS simulations conducted on EC02 and EC03 are compared with EC01.

Fig. 5.11 compares performance for different sweep angle with simulation results. The fan performance predicted by steady state simulation simulations match fairly well for all flow rates except below $2000 \text{ m}^3/\text{h}$. The maximum sweep angle shows the lowest pressure rise. This observation agrees with Smith and Yeh [102] who deduced that sweep deteriorates the

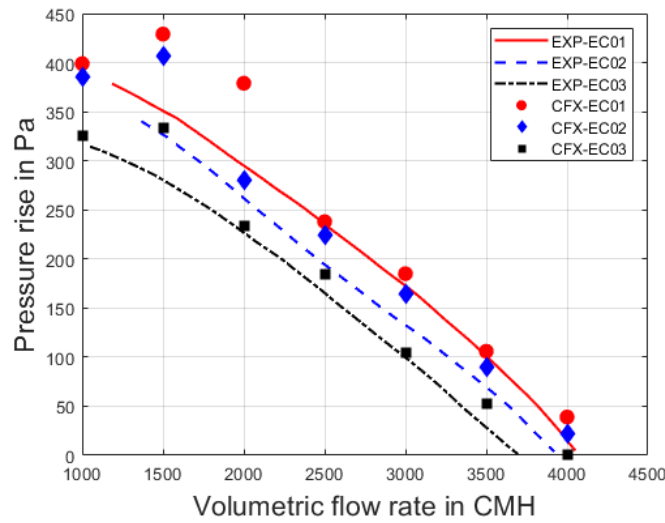


Figure 5.11 Aerodynamic performance of swept blades of ring fans from Valeo

lift: the higher the sweep angle is, the lower the lift is (increased losses). The correction suggested by Beiler and Carolus [9] doesn't follow the pressure rise trend accurately. In fact, we observed that the pressure rise scales more closely with $\cos(\lambda)^a$ times the pressure of EC01 for EC02 and EC03 at the design point where $a \approx 1$ (see exponent a for 2500 m³/h in the Table 5.1). Moreover, when the sweep angle varies along the span, our calculation considered the sweep angle near the tip. For other flow rates, the pressure rise can be scaled with an exponent added to $\cos(\lambda)$, but the exponent value varies from low to high flow rate and is always much larger than 0.62, refer to table 5.1.

| Flowrate in m ³ /h | Pressure rise in Pa | | | Exponent values | |
|-------------------------------|---------------------|------|------|-----------------|------|
| | EC01 | EC02 | EC03 | EC02 | EC03 |
| 1000 | 399 | 386 | 326 | 1.1 | 0.81 |
| 1500 | 429 | 407 | 334 | 1.25 | 0.93 |
| 2000 | 379 | 280 | 234 | 3 | 3.5 |
| 2500 | 238 | 225 | 184 | 1.25 | 0.95 |
| 3000 | 185 | 164 | 105 | 1.7 | 1.7 |
| 3500 | 106 | 90 | 53 | 2 | 2 |
| 4000 | 39 | 21.9 | 0.3 | 5 | 8 |

Table 5.1 Exponent (a) values calculated for different sweep angles (λ)

The chord length, the stagger angle and other design parameters are maintained the same in all fans because Valeo is deliberately seeking the sole influence of sweep on their fan performance and noise. All published studies mention sweep reduces pressure loading, but how isn't clearly explained in the literature yet. Hence, an investigation is carried out by

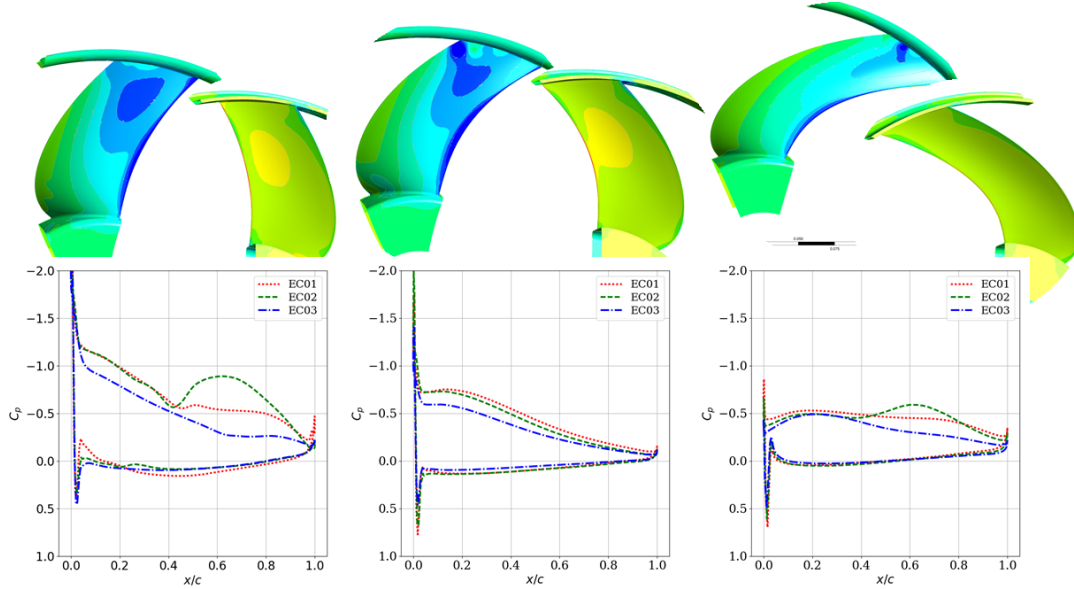


Figure 5.12 Static pressure contours and C_p plot; near hub (left), mid span (middle) and near tip (right)

plotting pressure coefficient (C_p) at different radial sections. Here, the pressure coefficient is defined as:

$$C_p = \frac{p - p_\infty}{0.5\rho_\infty U_c^2} \text{ where } U_c = r\Omega \quad (5.1)$$

where U_c is circumferential velocity of a blade, ρ_∞ and p_∞ are atmospheric density and pressure. In Fig. 5.12 at midspan in absence of secondary flow effects, it is noticed that the lift demonstrated by the pressure coefficient distribution along the chord is continuously reduced. It means that the highly swept blade is relatively less loaded than the base design. Further investigation is conducted to apprehend the causes for decreased loading. Hence, an axial plane is placed 10 mm before LE and velocity data extracted in the relative frame is azimuthally averaged which is shown in Fig. 5.13. It is noticed that the greater sweep angle experiences higher tangential velocity and lower radial flow for the same incoming axial flow. This indicates that the flow angle definition for all three fans doesn't remain the same. Therefore, the velocity triangle and angle definition are revisited and drawn in Fig. 5.15 for a typical axial machine in a simplified manner. Let's consider an airfoil of chord (C) but without any camber. The stagger angle (λ) is defined as the angle made by the chord with the axial direction. The incoming relative velocity (W) makes the inlet flow angle (β_1) with the blade rotating with the circumferential velocity (U_c). The incidence angle (i) is the angle made by the relative velocity with the chord.

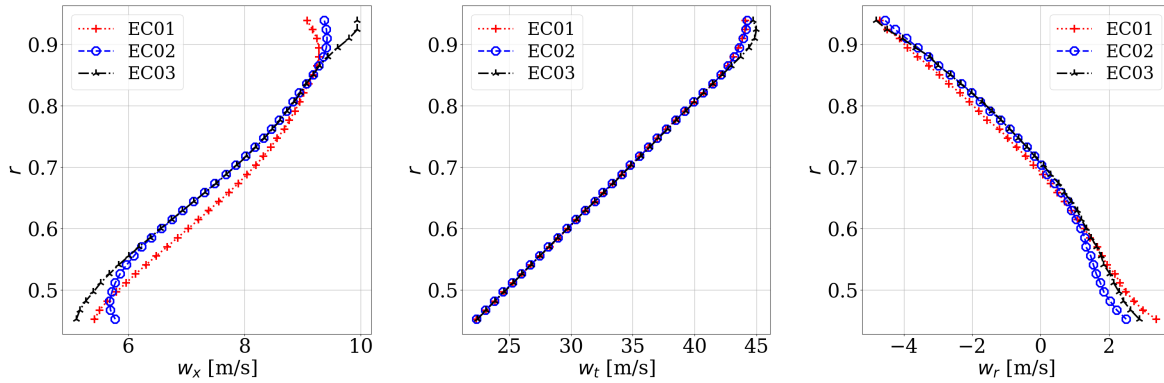


Figure 5.13 Azimuthally averaged velocity in relative frame extracted 10mm before LE and plotted along the span normalized with tip radius; left (axial velocity, U_x), middle (tangential velocity, U_t), right (radial velocity U_r)

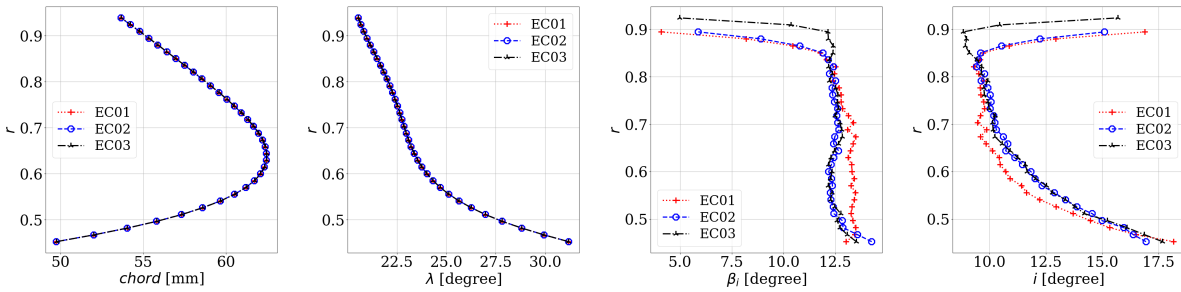


Figure 5.14 Blade geometrical extractions; left (chord), middle (stagger angle, λ), right (inlet flow angle, β_i and incidence angle (i)) for ring fans

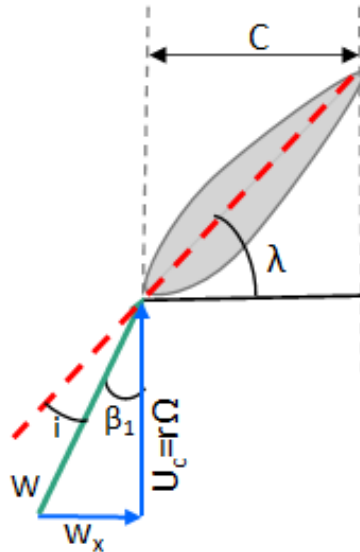


Figure 5.15 Simplified velocity triangle and angle definition for low speed axial fan

Usually, an unswept blade is designed by assuming the absence of any radial flow. However, the relative velocity at any constant radial section is strongly influenced by the radial flow formed at swept LE. Therefore, modified relative velocity (W') expression that swept blade experiences is as follows

$$W' = \sqrt{W^2 - w_r^2} = \sqrt{w_x^2 + w_t^2} \quad \text{where} \quad W = \sqrt{w_x^2 + w_r^2 + w_t^2} \quad (5.2)$$

Therefore, from Fig. 5.13 it is clearly noticed that for similar incoming axial velocity the tangential velocity remains same for all three fans. The highly swept blade experience higher axial velocity near tip and reversed the behavior near hub. If we calculate relative velocity by removing the radial flow effect using Eq. 5.2, it shows that the highly swept blade (EC03) meets higher relative velocity than the other two lower swept blades. The relative inlet flow angle is calculated as $\beta_1 = \cos^{-1} \frac{U_c}{W'}$ where U_c is circumferential velocity. Hence, augmented relative velocity increases β_1 that results into systematic reduction of incidence angle ($i = \lambda - \beta_1$) along the blade span as shown in Fig. 5.14 and tip region is affected more than rest of the span since, the blade is highly swept above midspan towards the tip. The pressure contours also show that most of the lift is generated from tip region than the remaining blade span. This explains why a highly swept blade has a lower lift than the other two blades at all span locations shown in Fig. 5.12.

Hence, to improve loading, one can increase the incidence angle by modifying the stagger angle or increase blade rotational speed. Caution! A larger stagger angle can induce 3D flow effects and increased speed can augment operating costs by raising power demand. So, it will be the subject of future study.

Reed and Sarik [88] studied swept wing, and stated that LE sweep induces a cross-flow effect that causes local instability i.e. Görtler vortices formation, and it can trigger early boundary layer transition. We suspect that increased crossflow forms a larger LE separation bubble for increasing sweep angles which is demonstrated with the help of streaklines in Fig. 5.16. However, further proof is needed to confirm the source of the LE bubble.

Streaklines in Fig. 5.16 and contour plots 5.17 also pinpoint thicker and increased corner vortex for EC02 (starting closer to mid-chord) whereas, for EC03 near the tip, the boundary layer remains attached almost until TE. Increased axial velocity near the tip improves the flow, and is responsible for delay in the stall in the forward swept fans [9, 69, 109]. However, in our case, apart from a slight increase in axial velocity, the increased tangential velocity in the relative frame and lower incidence angle are primarily responsible for attached flow near the tip region.

The contour plots in Figs. 5.18, 5.19 and 5.20 compare the different velocity components in stationary frame before LE and after TE. EC01 and EC02 don't possess any significant flow field differences since their sweep angles are almost similar. Nevertheless, EC03 shows lower axial, tangential velocity and increased radial velocity near TE compared to EC01. At LE, the tangential velocity is far lower for EC03 than EC01 near the tip. It means that reduced incoming tangential velocity is balanced by augmented axial velocity near the tip in a stationary frame. The shear layer formed tangentially to the ring as a result of reverse flow through the tip gap is captured with Q -criteria and is displayed in Fig. 5.23. It seems that the shear layer shows almost similar behavior despite the change in sweep angle.

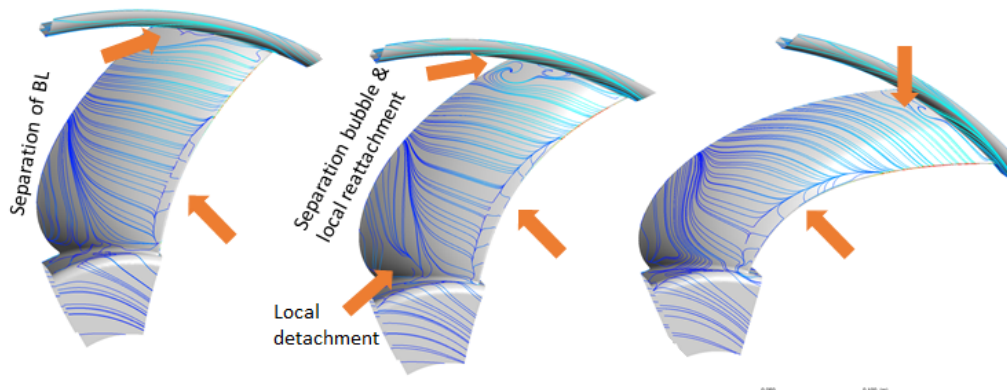


Figure 5.16 Streaklines for swept blades

The parameters within the boundary layer (BL) are extracted perpendicular to the wall at 85% of chord length. We can estimate the BL thickness (δ) after extracting the relative velocity profile. According to theoretical definition, the distance at which velocity reaches 99% of free stream velocity is considered as BL thickness. The blade shows some 3D flow structures, especially near the hub and tip where streamlines don't remain parallel to the chord (see 5.16 and 5.23). Usually vortical structures are visualized with gradient of velocity. The tensor of gradient of velocity is decomposed in symmetric and antisymmetric part. Q is then defined as the second invariant of the velocity gradient tensor, given by $Q = \frac{1}{2}(\|\Omega\|^2 - \|S\|^2)$. Such regions cause problems in BL thickness extraction. Therefore, Sanjose and Moreau [90] proposed a method where a second-order gradient of total pressure is extensively used in the identification of BL thickness. The distance at which $\left| \frac{\partial^2 P_t}{\partial^2 h} \right|$ is minimum, is considered as BL thickness. Using this method, the BL parameters calculated are displayed in Fig. 5.24. The external velocity of the BL is defined as $U_e = W(h = \delta)$, where W is relative velocity. The displacement thickness is calculated

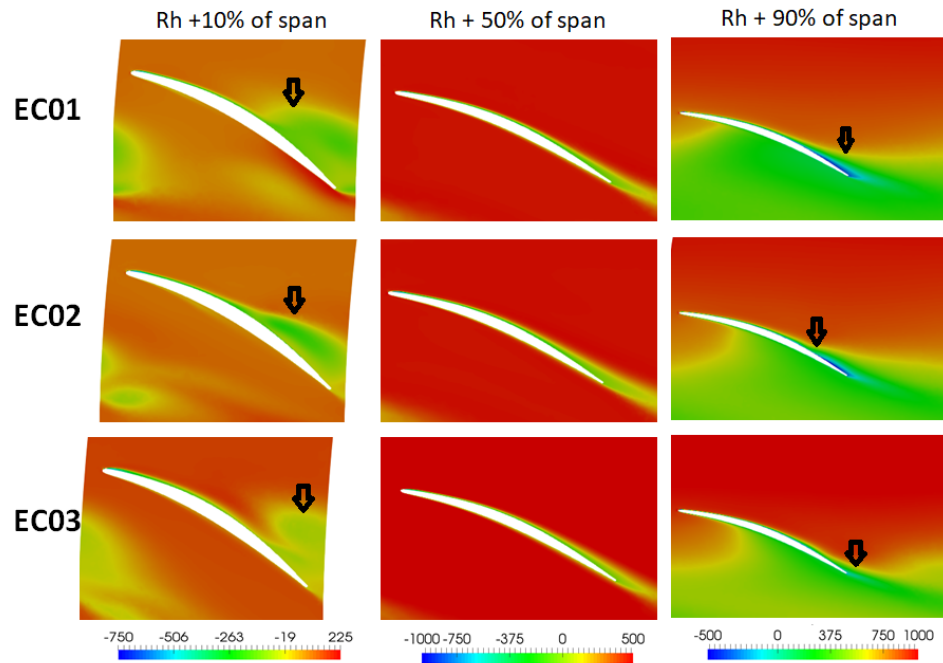


Figure 5.17 Isosurface of radial cut section colored with total pressure in relative frame

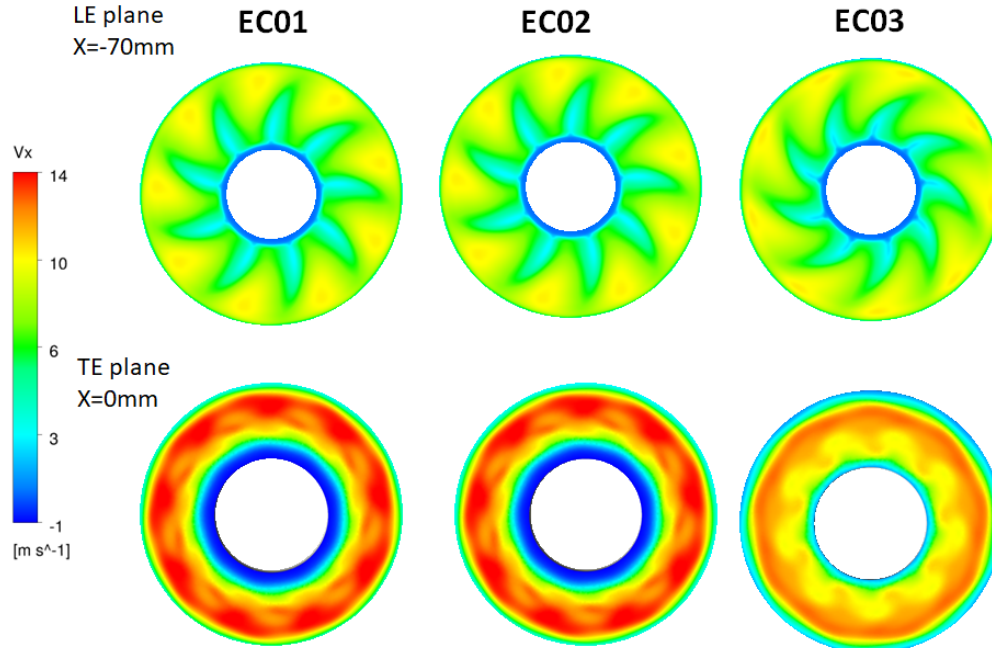


Figure 5.18 Axial velocity profiles in stationary frame taken before LE and after TE for EC01, EC02 and EC03

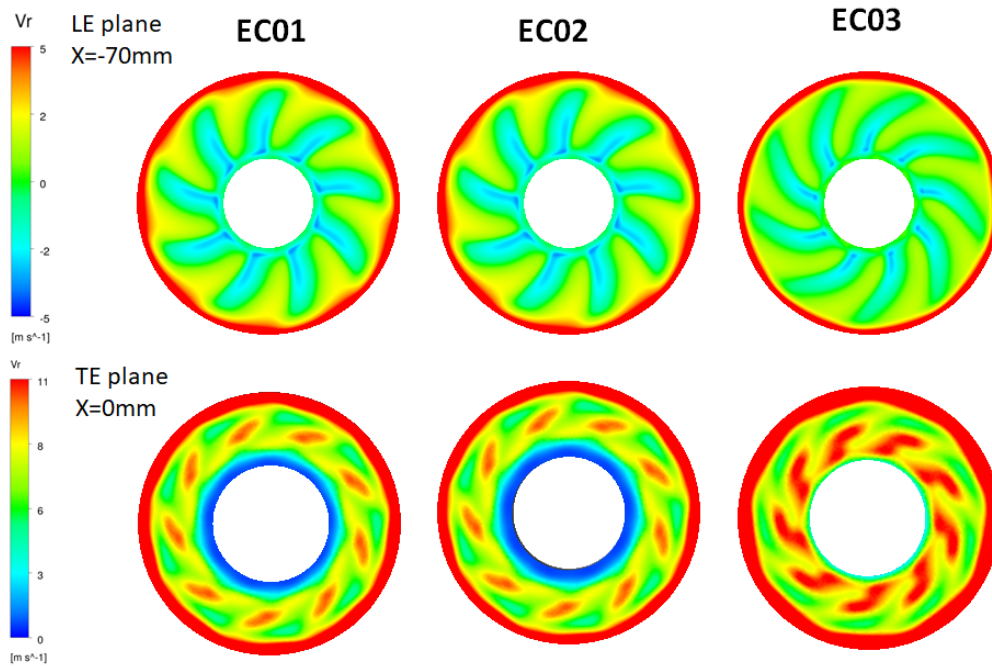


Figure 5.19 Radial velocity profiles in stationary frame taken before LE and after TE for EC01, EC02 and EC03

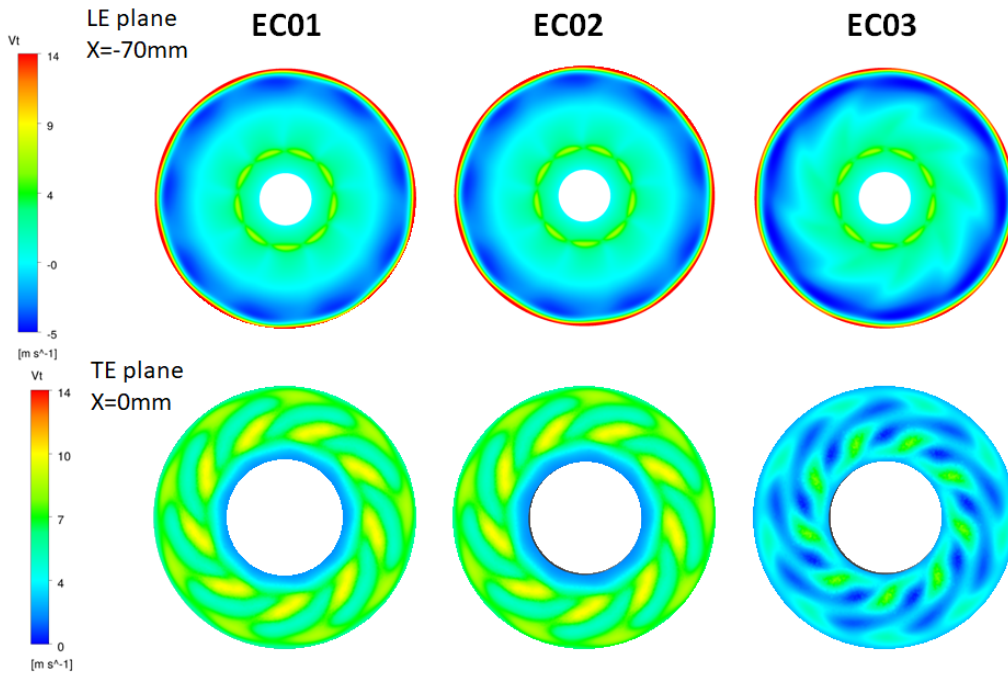


Figure 5.20 Tangential velocity profiles in stationary frame taken before LE and after TE for EC01, EC02 and EC03

as:

$$\delta^* = \int_0^\delta \left(1 - \frac{W(h)}{U_e}\right) dh \quad (5.3)$$

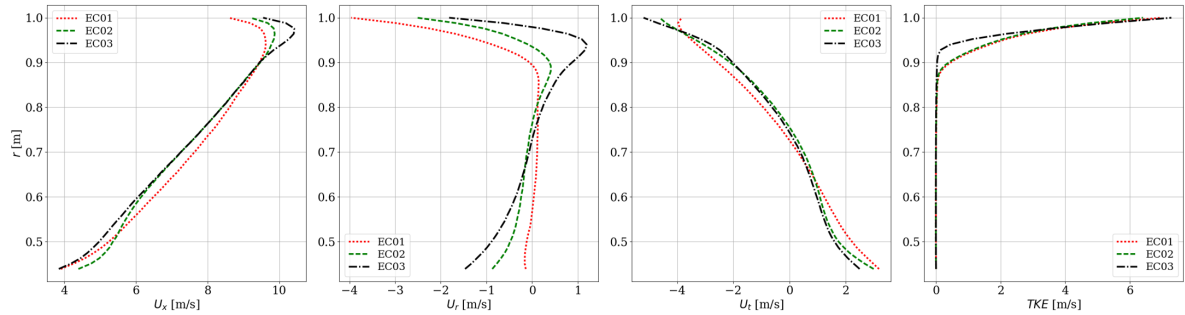


Figure 5.21 Azimuthally averaged profiles in stationary frame at LE for EC01, EC02 and EC03

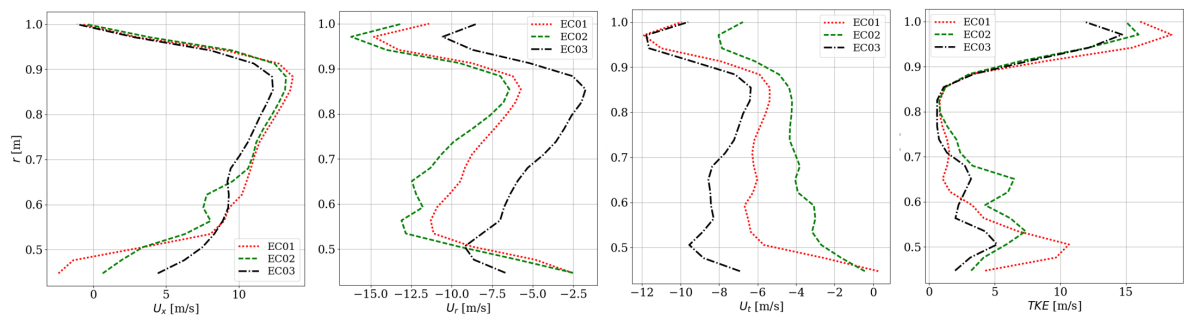


Figure 5.22 Azimuthally averaged profiles in stationary frame at TE for EC01, EC02 and EC03

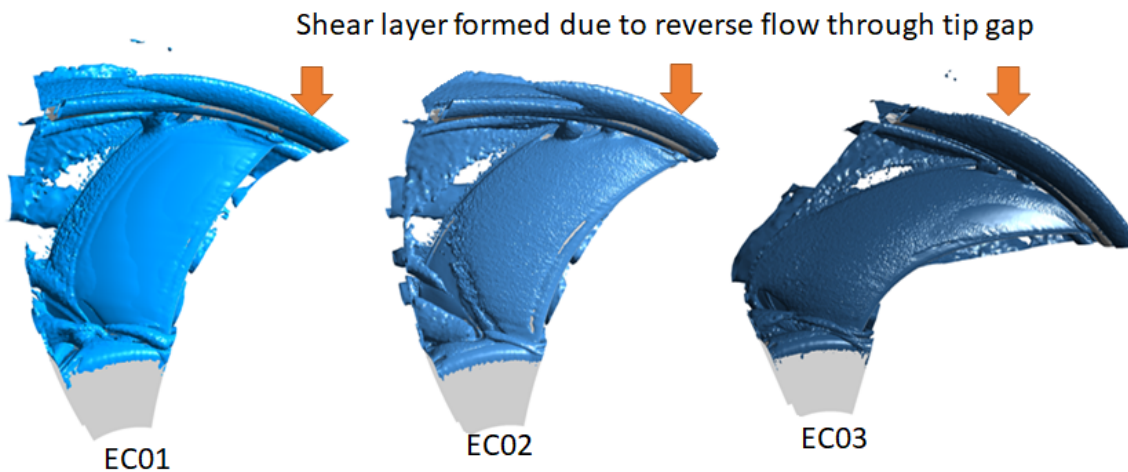


Figure 5.23 Isosurface of Q criteria at 100k

The EC03 shows higher U_e and δ than the other two swept blades, notably above midspan. Based on the theory provided by Yu and Joshi [121], that high Re_δ in sweep can increase TE noise. But the difference in Re is very small and perhaps it doesn't influence noise levels significantly. The displacement thickness specifies the shift of streamlines away from the wall. It also creates a velocity deficit in that region, and the streamlines no longer follow

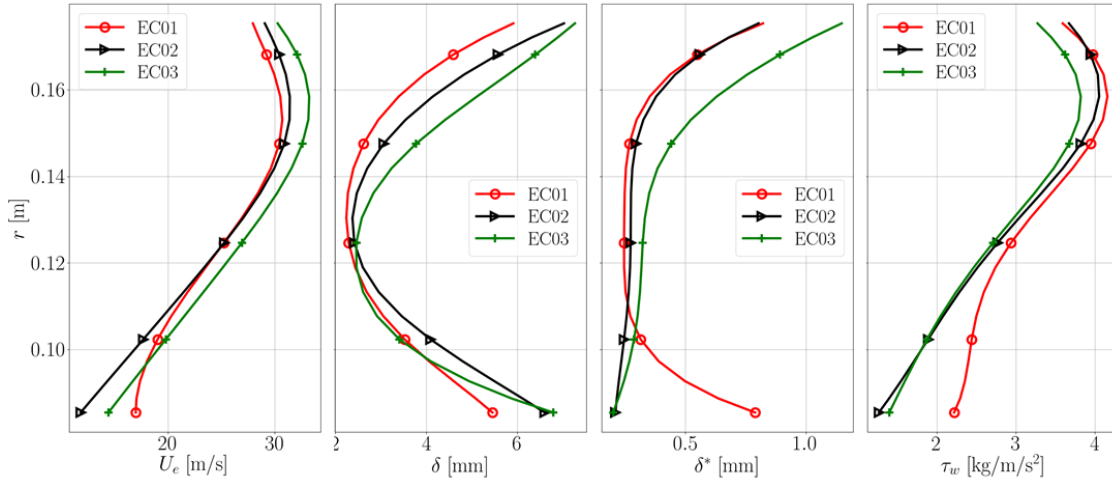


Figure 5.24 Boundary layer parameters extracted at 85% of chord length

the body shape. The δ^* plotted in Fig. 5.24 illustrates its distribution along the span. EC03 demonstrates an increase in δ^* from the hub to the tip, whereas EC01 possesses a more substantial δ^* caused by the corner vortex near the hub. The wall shear stress τ_w is defined as the product of dynamic viscosity, and the velocity gradient is calculated normal to the wall. Higher velocity gradients cause substantial shear and hence offer more frictional resistance. It also generates a greater drag force, and to overcome this drag force, the power consumed by the fan also augments usually. The reduction in τ_w for EC03 compared to the other two blades indicates reduced drag. The influence of sweep on power consumption is demonstrated with the example from Valeo test data recorded at 2200 RPM (see Fig. 5.25). The efficiency μ_f of these fans is defined as

$$\mu_f = \frac{q \times \Delta P}{P} \quad (5.4)$$

where q is the airflow rate in m^3/sec , ΔP is the pressure rise in Pa, P is power used by the fan in W. It yields 46.6%, 46.9% and 45.2% for the EC01, EC02 and EC03 respectively. Using the performance curve given in Fig. 5.25, if we calculate back their power consumption from the given efficiency, it shows that EC03 uses 25% less power than EC01 for the same RPM.

The study showed that as forward sweep angle is increased pressure rise is decreased by $\cos(\lambda)$ times at design point. The highest forward sweep shows thicker boundary layer from mid span to tip and lower wall shear stress along the blade. The reduced wall shear stress lowers the drag and reflects in to 1.5% less power consumption than its base design (EC01). These findings provide insight into the swept fan behavior when only the

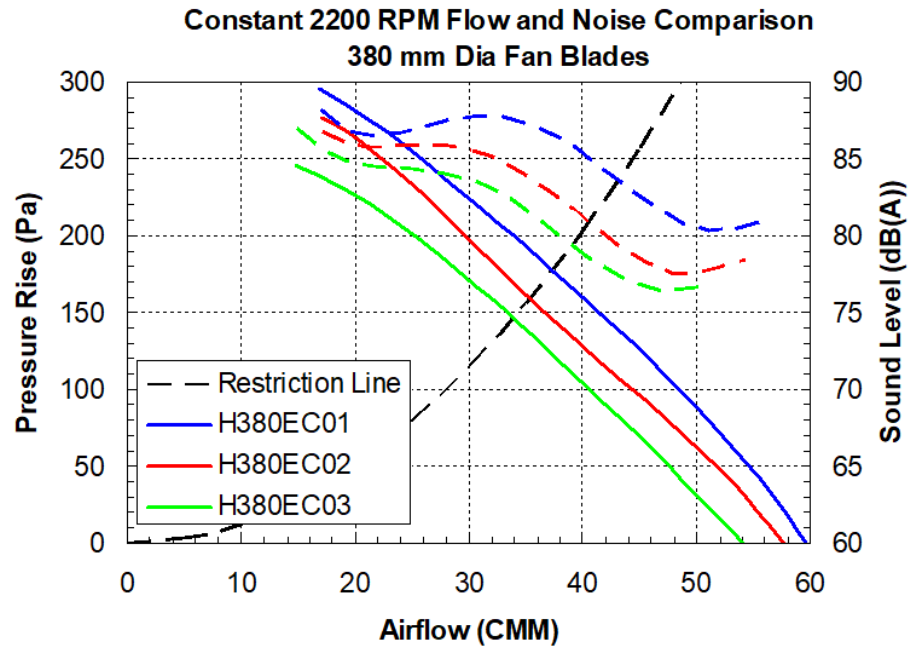


Figure 5.25 The fan performance tested at Valeo for 2200 RPM

sweep angle is changed. We are now interested in adding a sweep angle to the blade and maintaining the loading which is studied in the next section.

5.2 Ducted fans

Fig. 4.1 showcases the matrix of academic fans used in this study i.e. unswept, forward, and backward sweep fans. The generic fan design parameters are as follows: fan diameter 495 mm, tip gap 2.5 mm, hub diameter 124 mm, nine blades, and rotational speed 1500 RPM. The skewed versions were derived from the unswept fan (US) with $\pm 45^\circ$ sweep angle. The forward sweep fan (FS) has a positive sweep angle ($+45^\circ$) measured in the flow direction, and the backward sweep fan (BS) has a negative sweep angle (-45°) measured away from the flow direction. The chord length is increased in swept fans to achieve similar performance in all three fans. It accounts for the reduction in spanwise lift [102]. The Beiler and Carolus correction [9] is followed to maintain a similar loading. Besides, other design parameters are kept the same for all fans.

5.2.1 Numerical configuration for RANS

These three fans are simulated primarily with ANSYS CFX using steady state $k-\omega$ SST RANS solver for a single blade passage. The numerical setup and meshing strategy, like an industrial fan, are adapted here as well. The domain and mesh are displayed in Fig. 5.26. The total mesh count for this model is 15 million which includes prism and tetrahedral cells, as shown in Fig. 5.26 on the right. The first layer of prism cells is kept at 0.006 mm such that $y^+=1$ everywhere along the blade. These prisms are generated with incremental height using a stretching ratio of 1.3 to form 2.2 mm of total height by stacking 18 layers. The tetrahedra cells are generated on top of it. The overall mesh quality is achieved by keeping standard mesh parameters such as skewness < 0.97 , sliver < 7.0 and volume ratio < 10 . The sliver quality measure is defined as the ratio of the volume of the ideal tetrahedron to the volume of the given tetrahedron. The equivolume skewness quality measure is defined as the deviation between the volume of the given tetrahedron and the volume of the ideal tetrahedron. The volume quality measure is used to ensure that a given tetrahedron is not too small (minimum volume control) which is important in high order simulation where the time step is based upon the smallest mesh size.

5.2.2 Validation and flow field analysis

The characteristics curve of pressure rise (ΔP) versus volumetric flow (Q) for swept and unswept fans are plotted in Fig. 5.27. The nomenclature used to label plots indicates that S1 stands for fan series chosen from the design matrix, and later alphabets represent —F -forward sweep, B -backward sweep, U-unswept. Our predictions accurately validate for higher and lower flow rates, except FS. It exhibits a more significant deviation at a

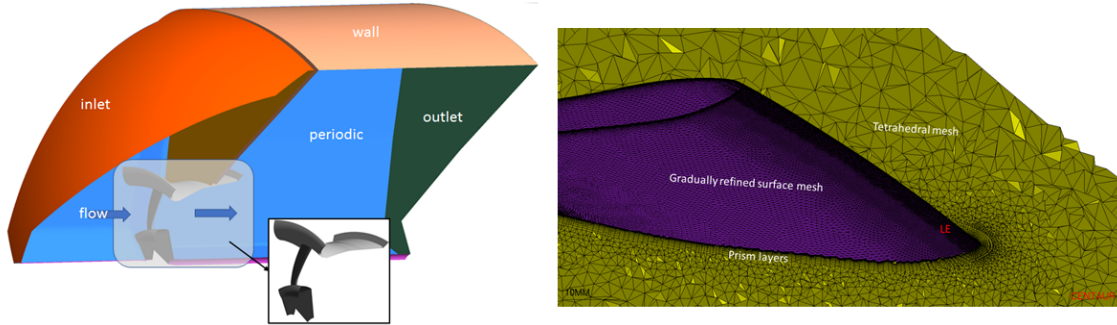


Figure 5.26 Computational domain for RANS simulation of ducted fans (left) and snapshot of meshing (right)

lower flow rate. At the design point, the prediction stays within $\pm 9\%$. This deviation is more significant than that in EC fans. Hence we investigated the cause of deviation systematically. Initially, we suspected perhaps a spherical inlet causing the variation because the test configuration has a rectangular plenum. Therefore, we modified the domain strategy and modeled the inlet from the flow straightener. Alas, different inlet domain configurations also failed to improve pressure rise predictions.

Later, we learned that recording is always performed from low to high flow rate in the experiment. Therefore, we varied the initialization, started the simulation from the lowest flow rate, and increased to the maximum flow rate stepwise. Interestingly, it yielded accurate pressure rise at design condition, whereas initialization performed other than the lowest flow rate exhibited significant deviation from experimental observations. Nevertheless, regardless of the initialization condition, pressure rise for higher flow rates remained unaltered. Hence a big hysteresis loop marked with the dotted line in Fig. 5.27 from $600 \text{ m}^3/\text{h}$ to $5500 \text{ m}^3/\text{h}$ is confirmed. The loop embraces the design point of all three fans. Note that although hysteresis marked in the plot is for representation purposes only, the experiments must be repeated from different initial conditions to understand presence of the hysteresis and its spread.

Moreover, the inflection and flattening of the curve indicate the presence of a stall region. This region is sensitive to the operating condition and possesses an unstable flow field. Although the present study is focused only on the design point, the opportunity to explore the stall region and hysteresis loop exists as a future scope.

When the pressure rise predictions for FS and BS are compared, they show a 45 Pa difference. Theoretically, FS and BS must provide similar pressure rise, but this considerable difference suggests that the aerodynamic behavior of these swept fans are different from each other. Therefore, we investigated pressure distribution along the chord at multiple

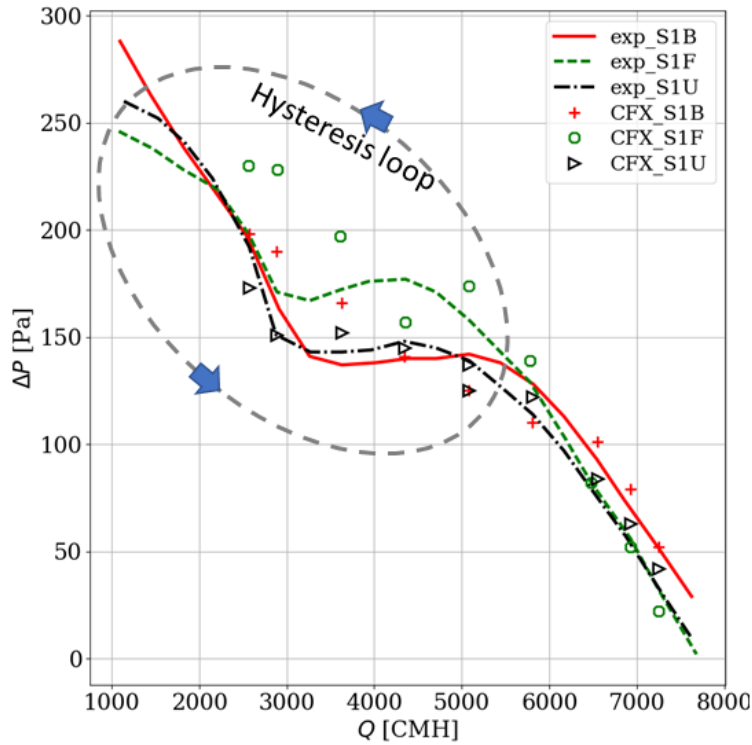


Figure 5.27 Aerodynamic performance of ducted fan for unswept, forward sweep and backward sweep fan

radial locations. The pressure coefficient calculated using Eq. (5.1) is plotted in Fig. 5.28 at 25% 50%, 75% and 95% span from left to right, respectively.

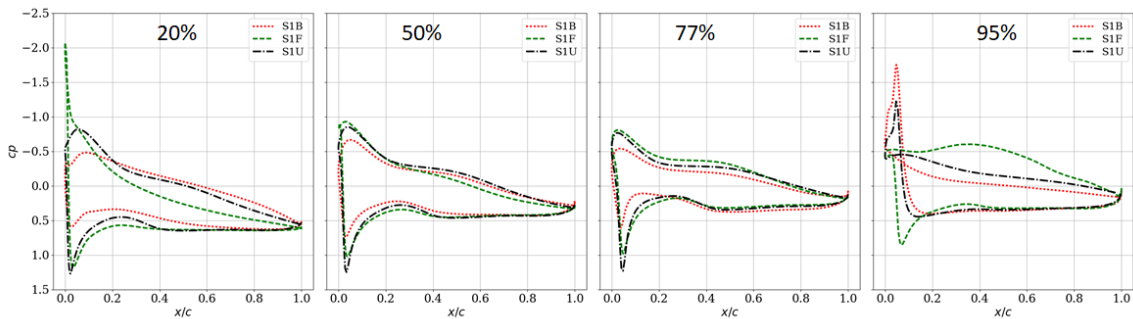


Figure 5.28 Pressure coefficient distribution along the normalized chord length at 20%, 50%, 77% and 95% radial locations plotted from left to right, respectively

Near the hub at 20% span (Fig. 5.28), BS and US exhibit similar C_p distribution but, FS shows a significantly higher angle of attack and also covers a smaller distribution area. This area under the curve signifies lift produced at a given chord location. The positive pressure in FS after $x/c = 0.2$ suggests a lower lift production. From midspan at 50% to

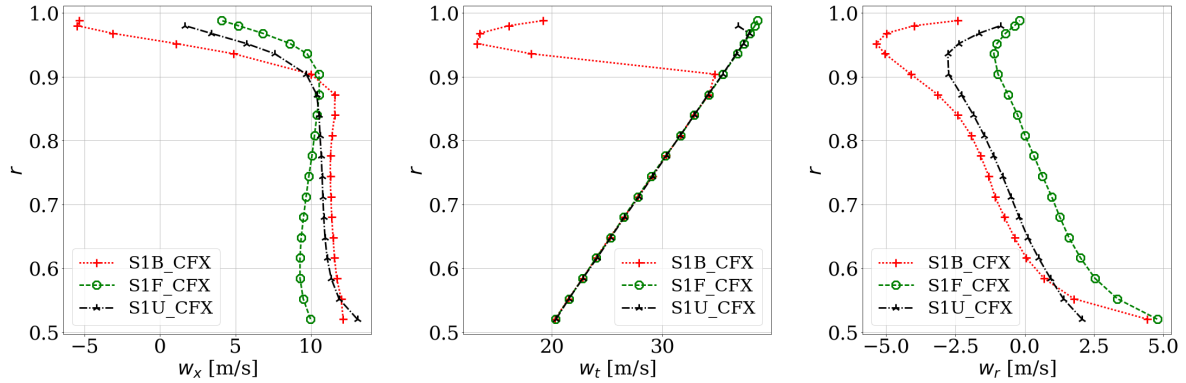


Figure 5.29 Azimuthally averaged velocity in relative frame extracted 10mm before LE and plotted along the span normalized with tip radius; left (axial velocity, w_x), middle (tangential velocity, w_t), right (radial velocity w_r) for ducted fans

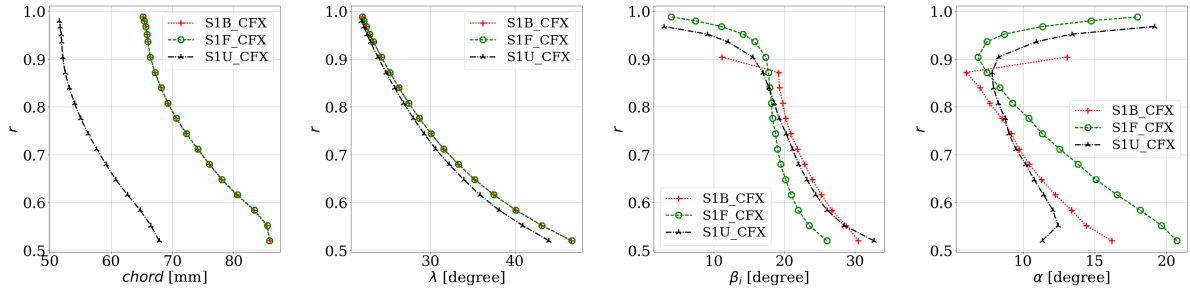


Figure 5.30 Blade geometrical extractions; left (chord), middle (stagger angle, λ), right (inlet flow angle, β_i and incidence angle (α)) for ducted fans

70%, the three fans show almost similar behavior but, US and BS start showing negative C_p on the pressure side at 95% span. When verified, it is observed that from 88% of the span towards the tip, US and BS have started showing such a C_p behavior. This loss in a lift near the tip supports lower global pressure rise observation in BS and US fans compared to FS. Like the previous study, the velocity profiles are extracted in the relative reference frame near LE and plotted in Fig. 5.29. The tangential velocity is exactly aligned for all three fans all over the span except near the tip. However, noticeable differences in axial and radial velocity distribution among the three fans are observed. To learn more about the blade geometry, further processing is done to plot chord, stagger angle and inlet flow angle. The chord length plot in Fig. 5.30 exhibits that chord correction is applied to swept fans to maintain the performance in the design stage itself. Almost similar stagger angles for all three fans are confirmed except small thickness correction is applied to swept blades. Nonetheless, notable differences in inlet flow angles suggest that FS fan experiences lower β_i near hub, but it increases near tip while the reverse is true for BS. The US develops a similar β_i profile that of BS up to midspan but later it mimics FS

near the tip. Using the velocity triangle shown in Fig. 5.15 and Eq.(5.2), we confirm the observation in Fig. 5.28 that near hub (20%) FS has a high angle of incidence compared to BS while conversely, near tip (95%) FS has lower incidence angle and produces higher lift than other two fans. Although the design is implemented in such a way that all three fans should behave likewise under similar operating conditions, BS and US demonstrate arbitrary β_i distribution than FS. BS and US suffer higher incidence angle starting from 88% of the span and it continues until the tip. Furthermore, the smaller area under C_p curve in Fig. 5.28 for BS and US indicate lower lift compared to near hub (20%). This discussion points to a flow separation near the tip which can be confirmed with either Q-criteria or λ_2 plots and with total pressure in relative frame plotted on a radial cut section near the tip region, discussed later in the section.

Furthermore, the flowfield recorded with LDA is compared with the results of the RANS simulations in Figs. 5.31 to 5.38. The data is extracted along the span in a rotational plane placed 10 mm before LE and after TE respectively. The simulation results agree quite well with the test data. The axial velocity plot at LE in Fig. 5.31 shows higher negative axial velocity, indicating increased tip leakage in US and BS than in the case of FS fan. The radial velocity behavior is slightly different at LE (see Fig. 5.32), whereas near TE (see Fig. 5.36), despite lower amplitudes, the flow field matches qualitatively with experiments. Note that the pattern is matched by intentionally modifying the scales of mean radial velocity at TE in Fig. 5.36. The predicted tangential velocity at TE is very well correlated with the experiment (see Fig. 5.37). Nonetheless, near LE, the TKE behavior is quite different than the experiment (Fig. 5.34). Again, heads up! Near tip TKE amplitude from RANS is very low compared to EXP and LBM, hence the scales are modified to highlight the patterns. On the contrary, the TKE distribution at TE matches very well with the experiment but shows a higher level of turbulence in the wake region and inside the tip region (see Fig. 5.38). Higher tangential velocity is witnessed near the tip at LE (see Fig. 5.33) showcasing a thicker tip vortex region, but the overall behavior agrees with the experimental flow distribution.

The velocity profiles are azimuthally averaged and then compared in Figs. 5.39 and 5.40. The axial flow enters in an almost similar fashion for all three fans but has near the tip a drastically different behavior. BS has more negative axial flow than FS. FS exhibits positive radial flow near LE while BS has negative radial velocity. This change of sign can be explained with a simplified stationary flat plate in Fig. 5.41 drawn for LE and its link to the positive and negative sweep angles. In a no sweep case, the resultant velocity (V) in a stationary frame is normal to the span where all the incoming flow travels along

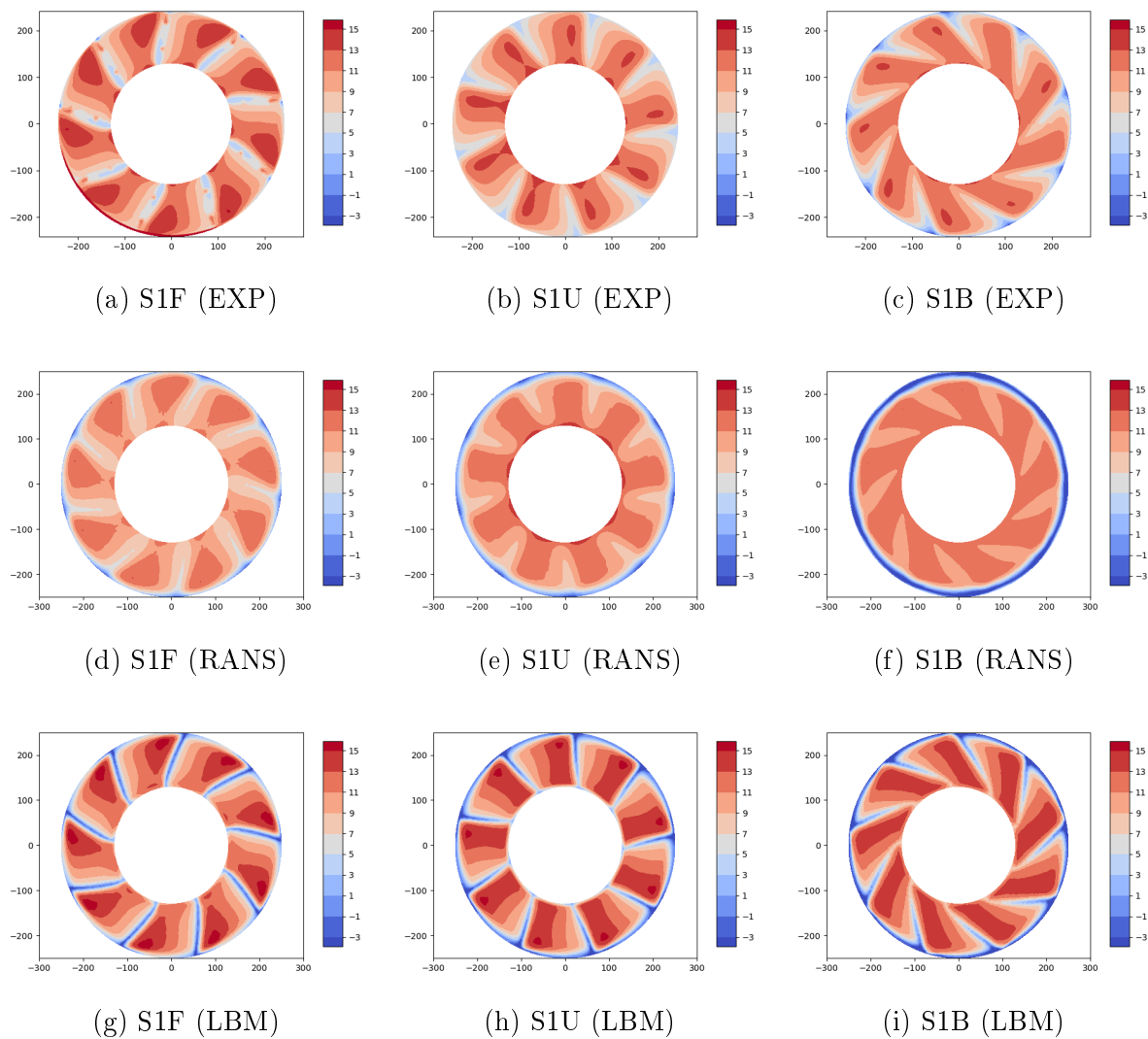


Figure 5.31 Contours of azimuthally averaged mean axial velocity extracted 10mm before and along LE extracted using LDA in experiment and compared with RANS and LBM

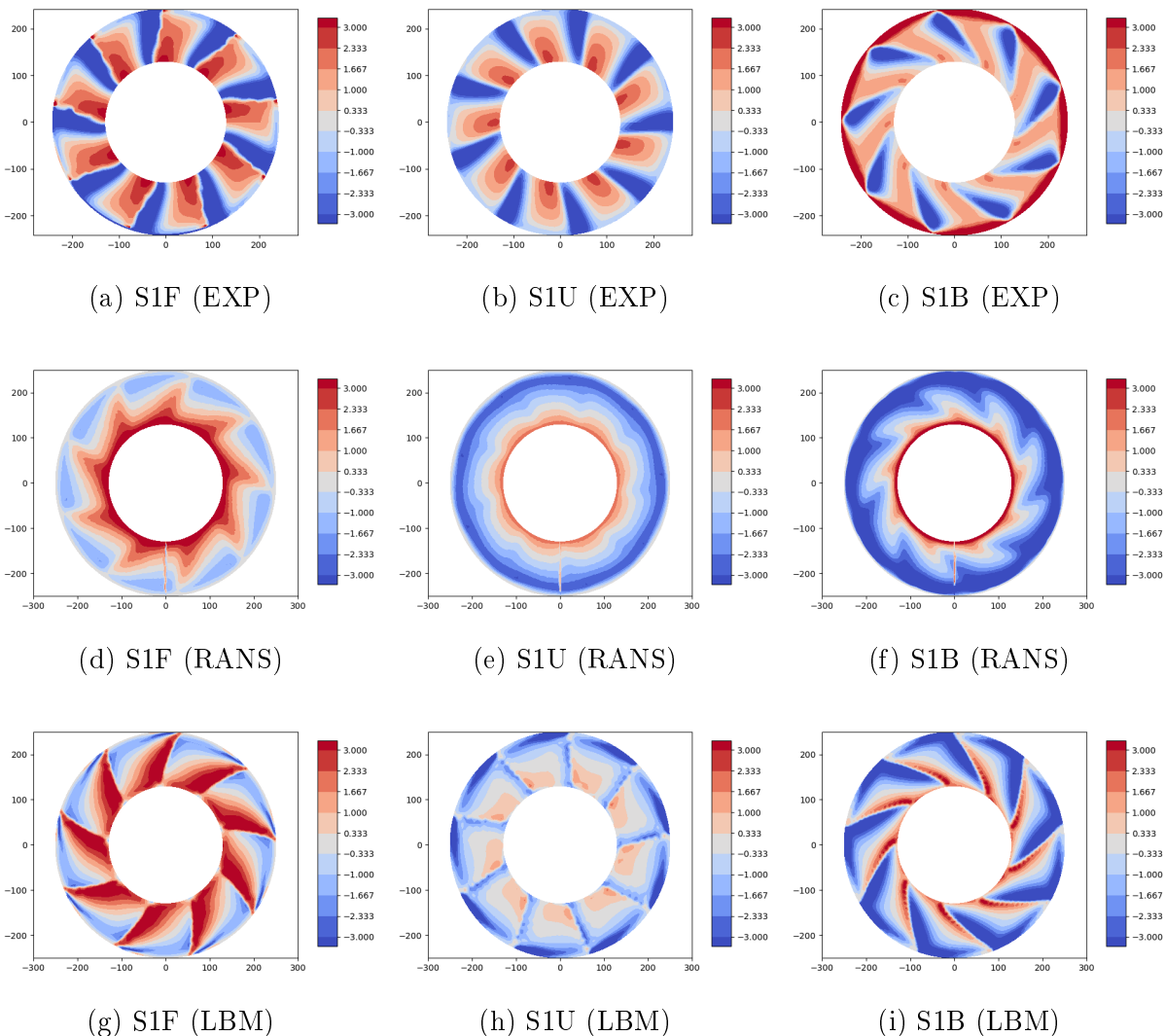


Figure 5.32 Contours of azimuthally averaged mean radial velocity extracted 10mm before and along LE extracted using LDA in experiment and compared with RANS and LBM

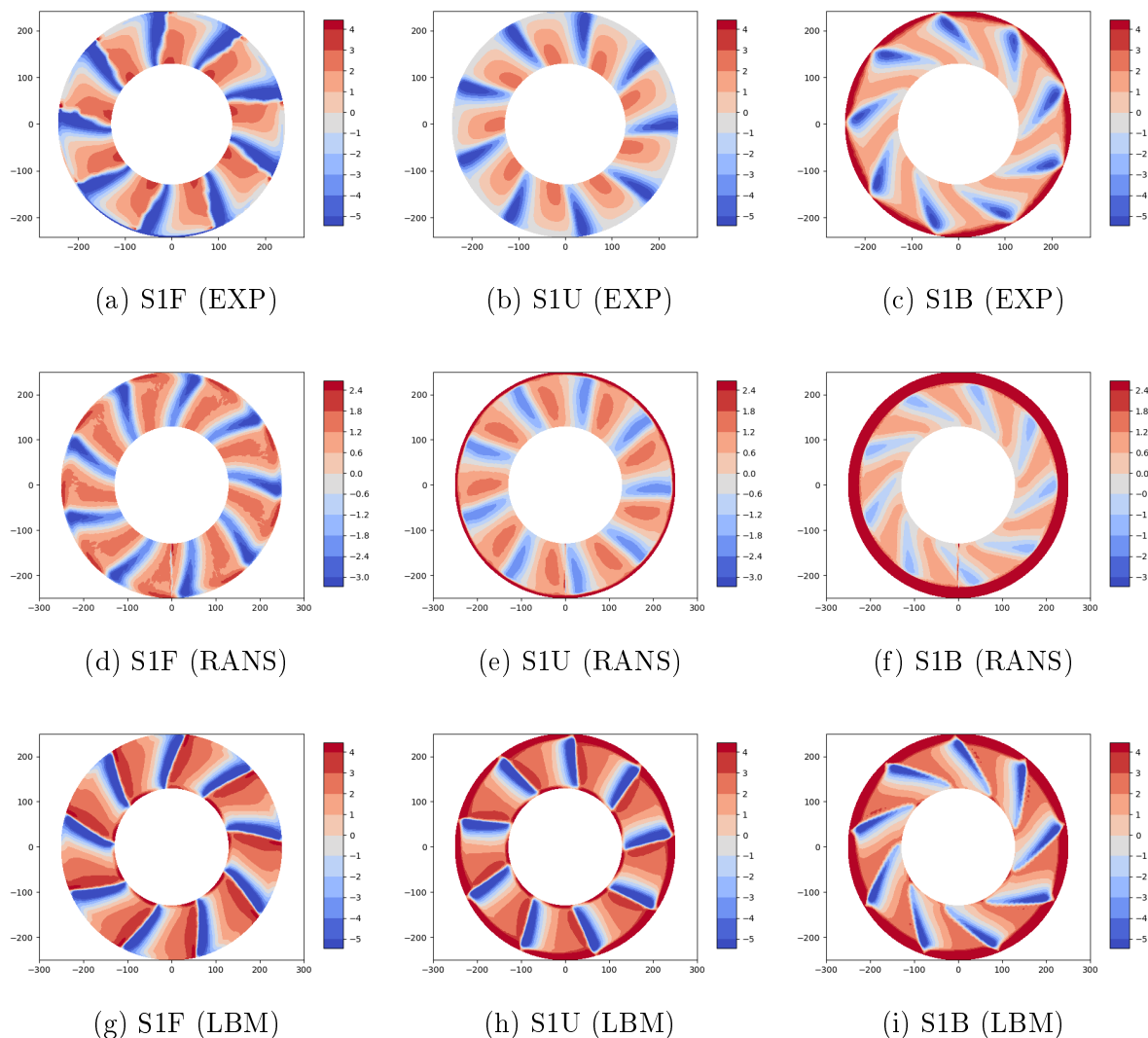


Figure 5.33 Contours of azimuthally averaged mean tangential velocity extracted 10mm before and along LE extracted using LDA in experiment and compared with RANS and LBM

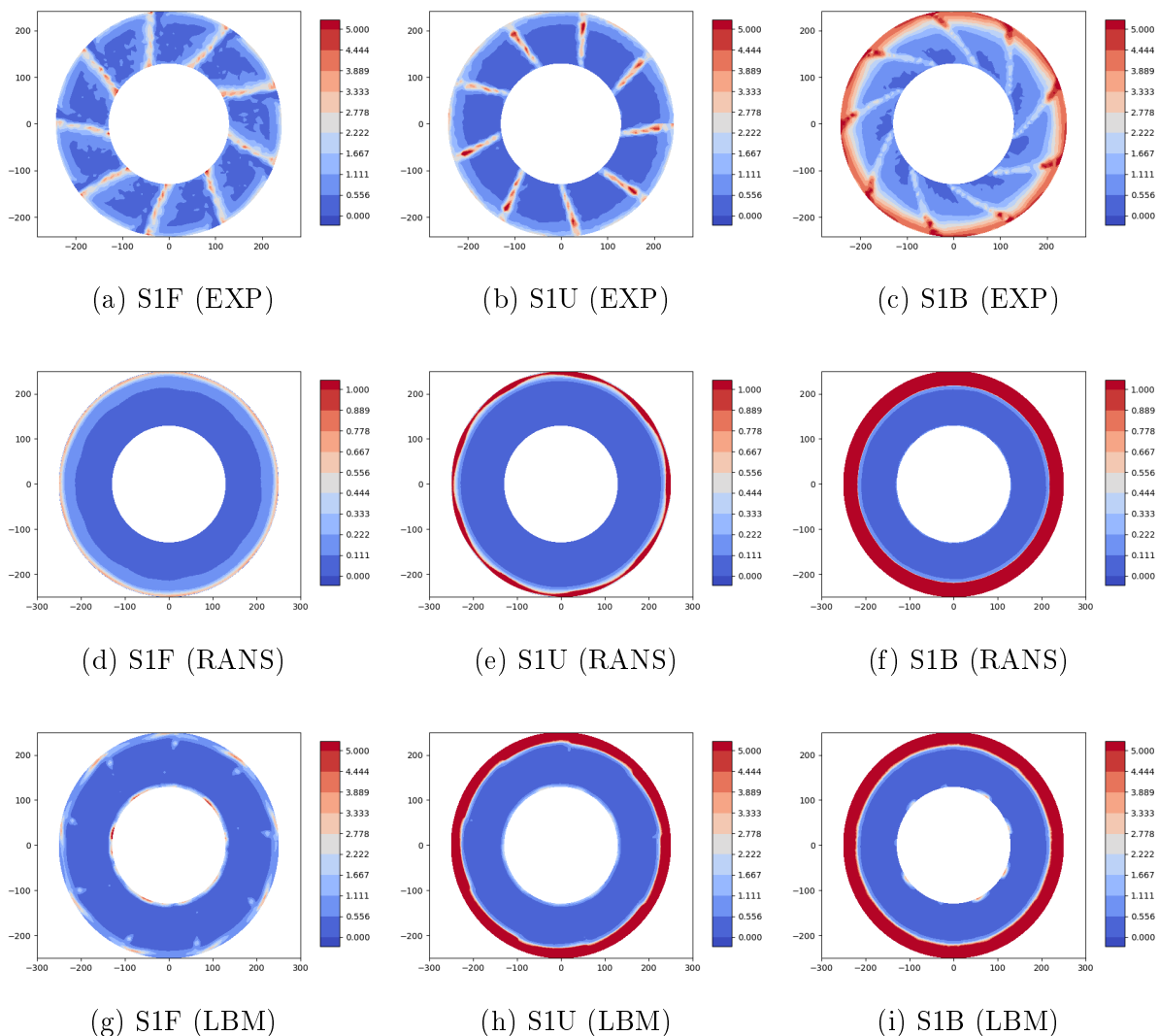


Figure 5.34 Contours of azimuthally averaged mean turbulent kinetic energy extracted 10mm before and along LE extracted using LDA in experiment and compared with RANS and LBM

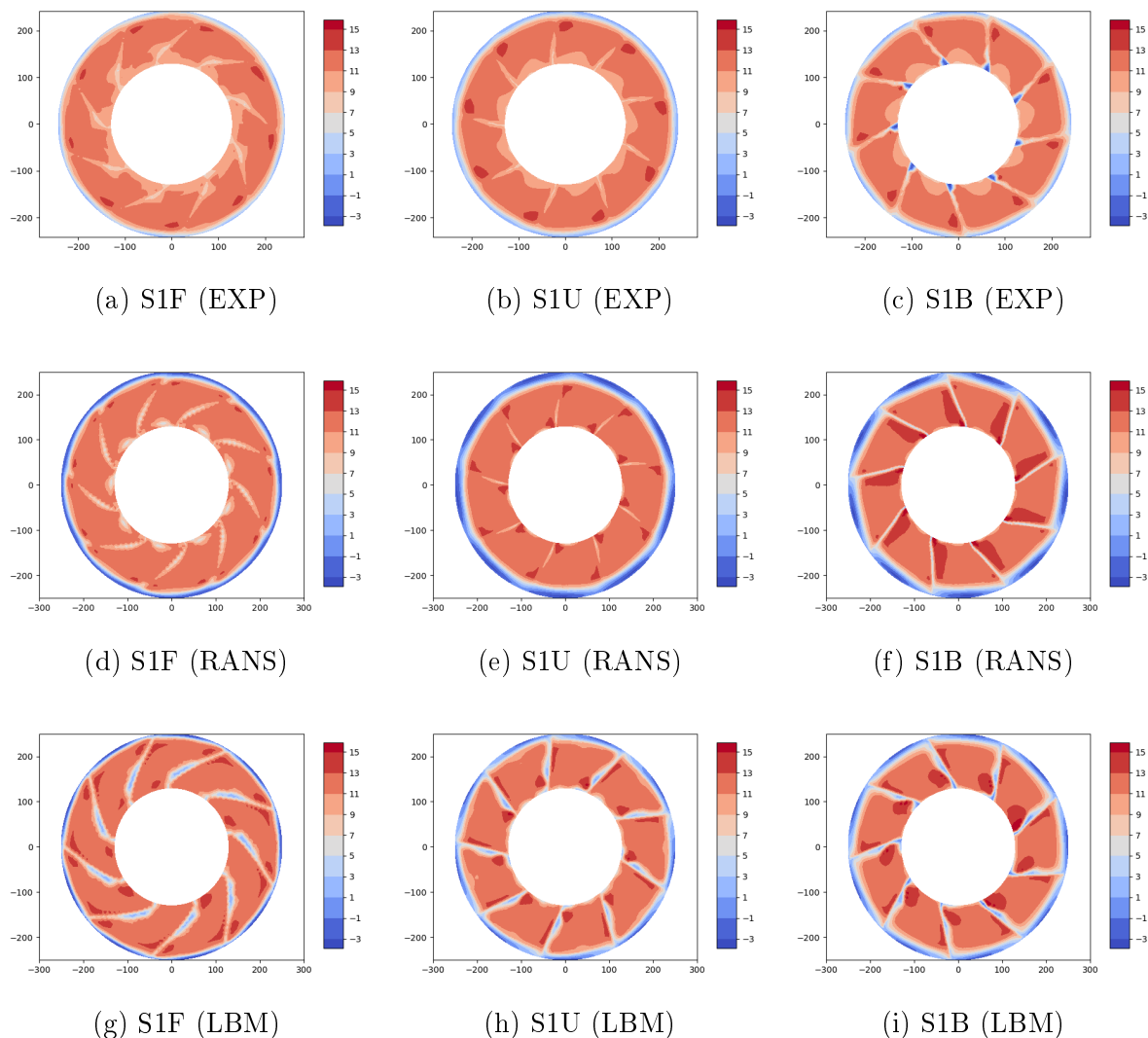


Figure 5.35 Contours of azimuthally averaged mean axial velocity extracted 10mm before and along TE extracted using LDA in experiment and compared with RANS and LBM

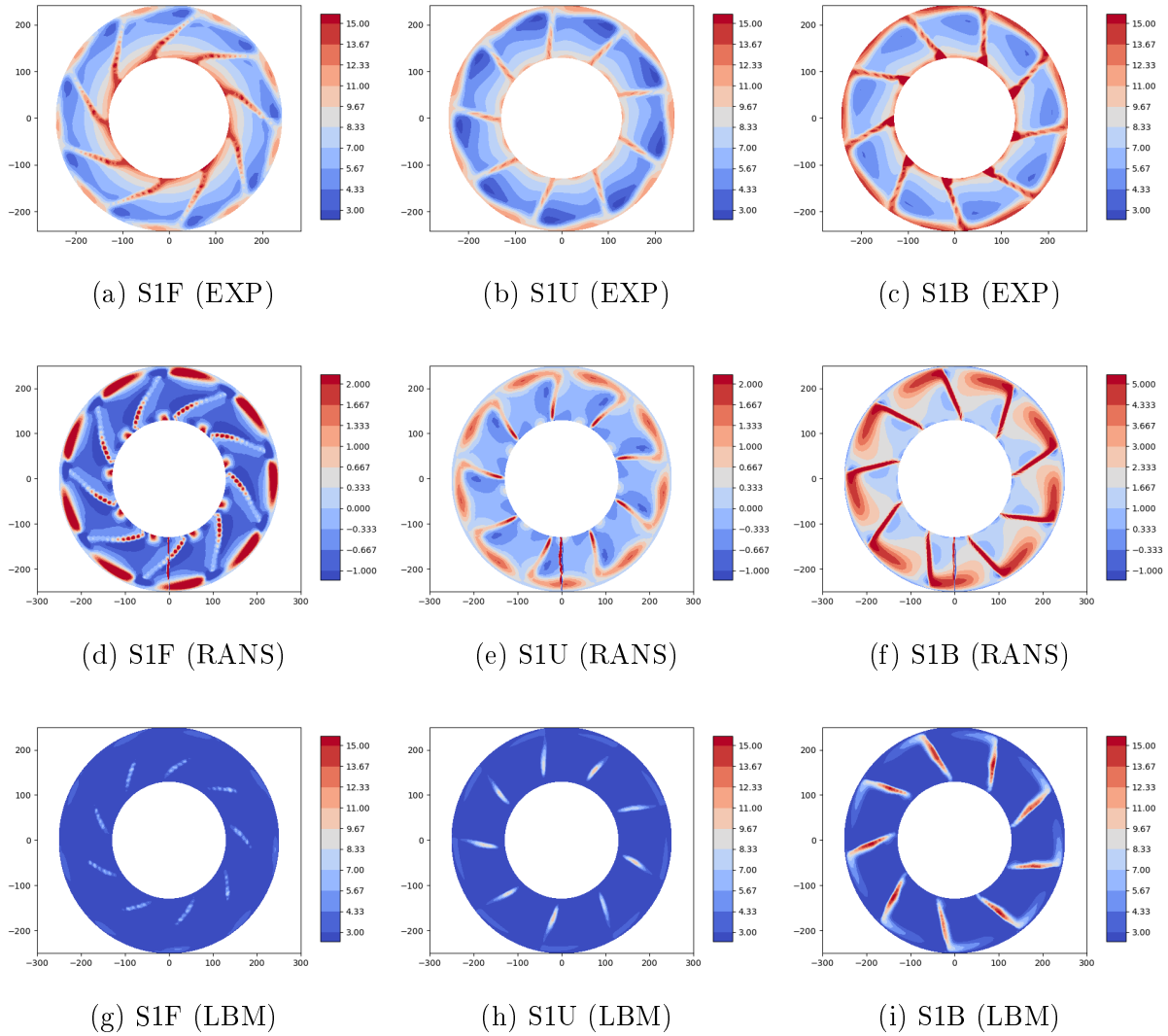


Figure 5.36 Contours of azimuthally averaged mean radial velocity extracted 10mm before and along TE extracted using LDA in experiment and compared with RANS and LBM

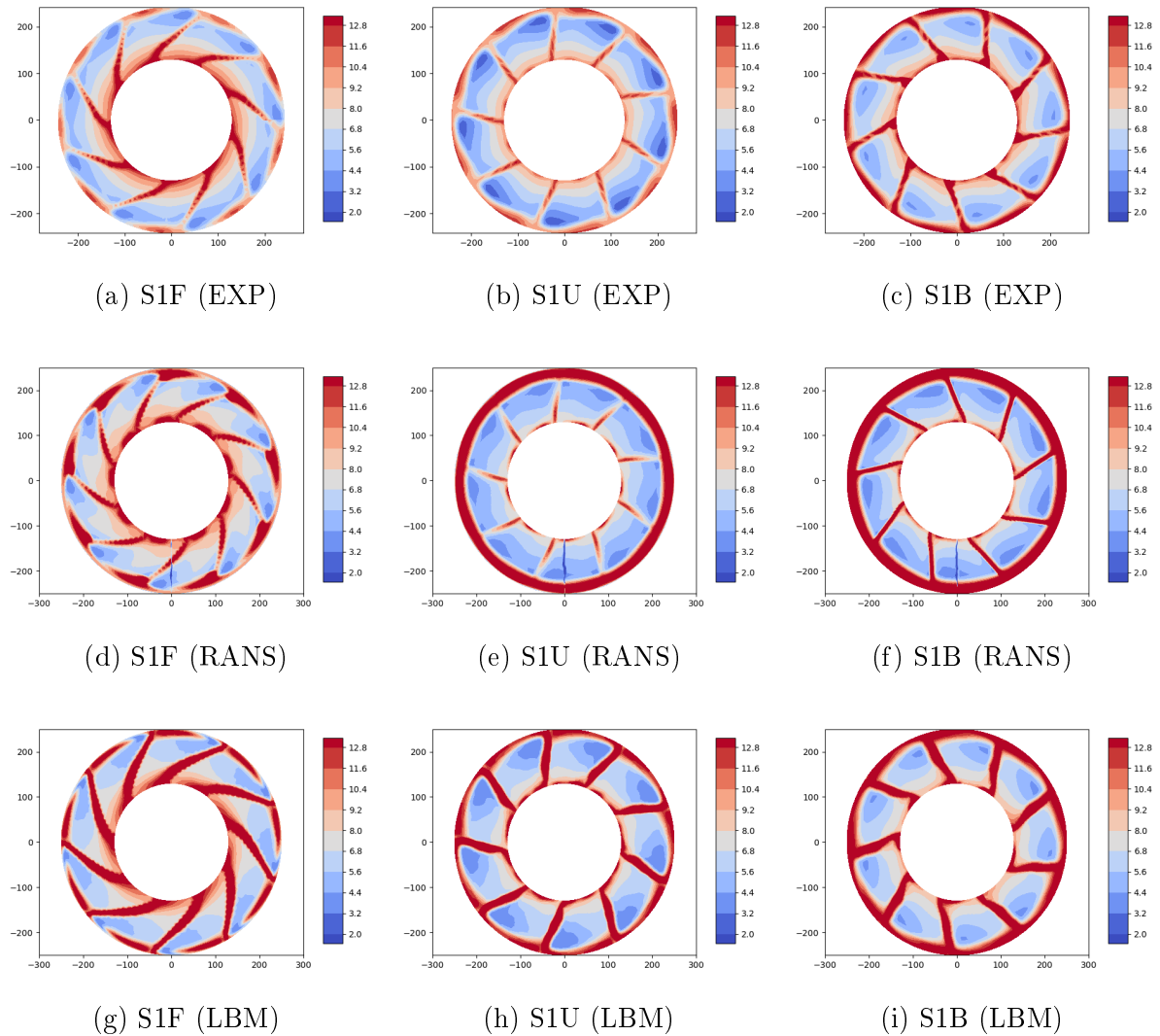


Figure 5.37 Contours of azimuthally averaged mean tangential velocity extracted 10mm before and along TE extracted using LDA in experiment and compared with RANS and LBM

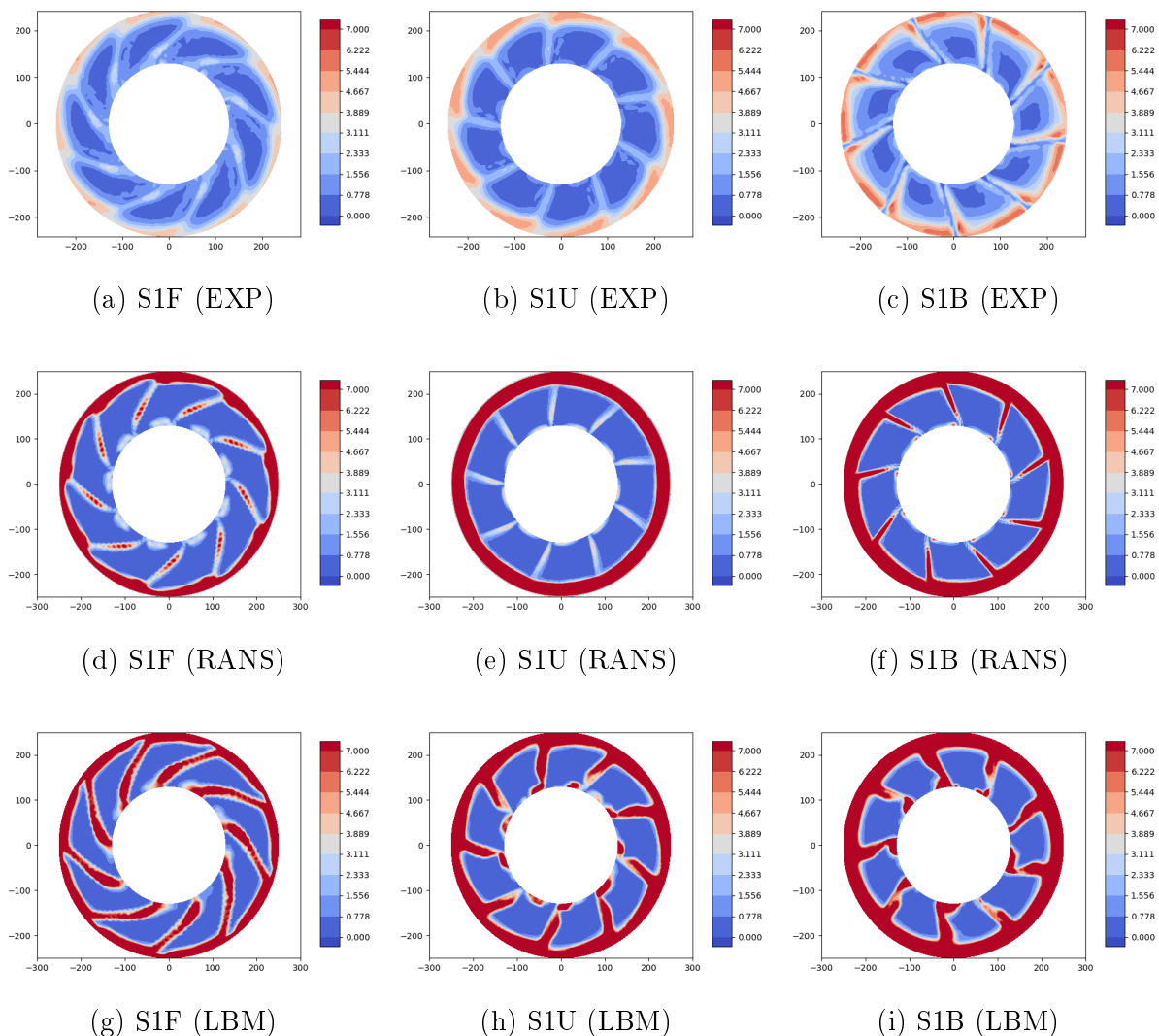


Figure 5.38 Contours of azimuthally averaged mean turbulent kinetic energy extracted 10mm before and along TE extracted using LDA in experiment and compared with RANS and LBM

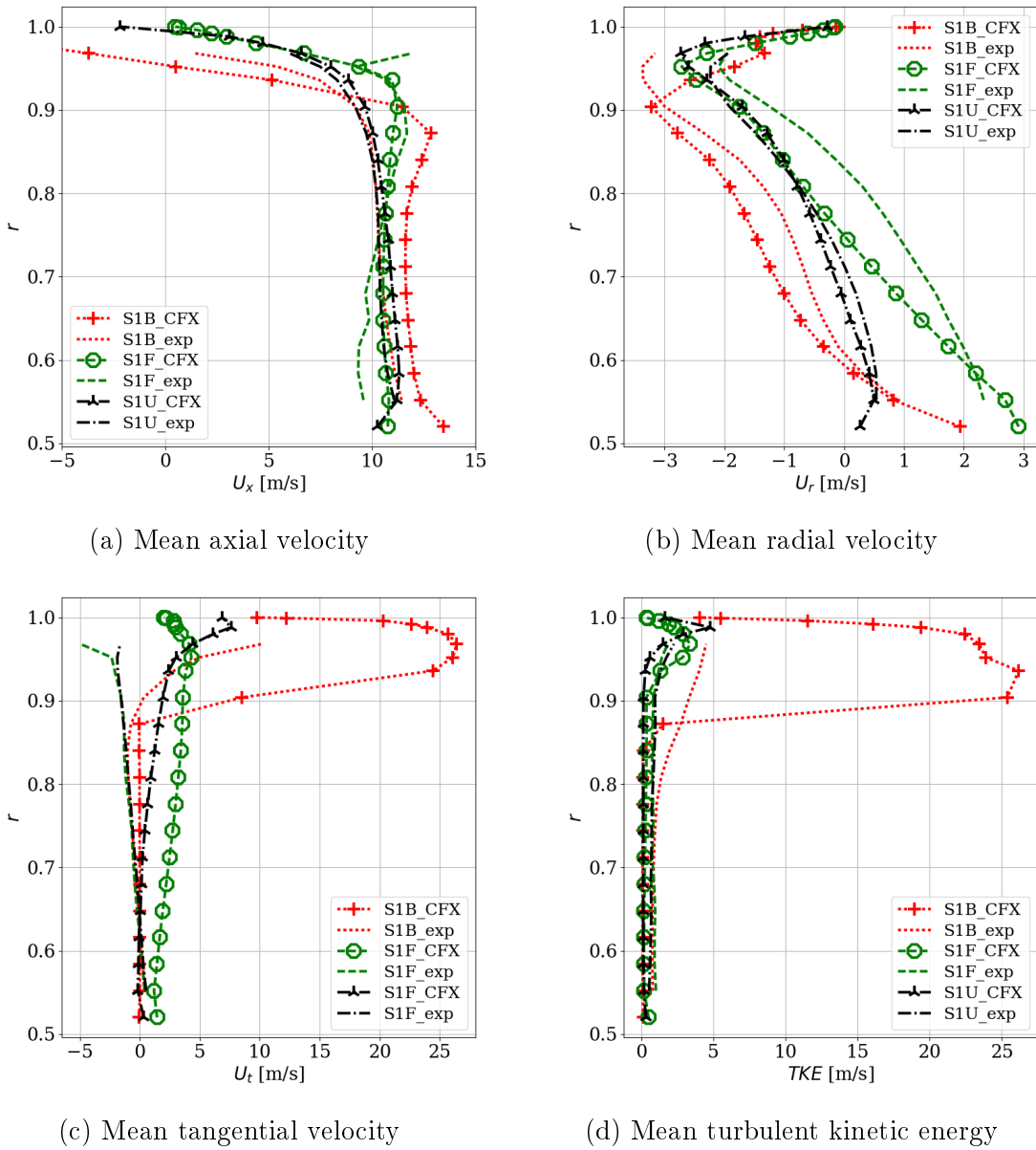


Figure 5.39 Azimuthally averaged mean velocity profiles at LE

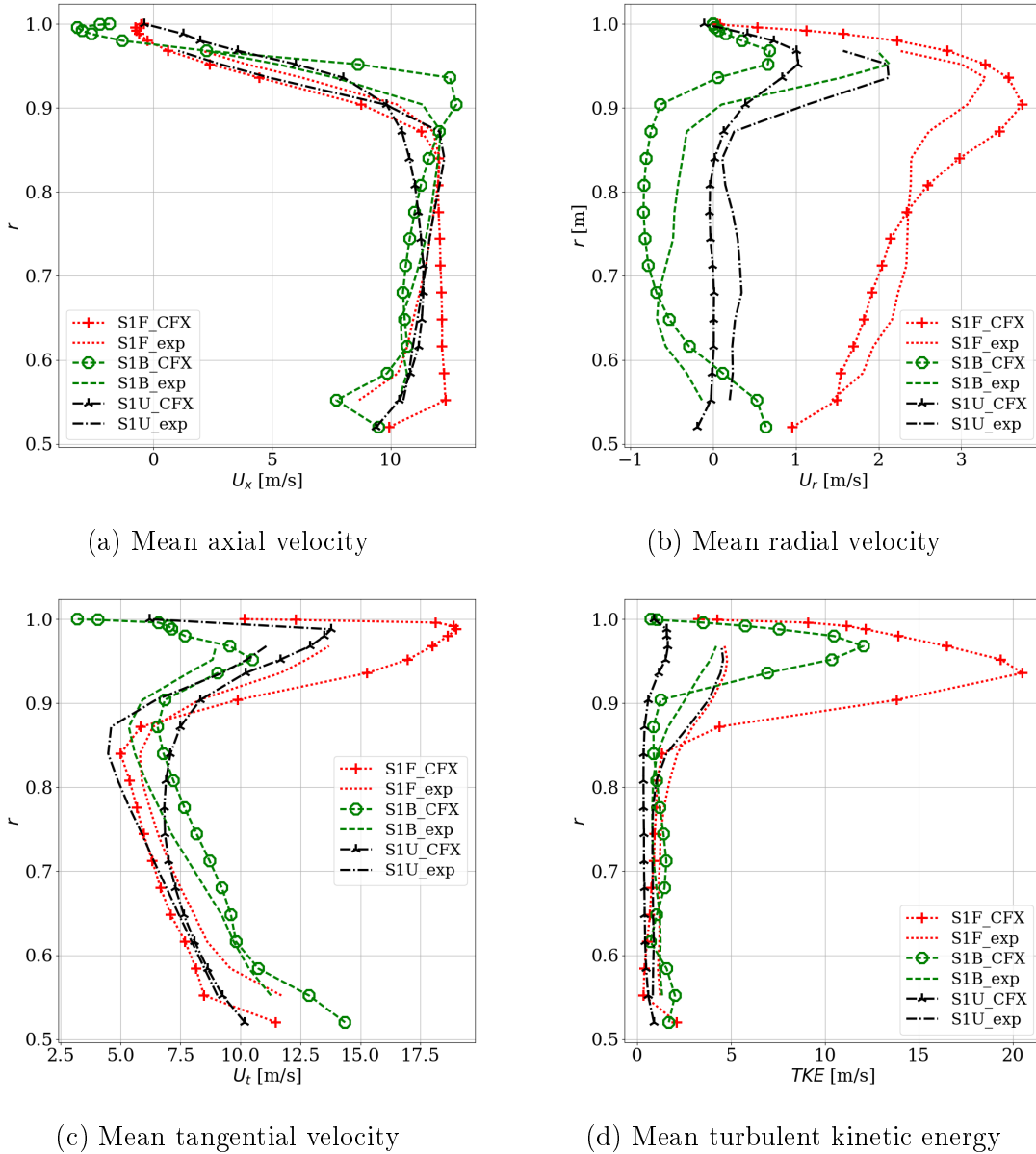


Figure 5.40 Azimuthally averaged mean velocity profiles at TE

the axial direction (X) and no flow along the span or radial direction (Y). However, forward and backward sweep blades create a sweep angle (ψ) along Y that results in components of V in X and Y direction in the stationary coordinate system. The radial flow V_y modifies its sign from positive to negative when the sweep angle is changed from forward to backward sweep at LE. Near TE change of sign can also be understood by drawing a similar vector diagram. Observing further, the more significant tip regions are occupied by higher tangential velocities and TKE for BS than for FS, i.e., above 88% of the span length. Besides, near TE, the axial velocity distribution is comparable for all three fans, but the radial velocity points opposite behavior to that of LE, shown in Fig. 5.40. The tangential velocities of US and BS have identical behavior, but FS has a lower velocity near the tip than the other two fans. All three fans show a unique TKE distribution near the tip while BS and US have identical levels.

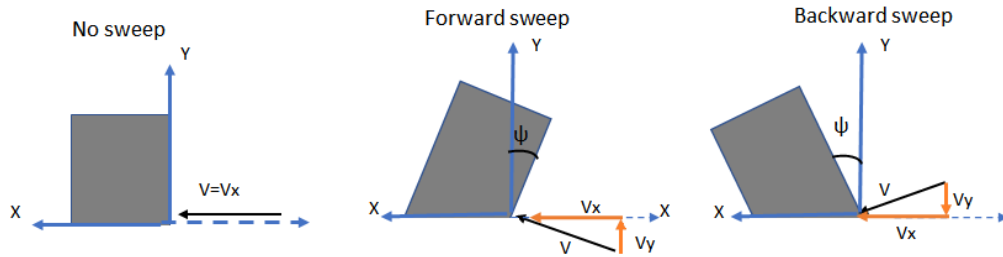


Figure 5.41 Demonstration of radial flow with vector diagram in stationary frame

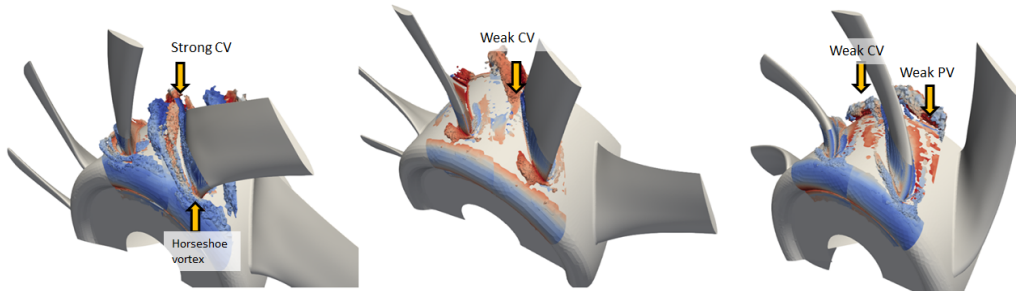


Figure 5.42 Isosurface of λ_{ci} at 100 colored by helicity varies from blue to red (-1 to +1) left-S1F, middle-S1U, right-S1B

The vortex structures are analyzed by calculating the imaginary part of the complex eigenvalues of the velocity gradient, referred as λ_{ci} [126]. It indicates the measure of the local swirling strength of a vortex. The corner vortex (CV), horseshoe vortex (HV) and passage vortex (PV) are visualized with an isosurface of λ_{ci} by selecting a threshold of 100 in Fig. 5.42. The HSV formed near the hub that divides into suction side CV and pressure side PV are marked in the Fig. 5.42. The FS exhibits solitary and distinct CV

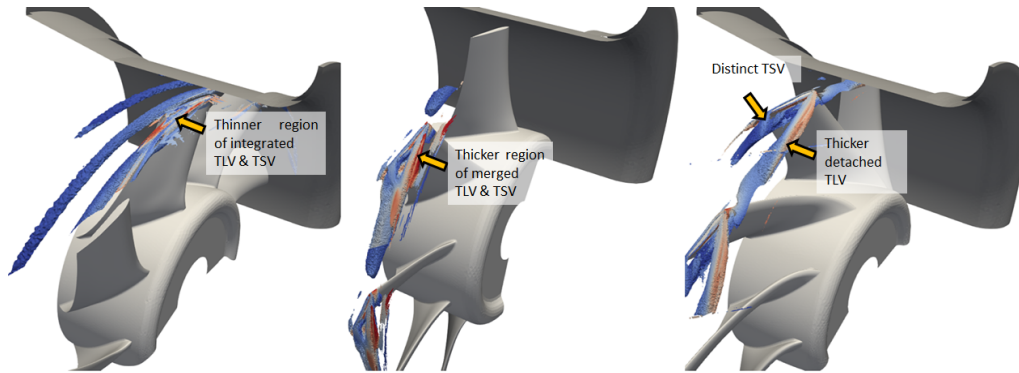


Figure 5.43 Isosurface of λ_{ci} at 315 colored by helicity varies from blue to red (-1 to +1) left-S1F, middle-S1U, right-S1B

behavior. It subdivides into two traces of counter-rotating vortices observed as red and blue patterns near the hub in Fig. 5.42. However, the other two blades form a weaker CV because low axial velocity and higher incidence angle for FS created local flow separation but BS and US show higher axial velocity and lower incidence angle. All three fans show weak PV formation. The axial velocity plot at TE in Fig. 5.40 confirms the strong corner vortex formation near the hub of FS. Yet, the other two fans do not show any such traces.

The 3D tip vortex consists of a tip leakage vortex (TLV) and tip separation vortex (TSV). It is examined by plotting isosurfaces of λ_{ci} by setting a threshold of 315 in Fig. 5.43. The forward sweep forms a thin region of TLV and TSV generating a merged tip vortex that displaces the tip vortex in the blade passage along the chord. The TLV formed at unswept LE merges with TSV yielding a bigger structure that stays in the rotational plane. The thicker TLV in itself generated at backward sweep LE does not merge with TSV. Relatively, TLV and TSV are much thicker in this case that interact more with the neighboring blade. Tip vortices in BS and FS fans display clearly different patterns where FS has a thinner tip leakage vortex that travels grazing pressure side of the adjacent blade and BS forms thicker TLV impacting LE and TSV strikes pressure side of the adjacent blade. This integrated tip vortex spreads approximately from 88% of the span towards the tip which is also confirmed with the highest TKE distribution near the tip in Figs. 5.39 and 5.40.

The velocity magnitude contours displayed in Fig. 5.44 showcase the flow behavior from hub to tip for all three fans. The low velocities near the hub of FS downstream of the chord confirm the presence of CV. However, US and BS don't show any such traces near the hub. The flow remains attached along the chord near midspan but velocities near the tip are distinctly different than one another. BS confirms the flow separation from LE itself

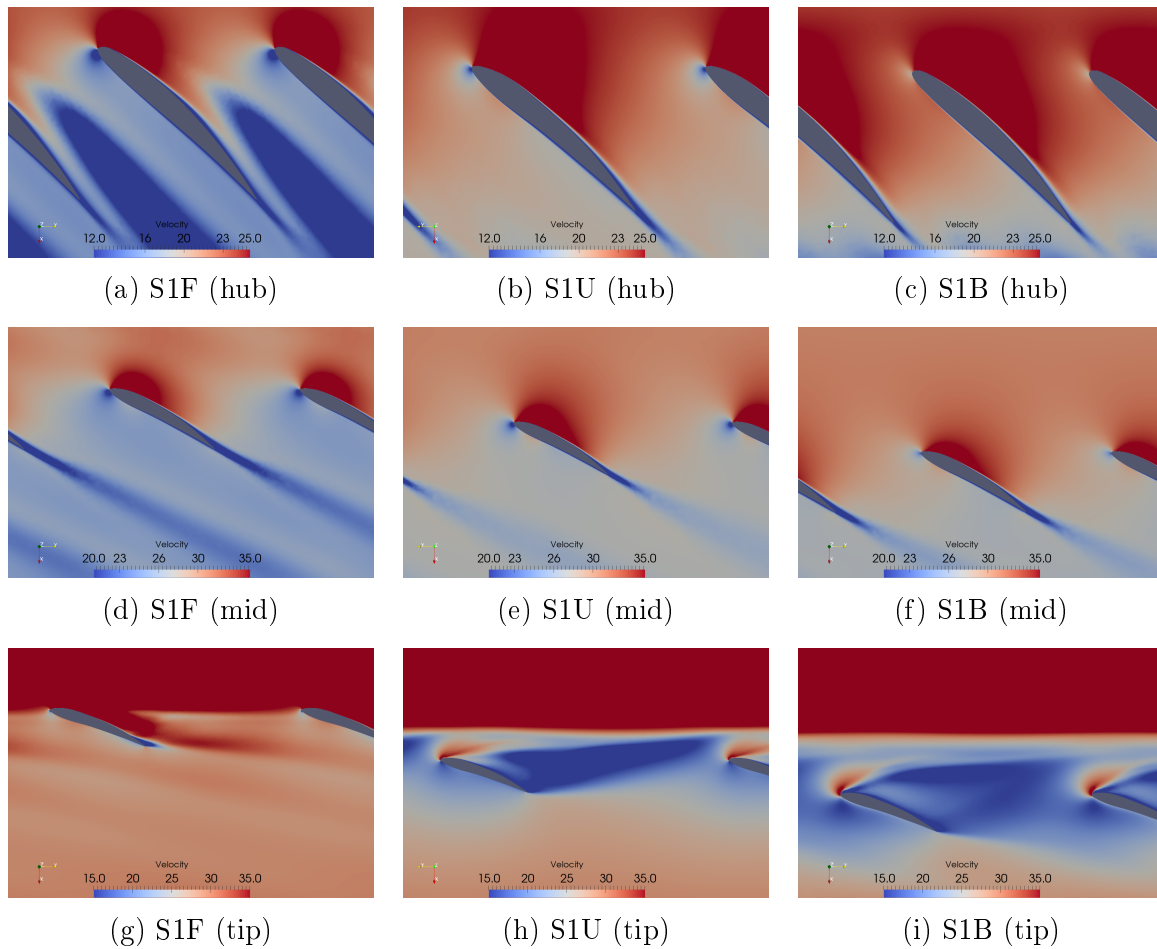


Figure 5.44 Contours of velocity in rel. frame taken near hub (10% of span), near mid (50% of span) and near tip(99% of span)

whereas the US has slightly delayed separation marked with low velocities. Nonetheless, FS shows higher velocity along the chord.

The velocity contours show similar attached flow on the blade with similar boundary layer development. To yield a more quantitative comparison like Valeo fans, BL parameters are extracted from the suction side and presented. In Fig. 5.45 (a), the edge velocity U_e shows a similar trend but varies near the tip for FS. Interestingly, BS forms a thinner boundary layer than FS and US until midspan but alters later as shown in Fig. 5.45 (b) and (c). If the BL was developing in a similar manner in all fans, the unswept fan should show smaller BL thickness than swept fans because the chord length in swept fans is increased from 72 mm to 94 mm. Nonetheless, we see the opposite behavior. Therefore, we can say that blade sweep alters the way the BL develops. Perhaps it causes early transition due to the crossflow formation inside the BL than the US [88] but this argument doesn't suit here because our RANS simulations don't include the boundary layer transition model. In Fig.5.45, similarly to the EC03 fan, FS shows slightly lower wall shear stress along the span except near the tip. On the other hand, BS exhibits similar wall shear stress as the US. This difference in wall shear stress formation can influence the skin friction drag produced by the fan and hence, the power requirement. Therefore, it seems that BS may consume slightly more power than FS when operated in similar loading conditions.

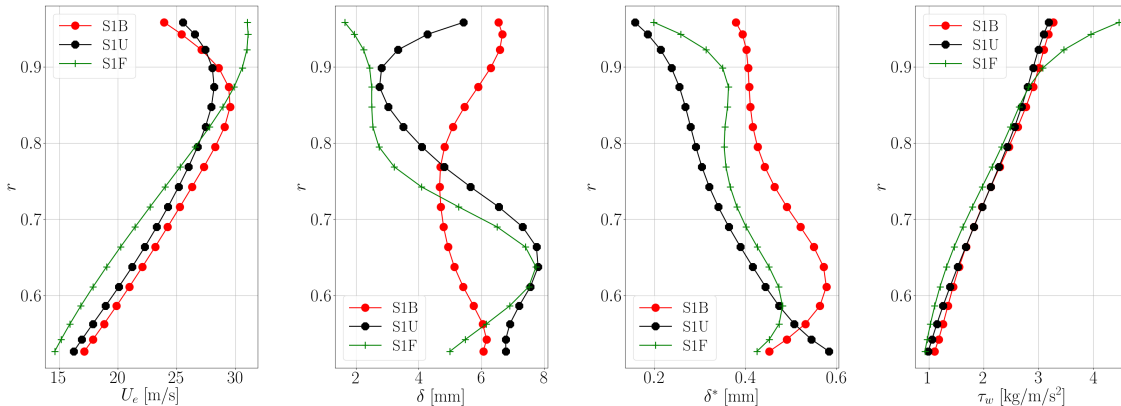


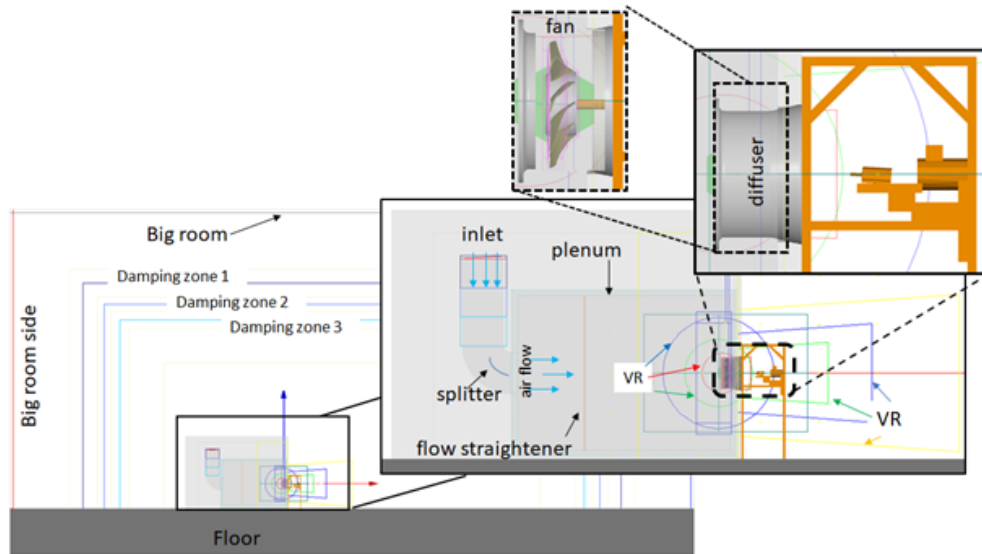
Figure 5.45 Boundary layer parameters extracted suction side at 85% of chord length

Despite these meaningful insights from mean flow extractions and the accurate validations with experimental data, steady simulation can't help predict flow-induced noise since it is transient in nature. Hence the next section is dedicated to study unsteady simulations using LBM.

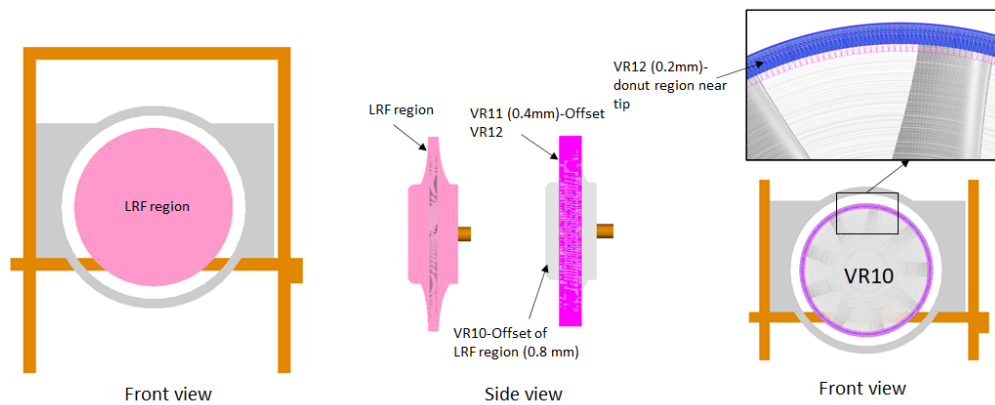
5.3 LBM for ducted fan

The primary purpose of LBM simulation is to predict fan noise directly. Before extracting acoustics, we have discussed set up, meshing strategy and the aerodynamic flow field validation with the experiment in the following section.

5.3.1 Numerical configuration



(a) Computational domain



(b) Near blade and near tip VR strategy

Figure 5.46 LBM set up

Our discussion in Chapter 4 identified that the rectangular box with bent inlet forms top to bottom flow asymmetry in the plenum that needs to be appropriately captured to simulate accurate incoming flow conditions. Therefore, Fig. 5.46a replicates the test configuration in which the velocity inlet is modeled from the bent section. The domain is discretized by

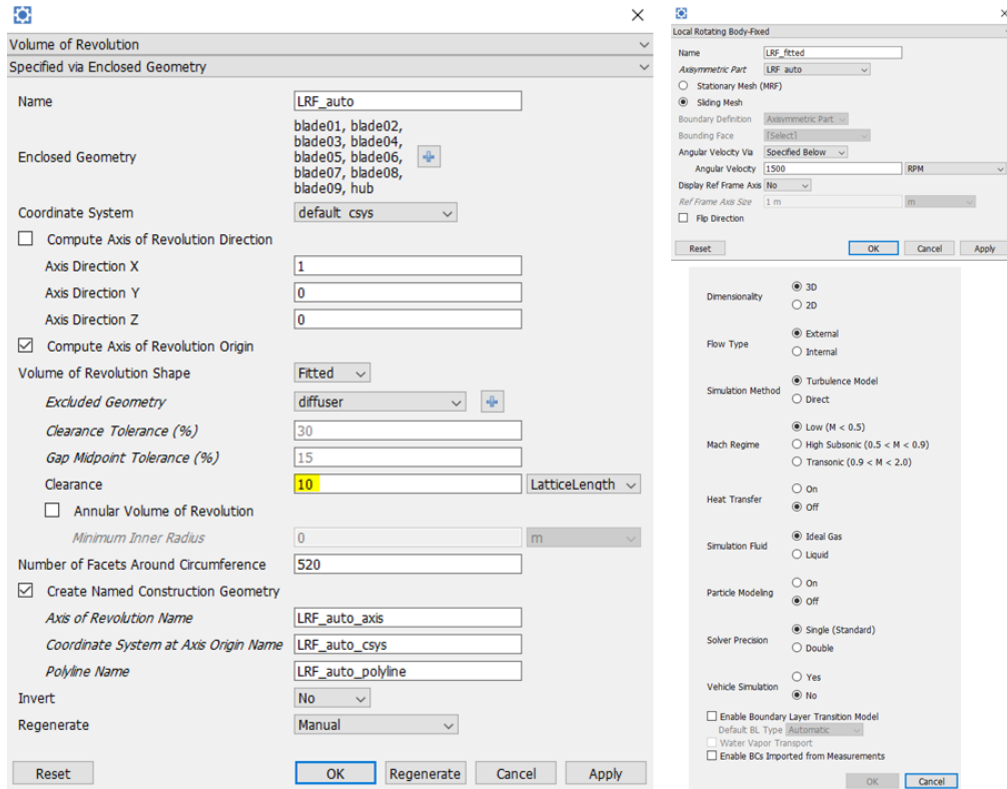


Figure 5.47 LRF creation using volume of revolution confined to blades and hub, sliding mesh setting and simulation parameter in Powercase

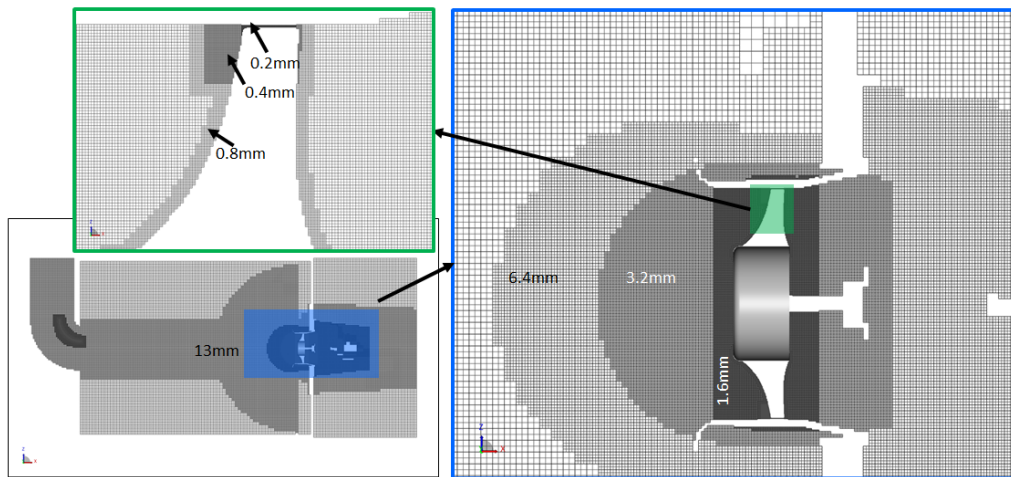


Figure 5.48 Meshing strategy executed in Powerflow discretizer

cubic elements called voxels as shown in Fig. 5.48. The discretization and computation are conducted with the commercial software PowerFLOW 5.5c. Geometrical features are resolved with Voxel Refinement (VR) regions that provide localized control over the finer voxels. Different colors of the VR region represent different voxel sizes. The small tip gap

| Voxel Counts | | | | | | | |
|-------------------|-----------|------------|-----------------|--------|-------------|------------------|--------------|
| | Fluid | Part Fluid | Near Surf Fluid | Porous | Part Porous | Near Surf Porous | Total Voxels |
| Scale 1 | 4120 | 3832 | 9056 | 0 | 0 | 0 | 17008 |
| Scale 2 | 117648 | 4708 | 10356 | 0 | 0 | 0 | 132712 |
| Scale 3 | 266520 | 5832 | 11756 | 0 | 0 | 0 | 284108 |
| Scale 4 | 2737741 | 40488 | 81299 | 0 | 0 | 0 | 2859528 |
| Scale 5 | 2838660 | 29788 | 59146 | 150430 | 86520 | 163028 | 3327572 |
| Scale 6 | 5450016 | 62092 | 115295 | 119926 | 11960 | 25814 | 5785103 |
| Scale 7 | 2568534 | 41432 | 80079 | 69316 | 4958 | 9652 | 2773971 |
| Scale 8 | 4996003 | 105252 | 132561 | 216702 | 6264 | 18306 | 5475088 |
| Scale 9 | 10058757 | 725754 | 1044345 | 69817 | 90983 | 103691 | 12093347 |
| Scale 10 | 16312468 | 2680033 | 3668272 | 0 | 0 | 0 | 22660773 |
| Scale 11 | 12691519 | 608416 | 898506 | 0 | 0 | 0 | 14198441 |
| Scale 12 (finest) | 63374998 | 7636637 | 10465422 | 0 | 0 | 0 | 81477057 |
| Total | 121416984 | 11944264 | 16576093 | 626191 | 200685 | 320491 | 151084708 |
| Fine Equivalent | 75567401 | 8710824 | 11975692 | 27486 | 12782 | 16084 | 96310270 |

| Surfel Counts | | | | | |
|-------------------|---------|----------------------------------|-------------|----------|---------------|
| | Wall | Static Pressure Free Flow Dir | LRF Sliding | Velocity | Total Surfels |
| Scale 1 | 306 | 5252 | 0 | 0 | 5558 |
| Scale 2 | 3260 | 2932 | 0 | 0 | 6192 |
| Scale 3 | 6376 | 564 | 0 | 0 | 6940 |
| Scale 4 | 42231 | 304 | 0 | 0 | 42535 |
| Scale 5 | 118582 | 0 | 0 | 0 | 118582 |
| Scale 6 | 79343 | 0 | 0 | 4047 | 83390 |
| Scale 7 | 63704 | 0 | 0 | 0 | 63704 |
| Scale 8 | 208171 | 0 | 0 | 0 | 208171 |
| Scale 9 | 703482 | 0 | 0 | 0 | 703482 |
| Scale 10 | 2064624 | 0 | 2288282 | 0 | 4352906 |
| Scale 11 | 414347 | 0 | 387072 | 0 | 801419 |
| Scale 12 (finest) | 2300943 | 0 | 6131712 | 0 | 8432655 |
| Total | 6005369 | 9052 | 8807066 | 4047 | 14825534 |
| Fine Equivalent | 3129556 | 8 | 6897318 | 63 | 10026946 |

Figure 5.49 The voxels and surfels distribution in different VR regions in Powerflow discretizer

is captured with a doughnut ring containing 12 voxels in VR12 that has 0.2 mm voxel size. The near blade region is discretized with 0.8 mm voxel size by offsetting LRF region (see Fig. 5.46b). The gradual refinement strategy is adapted to capture the microphone region and incoming jet profile with a 13 mm voxel. The rotating fluid containing the fan is modeled with a sliding mesh as displayed in Fig. 5.47 along with simulation parameters used during the simulation. The Fig. 5.48 demonstrates the voxels in different regions. The snapshot of the discretizer log file is provided in Fig. 5.49. It shows the number of voxels in each scale with respect to the VR region where scale 1 corresponds to VR1 and finest scale 12 corresponds to VR12. It appears that more than 75% of 96.3 million total fine equivalent voxels are occupied by the tip region (i.e. VR11 and VR12). Therefore, resolving such a small tip gap typically makes the simulation computationally expensive. The inlet of the duct is modeled as a velocity inlet and the sides of the big room as pressure outlets. The damping zones are provided to avoid acoustic reflections from the surrounding boundaries as indicated in Fig. 5.46a. A LBM simulation is conducted for

all three fans at the design point condition, where each case is initialized with the design point flow rate.

5.3.2 Flow field analysis and validation

Commonly, initialization strategy plays an important role in achieving an early convergence. As discussed in Chapter 4, we know that 15 seconds are required to establish the flow equilibrium. Hence, simulating 96M voxels case for that duration is extremely expensive. Therefore, the hub-only solution (discussed in Chapter 4) checkpoint file is used to seed the coarse case. The coarse case resolves up to scale 10 (i.e. VR10). It forms a very lighter file containing 33M total voxels and it is run for 139 fan revolutions ~ 5.56 s. The coarse solution is used to seed the finest case. The convergence is monitored for static pressure ($p - p_{atm}$) where $p_{atm} = 101325$ Pa in both simulations. The transient flow field is recorded with a probe placed 1 m away from the fan center near the top of the plenum in the fluid region unlike located in the test set up except that in the test the pressure tap is mounted on the top wall (see Fig. 4.3). The instantaneous pressure(p) development over the time from fine case is plotted in Fig. 5.50. The mean pressure for probe recording is calculated by using the time average formula given in Eq. 4.2. Besides, the flow field is averaged for each revolution (i.e. for 0.04 s) and then plotted with static pressure contours in Figs. 5.51a, 5.51b for coarse and fine cases respectively. The small jet effect observed is successfully damped by the flow straightener and results in uniform pressure distribution inside the plenum before the fan. The mesh refinement causes the pressure to rise from the coarse to the fine case. It is also confirmed that the mean calculated from the probe recording matches with the plenum pressure extracted at a similar probe location (follow black dot in Fig.5.51b) from the averaged flow field. Note that the LBM computations are performed on advanced Intel Platinum 8160F Skylake @ 2.1GHz processors containing 48 cores and 21 nodes, while RANS simulations are conducted on an older Intel E5-2683 v4 Broadwell @ 2.1GHz having 32 cores and one node at Compute Canada clusters. The usage summary is provided in Table 5.2.

A similar discretization, simulation and post processing strategy is followed for US and BS fans. The pressure rise calculated for all three fans is compared with the experiments

| Simulation type | Commercial code | Mesh count | Total CPUs | Time |
|-----------------|-----------------|------------|------------|-------|
| RANS | CFX | 15 M | 32 | 12 hr |
| LBM | Powerflow | 96 M | 1008 | 96 hr |

Table 5.2 Computational chart for LBM and RANS simulations

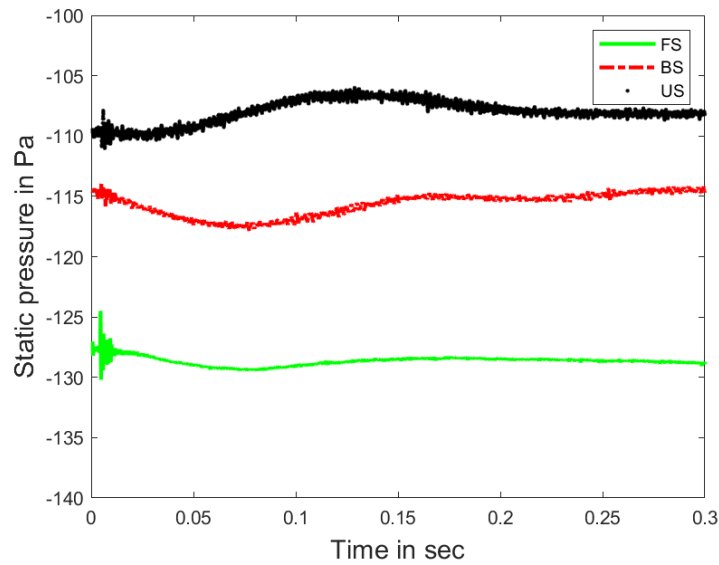


Figure 5.50 Static pressure convergence plot monitored inside plenum for fine cases

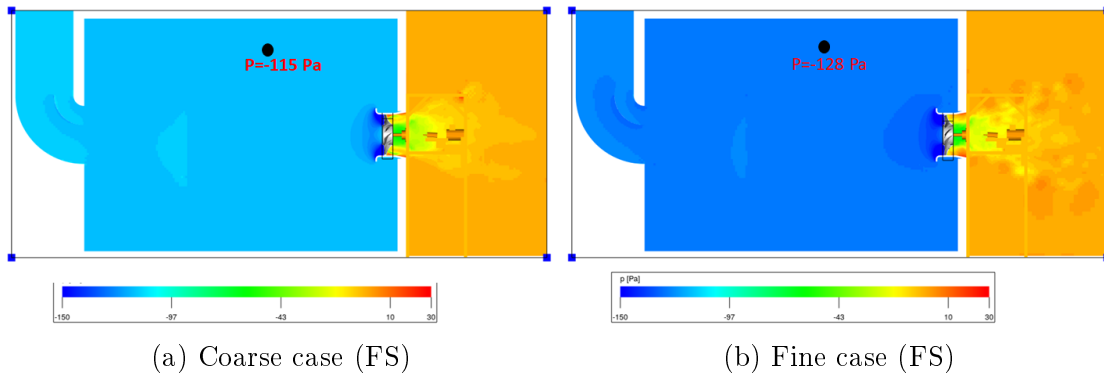


Figure 5.51 Mean flow field averaged over each fan revolution

in Table 5.3. Evidently, LBM shows consistently 16-18% error in pressure rise prediction compared to the test for all three fans whereas, except FS, BS and US nearly match the prediction with the RANS. Despite deviation in pressure rise prediction, the trend for these fans is properly captured by LBM. Perhaps, the combined effect of hysteresis, initialization condition and simplified computational domain are responsible for such deviations. They must be investigated either by initializing simulation with the lowest flow rate to mimic the initialization effect or by repeating the test to record the pressure at the design flow rate instead of starting the test from the lowest flow rate to omit any hysteresis or initialization issues.

The mean pressure contours plotted in Figs. 5.52 and 5.54 indicate similar suction pressure formation in LBM and RANS, respectively. The pressure coefficient calculated using Eq.

| Pressure rise in Pa | S1F | S1U | S1B |
|------------------------|-----|-----|-----|
| EXP | 158 | 132 | 142 |
| RANS | 170 | 119 | 125 |
| LBM | 128 | 110 | 117 |

Table 5.3 Pressure rise prediction using RANS and LBM (initialized from design point)

5.1 is plotted along the normalized chord in Fig. 5.53. All three fans show similar C_p behavior from midspan to $2/3^{rd}$ of the span but near the hub and near the tip the suction side pressure trend is reversed for FS and BS. The FS governs higher pressure rise near the tip (95%) despite a lower angle of attack observed with slightly higher C_p values near LE than that of BS while the reverse is true near the hub (20%). Once again, LBM and RANS agree with the C_p distribution trend along the span for all three fans.

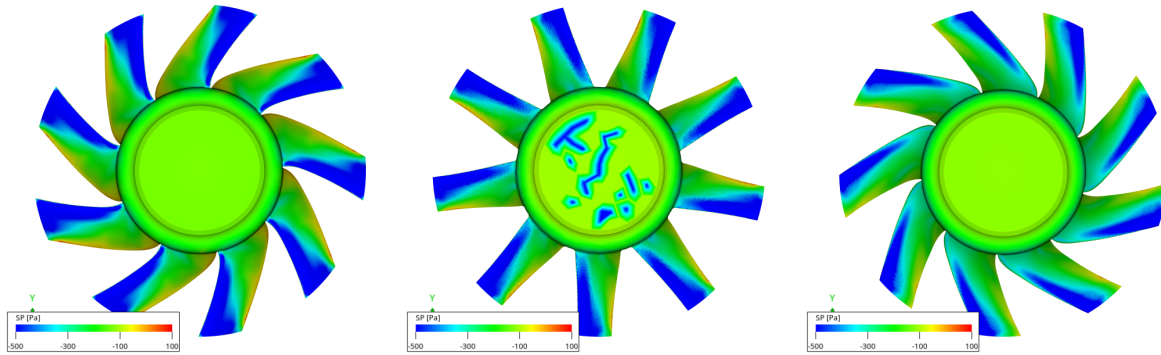


Figure 5.52 Static pressure contours from LBM simulations plotted for FS (left); US(middle), BS(right)

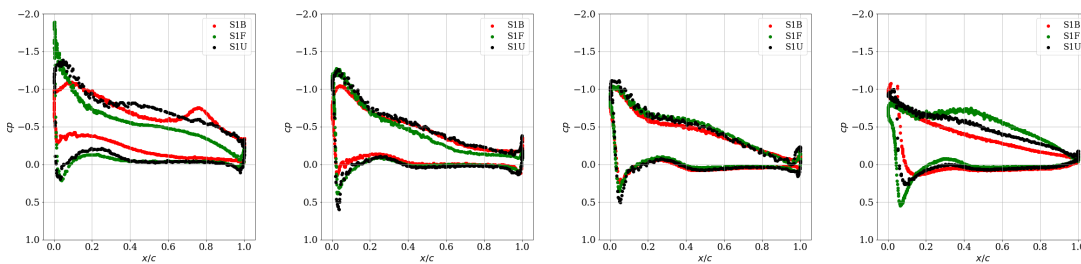


Figure 5.53 Pressure coefficient calculated from Eq. 5.1 and compared at 20%, 50%, 77%, 95% of span length from left to right respectively

The pressure rise predictions are highly dependent upon the quality of incoming and outgoing flow conditions. Therefore, velocity recorded before LE and after TE using LDA in the experiment are compared with LBM simulations in Figs. from 5.31 to 5.38. The axial

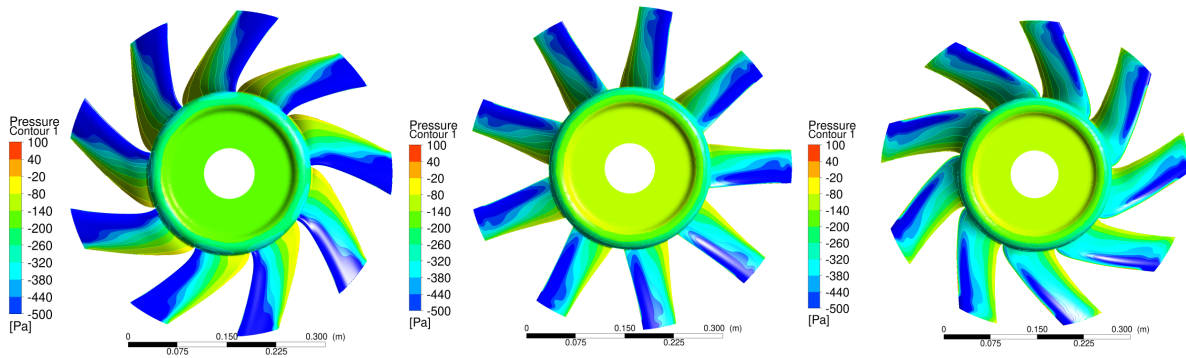
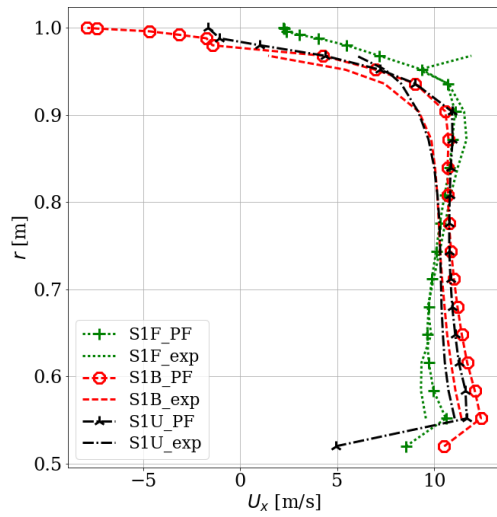


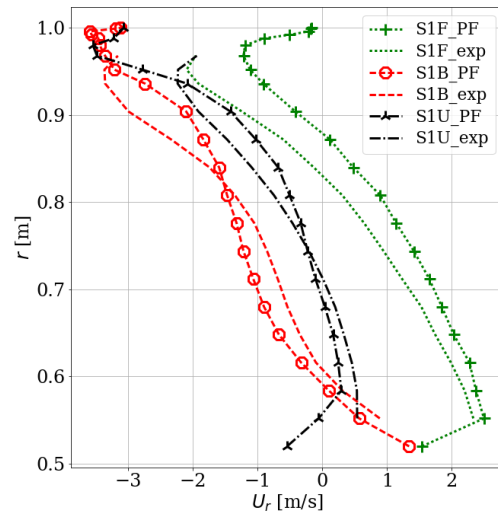
Figure 5.54 Static pressure contours from RANS simulations plotted for FS (left); US(middle), BS(right)

velocity contours from LBM match with that of experiments except for some noticeable differences near the tip region at LE (5.31 and 5.35). It shows a higher negative axial flow than the measurements. In addition, the azimuthally averaged axial velocity plot in Figs. 5.55 and 5.56 confirms negative flow near the tip but shows better match along the remaining span. This negative axial flow indicates more leakage and also explains one of the different causes for lower pressure rise in simulations. Near tip effect depend up on secondary flow i.e. tip flow which is again influenced by initial conditions. As observed in RANS, LBM also confirms the influence of sweep on radial flow behavior. The nature of sweep and its influence on radial flow is demonstrated in Fig. 5.41. Although the flow enters the blade passage with similar tangential velocity distribution along the span, the flow exits the blade passage with higher tangential velocities than in the experiment. However, near tip regions, the velocity profiles agree with experiments. Once again, LBM simulations are able to reproduce the behaviors induced by blade sweep as shown in Fig. 5.56 (c) i.e. higher tangential velocity for FS than BS. Nevertheless, LBM simulations predicted a slightly thicker and more turbulent wake than the experiment as observed in Fig. 5.38 but show lower TKE near tip regions when azimuthally averaged in Fig. 5.56.

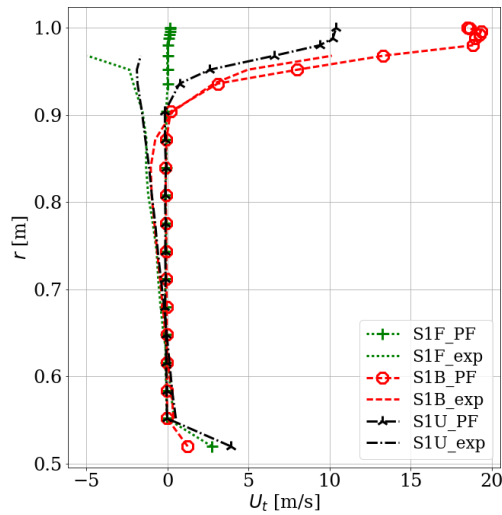
Further investigations are carried out to understand blade-to-blade flow behavior using instantaneous velocity plotted in the relative reference frame in Fig. 5.57. The corner vortex formation near the hub for FS is clearly visible but for US and BS the flow remains well attached until TE. All three fans show almost similar velocity distribution at midspan whereas near the tip three distinct flow patterns are observed. The FS shows higher velocity along the chord with some increased fluctuations near TE. On the other hand, BS shows a big chunk of low velocity shred all over the blade passage that interacts with the following blade. While US shows intermediate behavior i.e. unlike FS, higher velocity is observed near LE but later after midspan, the chunk of lower velocity convects towards



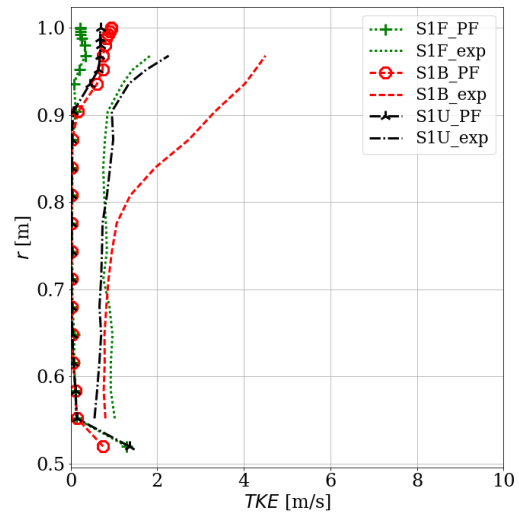
(a) Mean axial velocity



(b) Mean radial velocity

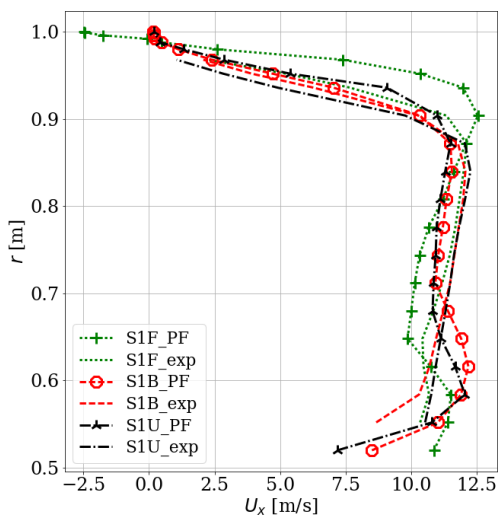


(c) Mean tangential velocity

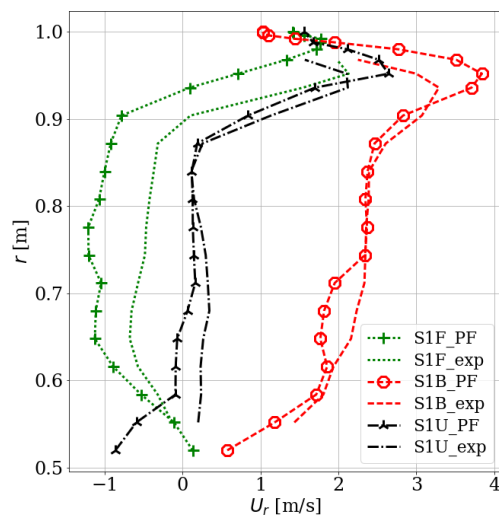


(d) Mean turbulent kinetic energy

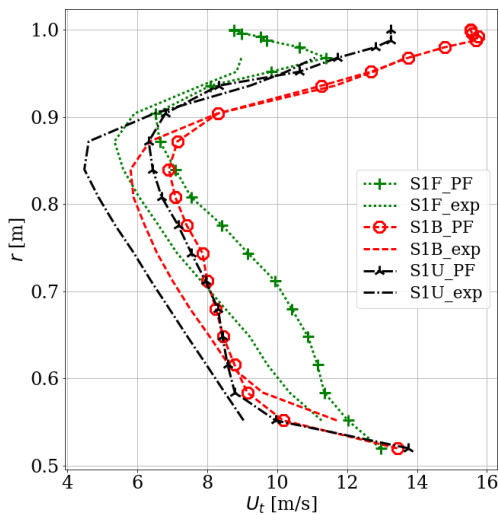
Figure 5.55 LBM Azimuthally averaged mean velocity profiles at LE



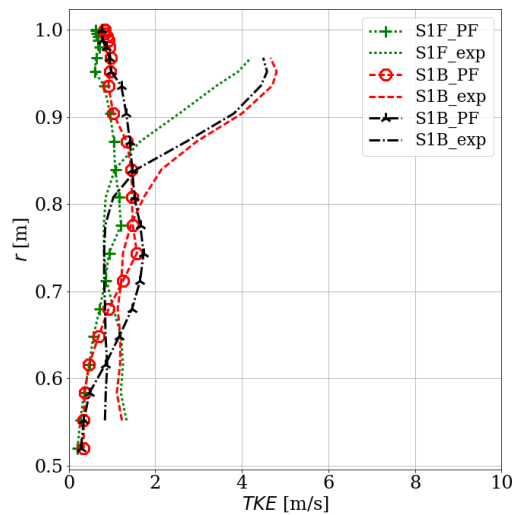
(a) Mean axial velocity



(b) Mean radial velocity



(c) Mean tangential velocity



(d) Mean turbulent kinetic energy

Figure 5.56 LBM Azimuthally averaged mean velocity profiles at TE

the following blade. These near tip behaviors are associated with tip vortex formation. It is further studied with some λ_2 plots as follows.

The spherical VR8 region meshed with 3.2 mm as shown in Fig. 5.48 is recorded with a period of 128 time steps ($dt = 4.22e - 5$ sec) for half a fan revolution i.e. 0.02 sec. This recorded instantaneous flow field is used to calculate λ_2 by accounting only for rotating region and colored by static pressure. Considering the study on tip vortex performed by Koch [49], the tip vortex formation can be divided into 1. Tip leakage vortex (TLV), 2. Induced vortex (IV), 3. Tip separation vortex (TSV). These three distinct zones are marked in Figs. from 5.58 to 5.60 and indicated with corresponding numbers. The FS in Fig. 5.58 illustrates remarkably the tip vortex formation and describes uniquely all three features. The TSV creates rib vortices that wrap around the TLV. They both merge in the aft portion of the tip blade profile while IV (2) stands out separately and later merges with the rest. This combined wake formed by these vortices travels towards an adjacent blade grazing the pressure side. On the contrary, BS exhibits thick and chaotic tip vortex formation and doesn't show clear distinction unlike FS. In fact, thin, spaghetti like structures are observed in Fig. 5.59 that travels downstream. Some of them partially interact with LE of an adjacent blade while others pass grazing pressure side. The tip wake in BS spreads over larger length of the span near the tip than that of FS. The tip vortex of US shares the behaviour from both. The TLV formed in US stays attached until mid of the chord and TSV much stronger, leaves earlier and changes the trajectory of the TLV [49] forming thicker wake than that of FS. Although US tip wake unlike BS interacts with LE of the adjacent blade, it covers lesser span length than BS. The LE interactions occurs nearly from 5%, 15%, and 25% of the span length measured from the blade tip for FS, US, and BS, respectively.

The time evolution of these tip vortices is studied by considering similar λ_2 plots but viewed from the top. Each frame is recorded for every ten time steps using above mentioned VR8 fluid volume and numbered as T=0,10,20,... in Figs. 5.61, 5.62 and 5.63. The FS in Fig. 5.61 exhibits a stable TLV formation that almost remains parallel to the tip chord in all frames. Conversely, BS TLV shows early separation near LE and highly unstable behavior that is traced in Fig. 5.62. The TLV starts disrupting from frame T=10 and completely detaches from the chord in frame T=30. Later these disrupted, elongated and rotating patterns travel downstream spreading over the blade passage and periodically interacting from LE to TE of an adjacent blade. Moreover, they also cause the TLV disturbance of the adjacent blade. It creates a domino effect causing the disturbance in all blades' TLV formation. For example, T= 50 to 70 frames show the TLV interaction with some vortical

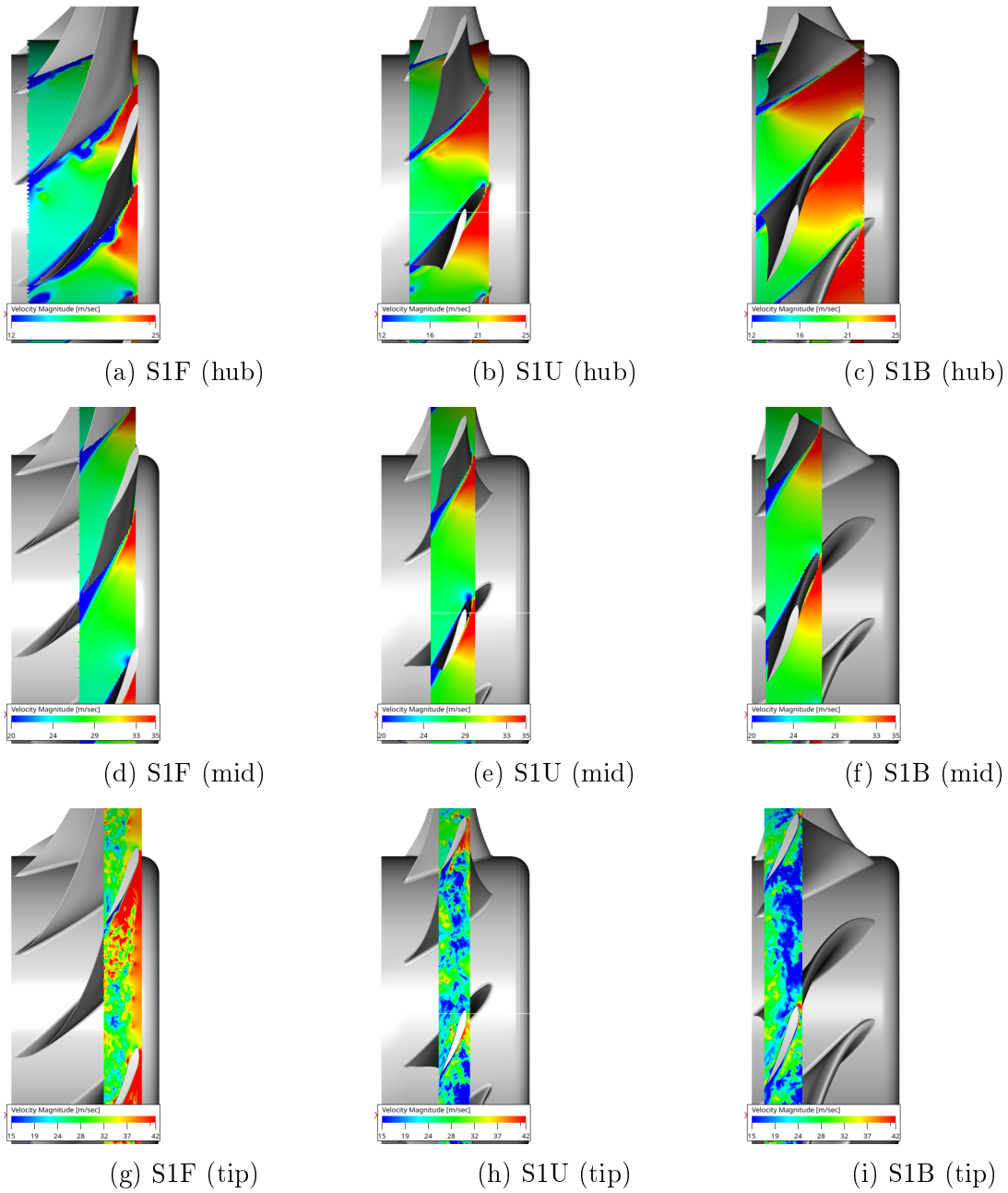


Figure 5.57 Contours of instantaneous velocity from LBM simulation taken near hub (10% of span), near mid (50% of span) and near tip (99% of span)

structures from the previous blade. These interactions are 3D in nature that lead the tip vortex spread over a larger span radius than compared to the other two fans. The US also shows some unstable nature of TLV but delays its separation compared to BS. It also exhibits similar oscillatory behavior but it is tracked further downstream after mid-chord, as observed in Fig. 5.63. Nonetheless, these oscillations disrupt the trajectory of the tip vortex that causing it to spread towards the LE of an adjacent blade while traveling downstream. Although the tip vortex spreads over LE, it barely disturbs the TLV of an adjacent blade near LE. Therefore, it appears that the US has fewer tip interactions than that BS.

Now, λ_2 is calculated using averaged flow field and its isosurface colored by turbulent kinetic energy (TKE) is plotted in Figs. 5.66 and 5.64. The TKE in LBM simulations is calculated by summing resolved and modeled parts of velocity fluctuations. The FS shows a vortex trajectory parallel to the chord whereas US and BS show similar widely spread tip vortex. The presence of TSV is marked for FS but for others, it isn't clearly noticeable. The RANS simulations also agree with the TSV trajectory trace from LBM that is compared in Fig. 5.65. BS from RANS shows TSV spread widely limited to the LE region of an adjacent blade than that of LBM. Nevertheless, the radial spread of the tip vortex agrees in both simulations, as noticed in Figs. 5.66 and 5.67.

In the experiment, capturing such highly complex 3D tip flow behavior is tricky. Therefore, to validate it, the wall pressure is recorded with 15 miniature pressure transducers flush-mounted on a diffuser wall as demonstrated with the FS fan in Fig. 5.68. We have chosen three probes such that the first probe lies before LE, the second probes lie near mid of the chord and finally, the third probe is situated near TE as shown in Fig. 5.69. These probes represent necessary flow conditions passing through the tip gap for the three different fans. However, all three blade tips are located at different axial positions so that chosen probes don't match. The following Table 5.4 summarises the position of probes with respective to LE of the given blade. The first probe is indicated with the negative sign which just means that it lies before LE. The aim of this extraction is to validate tip flow behavior with simulation. The time trace of wall pressure fluctuations captures the blade passing frequency noticed by the highest peak in Fig. 5.70. LBM simulation and experimental peaks aren't overlapped in the time trace plot because for example in the FS case the recording is conducted at 1486 RPM while the simulation is performed at 1500 RPM. It seems that during tests sometimes maintaining constant rotational speed is a bit challenging task. Nevertheless, only the BPF peak is visible to be altered by $\sim 3\text{Hz}$.

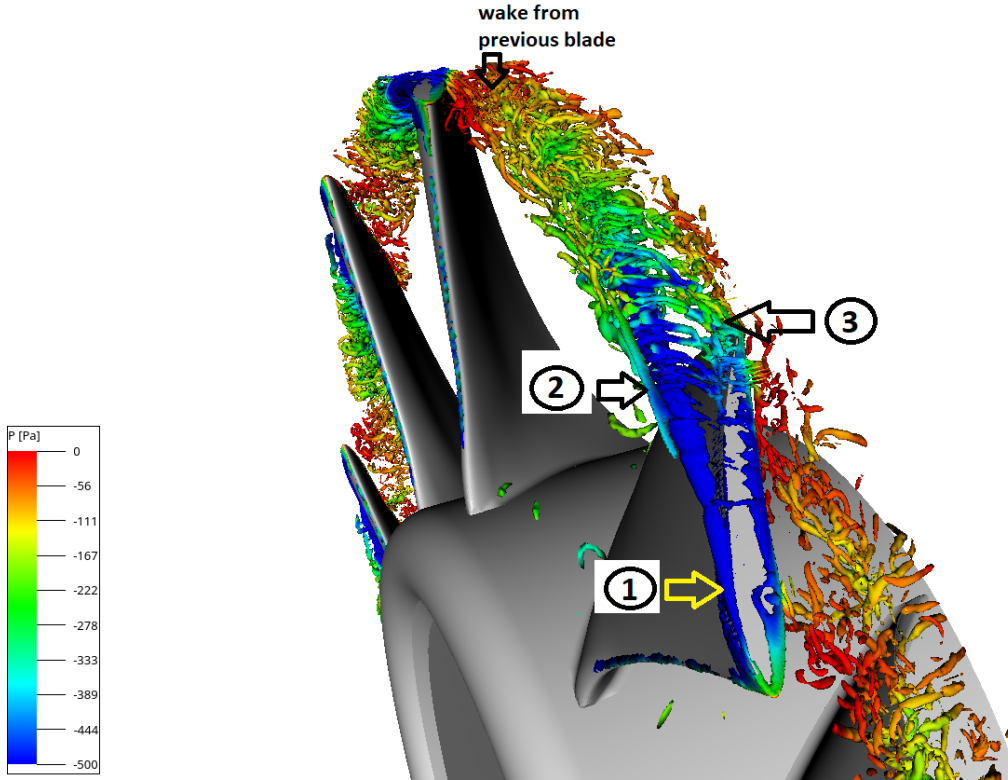


Figure 5.58 FS tip vortex plotted using isosurface of $\lambda_2 = -2e7$ calculated from instantaneous flow field

The time trace of wall pressure fluctuations for FS is plotted in Fig. 5.70 and its corresponding power spectral density (PSD) is given in Fig. 5.71. In all PSD calculations, reference pressure = $2e - 5$ pa is used to calculate sound pressure level (SPL). The 3rd probe is lying before LE and its time trace shows a clean pressure wave whose amplitude matches with the experiment and also shows good agreement in PSD. The time trace starts capturing more perturbations for the 6th probe since it is lying near TE where tip vortex trajectory is mainly observed in the above λ_2 plots. The PSD plots in Fig. 5.71 agrees with the experiment for all frequency region and for all probes except the 5th probe. It shows slightly lower SPL levels from 100 Hz to 800 Hz. The time trace of BS and US probes near LE doesn't show a clean pressure wave unlike FS but it exhibits some additional pressure fluctuations that can be interpreted as turbulent fluctuations. This observation is in-line with the above λ_2 investigation because it seems that the spread of TSV near LE is captured by these probes. However, separating just tip interactions is somewhat challenging. Their PSD plots are given in Figs. 5.73 and 5.75 compares well with the test for all frequency range except at lower frequency where slightly lower amplitudes are predicted by LBM. Overall, wall pressure fluctuation levels and its PSD are satisfactorily captured by LBM for all three fans.

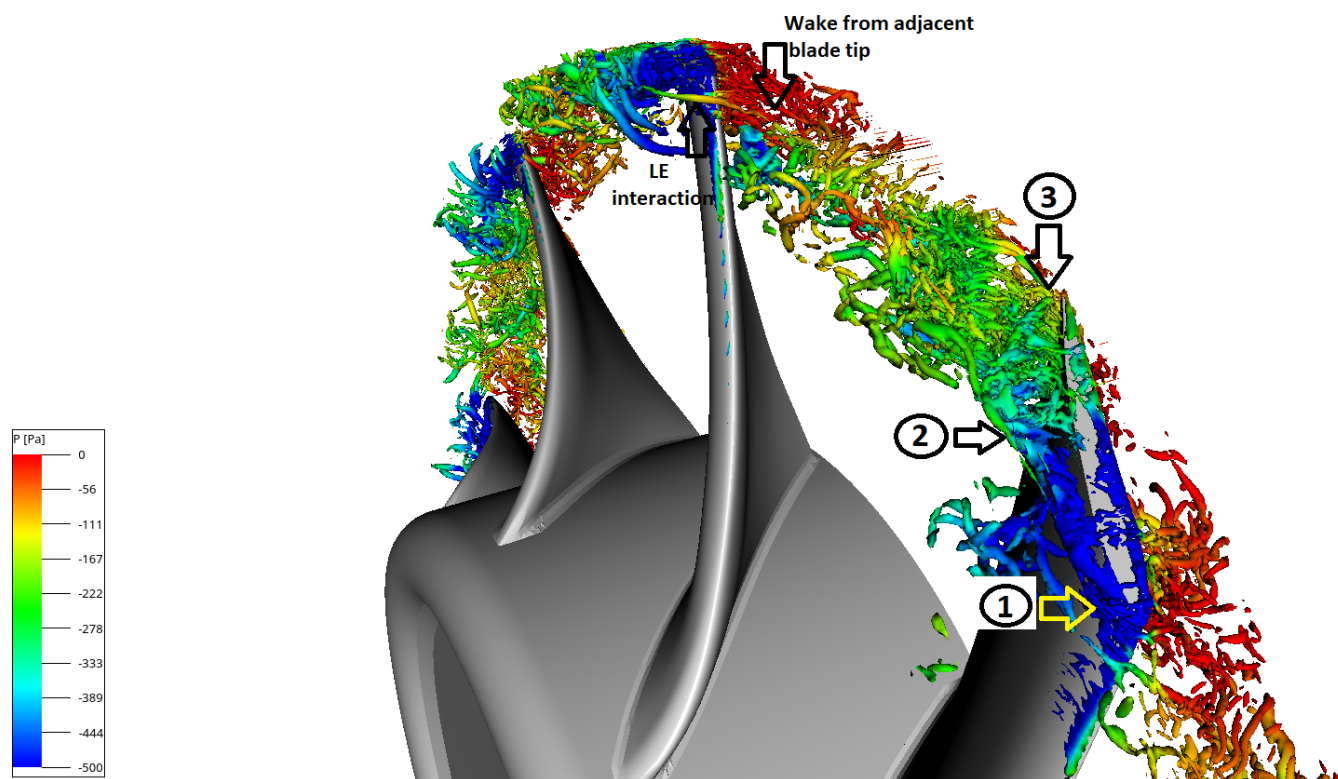


Figure 5.59 BS tip vortex plotted using isosurface of $\lambda_2 = -2e7$ calculated from instantaneous flow field

| | | | | |
|-----|---|------|------|------|
| Fan | | 1st | 2nd | 3rd |
| FS | Casing probe number | 3rd | 5th | 6th |
| | Distance measured from LE and normalized by tip axial chord | -26% | 50% | 93% |
| BS | Casing probe number | 10th | 11th | 12th |
| | Distance measured from LE and normalized by tip axial chord | -5% | 35% | 73% |
| US | Casing probe number | 7th | 8th | 9th |
| | Distance measured from LE and normalized by tip axial chord | -4% | 45% | 95% |

Table 5.4 Probes selection for different fans

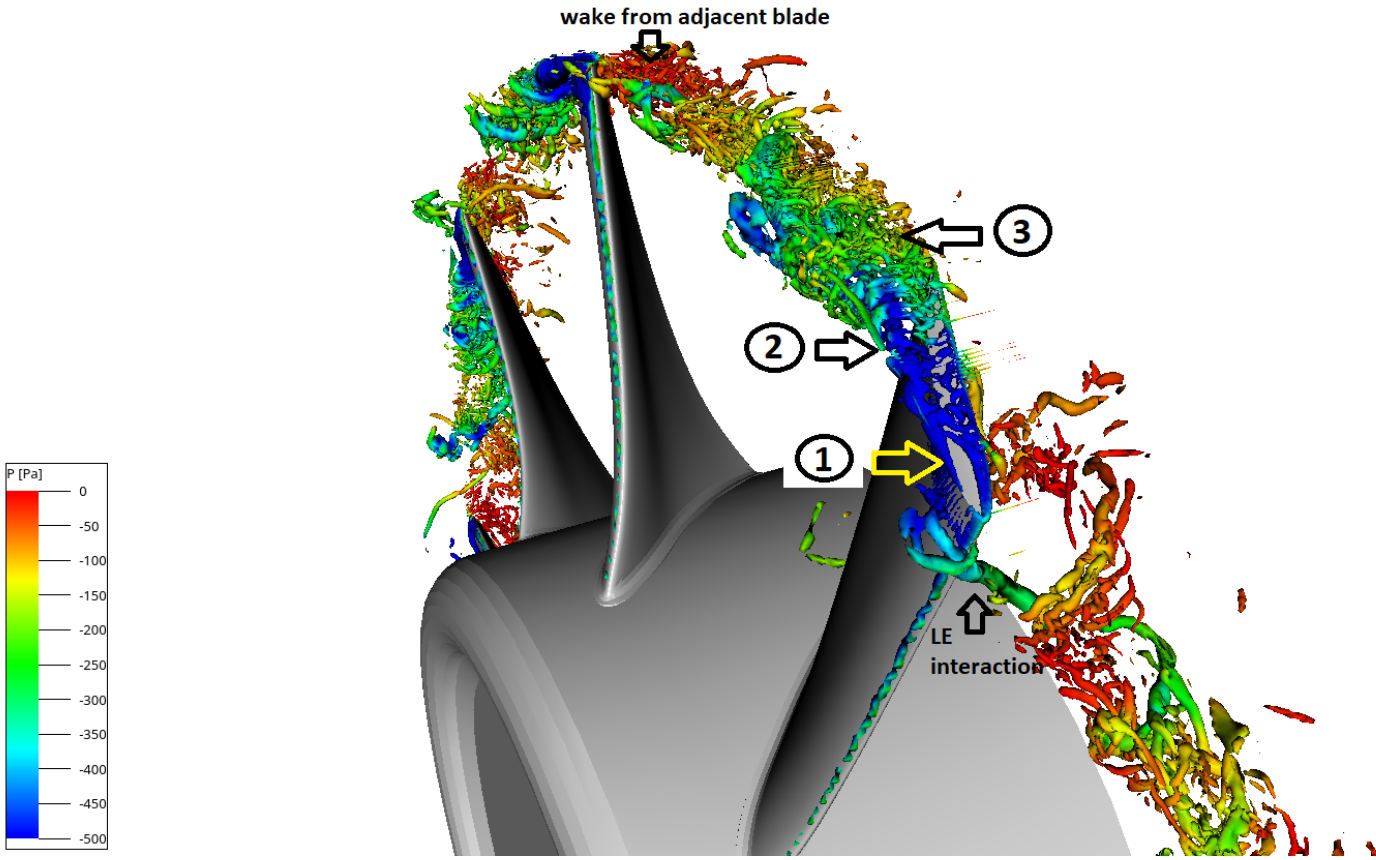


Figure 5.60 US tip vortex plotted using isosurface of $\lambda_2 = -2e7$ calculated from instantaneous flow field

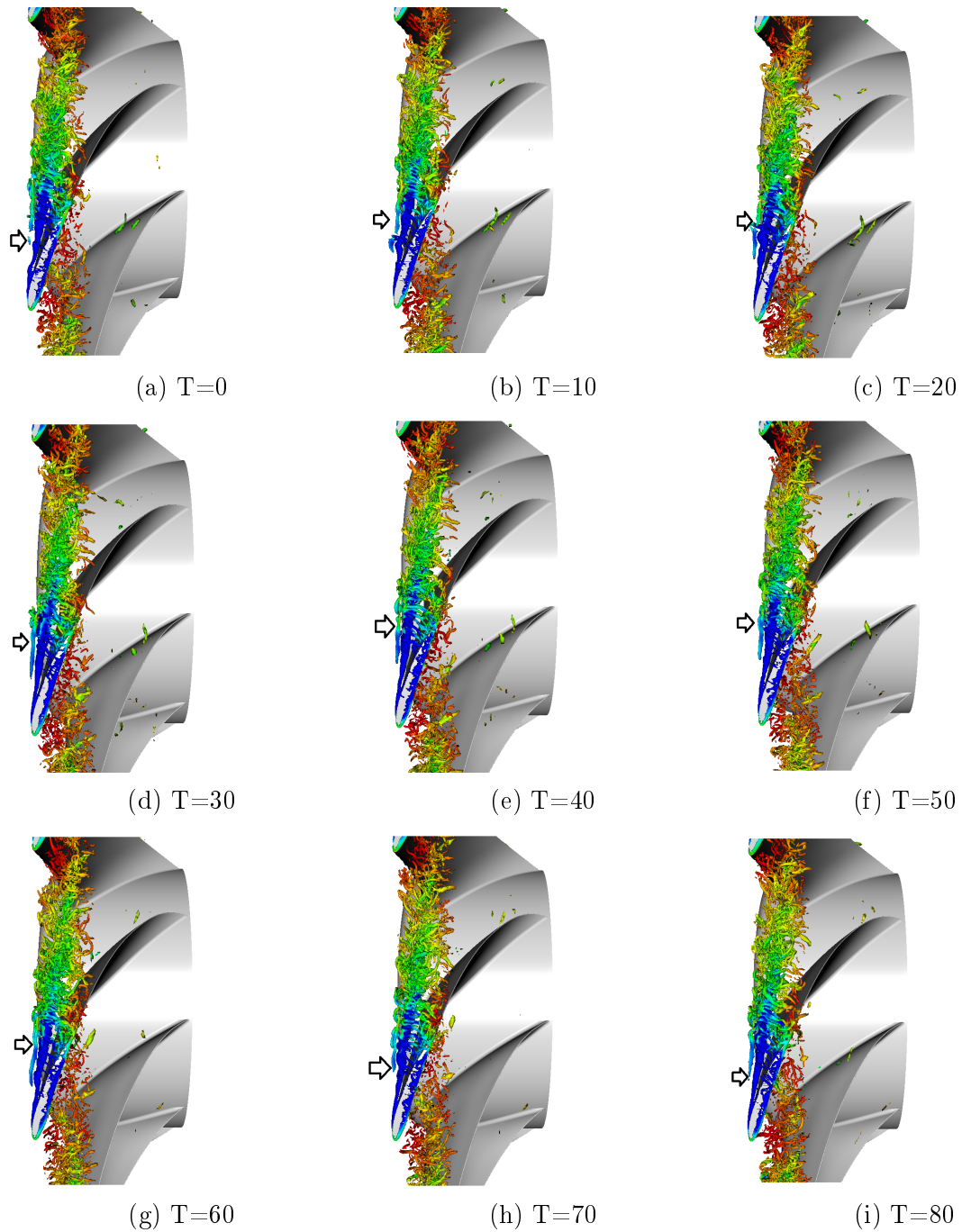


Figure 5.61 Time evolution of FS tip vortex plotted using isosurface of $\lambda_2 = -2e7$ calculated from instantaneous flow field

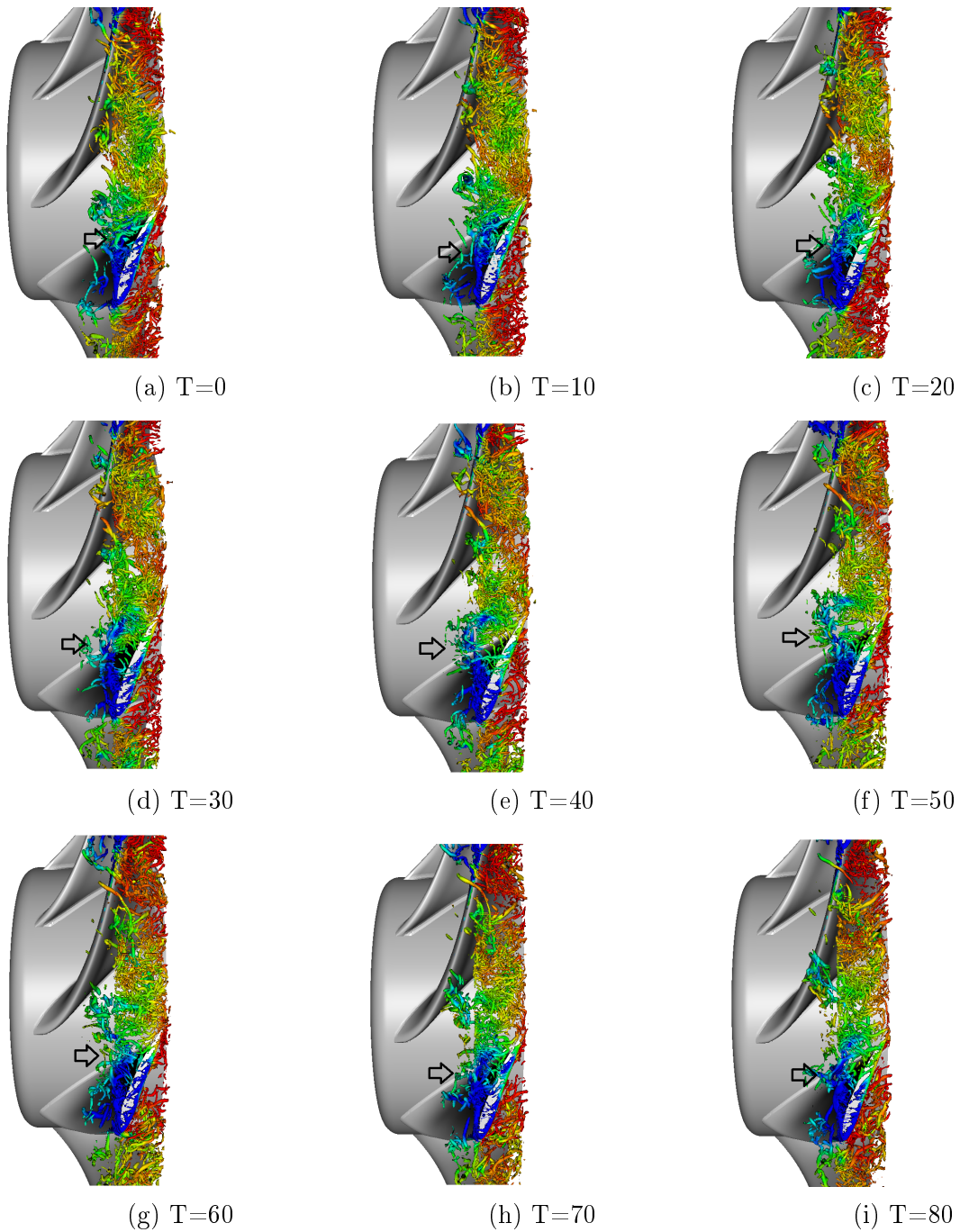


Figure 5.62 Time evolution of US tip vortex plotted using isosurface of $\lambda_2 = -2e7$ calculated from instantaneous flow field

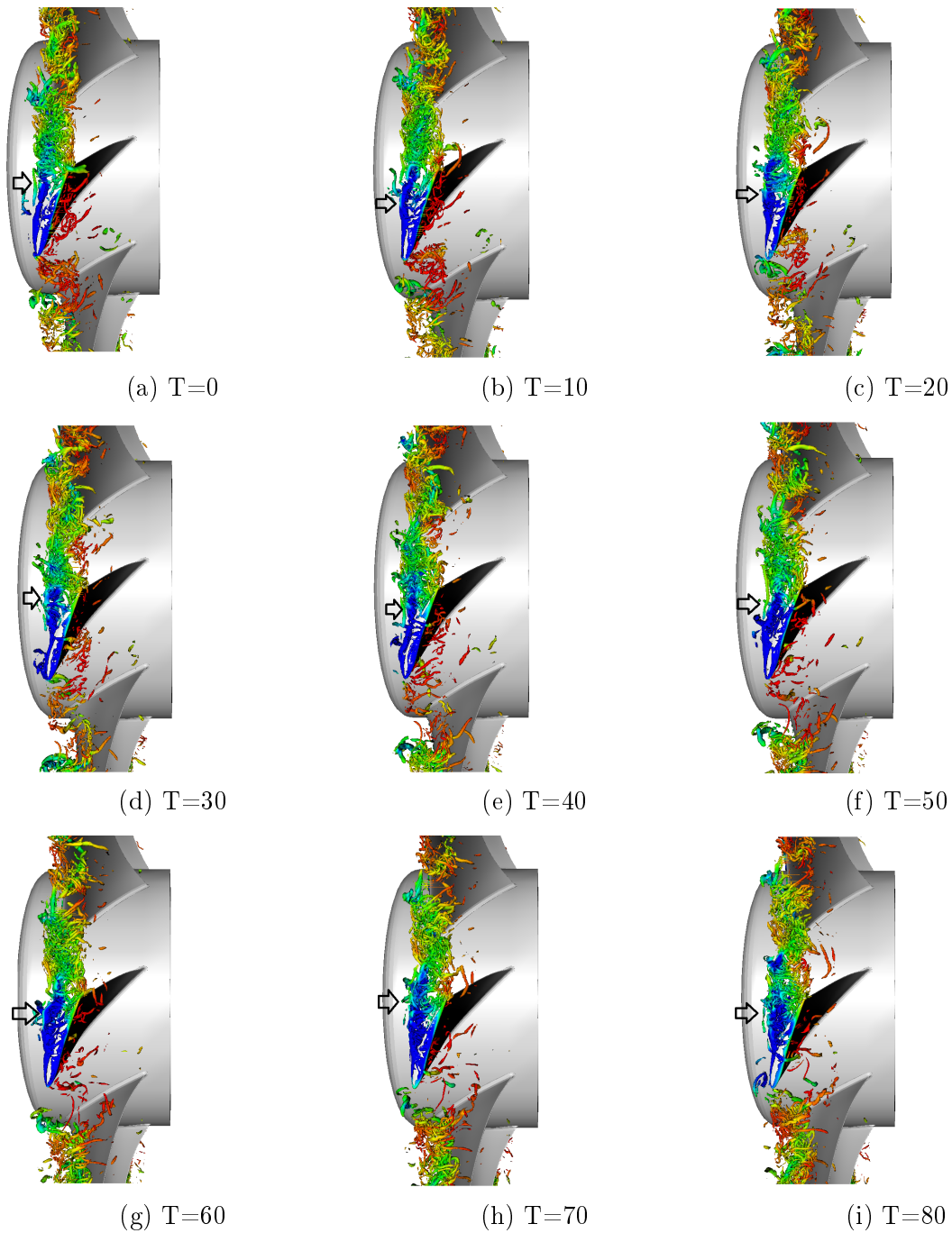


Figure 5.63 Time evolution of US tip vortex plotted using isosurface of $\lambda_2 = -2e7$ calculated from instantaneous flow field

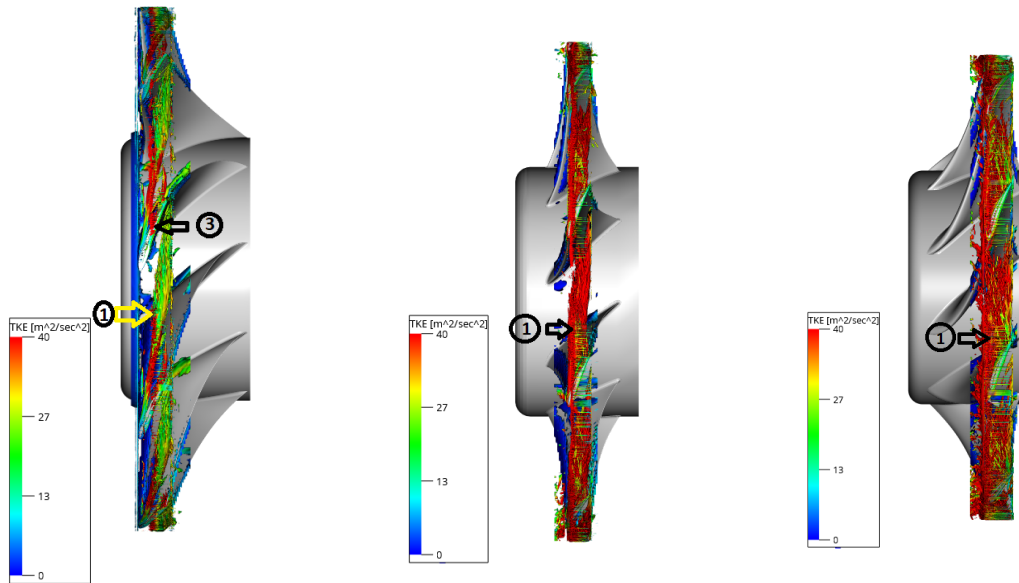


Figure 5.64 Top view of $\lambda_2 = -2e5$ isosurface from mean flow field of LBM simulations plotted for FS (left); US(middle), BS(right)

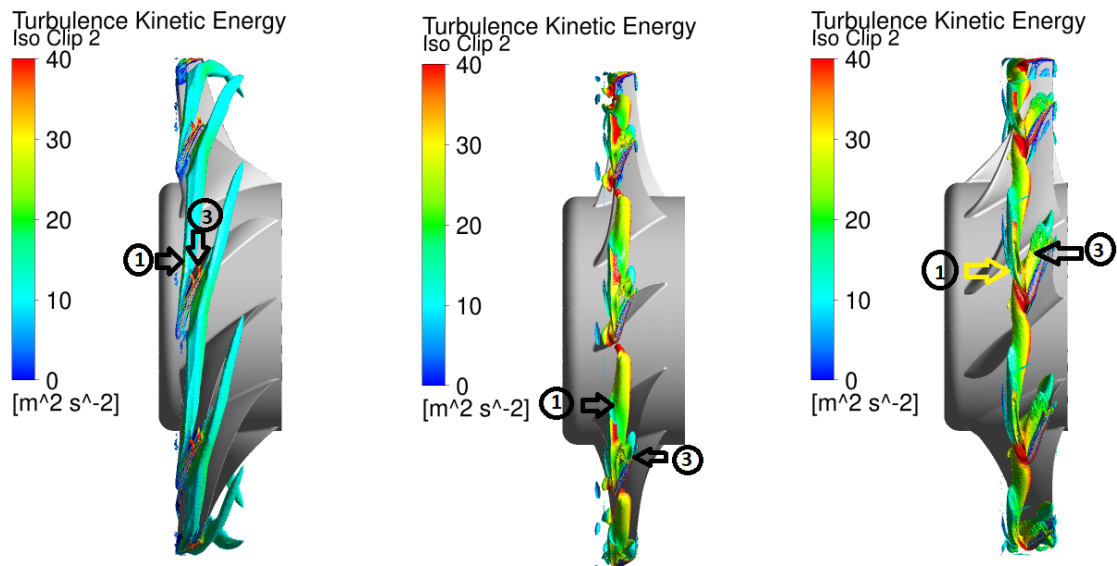


Figure 5.65 Top view of $\lambda_2 = -2e5$ isosurface from RANS simulations plotted for FS (left); US(middle), BS(right)

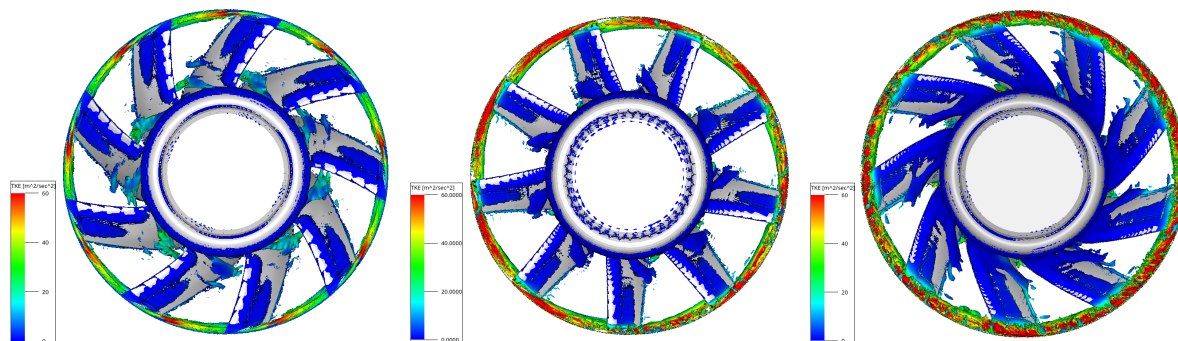


Figure 5.66 Front view of $\lambda_2 = -1e5$ isosurface from mean flow field of LBM simulations plotted for FS (left); US(middle), BS(right)

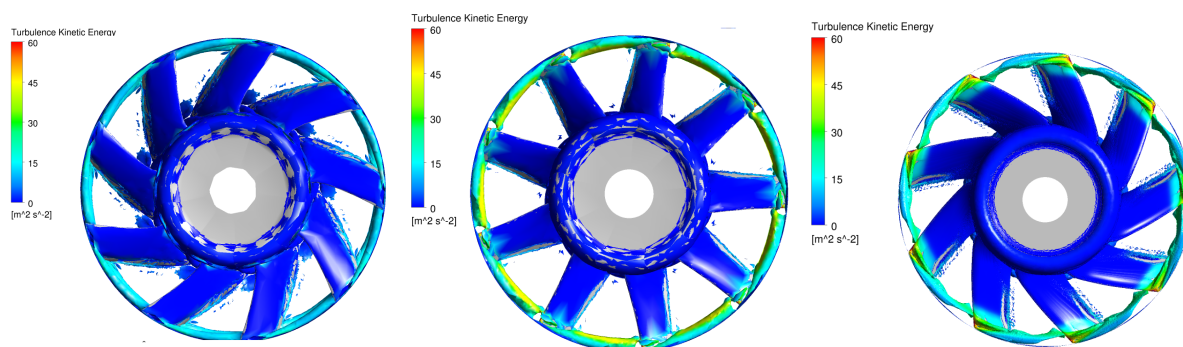


Figure 5.67 Front view of $\lambda_2 = -0.7e5$ isosurface from RANS simulations plotted for FS (left); US(middle), BS(right)

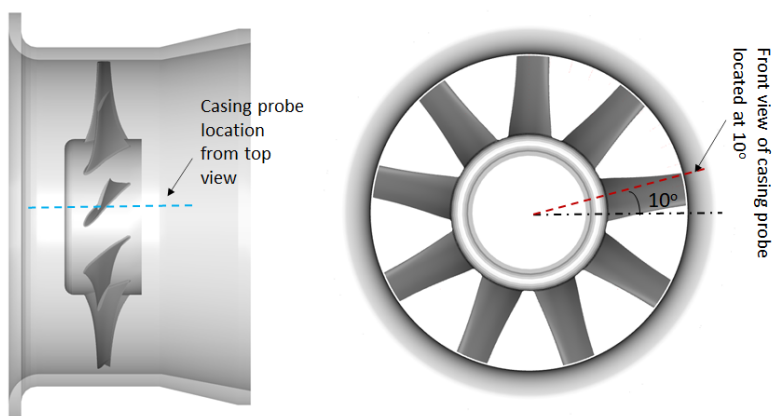


Figure 5.68 Probes provided in the casing to record pressure

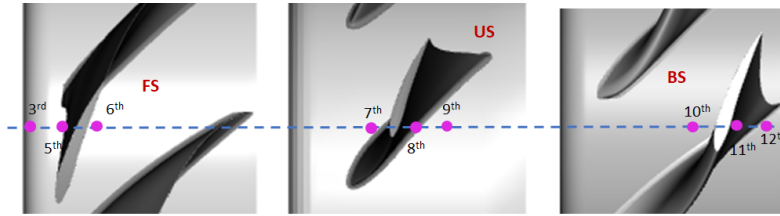


Figure 5.69 Probes provided in the casing to record pressure

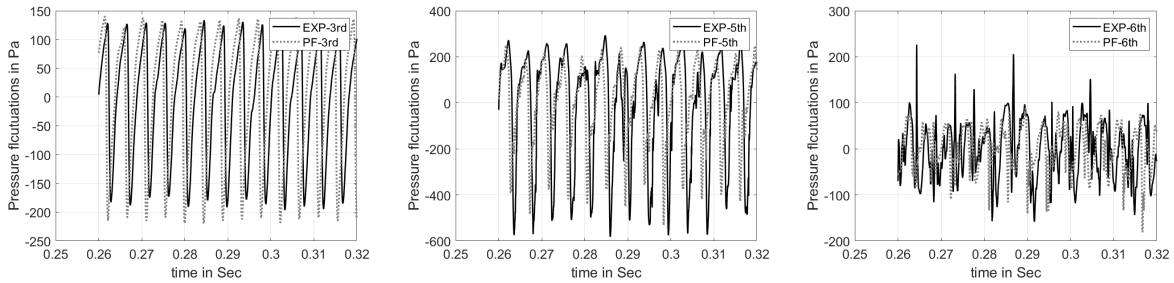


Figure 5.70 Time trace of wall-pressure fluctuations on the duct in the tip gap for FS

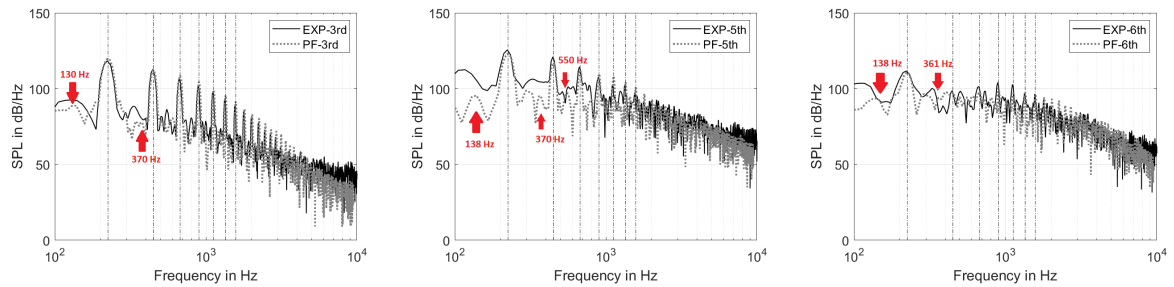


Figure 5.71 PSD of wall-pressure fluctuations on the duct in the tip gap for FS

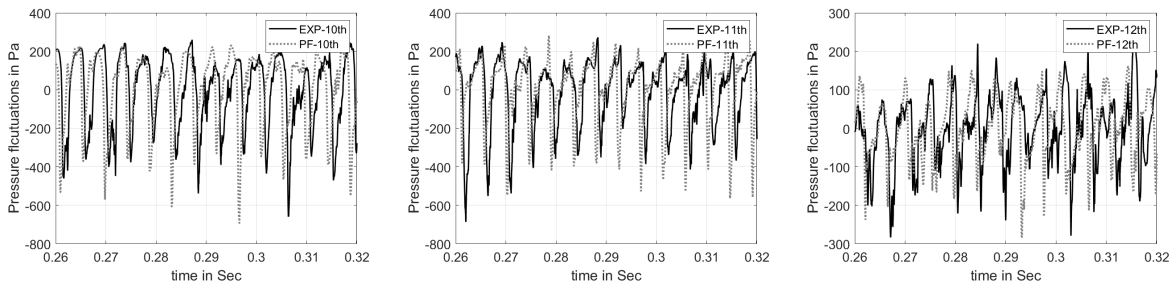


Figure 5.72 Time trace of wall-pressure fluctuations on the duct in the tip gap for BS

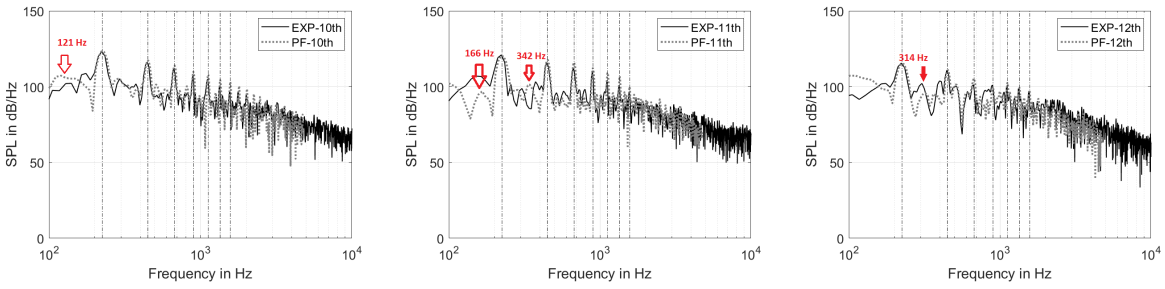


Figure 5.73 PSD of wall-pressure fluctuations on the duct in the tip gap for BS

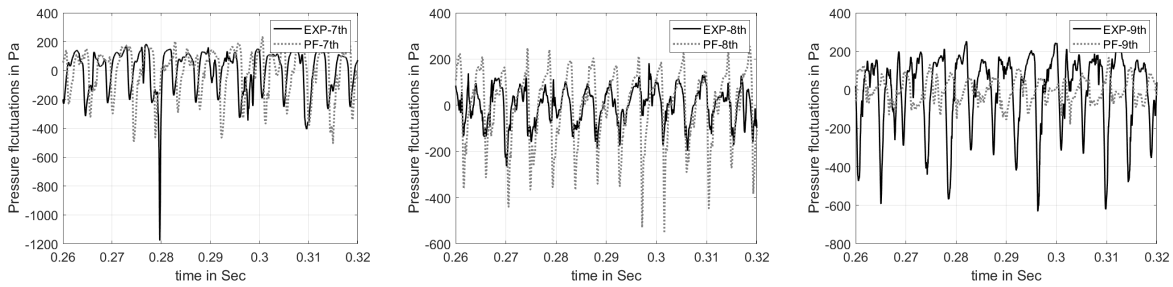


Figure 5.74 Time trace of wall-pressure fluctuations on the duct in the tip gap for US

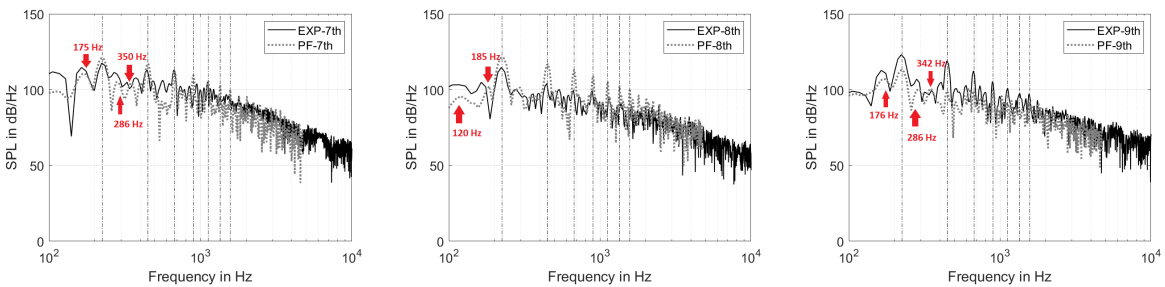


Figure 5.75 PSD of wall-pressure fluctuations on the duct in the tip gap for US

5.4 Conclusion

The present chapter is aimed at gaining aerodynamics knowledge of base design and its swept versions. In order to achieve that two design configurations are investigated in this chapter. Firstly, the industrial fan design and its two forward sweep variants designed only for sweep are analyzed. With the help of steady, incompressible RANS simulation, we confirmed the previous observation that the pressure rise is deteriorated with an increase in sweep angle by $\cos(\lambda)$ times than its base design. The C_p plot showed that the lift is reduced from hub to tip systematically for low to high forward sweep blade. Further investigations of velocity extraction in relative frame revealed that the modified relative velocity at any radial span location increases with an increase in forward sweep angle despite similar incoming axial velocities except near tip. The increased relative velocity results in a larger inlet flow angle in the relative frame which in turn reduces the incidence angle drastically near tip. This directly affects the lift produced by the blade at any given radial cross-section. In addition, this reduced incidence angle near the tip helps the airflow to remain attached and also helps in delaying stall. The forward sweep shows a thicker boundary layer and lowers shear stress than its base design. It indicates that the forward sweep blade experience lower friction drag and hence can consume low power to overcome the frictional resistance. Moreover, the Beiler and Carolus correction factor doesn't seem to fit in forward sweep fans. The design point pressure rise is scaled with $\cos \lambda$ instead. This study is validated with test data and provided the forward sweep behavior noteworthy insights.

Secondly, the fans designed with two sweep variants i.e. forward and backward sweep are simulated but in order to recover lost lift due to sweep, the chord length is increased by keeping the remaining design parameters the same. Similar RANS simulations are performed to gain sweep knowledge. The forward sweep showed improved performance from design flow rate to lower flow rate over unswept blade whereas the backward sweep exhibited deteriorated performance. Nonetheless, the higher flow rate above the design point doesn't show any improvement for the forward and backward sweep over the unswept blade. Interestingly, it is observed that the tangential velocity doesn't change when the blade is designed with a backward or forward sweep angle but the axial velocity distribution does change. The forward sweep shows reduced axial velocity near the hub and higher axial velocity near the tip but the backward sweep shows exactly the opposite behavior. This alters the radial equilibrium from its design. The C_p plot reveals that contrary to backward sweep, forward sweep produces lower lift near the hub and it slowly increases towards the tip. The backward sweep showed a lower lift among all three fans near the

tip. The flow extraction at LE in relative frame showed that backward sweep showed a higher inlet angle than FS from hub to mid span and it started slowly reducing. The lower inlet angle means a higher incidence angle. Although forward and backward sweep fans are designed for similar incidence angles from hub to tip, they don't replicate the same behavior during the test. This increased incidence angle near the tip caused the flow to separate earlier than in the forward or unswept case. It results in thick and turbulent tip vortex formation whose wake strongly interacts with an adjacent blade. The complex test set up is simulated with high fidelity, transient, compressible LBM using VLES. The simulation helped to capture the pressure rise trend, C_p behavior, and mean velocity along with exploration of the transient nature of the tip vortex. The forward sweep forms more stable TLV than the backward sweep and TSV wraps around TLV generating a turbulent wake that impacts the pressure side of an adjacent blade. However, backward sweep TLV is quite thick and showed an oscillating pattern that allows TSV and TLV mixing and spreads in blade passage causing strong interactions from LE to TE of an adjacent blade whereas unswept blade shared intermediate nature of tip vortex formation. These aerodynamic investigations certainly help us understand the nature of sweep and its influence on the flow field in detail.

Although all fans are designed for similar pressure rise, forward and backward sweep modifies the incoming flow conditions and generates various secondary flow effects that significantly affect the aerodynamic performance of any axial fan. This chapter certainly provides knowledge about the aerodynamic flow around blades but doesn't reveal much about noise-generating mechanisms. Therefore, efforts are dedicated to learning more about the effect of sweep on the noise spectrum, and on the identification of the noise generating sources in the next chapter. They are also directed toward the validation of the analytical model extended to swept blade described in Chapter 3.

CHAPTER 6

Aeroacoustic and Noise Sources Investigations

The previous chapter has described various simulations conducted using actual test configuration with the full fan mounted in a duct. Most numerical results are noted worthily compared with experiments on all levels except for a few discrepancies. However, we are focused on the broadband noise generation mechanism, mainly due to LE turbulence interaction and sub-harmonic hump generated due to periodic interactions of a tip vortex with an adjacent blade. Therefore, all the efforts are dedicated to identifying such noise-generating sources and acquiring know-how on the swept blade behaviors.

6.1 Validation of noise spectra

Microphones are arranged in the numerical setup as in the experiment shown in Fig. 4.4. The noise is recorded for 17 revolutions in a simulation with a sampling frequency of 47.3 kHz. The experimental signal is also sliced such that the spectra are plotted for 6 Hz bandwidth to make a fair comparison. The power spectral density is calculated using the PWELCH function available in Matlab using Hanning windows with 10% of signal length and 50% overlap. The 10% window is selected so that the averaged spectra keep the significant subharmonic humps observed in between BPF peaks and below BPF. The noise levels recorded for all microphones are compared for all three fans. In all plots, the first five BPFs are marked with the black dotted line. Moreover, the contribution from each noise mechanism is identified and discussed briefly while maintaining focus on the sweep effect on LE broadband noise.

The experiments showed the strong tonal noise emitted at blade passing frequency. In order to understand the origin of tonal source a small test is planned with coarse mesh. Initially, to establish the flow field and to save on computational cost, we have simulated the case with a coarse mesh as illustrated in Fig. 6.1 for FS. The case is simulated for 139 and 17 revolutions for the coarse and fine cases, respectively. The coarse mesh doesn't capture the right broadband noise levels but the tonal component is correctly captured at given BPFs. The fine mesh size is ~ 96 M and we couldn't afford to compute more than 17 revolutions. Moreover, according to Sturm et al. [105], the tonal noise is also caused by the asymmetric filling of the plenum yielding inflow distortion. Therefore, we investigated the flow field before the fan with streamlines and vorticity contours as shown in Fig. 6.2.

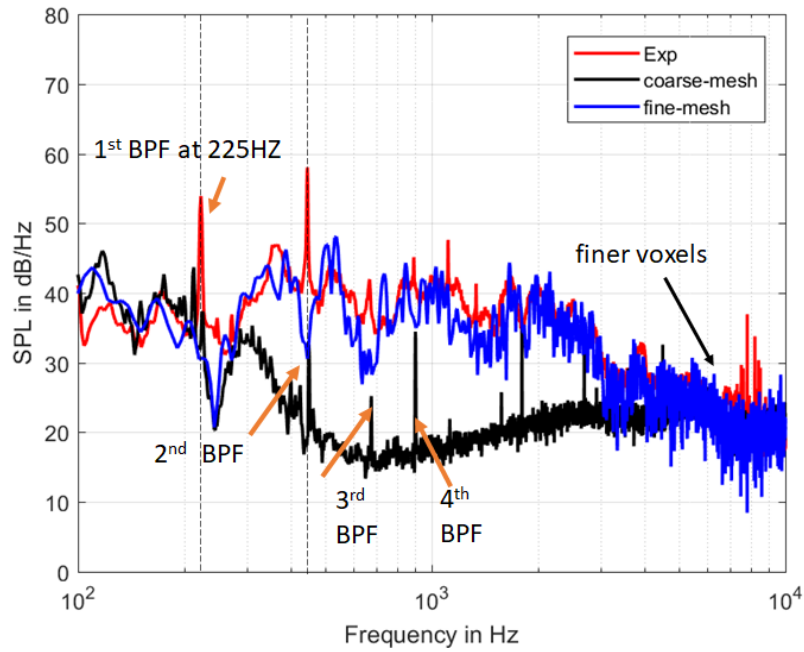


Figure 6.1 Comparison of noise spectra of FS fan for coarse and fine mesh

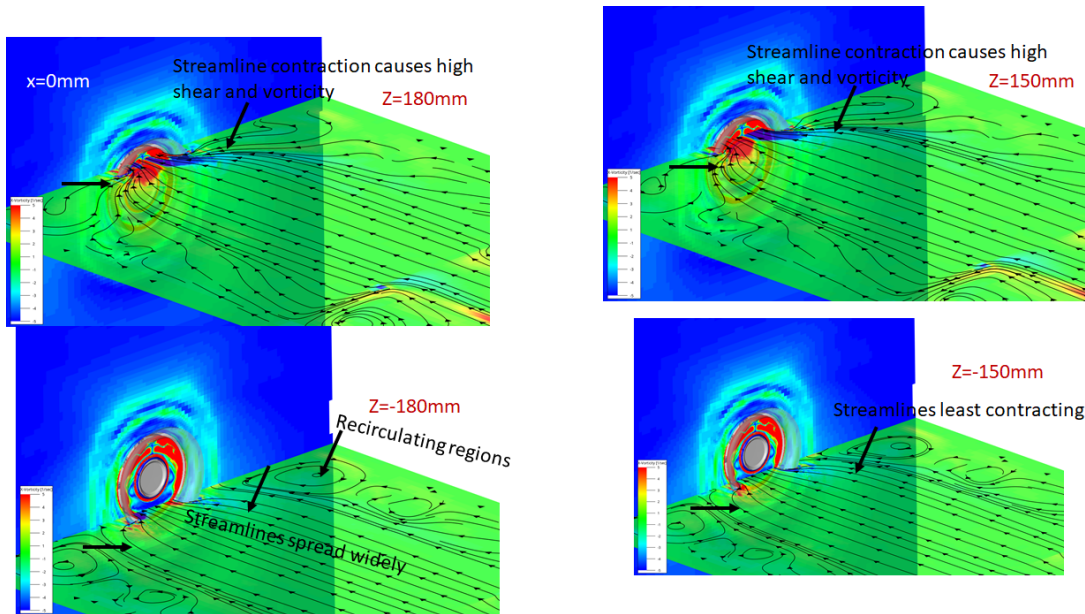


Figure 6.2 Contours of x -vorticity varying from $(-5,5)$ and projected streamlines showcasing flow field generated before the fan

The z plane height is varied from -180 mm to $+180$ mm i.e. along the duct diameter and the streamlines are projected on those planes. Clearly, we see that the streamlines are not identically distributed along the diameter. Moreover, the recirculating regions are dominantly present towards the floor from planes at -150 mm to -180 mm. Based on the

coarse case knowledge, the fine case is to be simulated for more than 110 fan revolutions to see a peak in the spectra. It requires a minimum of 4 s to develop inflow distortion inside the plenum. Then it interacts with fan blades to produce a tonal peak. Therefore, it is confirmed that the experimental set up is causing inflow distortion and it results in tonal noise and the possibility of other sources of tonal noise, i.e., rotor-stator wake interaction, is omitted since the stator is present downstream of the fan located at 500 mm from the fan center. As our focus is to study the effect of sweep on broadband noise and sub-harmonic noise. We didn't simulate it further.

The Fig. 6.3 shows the predicted noise spectrum of the unswept fan (PF-US) where PF in the legend stands for Powerflow. It is compared with experiment (EXP-US) and the previous simulation by Schoder *et al.* [96] (FWH and PCWE). Altogether, LBM showcased a decent noise prediction tool by capturing all the features of noise spectra. In Schoder *et al.* study, the acoustics is computed with two hybrid methods i.e., one with the help of FWH analogy by considering free-field Green's function and the other by solving PCWE (perturbed convective wave equation) in the time domain. The possible reasons for the observed differences are either that their signal length isn't sufficient to detain the low frequency resolution or that their inlet simplification influences the low-frequency humps. Interestingly, they also observed the two other distinct humps at 320 Hz and 480 Hz containing maximum power compared to whole spectra. Moreover, high frequency broadband noise is accurately predicted over the whole frequency range, with a slight under prediction beyond 2000 Hz in their study. The noise spectra from LBM simulations overlap test noise spectra overall frequency range, capturing low frequency humps from 1st to 4th peaks and high frequency broadband noise marked in Fig. 6.3 (d) for all microphones except slight deviation of peak frequencies. The first and seventh microphones show lower broadband noise starting from 600 Hz up to 3 kHz but above that they predict slightly higher amplitude. This behavior can be linked either to the directivity patterns or to the reflections caused by the sidewalls of the plenum. The LBM simulation handles inside plenum reflections by providing high viscosity porous layer lining to damp all the acoustics waves arriving towards it. The experiments are conducted in a non-anechoic chamber but the alternative arrangements are done to absorb acoustic reflection by covering plenum walls with an acoustic damping material. Nevertheless, the microphones from second to sixth are placed away from plenum walls satisfactorily correlate over all frequency ranges except slight deviation in subharmonic peaks frequency. The all microphones plot from LBM in Fig. 6.3 (h) shows the presence of directivity from low to high frequency. Thus, directivity plots are studied in Fig. 6.4. The directivity pattern is assessed by dividing noise spectra in five different regions as marked in Fig. 6.3

(d). The peaks 1, 2 3, and 4 are calculated by taking maximum values in specific frequency bands i.e. 100 to 150 Hz, 150 to 200 Hz, 300 to 400 Hz and 400 to 500 Hz respectively. The high frequency broadband noise is summed from 1 kHz to 10 kHz and overall SPL is calculated by considering whole spectra i.e. from 100 Hz to 10 kHz. In addition, the size of markers is scaled by the amplitudes to offer better readability. Peaks 1 and 2 show almost similar behavior in the case of experiment and LBM simulation but PCWE failed to capture them. On the contrary, FWH predictions are closer to experiments. LBM matches with the test for peak 3 at the center and near wall microphones but other microphones exhibit lower levels. Comparatively, FWH and PCWE display lower levels than test for all microphones. On the other hand, FWH and PCWE closely match with the test for peak 4 while LBM reveals scattered behavior and closely matches the amplitude at mic 2 and mic 6 but deviated almost by ~ 7 dB everywhere else. Regardless of these differences, overall high frequency noise in Fig. 6.4 (e) closely matches all microphones except the ones located near the wall. The same is true for overall SPL prediction in Fig. 6.4 (f). Notably, the shape of both plots uncovers the dipole nature of the noise source. The following section is dedicated to investigating noise sources associated with these specific regions but before that similar comparison is performed for FS and BS in the following discussion.

Similar satisfactory predictions are achieved for the FS and BS fans as shown in Fig. 6.5 and 6.7, respectively. Similar deviations like the US for first and seventh microphones are noticed. The directivity plot for FS in Fig. 6.10 indicates a good match for peaks 1 and 2 from 0° to 60° and later the trend is altered. Peaks 3 and 4 agree with the prediction for the central microphone while others show some deviations within 5 dB. The integrated high frequency noise and overall SPL match the trend for all microphones. BS also follows similar behavior as observed in Fig. 6.8 except for low frequency. The peak 1 and 2 show lower amplitude than the experiment for all microphones. Despite these differences, the overall behavior of noise spectra validates convincingly with experimental observation for all fans. In order to compare all three fans, the noise spectra from LBM simulation is compared in Fig. 6.9. At low frequency (peaks 1 and 2) BS produces higher noise than FS and US. US and FS have similar mid frequency peak 3 sound pressure levels while the US dominates peak 4 levels. The high frequency broadband noise appears to be similar for all three fans. However, when the high frequency noise is summed and plotted in Fig. 6.10, it shows that the US has slightly higher noise levels than the other two fans while BS and FS show almost similar levels. The OASPL plot ranks these fans based on total noise produced where US stands out to be the noisiest fan followed by BS and conversely, FS is noticed to be the quietest among all three fans. Yet BS emits the highest noise at low

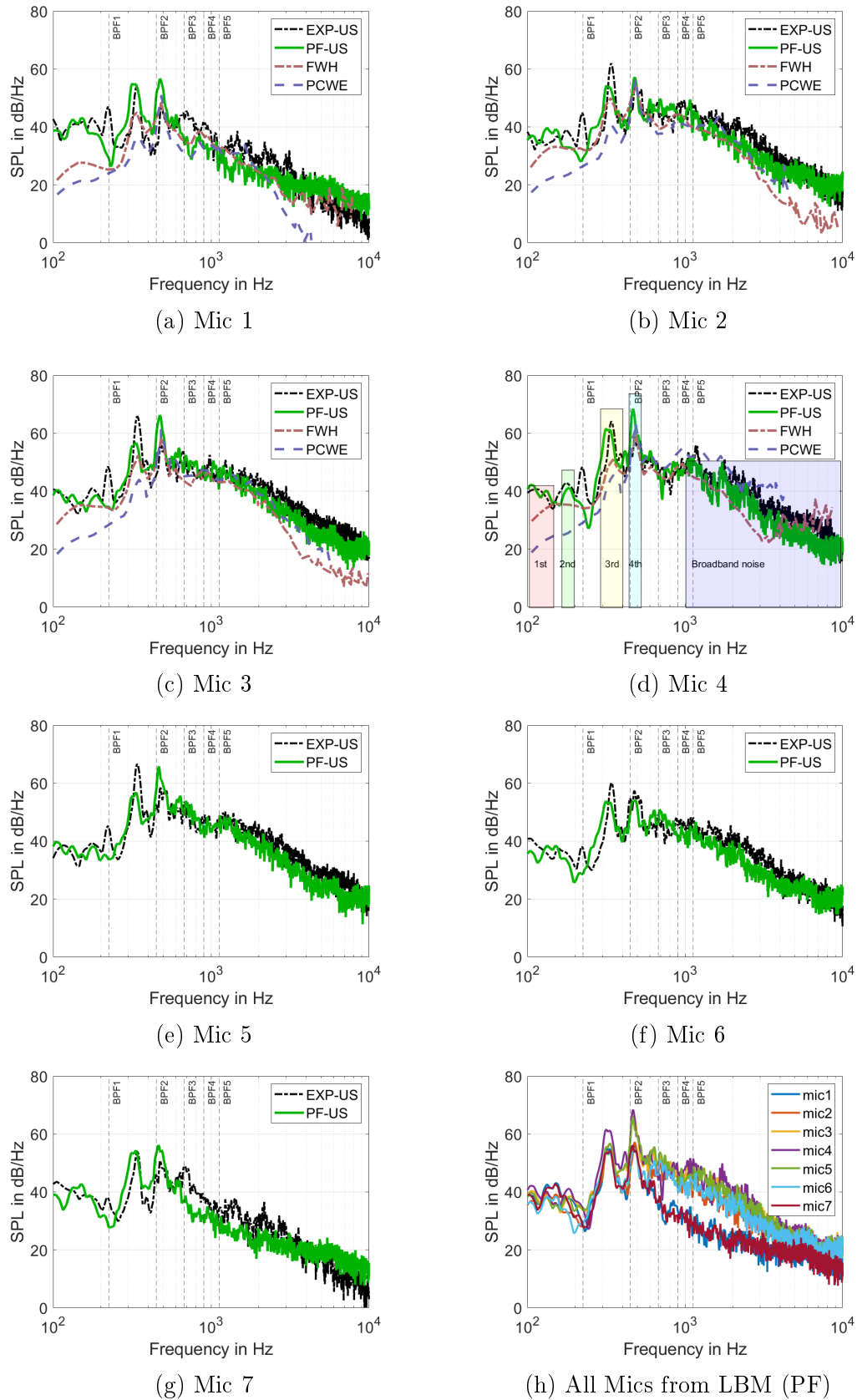
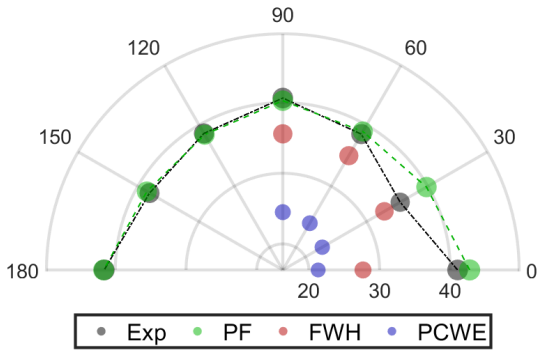
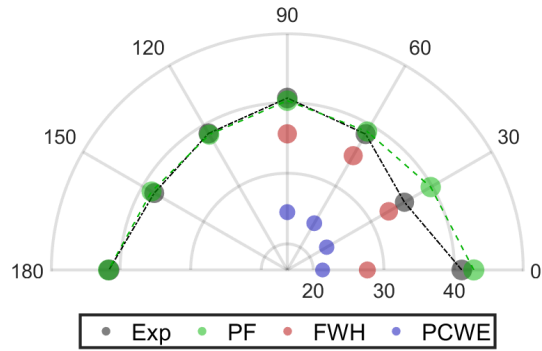


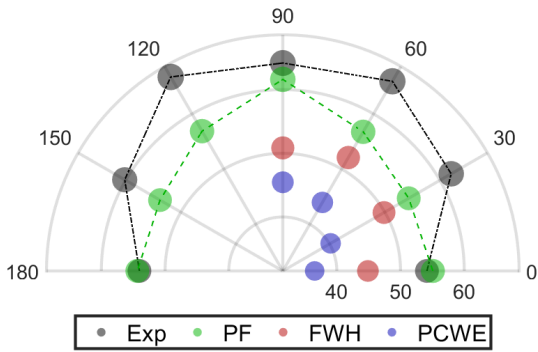
Figure 6.3 Comparison of sound pressure level at different microphones for US



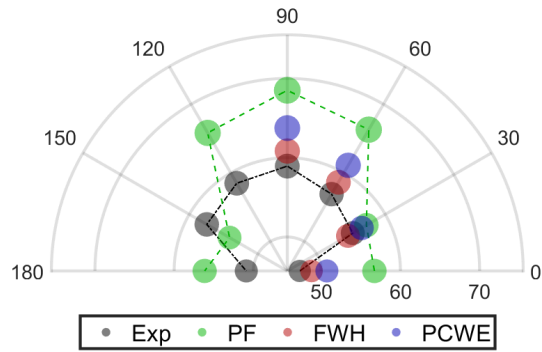
(a) Peak 1



(b) Peak 2



(c) Peak 3



(d) Peak 4

(e) High frequency SPL calculated summing over 1 kHz to 10 kHz

(f) OASPL calculated over 100 Hz to 10 kHz frequency range

Figure 6.4 Directivity plot for US

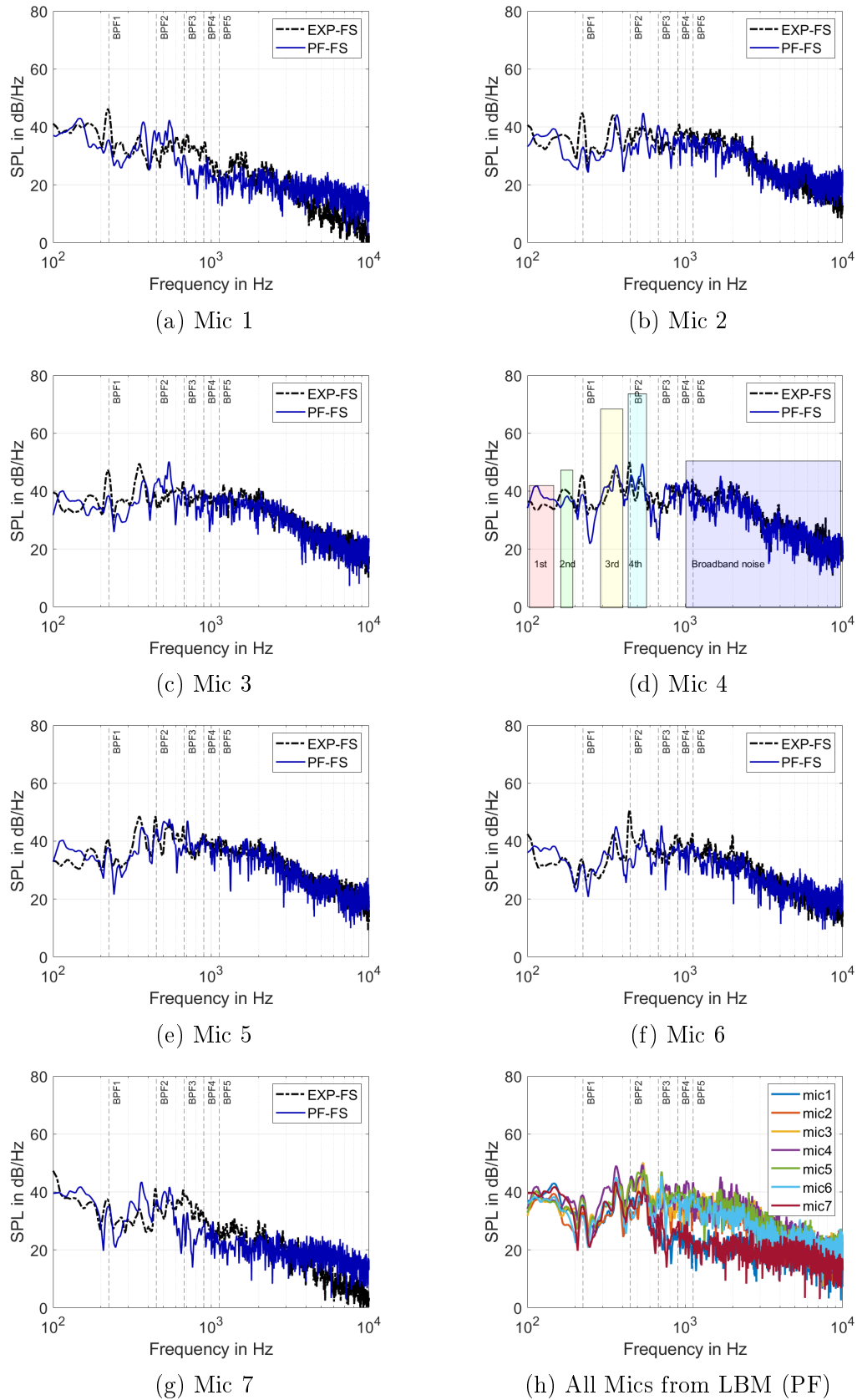
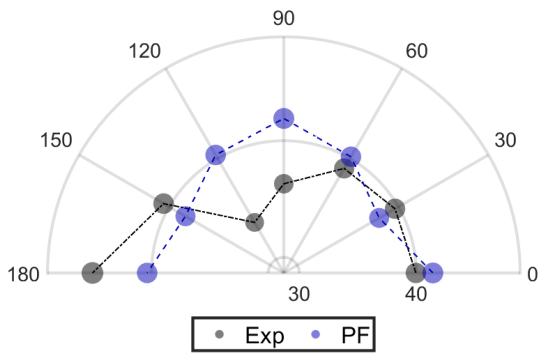
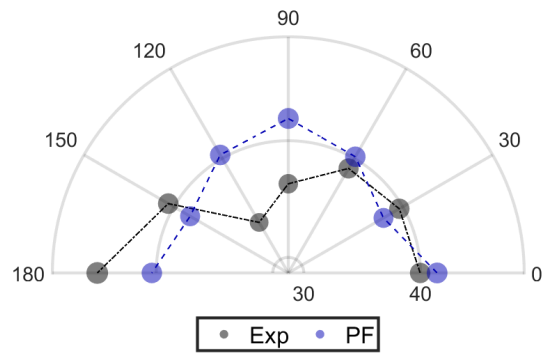


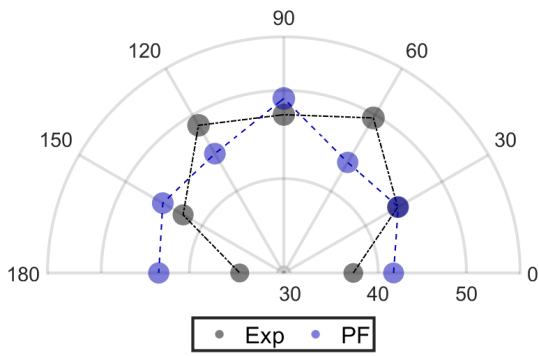
Figure 6.5 Comparison of sound pressure level at different microphones for FS



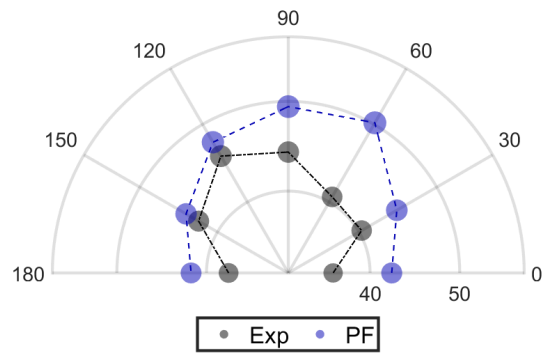
(a) Peak 1



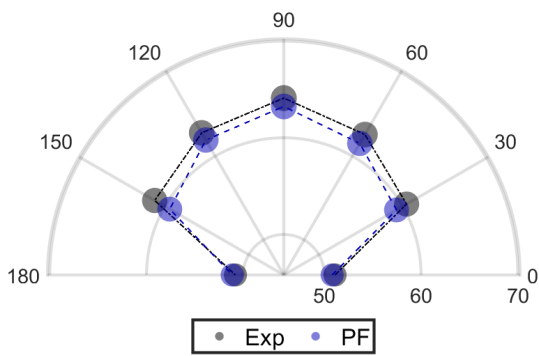
(b) Peak 2



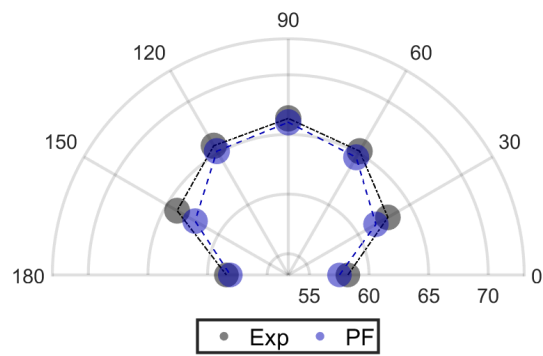
(c) Peak 3



(d) Peak 4



(e) High frequency SPL calculated summing over 1 kHz to 10 kHz



(f) OASPL calculated over 100 Hz to 10 kHz frequency range

Figure 6.6 Directivity plot for FS

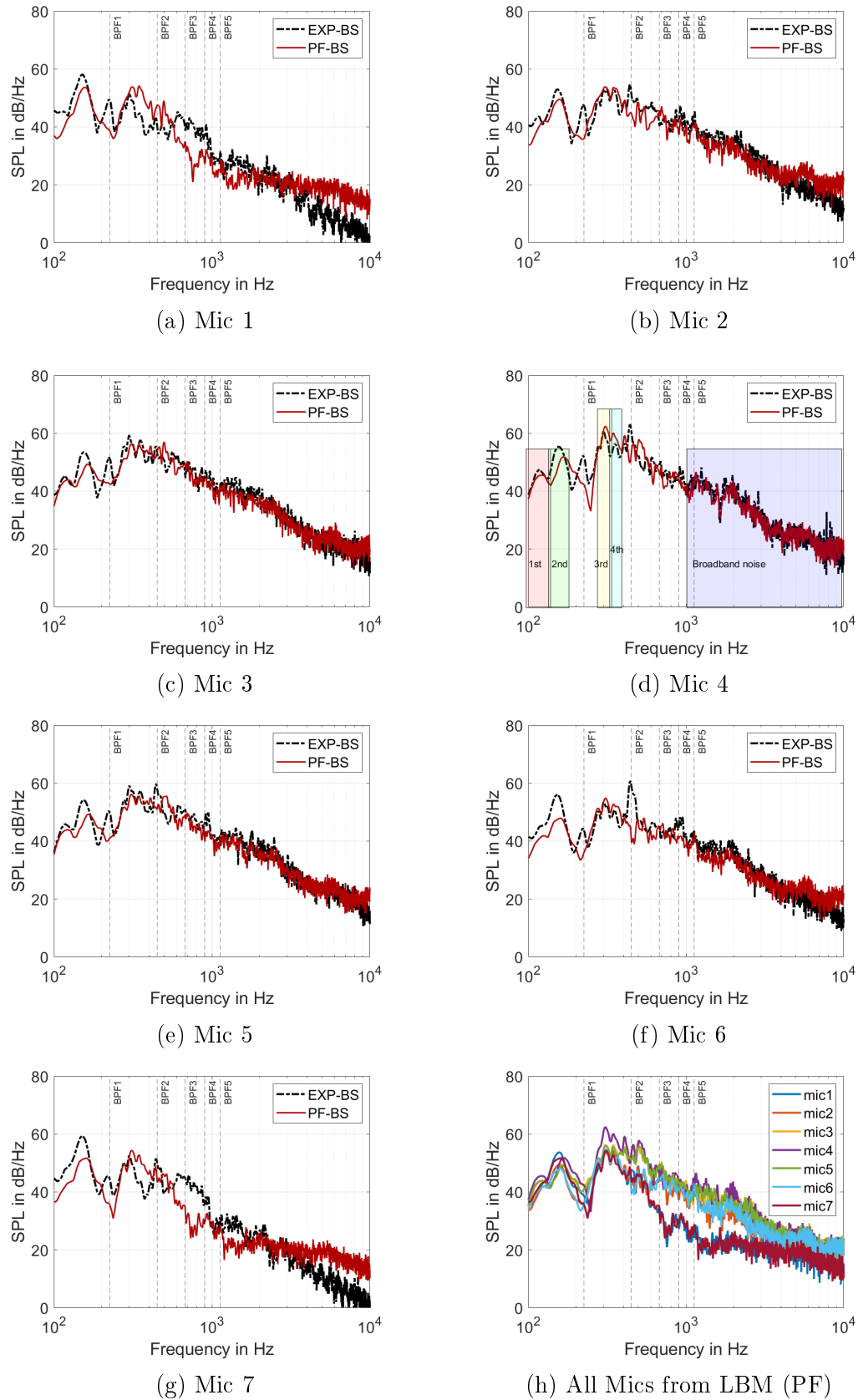
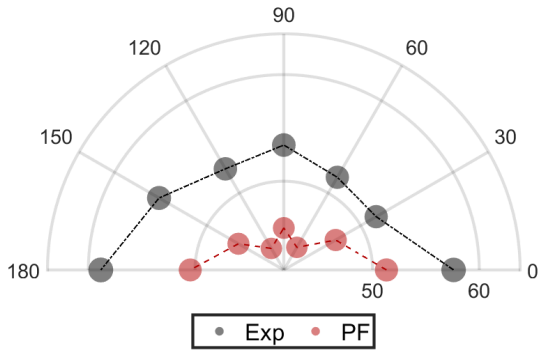
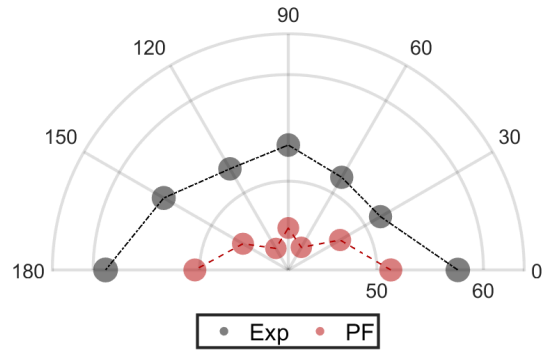


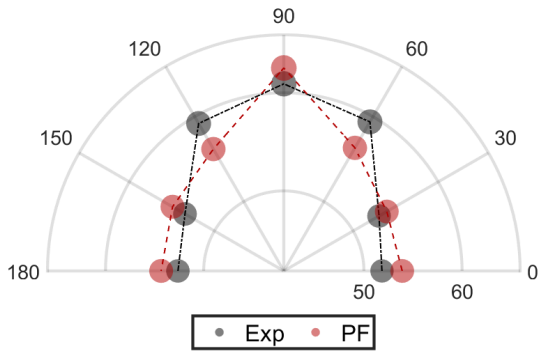
Figure 6.7 Comparison of sound pressure level at different microphones for BS



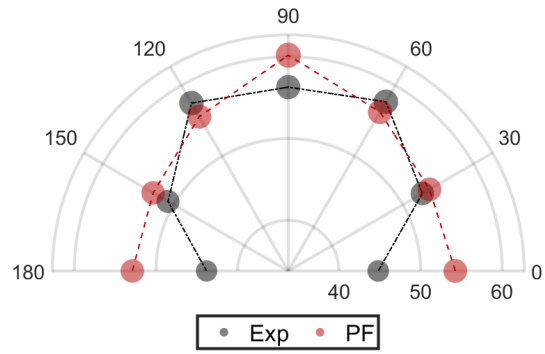
(a) Peak 1



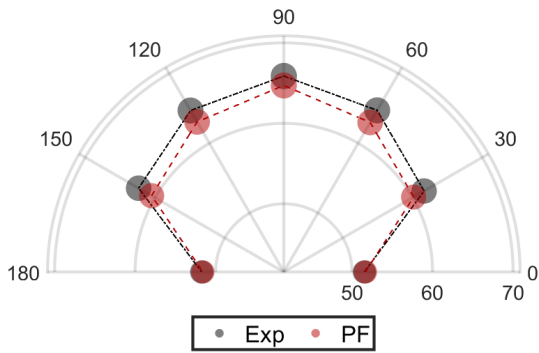
(b) Peak 2



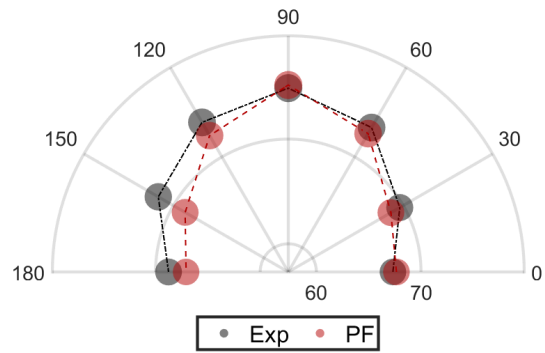
(c) Peak 3



(d) Peak 4



(e) High frequency SPL calculated summing over 1 kHz to 10 kHz



(f) OASPL calculated over 100 Hz to 10 kHz frequency range

Figure 6.8 Directivity plot for BS

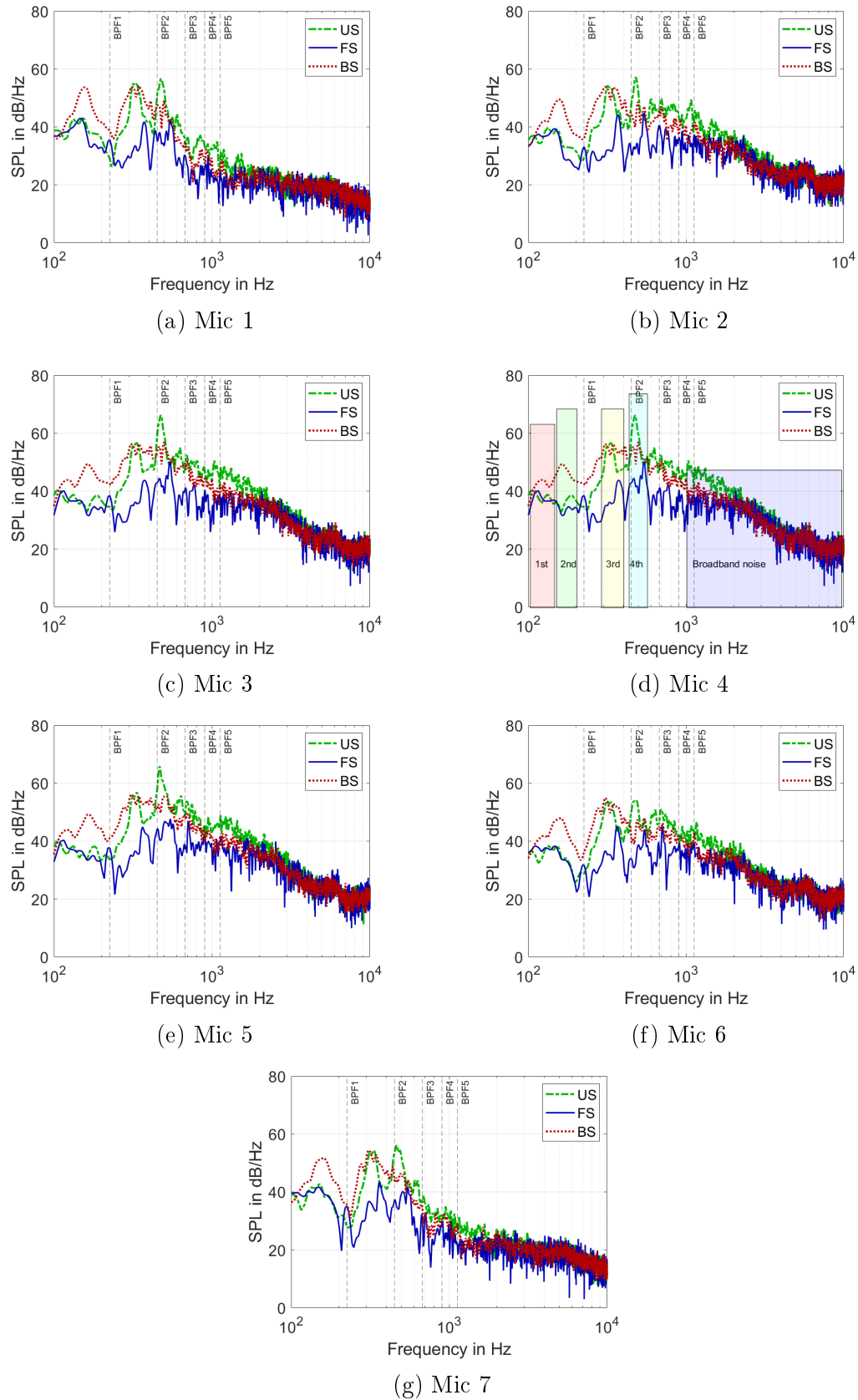
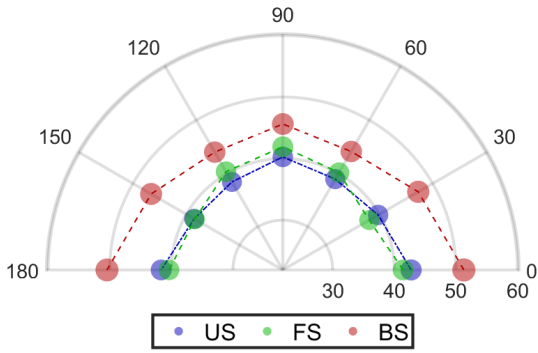
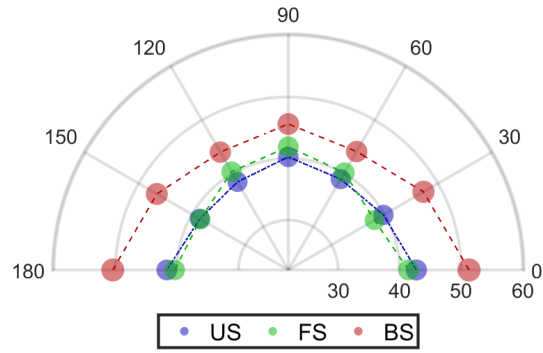


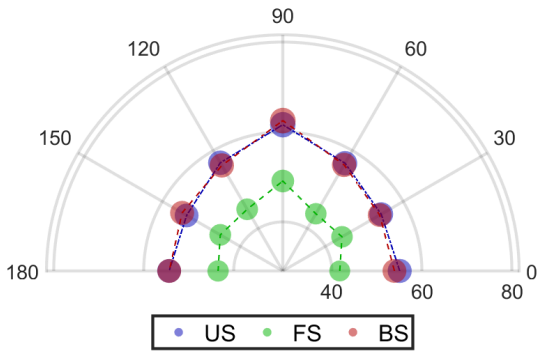
Figure 6.9 Comparison of noise spectra at different microphones for all fans



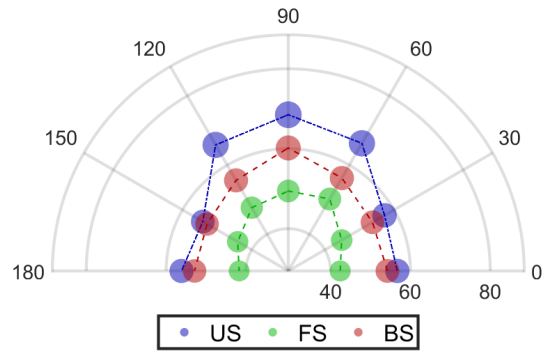
(a) Peak 1



(b) Peak 2



(c) Peak 3



(d) Peak 4

(e) High frequency SPL calculated summing over 1 kHz to 10 kHz
 (f) OASPL calculated over 100 Hz to 10 kHz frequency range

Figure 6.10 Directivity plot for compared for fans from LBM

frequency peaks but follows the US for peak 3. As observed in noise spectra comparison, US exceeds the sound level at peak 4. Although the peaks are evaluated at the highest amplitude in the indicated frequency bands in all directivity plots, the peak frequency differs slightly for each fan. The following table 6.1 compares the frequency respective to the peaks observed for the central microphone. The 90° microphone is selected for the comparison because it exhibited excellent correlation for all fans. It is observed that peaks in noise spectra are shifted in LBM simulation than in the experiment. These subharmonic frequencies can be related to the tip vortex interaction noise as observed and studied most recently by Lallier et al and Magne et al. [53, 63] respectively. If these peak frequencies are related to tip flow, then the deviation in peak frequency may be due to different tip gap flow behavior in LBM than experiment as observed from LDA plots of axial velocity in Fig. 5.31.

| Peaks | US | | BS | | FS | |
|-------|-----|-----|-----|-----|-----|-----|
| | EXP | PF | EXP | PF | EXP | PF |
| 1 | 117 | 133 | 146 | 121 | 105 | 115 |
| 2 | 175 | 185 | 152 | 167 | 170 | 179 |
| 3 | 340 | 318 | 298 | 306 | 351 | 364 |
| 4 | 480 | 468 | 351 | 347 | 515 | 537 |

Table 6.1 Peak frequency comparison

In order to investigate sources of these peak frequency and broadband noise, the data is processed using multiple techniques in the following section.

6.2 Noise sources identification

Although, LBM can predict noise levels appropriately, the identification of noise sources stays important. A designer can optimize a blade design based on the location and causes of noise source. Therefore, we investigated location by plotting wall pressure fluctuation in different frequency bands, studied time derivative of density fluctuations and used some other empirical and analytical modelling technique to gain knowledge of noise sources in this section.

6.2.1 dB maps of wall-pressure fluctuations

To assess the different contributions in the above noise spectra that match the experiment well, we first look at the wall-pressure fluctuations, which are the noise sources in the acoustic analogy shown in chapter 2. The recorded wall pressure is plotted in the frequency domain using bandpass filtered power spectral density. The contour plots for central

frequency varying from 150 Hz to 5 kHz are shown in Figs. 6.11 to 6.13. The plots proclaim unanimously that most of the noise radiation is coming from the tip region. At low frequency (100-200 Hz) BS appears to produce stronger pressure fluctuations spread along the chord near the tip (front and rear) among all three fans while FS has localized interactions at LE near the tip but also intense fluctuations are traced near the hub. These sources are particularly linked to a well-built corner vortex observed only for FS in Fig. 5.42 and it stays dominant almost until 1 kHz. From 300-500 Hz, the US tip starts showing a larger span occupied with strong pressure fluctuations than before. These frequencies correspond to the third and fourth peaks distinguished in Fig. 6.9. They behold almost similar levels of noise amplitude like BS. The tip region and part of the blade span seem to contribute to the noise spectra below 500 Hz but with increasing frequency, the span contribution reduces, and dominant sources near the tip stay intact, tracing the importance of TSV and TLV. Note that the strength of surface pressure fluctuations is indicative and doesn't represent the level in the noise spectra because they include not only acoustics but aerodynamic excitations also. Hence, we must be careful with this judgment because not all that is observed in PSD plots are propagating to the far field. Therefore, other visualization techniques such as dilatation maps are investigated below.

6.2.2 Dilatation fields

Acoustic wave propagation in the far-field where the hydrodynamic contribution is almost nil can be seen with the help of the time derivative of fluctuating density field equivalent to the dilatation field [117]. The latter field is filtered to visualize acoustics waves in different frequencies and visualized at $y=0$ plane as shown in Fig. 6.14 for all three fans. Mainly, FS show inclined wave propagations on the suction side but contrarily, BS produces inclined wavefronts on the pressure side. Their inclinations seem to be parallel to the LE and influenced by the dihedral angle —axial movement of the LE. FS has a positive dihedral angle causing LE to move towards the suction side. However, BS is designed with a negative dihedral angle causing LE to shift towards the pressure side but in absence of any dihedral angle, the symmetric wavefronts on either side are observed for the US. Despite different inclinations patterns, the direction of traveling wavefronts conveys that their dominant sources are present near the tip region for all fans. These observations are coherent with the high frequency pressure dB maps in Fig. 6.13. Moreover, FS indicates an extra source coming from the hub region again affirming the contributions of the corner vortex as observed in Fig. 6.12. The dilation field visualization is limited to a higher frequency because wavelength at a lower frequency is bigger than duct diameter and doesn't help to visualize propagation pattern. Despite the limitations, it is clear that

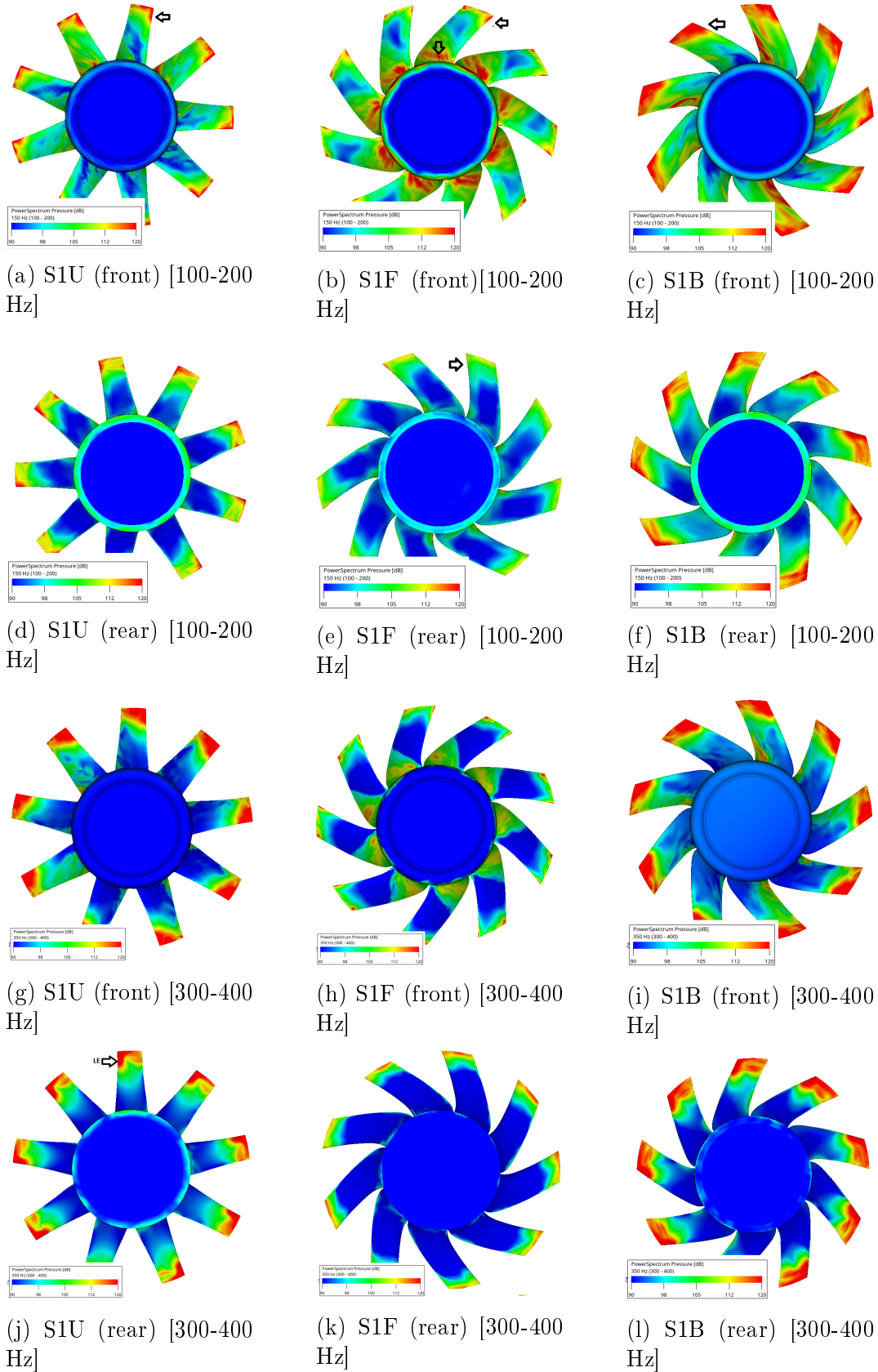


Figure 6.11 Contours of PSD of filtered wall pressure top -front view, bottom-rear view

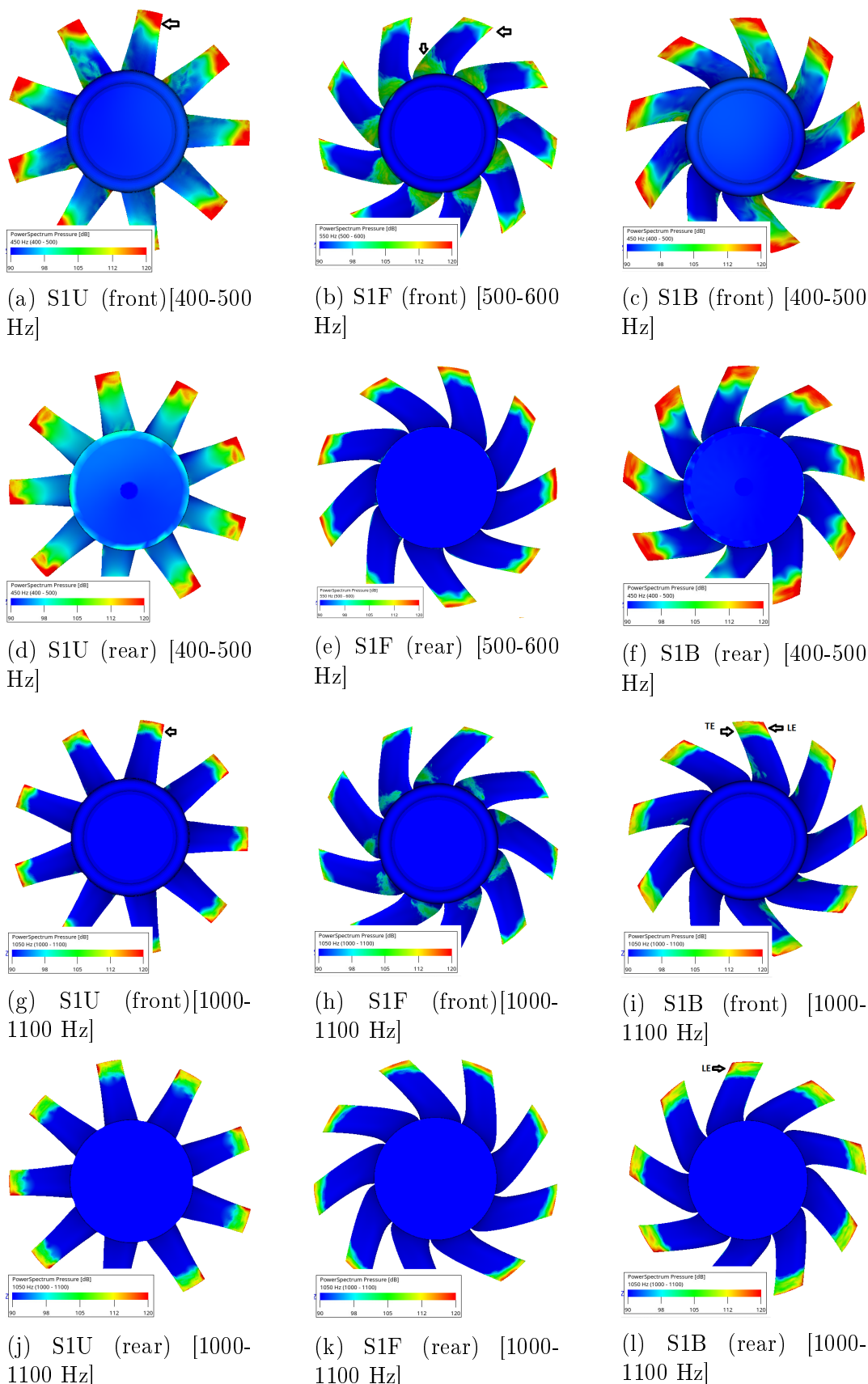


Figure 6.12 Contours of PSD of filtered wall pressure top -front view, bottom-rear view

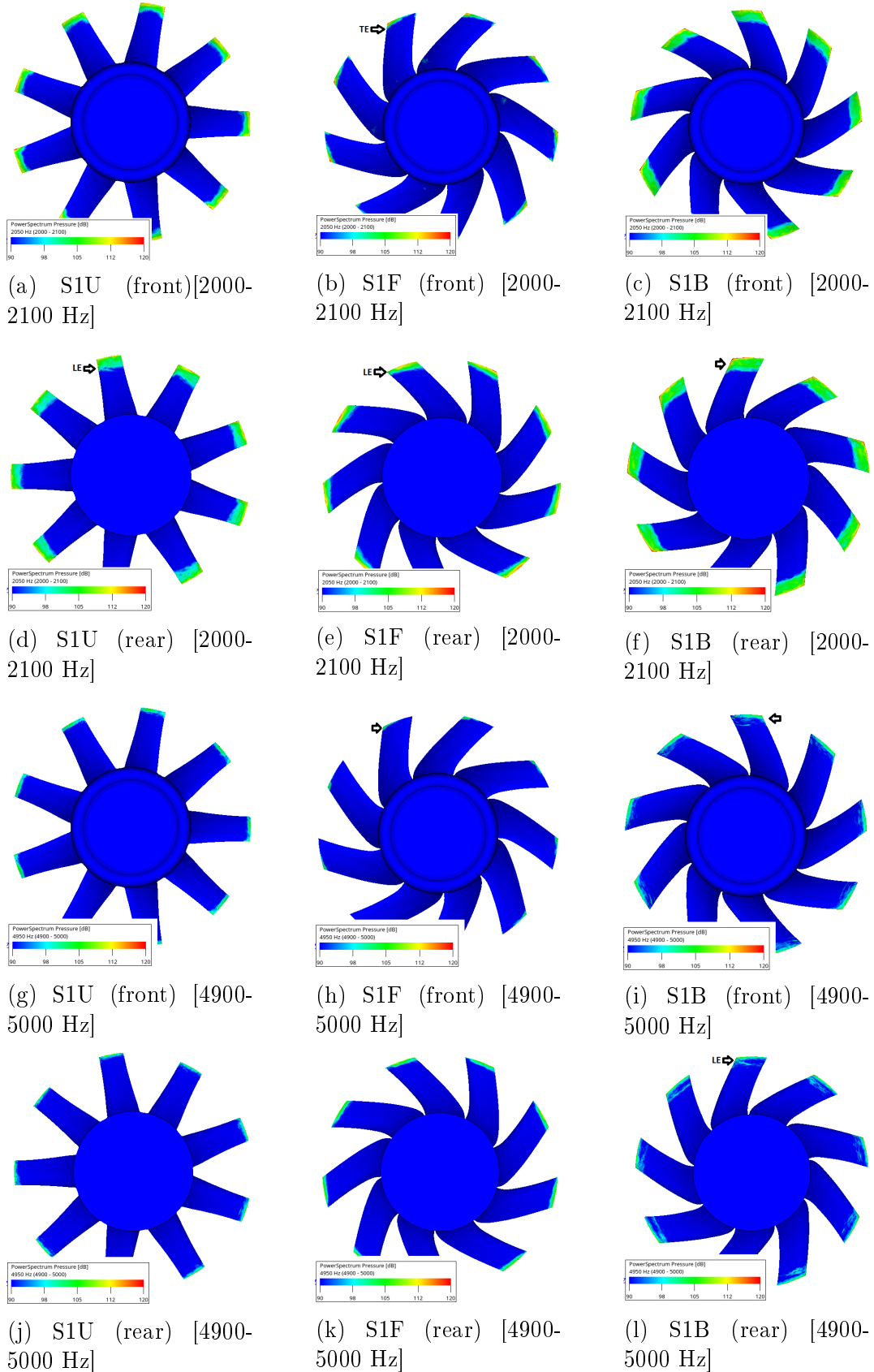


Figure 6.13 Contours of PSD of filtered wall pressure top -front view, bottom-rear view

tip is the dominant source for all fans. Hence, other investigation methods are studied to learn more about near tip noise sources in the next section.

6.2.3 Tip modal structure

In all previous sections, we have seen the importance of the tip region in noise generation. As seen in the wall-pressure PSD, the tip seems to dominate in most configurations. To confirm this, the flow field is also filtered using pressure and their contours are visualized in the frequency domain as shown in Figs. 6.15 and 6.16 by using iso-radial cut section at 99.79% of the span for two frequency bands centred around 1000 and 2000 Hz respectively. They exemplify modes as was found by Lallier-Daniels [53] in the tip region of various low-speed fans. These PSD contours inform how these modes are distributed in a blade passage and their propagation pattern. The orientation of mode suggests that modes are originating from TLV and TSV separately. These modes advance with mean speeds and encounter a collision with an adjacent blade. Quickly, their mean speed is assessed by calculating their wavelength, $\lambda = \frac{2\pi r}{N_b N_m}$ where, r is the radius, N_b is the number of blades and N_m is the number of modes counted manually from the radial cut section plots. These modes advance with a mean relative speed, $U_m = f\lambda$ and collide with the adjacent blade at a frequency, $f_i = f_{bpf} \frac{U_m}{\Omega}$ where $f_{bpf} = N_b \frac{N}{60}$ is the blade pass frequency, N is the fan RPM and Ω is the angular speed at a given radius. These modes travel with a speed of 20 m/s, 21.5 m/s and 31 m/s calculated for BS, US and FS respectively. They interact with a frequency of 117 Hz, 125 Hz and 181 Hz respectively. These frequencies are found closer to the first peak of BS and US and the second peak of FS given in Table 6.1. Although this method helps in identifying the approximate sub-harmonic peak frequencies in the noise spectra, the method doesn't account for the 3D nature of the source and embark difficulties in counting those obscured modes. Therefore, the speed of TLV and TSV are identified by using the distribution of velocity observed in the isosurface of λ_2 which is already demonstrated by Magne et al. [63] and Piellard *et al.* [81] in their study.

The isosurface of λ_2 calculated with instantaneous flow field is shown in Fig. 6.17. The isosurface is clipped such that it only represents tip vortex structures. US and BS show almost similar behavior of TLV, TSV and average speed of tip wake except that BS has additional relatively slow-moving structures in front of LE. Contrarily, FS has slow-moving TLV and reversed TSV behavior. Near TE it travels faster than near LE and wake speed is relatively less than BS. Their distribution of relative velocity is studied with the histogram as displayed in Fig. 6.18 and fitted with the probability distribution function available in SciPy libraries. The US and BS tip structures are traveling with similar mean

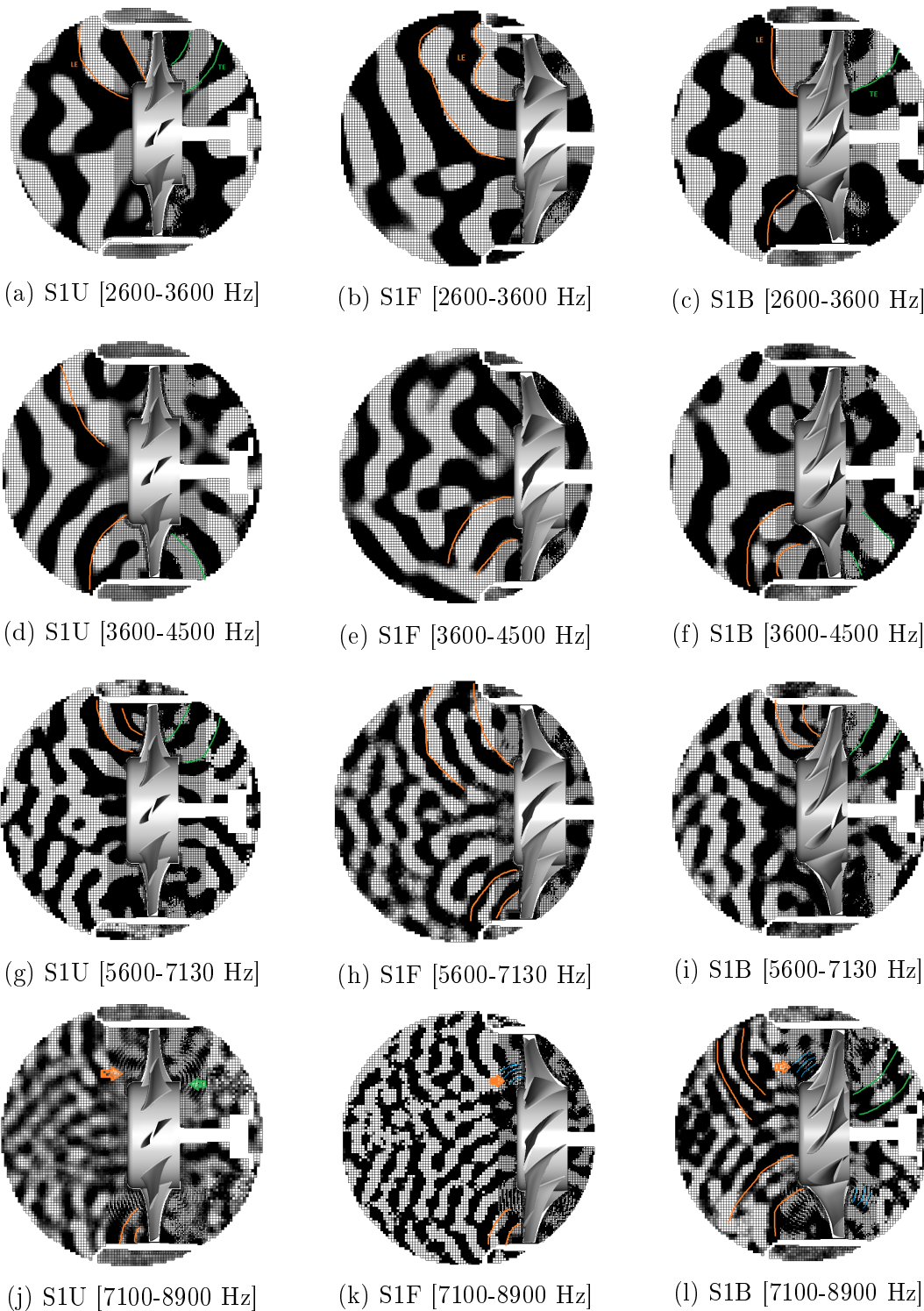


Figure 6.14 Band pass filtered time derivative of density fluctuations (-0.001 to $0.001 \text{ Kg/m}^3\text{s}$)

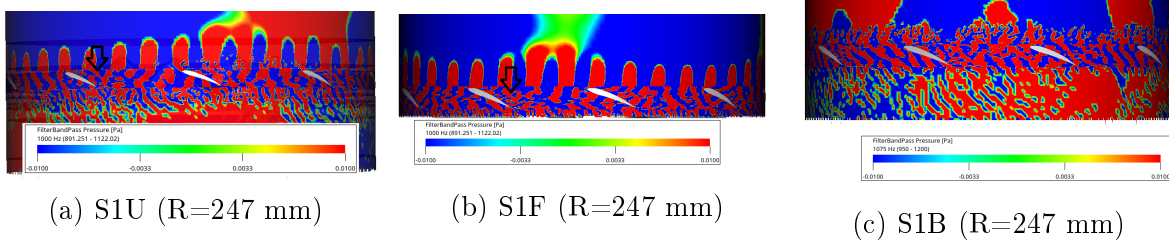


Figure 6.15 Contours of band pass filtered [900-1100 Hz] pressure fluctuations

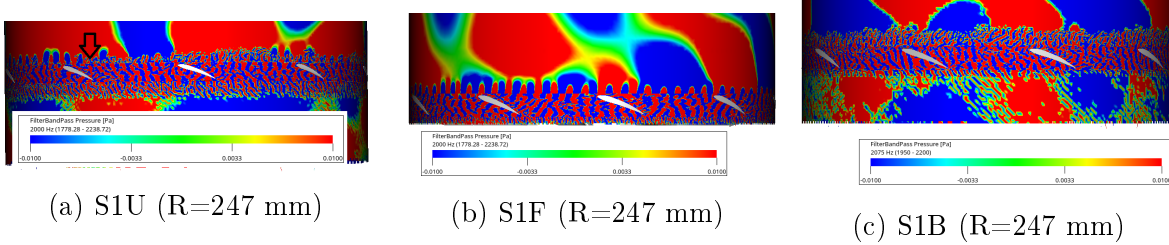
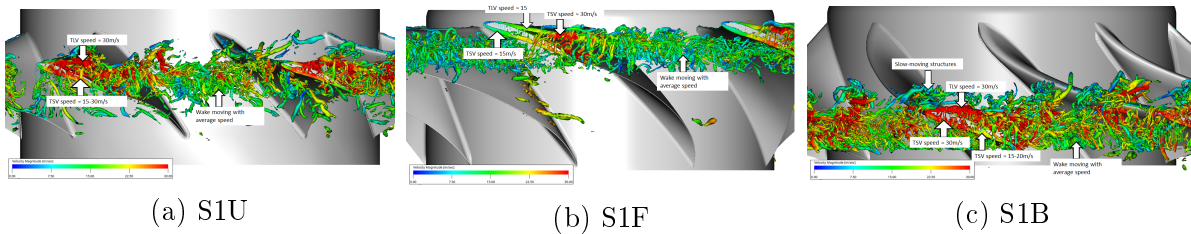


Figure 6.16 Contours of band pass filtered [1700-2300 Hz] pressure fluctuations

Figure 6.17 Isosurface of instantaneous $\lambda_2 = -2e7$ colored by relative velocity

velocity while for FS, the speed is comparatively slow. This confirms the above observation. Their interaction frequency calculated using the above formula indicate that the second harmonics of FS (171 Hz) become dominant while BS and US have a dominant peak at their first harmonic. The calculation is based on the collective speed of tip structures. However, it is possible that perturbations coming from TLV and TSV at different speeds are responsible for various peaks observed in Fig. 6.9 and mentioned in Table 6.1. Only for FS, second and third harmonics of 171 Hz match closely with third and fourth peaks listed in the Table 6.1. Like Kromer et al. [51] tried to relate the subharmonic humps from casing wall pressure PSD to that in the noise spectra. It reveals some interesting details —

1. FS - The 5th probe in Fig. 5.70 placed at the suction side (before LE) indicates two peaks at 370 Hz and 550 Hz that corresponds to the third and fourth peak in the spectra but the low frequency at 138 Hz isn't represented as a peak but it is part of the hump in the noise spectra. The 6th probe on the pressure side also shows similar frequency peaks but with slightly lower amplitude

2. US - The 7th probe in Fig. 5.74 on the suction side identifies three different peaks. The peak at 175Hz closely matches the second peak in the noise spectra while the mean of similar strength peaks (286 Hz, 350 Hz) agree with the third peak in the noise spectra ≈ 318 Hz. The 8th probe on the pressure side shows two dominant peaks at 120 Hz and 185 Hz that corresponds to the 1st and 2nd peak in noise spectra. Interestingly, 120 Hz matches the frequency calculated using the histogram method.
3. BS - The suction side 10th probe in Fig. 5.72 matches shows the peak at 120 Hz which is similar to the first peak of noise spectra and the frequency identified with the histogram method. The 11th probe on the suction side traces peaks at 166 Hz and 342 Hz. These frequencies closely agree with the second and third peaks of the spectra.

Moreover, PSD plots of FS also exemplify the importance of corner vortex at low frequency. Therefore, a similar method is used to calculate their interaction frequency from relative velocity distribution.

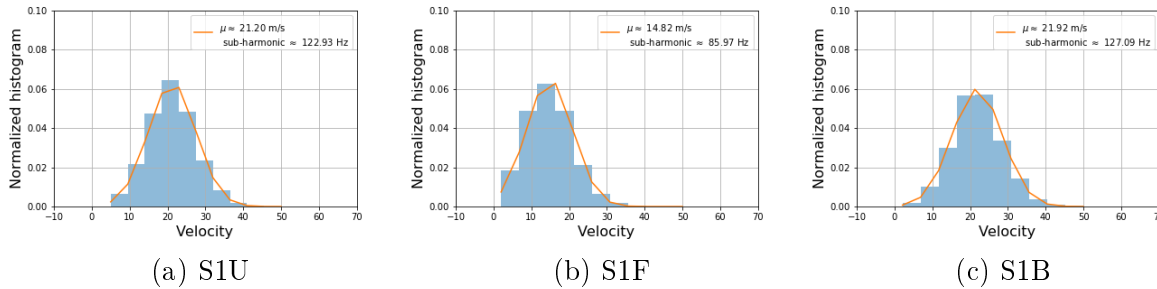


Figure 6.18 Histogram of relative velocity take from isosurface of λ_2

The isosurface of λ_2 plotted in Fig. 6.19 illustrates the spread of vortical structures. A larger chord near the hub is occupied by these structures but as the radius increases, the structures are concentrated towards TE. The calculated f_{int} from histogram is ~ 118 Hz. This frequency is closer to the first peak mentioned in Table 6.1. This analysis tells us that if the mean speed of these near tip structures is known in advance, one can locate their frequency in the noise spectra. Therefore, a similar method is applied to steady state RANS simulation. Only difference is that isosurface λ_2 is plotted using mean flow field at a threshold value of $-2e5$ as given in Fig. 6.20.

RANS results are able to capture BS slow-moving (low frequency) and FS fast-moving (higher frequency) structures and also agree well with the values listed in Table 6.1. Like LBM, RANS simulation for FS quantifies the mean speed structures such that their first harmonic matches with the second peak in the noise spectra of Fig. 6.5. The corner vortex

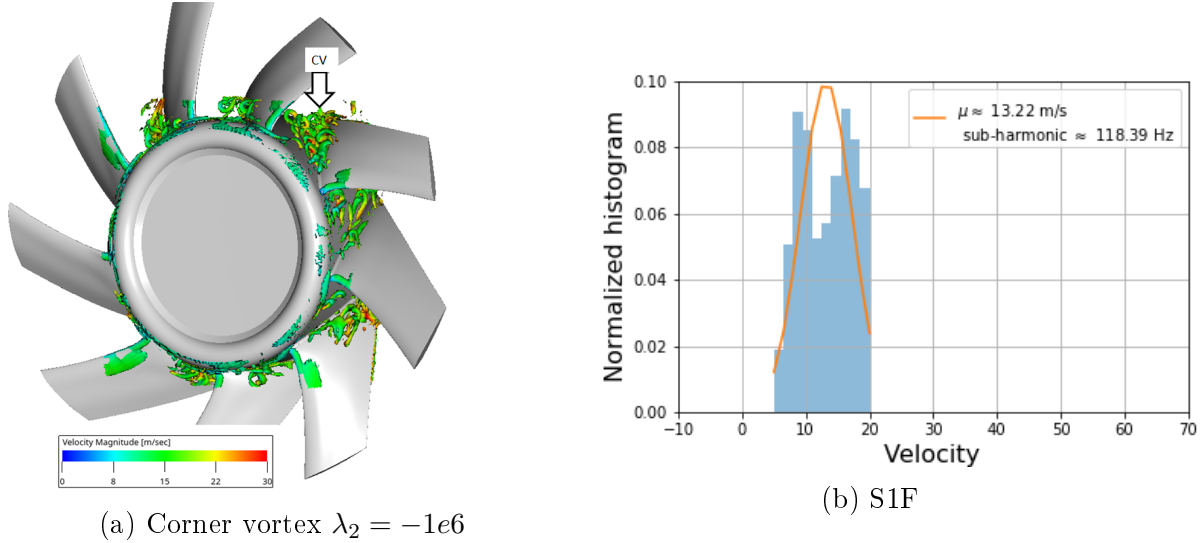
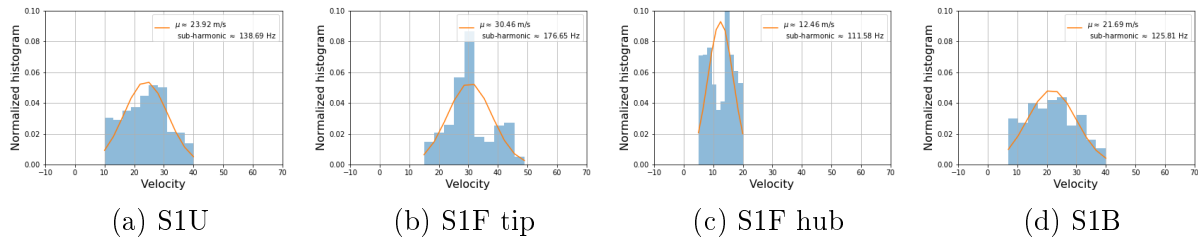


Figure 6.19 Interaction frequency calculated for CV of S1F

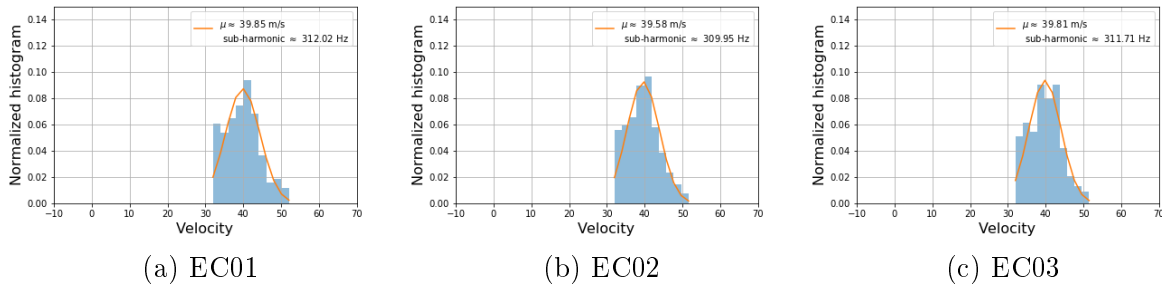
Figure 6.20 Histogram of isosurface of λ_2 from RANS

histogram plot has a similar behaviour as of LBM, pointing f_{int} is ≈ 111 Hz. This confirms that the first peak in the noise spectra is primarily coming from the corner vortex.

After gaining the confidence in f_{int} prediction method, it is also tested on RANS results for ring fans. In a similar fashion, histograms are plotted for the relative velocity from the clipped isosurface of λ_2 and fitted with the curve. Like ducted fans, a strong tip source is observed in PSD plots of EC01 studied by Lallier-Daniels [53] (see page 159). Tip contribution is traced from 225 Hz to 1200 Hz. The calculated frequency from below plotted distribution is ≈ 311 Hz which is in the ballpark of frequency marked with H1 in the Fig. 6.34.

6.2.4 Broadband noise prediction

The above analysis has supported finding noise sources related to subharmonic frequencies. From directivity plots, it is observed that high-frequency noise contributes significantly to overall noise levels. Therefore, it is also important to identify the contribution and location of such noise sources. The literature review stated that turbulence interactions

Figure 6.21 Histogram of relative velocity take from isosurface of λ_2

at the LE and boundary layer scattering near TE are primarily responsible for broadband noise generation. Although high fidelity solutions like LBM are accurate, the time and cost involved in such computations can be seen as prohibitive at the early stages of design. Therefore, a quick analytical is used to predict noise levels using steady RANS simulation. This tool helps study different noise sources and the distribution of these sources along the blade span (strip theory). Amiet's model extended for the sweep, already discussed in Chapter 3 has been used to study LE noise. The step-by-step process to calculate LE noise for swept blades is explained in Section 3.4. The blade is divided into ten equal strips, as mentioned in step 3. The sweep angle calculations explained in steps 2 and 3 of Fig. (3.2) are extracted from the blade geometry along the span and with respect to strip number as shown in Fig. 6.30a . The flow field data is extracted by placing an axial plane parallel to LE as demonstrated in Fig. 6.30b.

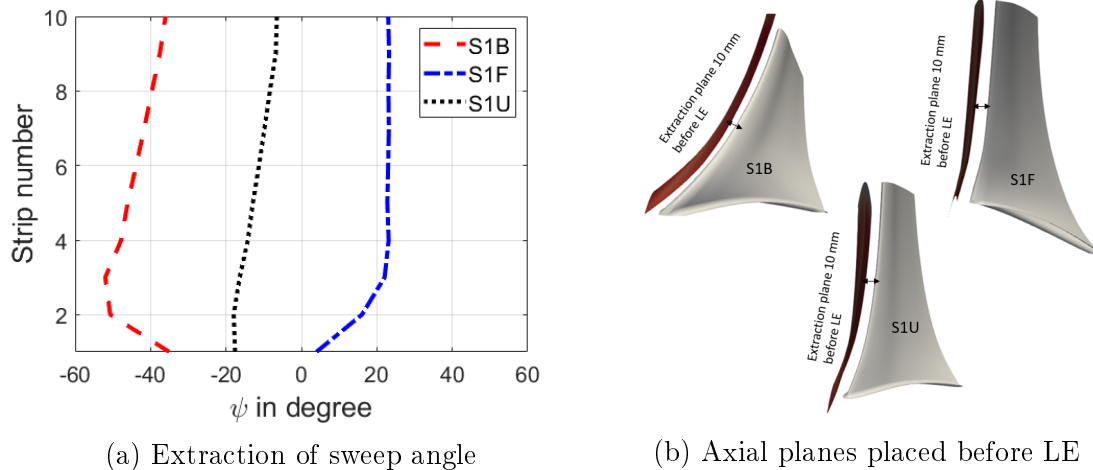


Figure 6.22 Sweep angle (left) and extraction planes (right) for ducted fans

As exhibited in our published study [26], the homogeneous isotropic turbulence spectrum given by Eq. (3.45) is constructed from the two-dimensional wavenumber spectrum of the velocity component normal to the chord using the von Kármán model. It is derived by

integrating the velocity spectrum over the spanwise wavenumber. The necessary input to the model like turbulent kinetic energy (k) and turbulent dissipation rate is extracted at the plane before LE as displayed in Fig. 6.30b from the steady RANS simulations of ducted fan and then, azimuthally averaged and plotted along the normalized radius as given in Fig. 6.23. The incoming turbulent fluctuations $\overline{u^2}$ and turbulent length scales are calculated as follows:

$$\overline{u^2} = \frac{2}{3}k \quad \text{and} \quad \Lambda_f = \frac{\sqrt{\pi} \Gamma(5/6)}{k_e \Gamma(1/3)} = D \frac{k^{3/2}}{\epsilon} \quad (6.1)$$

The most energetic scales k_e can be recovered from Λ_f using the above equation. The coefficient D varies with the Reynolds number. In this study, a high Reynolds asymptotic value from experimental database $D=0.43$ is used [82]. The axial velocity profiles extracted from the RANS are compared with dotted lines representing LDA data from experiments and their color corresponds to the respective blade. We see a small variation in the data because the LDA plane and extraction planes don't overlay exactly. The non-linear behavior above 90% of the span indicates the tip vortex presence as discussed in the previous chapter. Again TKE and Λ_f reveal the turbulent nature of the flow near the tip region than the remaining span. The relative velocity (w_r) plot indicates the speed with which these turbulent structures impact the LE. As observed in the previous section, the mean speed of near tip turbulence differs for the swept and unswept blades. The FS turbulent structures travel faster than the other two fans. Moreover, BS constructs thicker and highly turbulent structures moving slowly than US and FS.

The extracted parameters are fed to the model and calculated turbulence spectrum (Φ_{ww}) is plotted in Fig. 6.24 in dB. As discussed earlier, the top most strip (strip 10) near the tip region encounters maximum turbulent energy than the rest of the strips. US and FS contain the peak energy above 1 kHz but BS exhibit higher energy content in the low frequency region for the top strip. FS seems to interact with the lowest turbulent energy among all three fans. The far-field radiated sound power from each strip is calculated by using Eqn. 3.44 described in step 8 and compared in Fig. 6.24. The solid lines represent Amiet's model and lines with symbols mean Amiet's model extended for sweep effect in low speed fan. As expected, the US doesn't show any difference between the corrected and uncorrected model but BS exhibits an increase in power level by 2-3 dB due to correction. Nonetheless, FS has less than 1 dB difference over the frequency range. As speculated from turbulence distribution, the top strip seems to radiate the highest sound power for all fans. The strip09 also radiates along with strip10 but the frequency region dominance is observed to be altered in case of BS. In total, strip numbers from 8 to 10 generate maximum noise

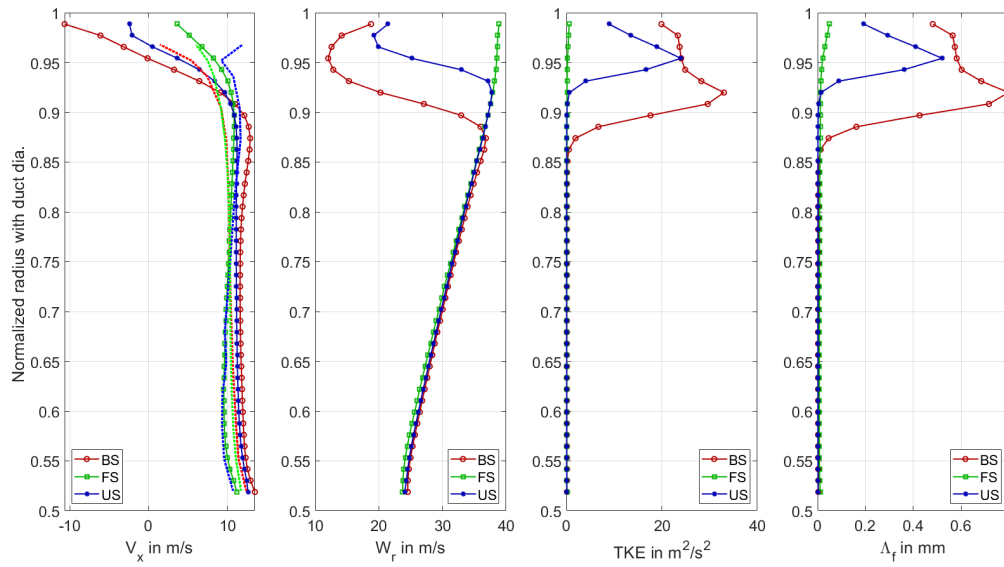


Figure 6.23 Parameters for Amiet's model and von Kármán spectrum extracted for ducted fans

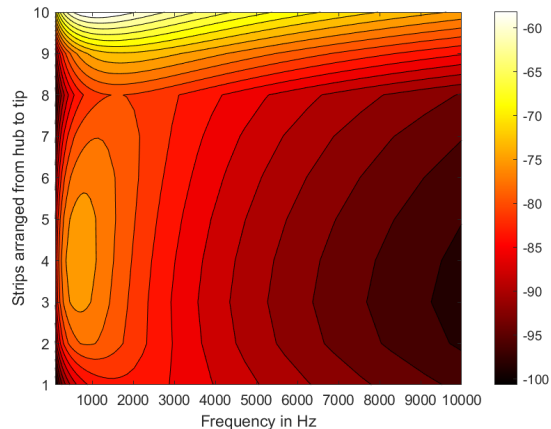
compared to other strips. So, to summarize, almost one-third (30%) of the span acts as a potential noise source for BS. In the case of FS, strip10 exhibits the highest contribution from 2 kHz onwards while strip02 and strip04 are observed to produce higher noise levels below 1 kHz than the rest of the strips. Also for the US, the topmost strip is showcasing the highest noise levels but strip08 has increased levels above 2 kHz than the strips present below. It appears that only 10% of FS span acts as a noise source while almost 20% of US span contributes to noise generation. When mediated on their causes, all the proofs point towards the soup of turbulent structures near the tip. For instance, the TKE and Λ_f from Fig. 6.23 indicate that the significant turbulence comes from the tip region. Fig. ?? confirms the top part of the span contains an elevated level of pressure fluctuations that acts as the pronounced noise source. Even noise source localization performed with beamforming method by Zenger [124] reveals similar information, displayed in Figs. 6.25, 6.26a and 6.26b. All fans suggest the dominance of the tip region for the high frequency region and especially displayed for the US from 1.6 kHz to 6.3 kHz. The locus of noise sources is found near LE starting from 1.6 kHz and it starts spreading along the chord towards TE. FS exhibits high concentration of sources near LE at 2 kHz and as frequencies are higher, the sources are traced at mid chord (3.15 kHz) and near TE (6.3 kHz)(also see 2.26). The sources are distributed all over the chord from LE to TE (see Fig. 2.27) and partly over the span in case of BS. Notice that the strength of noise sources is higher for the US than swept blade at $f_c=2$ kHz. Now, we can appreciate more the details given by

tip vortex visualization in Figs. 5.43, 5.58, 5.59 and 5.60. Noticeable differences are found in tip vortex behavior for these fans. A widespread of thin elongated vortices across blade passage hitting LE and pressure side of an adjacent blade is observed near the tip for BS, while the FS exhibit a relatively thinner tip region impacted by turbulent structures traveling across the blade passage and grazing pressure side of an adjacent blade near TE, as noticed in Fig. 5.58. However, the US showed somewhat intermediate behavior. These arguments confirm that the unstable, highly turbulent region can be responsible for broadband noise.

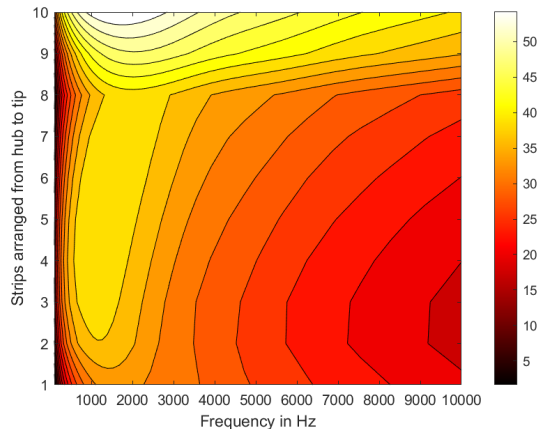
Therefore, to understand the total noise radiated by the fan, the noise generated by each strip is integrated using the equations mentioned in the ninth and tenth steps of Fig. 3.3. The 90° microphones located 1 m away from the fan center are used for the comparison. The total power radiated is converted to sound pressure level using $L_p = \frac{L_w \rho c_0}{A}$ where L_p is sound pressure in Pa, L_w is sound power in W, A is the area of the sphere in m² on which sound pressure is integrated. The PSD of sound pressure in dB/Hz (SPL) predicted from the model for each fan is compared with the experimental results in Fig. 6.27 for ducted fans. Note that the directivity and duct effects aren't accounted for in this comparison.

The BS produces higher noise than the US and FS. This ranking of noise levels is in agreement with experimental observation. The broadband noise follows the spectral shape over the frequency greater than 1 kHz onwards for all fans, although the levels have slightly deviated by 2-4 dB. It means that broadband noise generated by LE interaction spreads over the frequency range from 1 kHz to 10 kHz. The BS shows a good correlation in the low frequency region, i.e., from 800 Hz to 2 kHz, but over predicts by 2dB for higher frequency. Above 2 kHz, BS and US are producing almost similar noise behavior while FS noise levels are lower by 5dB. The US and the FS follow experimental spectra from 3 kHz onwards. Although the levels seem acceptable, we can't deny TE noise contribution to high frequency.

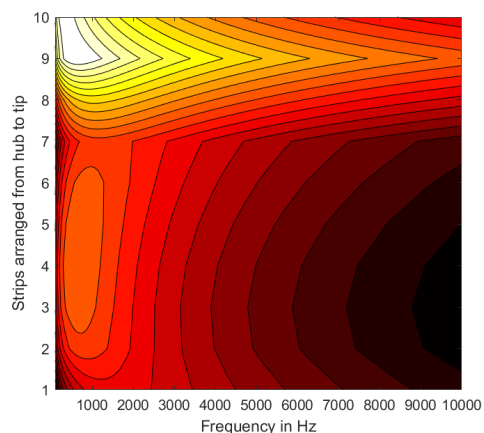
Therefore, TE noise is also calculated using Amiet's model as described in chapter 3 but the only difference is that the thin airfoil theory equations are derived for wall pressure fluctuations coming from turbulent boundary layer at TE instead of incoming velocity perturbations at LE. More detailed description about the TE model can be found in [5, 89]. In this study, we have followed the method described by Sanjose et al. [92] in their study of broadband noise prediction using input from RANS simulation. Interested readers are directed to [26, 92] for further information on the method. The broadband noise was calculated using RANS simulations performed on ducted fans and compared in Fig. 6.27. Note that the necessary boundary layer parameters to construct the pressure spectrum



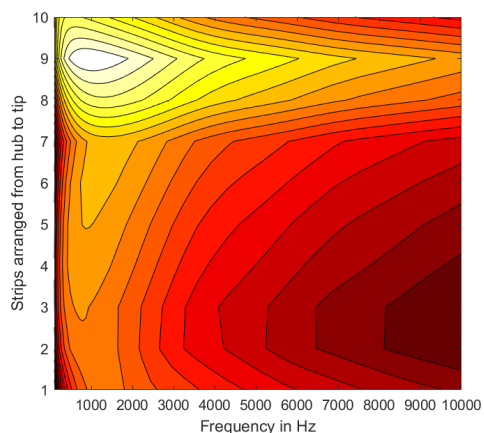
(a) VK spectrum for US



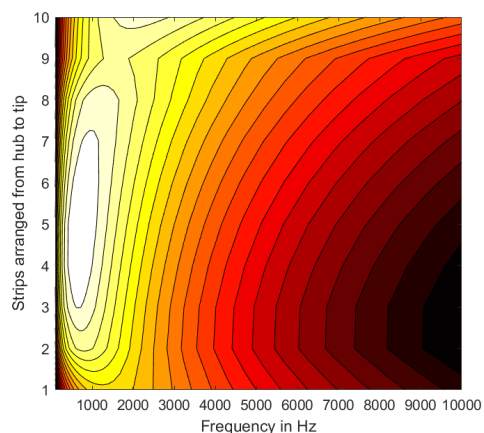
(b) SWL for US



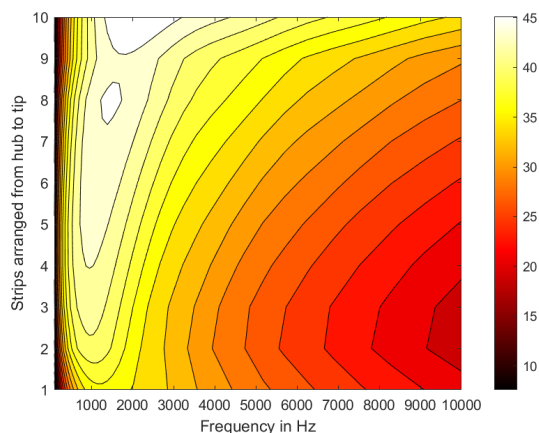
(c) VK spectrum for BS



(d) SWL for BS



(e) VK spectrum for FS



(f) SWL for FS

Figure 6.24 Stripwise distribution of turbulence spectrum and sound power prediction using Amiet's model

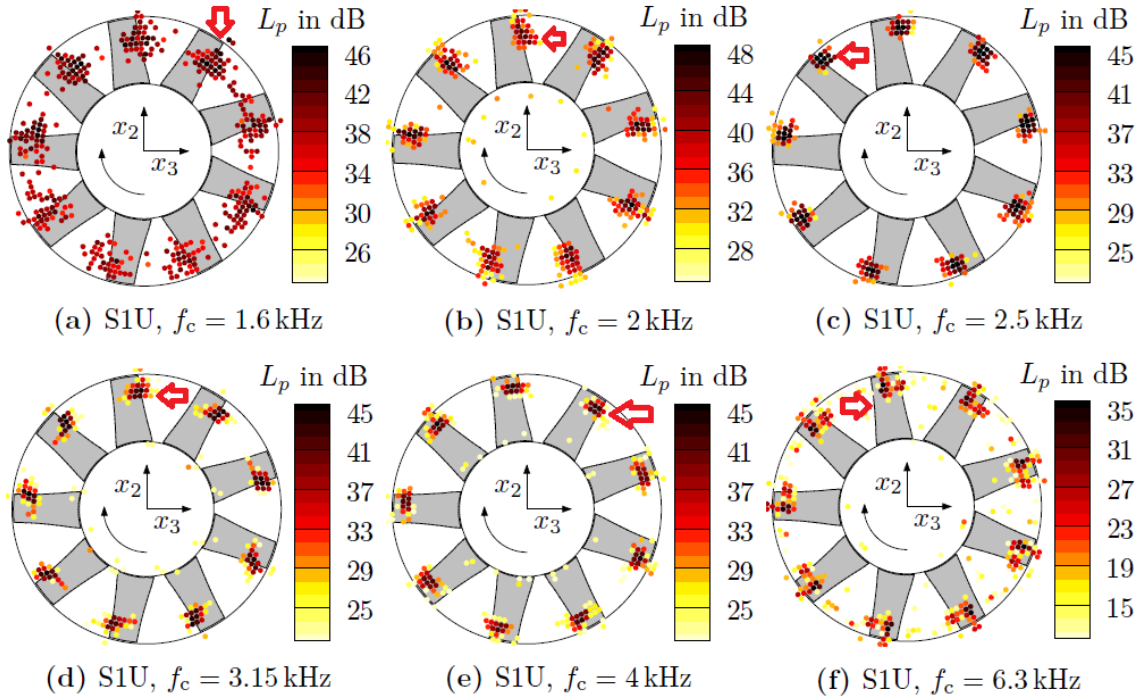
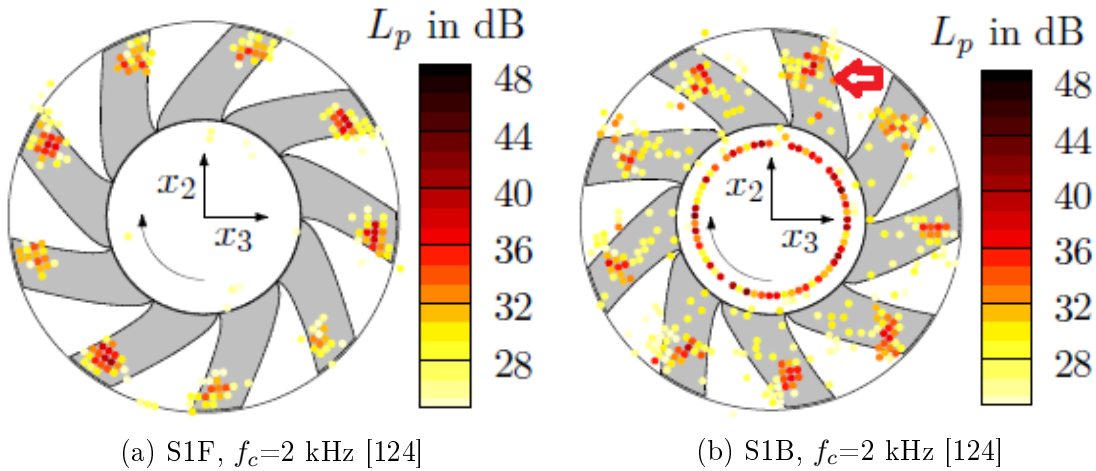


Figure 6.25 Sound maps for S1U from beamforming method used in experiment by Zenger [124]



near TE are used from Fig. 5.45. It is observed in Fig. 6.27 that TE is contributing least to the noise spectra. Nevertheless, BS appears to produce more noise than FS and US. A slight difference is observed with FS than our previously published results in [26] because in this study the inlet domain for all three fans is kept the same. Previously, we modified the inlet domains to investigate pressure rise deviations from test results. Finally, we understood that modifying the inlet domain didn't change any pressure rise but slightly altered the boundary layer behavior and tip vortex. One more thing to be noted here is that again the directivity and duct effects are neglected in TE noise. The addition of the

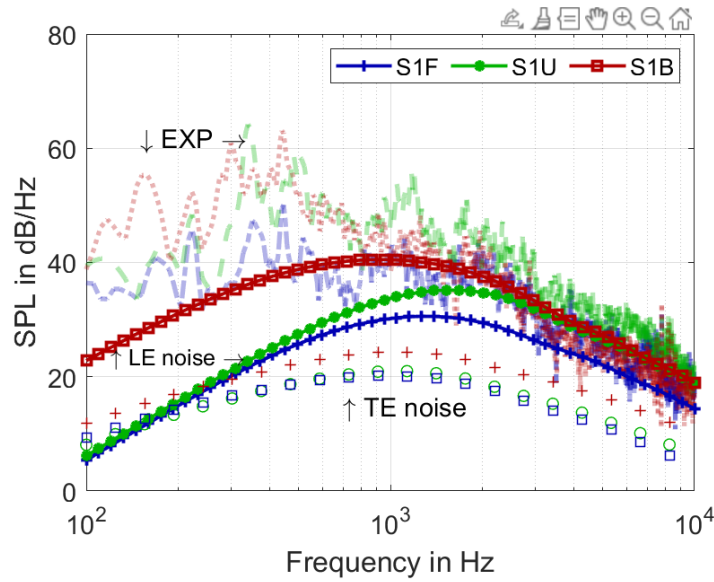
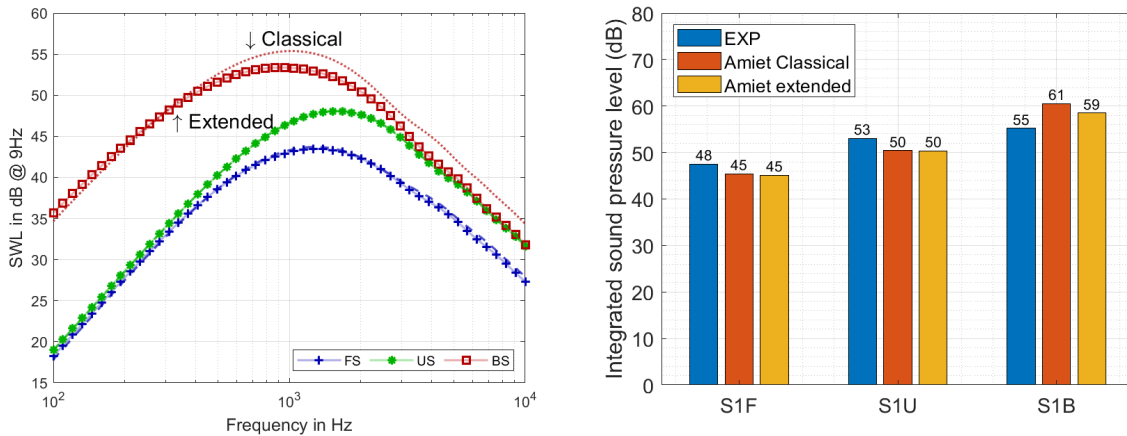


Figure 6.27 Validation of ducted fan noise spectra with experiments represented with EXP-dot/dash linestyle, LE Amiet extended-line with markers, TE Amiet classical-markers



(a) Sound pressure spectra

(b) Integrated spectra for high frequency

Figure 6.28 Comparison of classical vs extended Amiet's model prediction for free-tip fans

LE sweep effect in Amiet's modeling is studied in Fig. ?? for sound power spectra. BS shows 2 dB difference starting from 800 Hz but FS exhibit 0.5 dB difference from 2 kHz onwards. Therefore, the sound spectra are integrated for large bands i.e for BS (800 Hz to 10 kHz) and FS and US (2 kHz to 10 kHz) and compared with the bar chart in Fig. 6.28b. Amiet's extended model is able to capture the trend properly by ranking FS being the quieter and BS as being the loudest fan.

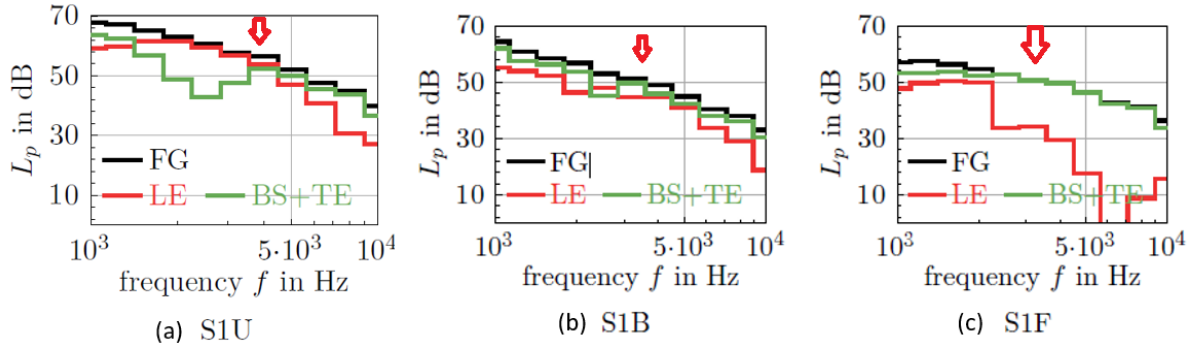


Figure 6.29 Integrated octave band spectra [124]

The model predictions are assessed against the integrated spectra calculated from the beamforming method. It provides further information on sound emitting sources from different regions of the blade. It is obtained by energy-summing third octave band spectra of the considered integration region for each fan [124] as shown in Fig. 6.29. It demonstrates noise spectra contribution from LE and blade surface (BS) and TE. The noise spectra show equal importance of LE sources as we demonstrated with Amiet's model in Fig. 6.27. On the contrary, although BS+TE noise appears to contribute to the spectra predominantly, the question is what are their original source? Is it turbulent interactions or turbulence formed within boundary layer? Well, although sources are located near TE all our earlier discussions pointed out that TLV and TSV are the major sources that spread along the chord. Therefore, from sound maps in Fig. 6.25, although high frequency sources appear to arise from the TE, their location near the tip confirms that it is originally coming from the perturbations originated in TLV and TSV. Therefore, those contributions are still considered as part of turbulence interaction noise and not from typical boundary layer scattering at TE. In the case of BS and US, a wider wake of TLV and TSV that spread azimuthally along the blade passage and interact with the adjacent blade are partially captured by the LE plane but for FS, the wake follows the chord and the turbulence formed by LE isn't completely accounted by the plane. This can be further visualized with the LDA plot for TKE at LE, given in Fig. 5.34. It suggests that the data recorded before the LE plane contain local information related to the turbulence present before LE. However, uncorrelated noise caused by turbulence produced in TLV and TSV present outside the LE plane isn't accounted for here. These meaningful validations on different levels have provided confidence in the method. Therefore, a similar broadband noise prediction method is applied to ring fans as discussed below.

Recall Longhouse study [59] discussed in Chapter 2 where he realized tip effect causing noise and then he added a ring to fans to reduce noise. Unfortunately, we don't have

similar fans with rings but at least, we can figure out noise behavior in such fans when the sweep is added. From Figs. 5.23 and 5.43, it is observed that TLV isn't directly interacting with TSV due to ring. In fact, instead of TSV wrapping around TLV, now the tip gap reverse flow travels through the gap formed by the ring and shroud from the pressure side to the suction side interacting with LE. Therefore, the LE plane can capture the turbulence details more appropriately in the ring fan. Like ducted fans, similar extractions are performed on ring fans too. The sweep angles are plotted in Fig. 6.30a in which sweep angles are positive for all blades —forward sweep. Generally, the plane normal to the axial direction is placed in between a quarter chord length to 10% of the chord length measured from LE of the blade [90] in absence of any dihedral angle. Hence, all the extraction planes here are normal to flow direction placed before LE at a distance of 25% of the tip chord.

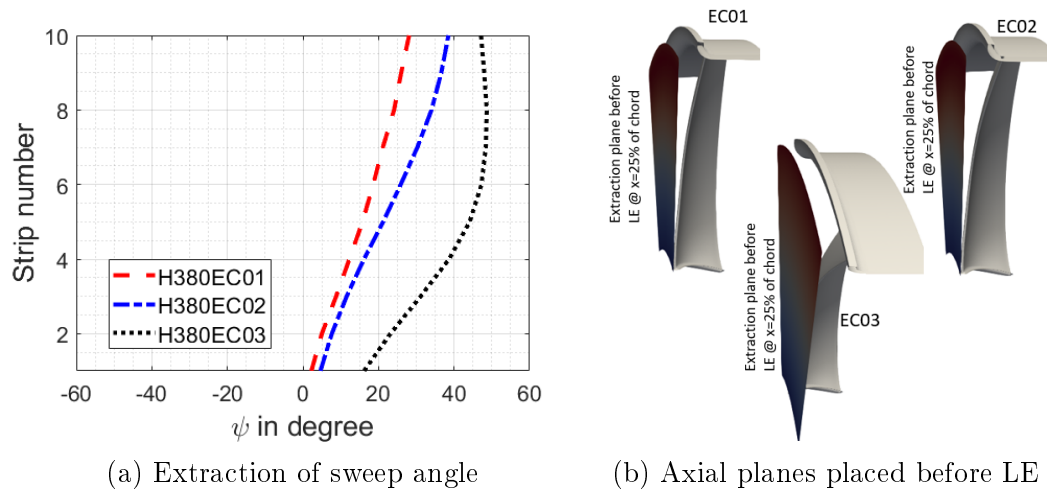


Figure 6.30 Sweep angle (left) and extraction planes (right) for ring fans

The flow parameters needed to construct the von Kármán spectrum are calculated from RANS simulation using the above extraction plane by averaging data azimuthally and plotted in Fig. 6.31. The TKE and W_r distribution explain that almost the same level of turbulence is interacting with the blade at the same speed irrespective of the sweep angle but with different length scales Λ_f . The turbulence spectrum is plotted in Fig. 6.32 (left) for each strip. All three fans show a similar distribution of turbulence levels among which strip10 i.e. strip near the tip is carrying significantly high turbulent energy than other strips. Based on our understanding, we can directly relate it to turbulence formed due to TSV. Using this turbulence information sound power radiated in the far field is calculated for each strip and showcased in Fig. 6.32 (right). The solid lines represent classical Amiet while a line with markers accounts for the sweep effect present an extended model. The sweep effects become active after 1 kHz for all fans but the major difference is observed for the highest swept blade —EC03. The strip10 of EC03 is showing 2-3 dB difference

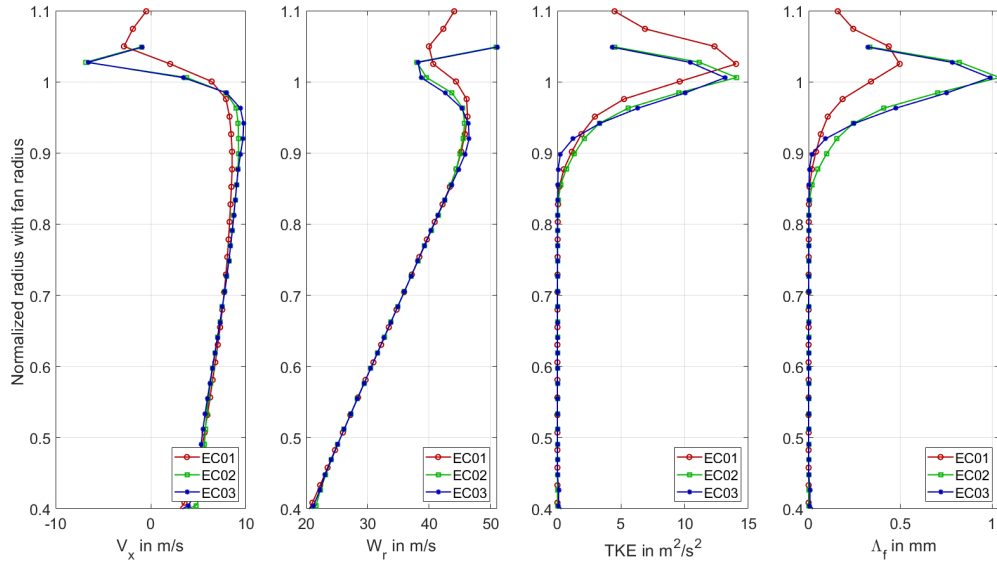


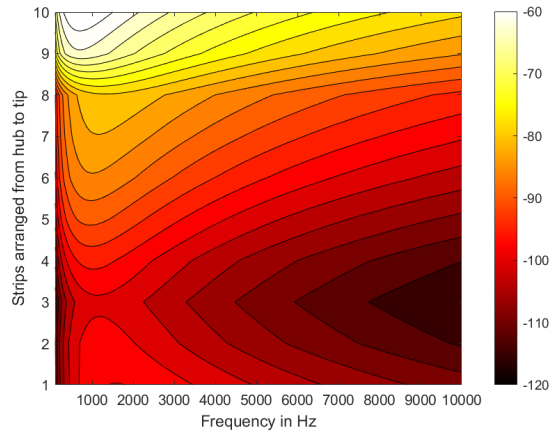
Figure 6.31 Parameters for Amiet's model and von Kármán spectrum extracted for ring fans

due to added sweep effect. The total power radiated by all the blades is calculated by integrating each strip contribution and multiplied by the number of blades as discussed in section 3.4. Before comparing model results, the scaling of experimental results to match design RPM is discussed below.

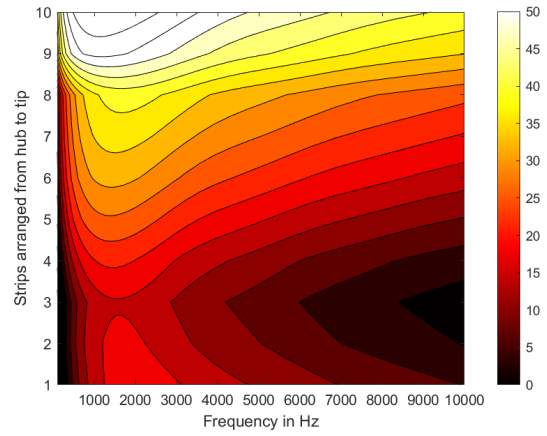
The experiment reported the loss of pressure rise when the sweep is added. Therefore, to maintain similar loading conditions, experiments are performed at 2000 and 2200 RPM, but simulations are conducted at the design point, i.e., 2500 RPM. Therefore, the experimental data is scaled to 2500 RPM using ANSI/AMCA standard 301-14 Methods [3] for scaling fan sound power with different RPM, as given below:

$$L_{w2} = L_{w1} + 50 \log_{10}\left(\frac{RPM_2}{RPM_1}\right) \quad (6.2)$$

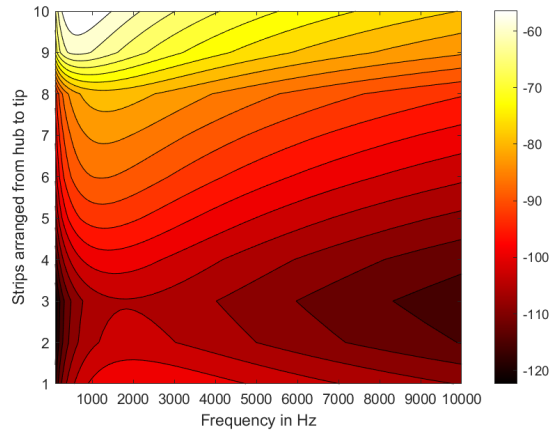
The scalability check is performed using LBM simulation. Previously Lallier [53] studied EC01 using LBM and noise spectra from his thesis are digitized to compare EC01 scaling displayed in Fig. 6.33a. Additionally, we simulated EC03 using his EC01 setup and compared it in Fig. 6.33b. The EC03 spectra show some initial fluctuations because the data is recorded for a short duration. So, it isn't averaged similar to EC01 but it is sufficient to perform a scaling check. Interested readers are directed to section 5.6.1 in his



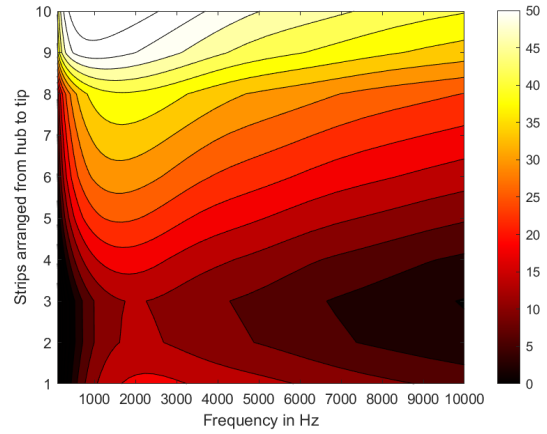
(a) VK spectrum for EC01



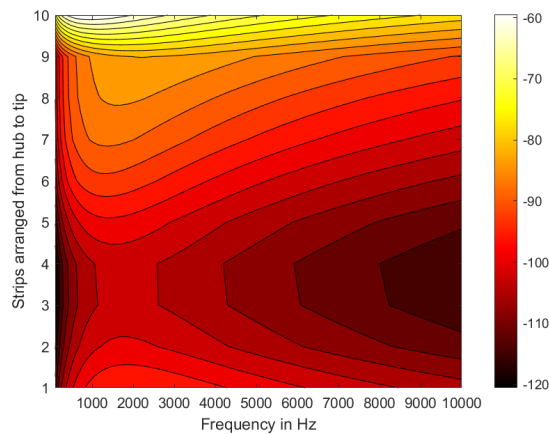
(b) SWL for EC01



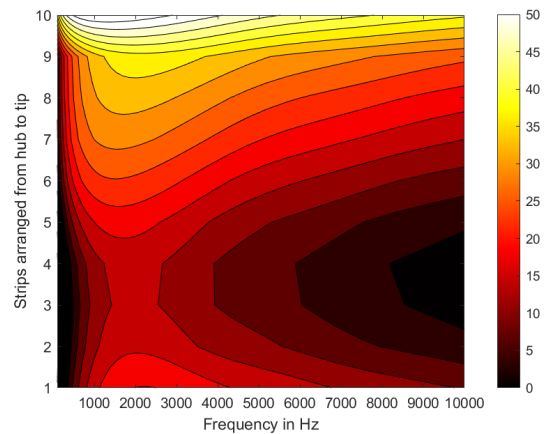
(c) VK spectrum for EC02



(d) SWL for EC02



(e) VK spectrum for EC03



(f) SWL for EC03

Figure 6.32 Stripwise distribution of turbulence spectrum and sound power prediction using Amiet's model for ring fans

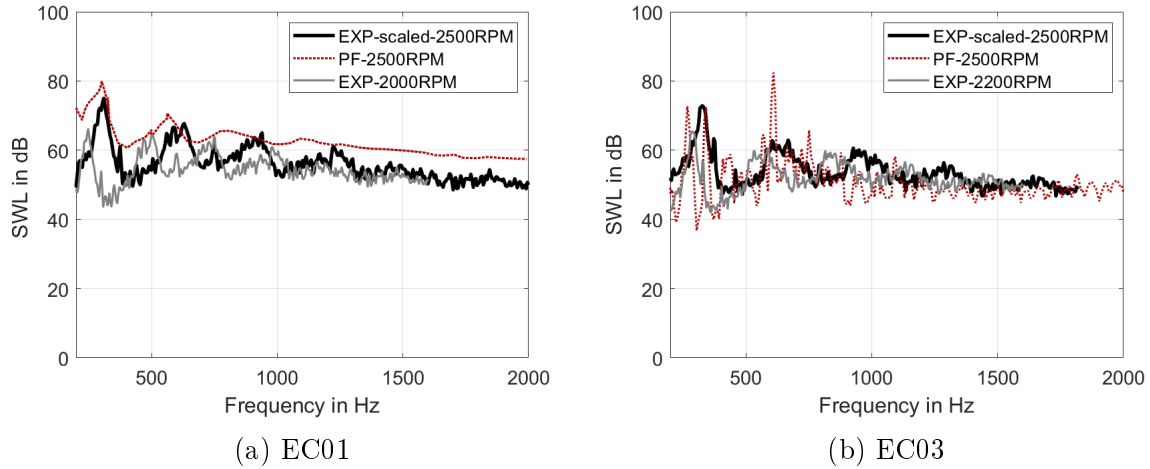


Figure 6.33 RPM scalability check using LBM

thesis. It seems that scaling shifts the sub-harmonic humps and modifies broadband level slightly. LBM simulations confirm the validity of Eq. 6.2.

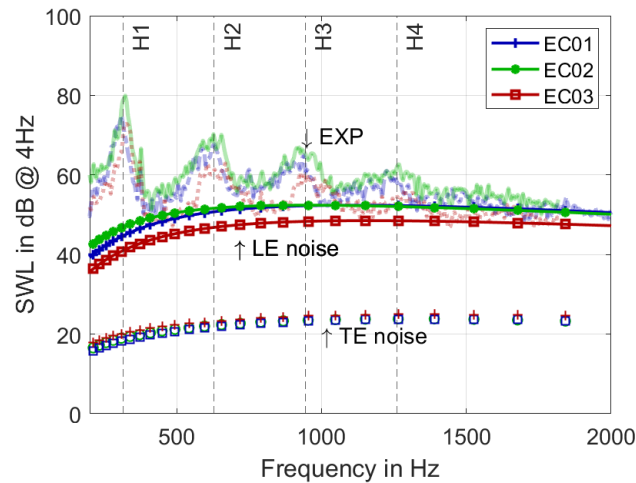
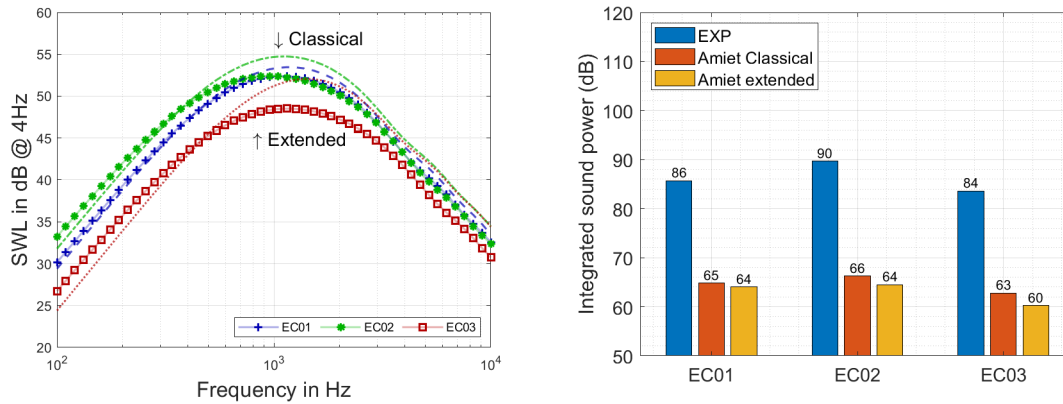


Figure 6.34 Validation of ring fans noise spectra with experiments represented with EXP-dot/dash linestyle, LE Amiet extended-line with markers, TE Amiet classical-markers

These scaled spectra for 2500 RPM are used to validate Amiet's model predictions. The strips' power shown in Fig. 6.32 is integrated to calculate the total power radiated by the fan. The prediction is compared in Fig. 6.34. If sub-harmonic humps are ignored and only the base level of experimental noise spectra is considered, then LE noise calculated from Amiet's extended model for EC01 and EC02 start matching with the test from 500 Hz onwards while EC03 compares well with the test level from 700 Hz onwards. TE noise calculated from classical Amiet's model is also compared. It yields the least contribution



(a) Sound power spectra; Extended-line and markers; classical-dot/dash linestyle (b) Large band integrated spectra from 200 Hz to 2 kHz

Figure 6.35 Comparison of Amiet's model prediction for ring fans

to the spectra. The boundary layer parameters needed are plotted in Fig. 5.24. The addition of sweep effect on the noise spectra is presented in Fig. 6.35a. The extended model starts influencing spectra after 700 Hz for EC03, showcasing 2-4 dB lower level of noise than the classical Amiet model. The EC01 and EC02 exhibit up to 1-2 dB reduction for the sweep correction. To understand overall noise contribution from broadband noise, large band integration from 200 Hz to 2 kHz is performed and differentiated with a bar chart in Fig. 6.35b. The experimental levels are high because they include the contribution from sub-harmonic humps. Amiet's model showcase that almost 75% of the total noise radiated is coming from broadband noise. Both Amiet's models capture the trend correctly but extended Amiet's model accounts for the sweep effect showing 4dB noise reduction for EC03 than EC01. In summary, the extended model predicts the broadband levels satisfactorily for ring fans also.

6.3 Conclusion

The primary objective of this study is to test the basic physics principle of creating interference patterns with non-linear LE (swept LE) to reduce broadband noise in presence of incoming turbulence. Therefore, the analytical model extended for the sweep is used in this study. The input from RANS simulations of different sweep angles used in the model has correlated well with far-field broadband noise measurement. It is observed from ring fans that as the forward sweep angle is increased the noise is reduced. The overall noise is reduced by 4 dB from EC01 to EC03. However, this benefit is associated with the cost —loss of aerodynamic performance scaled by $\cos \lambda$, the sweep angle. Therefore, the second set of configurations is studied in which aerodynamic performance is kept similar

by adding extra chord length to the unswept blade. Again use of the analytical model predicted that FS has shown 5 dB of noise reduction compared to US when spectra are integrated for high frequency but BS has exhibited 9 dB higher noise level than US. In fact, if the interference principle is applied equally to both FS and BS, both must show noise reduction. Nevertheless, it is understood that applying the non-linear LE principle directly to the blade without considering aerodynamic behavior doesn't provide the real sweep benefit.

Ducted free tip fans are further analyzed with LBM simulation. The direct noise predicted from the simulations matches the measured noise spectra well. After achieving a satisfactory correlation, various methods are employed to identify different noise sources. Although all the design parameters are kept the same except sweep angle, tip flow behavior is modified drastically from US to FS to BS showcasing their importance in dB maps. The dilation plot exhibits propagation of spherical acoustic waves pointing their center as origin towards the tip region for all fans. However, compared to US and BS, only FS has discerned a significant contribution coming from the corner vortex which is also noticed in dB maps. Once, the tip sources are confirmed, the modes near the tip are explored, and found that they travel with mean velocity. Hence, the mean speed of turbulence formed due to TLV and TSL are visualized with λ_2 near the tip and their relative velocity distribution is examined with the probability density function. The peak of such distributions is identified with the peak frequency of subharmonic humps observed in the noise spectra. It is revealed that US and BS show a peak at an almost similar frequency while FS peak is moved to a higher frequency. Moreover, its low frequency peak is caused due to corner vortex, analyzed with a similar process. These observations are confirmed with the wall pressure PSD recorded at casing. However, EC01 and its forward swept version indicated almost similar peak frequency irrespective of sweep angle which also validate with test results. Furthermore, the strip-wise broadband noise predicted with analytical model display strip near tip radiates maximum LE noise than others. Again, turbulence formed due to TLV and TSV interactions confirms remarkable broadband noise contribution to the spectra. Before establishing a final opinion, the other broadband noise source coming from boundary layer scattering near TE is evaluated using the analytical model. Both configurations assert the lowest contribution of TE noise to the noise spectra. All these assessments indicate that end wall-induced secondary flows near the tip are to behold as the strong source in the absence of any external disturbances.

In summary, although free tip fans are designed for similar pressure loadings, forward sweep performed better than backward sweep or unswept fan. The study confirms that

axial velocity accelerates near tip region causing modified incidence angle for all three fans. It reflected in how tip leakage and tip separation vortices are formed and their orientation. Backward sweep becomes noisier than unswept fan. The forward sweep become quietest fan than unswept fan. The TLV and TSV showed greater impact over all frequency range i.e. from 100 Hz to 10 kHz in terms of sub-harmonic hump and high frequency LE broadband noise. Therefore, designers can use this information and carefully load the tip region by adjusting incidence angle to avoid any large wake formation near tip region by accounting for secondary flow effect and radial flow generation due to sweep. The additional noise source near the hub can be also addressed by increasing axial velocity and by lowering incidence angle.

CHAPTER 7

Conclusion Français

L'objectif de cette étude est de déterminer comment réduire au maximum le bruit causé par l'angle de flèche tout en conservant les performances aérodynamiques. De plus, cette étude tente de résoudre l'ambiguïté établie par les recherches publiées à ce jour refusant d'accepter unanimement les aspects prometteurs de l'angle de flèche afin de réduire le bruit. L'angle de flèche des ventilateurs axiaux à basse vitesse est principalement utilisé afin d'adresser le bruit de large bande LE. L'idée est de produire une interaction non linéaire à l'aide des turbulences entrantes afin de supprimer le bruit en construisant un patron déphasé obligatoire et de réduire au maximum la propagation du bruit dans le champ lointain. Cette présupposition est testée avec un concept de base ainsi que deux variantes de dévers avant dérivé du ventilateur. Le modèle analytique étendu du bruit LE a prouvé que le concept à angle de flèche supérieur réduit le bruit large bande de 4 décibels par rapport au modèle de base. Cependant, il a été découvert que le rendement aérodynamique est détérioré par facteur $\cos(\lambda)$. Cette observation est en accord avec les autres études. Vad et al. [111] ont démontré que la vitesse axiale augmente près de la pointe du ventilateur et défend l'idée que réduire l'angle d'incidence réduit l'augmentation de la pression. Au contraire, nos données indiquent une vitesse axiale similaire du centre vers la pointe des trois ventilateurs. Comme résultat, cette étude jette un regard neuf sur les causes de la perte de pression. La vitesse tangentielle et radiale dans une cadre de référence relatif sont également à l'étude. Les découvertes indiquent qu'un angle de flèche plus grand cause une vitesse tangentielle plus grande pour une même vitesse entrante. Ceci provoque une augmentation de l'angle d'entrée dans une cadre relatif et réduit l'angle d'incidence pour toutes les fixation radiales par rapport au concept de base. Désormais, nous savons que pour maintenir une charge équivalente, l'angle d'incidence doit être corrigé ou la corde doit être allongée. Par conséquent, les soufflantes ont été choisies pour la prochaine évaluation. Même si elles ne représentent pas les ventilateurs à couronne, leurs résultats peuvent être utilisés directement. Leur bruits sont évalués à l'aide de la méthode directe par simulations LBM. Le ventilateur FS devient le ventilateur le plus silencieux en réduisant le SPL global par 12 décibels. En opposition, le ventilateur BS démontre une réduction de 2 décibels. FS et BS devraient donner les mêmes résultats, cependant BS ne respecte pas le cadre théorique. Une observation similaire est citée par Fukano et al. [30] indiquant qu'un dévers avant est mieux qu'un dévers arrière, mais

Gray [37] indique une réduction de 6 décibels. Il est important de mentionner que la génération du bruit est directement associée au comportement aérodynamique. Même si les ventilateurs ont été conçus pour des performances équivalentes, FS démontre une plus grande augmentation de la pression par rapport aux autres modèles. La vitesse axiale est également étudiée: FS démontre une plus grande vitesse axiale près de la pointe par rapport à US et BS. Ceci a été également étudié par Vad et al. [111]. La distribution de la pression au long de la corde met la lumière sur la différence de portance entre FS et BS. FS démontre une plus petite portance au centre, mais une plus grande aux pointes. BS a le comportement opposé. Ce comportement renvoie à la vitesse axiale et l'angle d'incidence. FS a un angle d'incidence inférieur causant un écoulement attaché jusqu'à TE. BS affecté par son angle d'incidence inférieur causé par la perte de vitesse axiale sépare l'écoulement à LE. Les conséquences des différentes conditions d'opérations peuvent être comprises grâce aux cartes de décibels appliquées aux fluctuations de pression en surface. La pointe montre une plus grande fluctuation de pression que le reste de l'envergure des trois ventilateurs suggérant des traces de fortes sources de bruit. Les tracés de dilatation permettent de confirmer d'origine des ondes acoustiques à la pointe. La perspective en isosurface de λ_2 donne un aperçu intéressant de l'écoulement à la pointe. FS forme une TLV en forme de corde au long de la corde et les structures haute-vitesse allongés de TSV l'enveloppent. Ce phénomène forme un sillage turbulent d'air passant au travers des pales venant froter la pression d'une pale voisine. Ceci explique leur contribution significative à la plage de fréquence globale tracée par la carte de décibels. D'un autre côté, BS interfère TLV ce qui vient interagir avec TSV afin de former un sillage de structure allongée répandu sur le passage de la pale de LE vers TE causant une forte interaction entre le côté aspiration et le côté pression interagissant avec la pale adjacente. Ceci est également confirmé grâce aux cartes de décibels indiquant une distribution de bruit égale de chaque côté. L'approche US offre un comportement intermédiaire confirmant que FS performe mieux que US. À l'aide de recherche additionnelle [53, 63, 81, 127], nous avons démontré que ces processus d'écoulement provoquent des perturbations sous-harmoniques dans le spectre de bruit ainsi que la fréquence centrale est identifiée par la moyenne de vitesse des structures turbulentes. Le bruit de la pointe des modèles US et BS sont identifiés à ≈ 122 - 127 Hz ce qui correspond au premier maximum et quatrième maximum observé sur le spectre de bruit. Cependant, le bruit de l'écoulement à l'extrémité de FS est tracé à proximité du deuxième pic (environ 179 Hz) dans le spectre de bruit et ses deuxième et troisième harmoniques correspondent aux troisième et quatrième pics du spectre. De plus, la vitesse axiale plus faible près du moyeu dans le cas de FS a entraîné une forte formation de CV, qui est identifiée avec le premier pic dans les spectres de bruit. Ces pics

de fréquence sont également observés dans le tracé PSD de la paroi, ce qui montre leur présence remarquable du côté de la pression et de l'aspiration. Les pics multiples dans les spectres de bruit proviennent effectivement de l'écoulement en bout de pale, mais la vitesse variable observée dans la structure de l'écoulement en bout de pale est unique dans les spectres. Cela est vrai pour les ventilateurs à pointe libre, mais pour les ventilateurs canalisés, la fréquence de pointe est identifiée par une seule vitesse d'écoulement moyenne et ses harmoniques, ce qui permet de les manipuler très facilement à l'avenir. Une fois que les sources de bruit pour les bosses subharmoniques sont localisées, le bruit LE dû aux interactions turbulentes est évalué avec le modèle d'Amiet étendu pour la flèche. On observe que FS est le moins producteur de bruit large bande haute fréquence et que BS est le plus bruyant que US. Dans les ventilateurs annulaires et à bouts libres, le bénéfice maximal du balayage est observé dans la région des hautes fréquences et le modèle d'Amiet étendu pour le balayage peut bien capturer le classement. La seule limite de ce processus est qu'il prend en compte les informations de turbulence capturées avant le plan LE, mais d'autres sources potentielles de turbulence dans l'écoulement d'extrémité qui interagissent avec le reste de la corde ne sont pas prises en compte. Elles doivent être traitées séparément. De plus, la contribution du bruit TE reste la plus faible dans les spectres.

Les méthodes utilisées dans cette étude sont bien validées avec un large ensemble de données disponibles provenant d'expériences menées dans différentes universités à différents moments. Ainsi, la corrélation établie renforce la confiance dans les méthodes et les conclusions qui en découlent.

En conclusion, cette étude a répondu avec succès aux raisons de la perte de performance aérodynamique en présence d'une flèche. Nos résultats suggèrent qu'au lieu d'utiliser la correction avec et sans exposant $\cos(\lambda)^{0.67}$, on peut améliorer l'angle d'incidence en se basant sur le cas du balayage avant et arrière indépendamment. Les connaissances acquises sur les sources de bruit localisées en comprenant les différents mécanismes de sources de bruit dans les ventilateurs balayés et non balayés et leur cause associée peuvent améliorer davantage les niveaux de bruit des ventilateurs. Il a également été prouvé que la mise en œuvre du modèle de balayage étendu peut améliorer les prédictions du modèle analytique pour s'attaquer au mécanisme de bruit LE.

7.1 Recommandations et perspectives d'avenir

Cette recherche élaborée a ajouté un autre niveau de brique de fondation aux connaissances existantes. Il est possible d'optimiser de manière aérodynamique la charge au niveau de chaque section radiale à l'aide d'un angle de décalage au lieu d'augmenter la longueur de

la corde. L'augmentation de la longueur de la corde peut augmenter la masse du véhicule au niveau des composants et peut nécessiter une puissance supplémentaire pour les faire fonctionner. Cela peut nuire à l'autonomie du véhicule électrique - une préoccupation croissante dans l'industrie automobile.

Le bruit TE dû à la formation de la couche limite est la préoccupation principale, mais la traînée par frottement de peau et son influence sur la consommation d'énergie doivent être confirmées à nouveau.

Bien que la fréquence subharmonique du bruit de l'écoulement en bout de pale soit située dans les spectres, leur quantification à l'aide d'une simulation RANS régulière et d'un modèle analytique doit être développée pour évaluer rapidement les conceptions initiales.

Dans cette étude sur les ventilateurs à pointe libre, l'angle dièdre ne joue aucun rôle dans les performances aérodynamiques mais il peut influencer l'angle de propagation des ondes acoustiques. Lorsque le ventilateur est installé derrière le radiateur du véhicule, le déplacement axial retardé peut fournir un espace de dégagement pendant l'installation. En outre, il peut permettre aux turbulences de se dissiper davantage avant d'atteindre la pale et la directivité peut être utilisée pour diriger les ondes vers le sol plutôt que de les propager directement à travers les ouvertures de la grille.

CHAPTER 8

Conclusion-English

The purpose of the current study is to determine how to get the maximum noise reduction benefit of the sweep by keeping its aerodynamic performance. This study also tries to address the ambiguity in till-date published research that couldn't unanimously accept the promising aspect of sweep in noise reduction. The sweep in low-speed axial fans is mainly aimed to tackle LE broadband noise. The idea is to produce non-linear interactions with incoming turbulence to arrest noise by constructing a compulsory de-phasing pattern and cancel or lower the noise propagation in the far-field. This presupposition is tested with the base design and its two variants of forward sweep derived from the ring fan. The extended analytical model for LE noise proved that the highest sweep blade reduces broadband noise by 4 dB than its base design. However, it is also found that their aerodynamic performance is deteriorated by $\cos(\lambda)$ times than the base design. This observation is in agreement with the published study. Vad et al.[111] showed that axial velocity increases near tip in forward fan and argued that reduced incidence angle causes lower pressure rise. On the contrary, our data indicate alike axial velocity from hub to tip for all three fans. As result, it casts a new light on understanding other associated causes for pressure loss. Therefore, tangential velocity and radial velocity in the relative reference frame are studied and it is found that the highest sweep experiences higher tangential velocity for similar incoming velocity that causes an increase in inlet flow angle in a relative frame and in turn reduces incidence angle for all radial location than its base design. Now, we know that the incidence angle needs to be corrected in sweep blades or increase chord length to maintain a similar loading. Therefore, ducted fans are selected in our next assessment. Although they don't represent the ring fan configurations, their outcomes can be directly employed.

The free-tip US and its swept versions FS and BS are studied. Their noise is assessed with the direct method using LBM simulation. The FS becomes the quietest fan by reducing overall SPL by 12 dB and contrarily, BS has shown just 2 dB reduction in overall SPL than its base design, US. Rather FS and BS must perform similarly but BS doesn't obey the theoretical framework here. A similar observation is also quoted by Fukano et al. [30] who claimed forward sweep is better than backward sweep but Gray [37] showed 6 dBA reduction in noise. Well, not to forget that noise generation

is directly associated with aerodynamic behavior. It is found that although the fans are designed for similar performance, FS showed a higher pressure rise than others at the design point. So, the axial velocity distribution is investigated and this time FS does show higher axial velocity near the tip than US and BS like already observed by Vad et al.[111]. Then pressure distribution along the chord unfolds the truth of dissimilar lift distribution from FS to BS. FS displays a lower lift near the hub but a higher lift near the tip while BS behaves exactly opposite to FS. Again, it links back to the axial velocity and the incidence angle. FS has a lower incidence angle such that flow remains attached until TE but BS experiences a higher incidence angle as a result of reduced axial velocity, separating the flow at LE itself. The implications of different operating conditions are understood through dB maps of surface pressure fluctuations. The tip shows higher levels than the rest of the span for all three fans, suggesting traces of strong noise sources. It is also confirmed with dilatation plots indicating the origin of acoustic waves near the tip. Isosurface of λ_2 provided interesting insight about tip flow behavior. FS formed a rope-like TLV along the chord and high-speed elongated structures of TSV wrapped around it forming a turbulent wake that passes through blade passage grazing the pressure side of an adjacent blade, tracing their significant contribution in dB maps overall frequency range. On the other hand, BS forms disrupted TLV that interact with TSV to form a wake of elongated structures spreading across the blade passage from LE to TE causing strong suction side and pressure side interactions with an adjacent blade. It is also confirmed with dB maps, showcasing equal noise source distributions on either side. The US offers intermediate behavior, confirming FS indeed performed better than US. In assistance with the published research [53, 63, 81, 127], we also successfully showed that these flow processes are causing the subharmonic narrowband in the noise spectra and their center frequency is identified with the mean speed of turbulent structures. The tip noise of US and BS are identified at ≈ 122 - 127 HZ which matches with the first peak and the fourth peak observed in the noise spectra. However, FS tip flow noise is traced close to the second peak ≈ 179 Hz in the noise spectra and its second and third harmonics matches with the third and fourth peak in the spectra.

Moreover, lower axial velocity near the hub in the case of FS resulted in strong CV formation, which is identified with the first peak in the noise spectra. These peak frequencies are also observed in the wall PSD plot showcasing their remarkable presence on the pressure and suction side. The multiple peaks in noise spectra are indeed coming from tip flow but the variable speed observed in the tip flow structure stands uniquely in the spectra. This is true for free-tip fans but for ducted fans the peak frequency is identified with just one mean flow speed and its harmonics, making them to handle very easily in the future. Once

the noise sources for subharmonic humps are located, the LE noise due to turbulent interactions is assessed with Amiet's model extended for the sweep. FS is observed to be the least producer of high-frequency broadband noise and BS is the loudest than US. In both ring and free-tip fans, the maximum benefit of sweep is observed in the high-frequency region and the extended Amiet's model for the sweep can capture the ranking well. The only limitation to this process is that it accounts the turbulence information captured before the LE plane but other potential turbulent sources in tip flow that interacts with the rest of the chord aren't captured. They need to be handled separately. Furthermore, TE noise contribution remained the lowest in the spectra.

The methods used in this study are well validated with a wide data set available from the experiments conducted at different universities at different times. Hence the established correlation builds the confidence in the methods and the conclusions derived from them.

In conclusion, this study successfully answered the reasons for the loss of aerodynamic performance in the presence of a sweep. Our findings suggest that instead of using correction with and without exponent $\cos(\lambda)^{0.67}$, one can improve incidence angle based on the case of forward and backward sweep independently. It suggest that when changing from unswept to swept fans, radial equilibrium modifies and based on forward and backward sweep, one can individually adjust radial equilibrium by uniformly loading blade from hub to tip and tip must be always designed with lower loading than rest of the blade.

The knowledge gained from localized noise sources by understanding different noise source mechanisms in swept and unswept fans and their associated cause can further improve the fan noise levels. Also proved that implementing the extended sweep model can improve the analytical model predictions to tackle the LE noise mechanism.

8.1 Recommendations and future perspective

This elaborated research has added another level of foundation brick to existing knowledge. One can aerodynamically optimize the loading at each radial section with the help of a stagger angle instead of increasing chord length. Usually, in order to control full vehicle mass, the mass targets are defined on vehicle level. So, increasing chord length can increase mass on component level and also may require extra power to operate them. It can hurt the range of the electrical vehicle —a growing concern in the automotive industry at present.

The TE noise due to boundary layer formation is the list concern but the skin friction drag and its influence on power consumption need to be confirmed again.

Although the subharmonic frequency of tip flow noise is located in the spectra, their quantification by using steady RANS simulation and analytical model must be developed to quickly assess initial designs.

In this study of free-tip fans, the dihedral angle doesn't play any role in aerodynamic performance but it can influence the acoustic wave propagation angle. When the fan is installed behind the radiator in the vehicle, the delayed axial displacement can provide clearance room during the installation. Furthermore, it can allow turbulence to dissipate further before reaching the blade and directivity can be used to direct waves towards the ground than propagating directly through the grille openings.

The designers can use this information by carefully loading blade from the hub to the tip. The higher loading near the tip region can form larger tip vortices that are responsible for noise. Therefore, a special attention need to be provided in understanding variation of axial velocity near the tip region. The inlet flow angle is slowly increased from hub to tip designing lightly loaded tip. It will help in both free tip and ring fans. The lower loading near tip will reduce reverse flow through tip gap and in turn will also reduce subharmonic and high frequency broadband levels in the noise spectra. The additional corner vortex source can also be adjusted by lowering incidence angle near hub. Moreover, sweep can handle low and mid frequency incoming turbulence, providing maximum noise benefit when installed on the vehicle. One can refer the small exercise performed in Fig. 3.5 on an isolated blade case for further understanding of influence characteristics of turbulence and sweep. The sweep angle can be optimized based on the incoming turbulence signature. These design guidelines can help to build quieter fans than before in presence of sweep.

LIST OF REFERENCES

- [1] Adamczyk, J. (1973). Analytical investigation of compressibility and three-dimensionality on the unsteady response of an airfoil in a fluctuating flow field. In *6th Fluid and Plasma Dynamics Conference*. American Institute of Aeronautics and Astronautics. (Cited on page 46.)
- [2] Adamczyk, J. J. (1974). Passage of a Swept Airfoil through an Oblique Gust. *Journal of Aircraft*, volume 11, number 5, pp. 281–287. (Cited on page 46.)
- [3] AMCA (2020). AMCA Standard 301-14 | Methods for Calculating Fan Sound Ratings from Laboratory Test Data. (Cited on page 168.)
- [4] Amiet, R. (1975). Acoustic radiation from an airfoil in a turbulent stream. *Journal of Sound and Vibration*, volume 41, number 4, pp. 407–420. (Cited on pages 15 and 46.)
- [5] Amiet, R. K. (1976). Noise due to turbulent flow past a trailing edge. *Journal of Sound and Vibration*, volume 47, number 3, pp. 387–393. (Cited on page 162.)
- [6] Amiet, R. K. (1977). Noise Produced by Turbulent Flow into a Propeller or Helicopter Rotor. *AIAA Journal*, volume 15, number 3, pp. 307–308. (Cited on pages 8 and 15.)
- [7] Bamberger, K. and Carolus, T. (2012). Optimization of axial fans with highly swept blades with respect to losses and noise reduction. *Noise Control Engineering Journal*, volume 60, number 6, pp. 716–725. (Cited on page 30.)
- [8] Batchelor, G. K. (1953). *The Theory of Homogeneous Turbulence*. Cambridge University Press. (Cited on page 16.)
- [9] Beiler, M. G. and Carolus, T. H. (1999). Computation and Measurement of the Flow in Axial Flow Fans With Skewed Blades. *Journal of Turbomachinery*, volume 121, number 1, pp. 59–66. (Cited on pages 26, 27, 28, 30, 32, 84, 87, and 94.)
- [10] Bianchi, S., Corsini, A., Rispoli, F. and Sheard, A. G. (2009). Detection of aerodynamic noise sources in low-speed axial fans with tip end-plates. *Proceedings of the Institution of Mechanical Engineers, Part C: Journal of Mechanical Engineering Science*, volume 223, number 6, pp. 1379–1392. (Cited on page 18.)
- [11] Brooks, T. F., Marcolini, M. A. and Pope, D. S. (1986). Airfoil trailing-edge flow measurements. *AIAA Journal*, volume 24, number 8, pp. 1245–1251. (Cited on pages 9, 12, and 29.)
- [12] Brooks, T. F. P. (1989). *Airfoil self-noise and prediction* (Technical Report 19890016302). NASA, USA, 145 pp. (Cited on pages xiii, 9, 10, and 14.)

-
- [13] Brès, G., Pérot, F. and Freed, D. (2009). Properties of the Lattice Boltzmann Method for Acoustics. In *15th AIAA/CEAS Aeroacoustics Conference (30th AIAA Aeroacoustics Conference)*. American Institute of Aeronautics and Astronautics. (Cited on page 43.)
- [14] Camussi, R. (2013). *Noise Sources in Turbulent Shear Flows: Fundamentals and Applications*. Springer-Verlag. (Cited on page 44.)
- [15] Canepa, E., Cattanei, A., Mazzocut Zecchin, F. and Parodi, D. (2019). Large-scale unsteady flow structures in the leakage flow of a low-speed axial fan with rotating shroud. *Experimental Thermal and Fluid Science*, volume 102, pp. 1–19. (Cited on page 82.)
- [16] Carolus, T. H. and Starzmann, R. (2011). An Aerodynamic Design Methodology for Low Pressure Axial Fans With Integrated Airfoil Polar Prediction. American Society of Mechanical Engineers, pp. 335–342. (Cited on page 7.)
- [17] Chapman, S., Cowling, T. G. and Cercignani, C. (1991). *The Mathematical Theory of Non-uniform Gases: An Account of the Kinetic Theory of Viscosity, Thermal Conduction and Diffusion in Gases*, 1st edition. Cambridge University Press, Cambridge ; New York. (Cited on page 37.)
- [18] Chen, H., Kandasamy, S., Orszag, S., Shock, R., Succi, S. and Yakhot, V. (2003). Extended Boltzmann Kinetic Equation for Turbulent Flows. *Science*, volume 301, number 5633, pp. 633–636. (Cited on page 37.)
- [19] Chen, H., Orszag, S. A., Staroselsky, I. and Succi, S. (2004). Expanded analogy between Boltzmann kinetic theory of fluids and turbulence. *Journal of Fluid Mechanics*, volume 519, pp. 301–314. (Cited on page 37.)
- [20] Choi, H. and Moin, P. (2012). Grid-point requirements for large eddy simulation: Chapman’s estimates revisited. *Physics of Fluids*, volume 24, number 1, p. 011702. (Cited on page 40.)
- [21] Christophe, J. (2011). *Application of Hybrid Methods to High Frequency Aeroacoustics*. Ph.D. thesis, Université Libre de Bruxelles and Von Karman Institute for Fluid Dynamics, Brussels, Belgium. (Cited on page 48.)
- [22] Clark, L. T. (1971). The Radiation of Sound From an Airfoil Immersed in a Laminar Flow. *Journal of Engineering for Power*, volume 93, number 4, pp. 366–376. (Cited on page 12.)
- [23] Corsini, A. and Rispoli, F. (2003). The Role of Forward Sweep in Subsonic Axial Fan Rotor Aerodynamics at Design and Off-Design Operating Conditions, pp. 543–553. (Cited on pages 26 and 27.)
- [24] Corsini, A. and Rispoli, F. (2004). Using sweep to extend the stall-free operational range in axial fan rotors. *Proceedings of the Institution of Mechanical Engineers*,
-

- Part A: Journal of Power and Energy*, volume 218, number 3, pp. 129–139. (Cited on pages 26 and 27.)
- [25] Curle, N. (1955). The influence of solid boundaries upon aerodynamic sound. *Proc. R. Soc. Lond. A*, volume 231, number 1187, pp. 505–514. (Cited on pages 7, 29, 44, and 46.)
- [26] D., G., M., S., S., M. and Henner, M. (2019). Modification of noise sources by virtue of sweep in low speed fan. International Congress on Sound and Vibration. (Cited on pages 159, 162, and 164.)
- [27] Ffowcs Williams, J. E. and Hawkings, D. L. (1969). Theory relating to the noise of rotating machinery. *Journal of Sound and Vibration*, volume 10, number 1, pp. 10–21. (Cited on page 44.)
- [28] Filleul, N. I. S. (1966). An investigation of axial flow fan noise. *Journal of Sound and Vibration*, volume 3, number 2, pp. 147–165. (Cited on pages 14 and 16.)
- [29] Foss, J., Neal, D., Henner, M. and Moreau, S. (2001). Evaluating CFD Models of Axial Fans by Comparisons with Phase-Averaged Experimental Data. (Cited on pages 59, 78, and 80.)
- [30] Fukano, T. and Jang, C. M. (2004). Tip clearance noise of axial flow fans operating at design and off-design condition. *Journal of Sound and Vibration*, volume 275, number 3, pp. 1027–1050. (Cited on pages xiii, 18, 20, 21, 22, 23, 175, and 179.)
- [31] Fukano, T., Kodama, Y. and Takamatsu, Y. (1978). Noise generated by low pressure axial flow fans, III: Effects of rotational frequency, blade thickness and outer blade profile. *Journal of Sound and Vibration*, volume 56, number 2, pp. 261–277. (Cited on pages 26, 29, and 30.)
- [32] Fukano, T., Takamatsu, Y. and Kodama, Y. (1986). The effects of tip clearance on the noise of low pressure axial and mixed flow fans. *Journal of Sound and Vibration*, volume 105, number 2, pp. 291–308. (Cited on pages 18 and 20.)
- [33] Ghorbaniasl, G., Siozos-Rousoulis, L. and Lacor, C. (2016). A time-domain Kirchhoff formula for the convective acoustic wave equation. *Proceedings. Mathematical, Physical, and Engineering Sciences / The Royal Society*, volume 472, number 2187. (Cited on page 45.)
- [34] Giez, J., Vion, L., Roger, M. and Moreau, S. (????). Effect of the Edge-and-Tip Vortex on Airfoil Selfnoise and Turbulence Impingement Noise. In *22nd AIAA/CEAS Aeroacoustics Conference*. American Institute of Aeronautics and Astronautics. (Cited on pages xiv, 53, and 54.)
- [35] Goldstein, M. E. (1976). *Aeroacoustics*. McGraw-Hill International Book Company. (Cited on pages 44 and 45.)
- [36] Gray, L. M. (U.S. Patent 4358245A, Nov. 1982). Low noise fan. (Cited on page 29.)
-

-
- [37] Gray, L. M. (U.S. Patent 4569632, Nov. 1986). Backskewed fan. (Cited on pages xiii, 25, 30, 176, and 179.)
- [38] Guo, Z., Zheng, C. and Shi, B. (2002). Discrete lattice effects on the forcing term in the lattice Boltzmann method. *Physical Review E*, volume 65, number 4, p. 046308. (Cited on pages 35 and 36.)
- [39] Gutin, L. (1948). *On the Sound Field of a Rotating Propeller* (Technical report). (Cited on page 15.)
- [40] Hanson, D. B. (1974). Spectrum of rotor noise caused by atmospheric turbulence. *The Journal of the Acoustical Society of America*, volume 56, number 1, pp. 110–126. (Cited on pages xiii, 14, 16, and 17.)
- [41] Hinze, J. O. (1975). *Turbulence*. McGraw-Hill. (Cited on pages 16 and 53.)
- [42] Hurley, N., Mirfin, R., Morgan, R. and Tunstill, M. (1995). *Propeller with shrouding ring attached to blade*. Google Patents. (Cited on page 23.)
- [43] Hutcheson, F. V. and Brooks, T. F. (2006). Effects of Angle of Attack and Velocity on Trailing Edge Noise Determined Using Microphone Array Measurements. *International Journal of Aeroacoustics*, volume 5, number 1, pp. 39–66. (Cited on pages 11 and 12.)
- [44] Kameier, F. and Neise, W. (1997). Experimental Study of Tip Clearance Losses and Noise in Axial Turbomachines and Their Reduction. *Journal of Turbomachinery*, volume 119, number 3, pp. 460–471. (Cited on pages 19 and 20.)
- [45] Kameier, F. and Neise, W. (1997). ROTATING BLADE FLOW INSTABILITY AS A SOURCE OF NOISE IN AXIAL TURBOMACHINES. *Journal of Sound and Vibration*, volume 203, number 5, pp. 833–853. (Cited on pages 18 and 20.)
- [46] Karman, T. V. (1938). Airfoil Theory for Non-Uniform Motion. *Journal of the Aeronautical Sciences*, volume 5, number 10, pp. 379–390. (Cited on page 46.)
- [47] Küçükcoskun, K. (2012). *Prediction of free and scattered acoustic fields of low-speed fans*. phdthesis, Ecole Centrale de Lyon. (Cited on page 44.)
- [48] Kimball, R. (1990). Multi sweep blade with abrupt sweep transition, International Patent published under Patent Corporation Treaty wo 91/07593, issued on November 16, 1990. (Cited on pages xiii and 25.)
- [49] Koch, R. (2021). *Identification des sources de bruit aérodynamique liées aux écoulements de jeu en tête de pale de soufflante de turboréacteur*. Ph.D. thesis. (Cited on page 122.)
- [50] Krüger, T., Kusumaatmaja, H., Kuzmin, A., Shardt, O., Silva, G. and Vigen, E. M. (2017). Analysis of the Lattice Boltzmann Equation. In Krüger, T., Kusumaatmaja, H., Kuzmin, A., Shardt, O., Silva, G. and Vigen, E. M., *The Lattice Boltzmann*
-

- Method: Principles and Practice*. Graduate Texts in Physics, Springer International Publishing, Cham. (Cited on pages 35, 36, 37, and 38.)
- [51] Krömer, F. J., Moreau, S. and Becker, S. (2019). Experimental investigation of the interplay between the sound field and the flow field in skewed low-pressure axial fans. *Journal of Sound and Vibration*, volume 442, pp. 220–236. (Cited on page 156.)
- [52] Lakshminarayana, B. (1970). Methods of Predicting the Tip Clearance Effects in Axial Flow Turbomachinery. *Journal of Basic Engineering*, volume 92, number 3, pp. 467–480. (Cited on page 18.)
- [53] Lallier-Daniels, D. (2018). *Analysis of Tip Leakage Flow Noise Inception in Axial Fans*. Ph.D. thesis, University of Sherbrooke, Sherbrooke, Canada. (Cited on pages 80, 149, 154, 158, 168, 176, and 180.)
- [54] Laratro, A., Arjomandi, M., Cazzolato, B. and Kelso, R. (2017). Self-noise of NACA 0012 and NACA 0021 aerofoils at the onset of stall. *International Journal of Aeroacoustics*, volume 16, number 3, pp. 181–195. (Cited on pages xiii, 13, and 14.)
- [55] Lewis, R. I. (1996). 1 - Basic equations and dimensional analysis. In *Turbomachinery Performance Analysis*. Butterworth-Heinemann, Oxford, pp. 1–20. (Cited on pages xiii and 6.)
- [56] Li, Y., Shock, R., Zhang, R. and Chen, H. (2004). Numerical study of flow past an impulsively started cylinder by the lattice-Boltzmann method. *Journal of Fluid Mechanics*, volume 519, pp. 273–300. (Cited on page 37.)
- [57] Lighthill, M. J. (1952). On sound generated aerodynamically I. General theory. *Proc. R. Soc. Lond. A*, volume 211, number 1107, pp. 564–587. (Cited on pages 7 and 44.)
- [58] Lighthill, M. J. and S, F. R. (1954). On sound generated aerodynamically II. Turbulence as a source of sound. *Proc. R. Soc. Lond. A*, volume 222, number 1148, pp. 1–32. (Cited on page 44.)
- [59] Longhouse, R. E. (1976). Noise mechanism separation and design considerations for low tip-speed, axial-flow fans. *Journal of Sound and Vibration*, volume 48, number 4, pp. 461–474. (Cited on pages 20 and 166.)
- [60] Longhouse, R. E. (1977). Vortex shedding noise of low tip speed, axial flow fans. *Journal of Sound and Vibration*, volume 53, number 1, pp. 25–46. (Cited on page 12.)
- [61] Longhouse, R. E. (1978). Control of tip-vortex noise of axial flow fans by rotating shrouds. *Journal of Sound and Vibration*, volume 58, number 2, pp. 201–214. (Cited on pages xiii, 18, 19, 20, 21, 22, and 23.)
- [62] Lyrantzis, A. S. (1995). The use of kirchhoff’s method in jet aeroacoustics. *NASA NASA/CR-97-112990*, p. NAS 1.26:112990. (Cited on page 46.)
-

-
- [63] Magne, S., Moreau, S. and Berry, A. (2015). Subharmonic tonal noise from backflow vortices radiated by a low-speed ring fan in uniform inlet flow. *The Journal of the Acoustical Society of America*, volume 137, number 1, pp. 228–237. (Cited on pages xiii, 20, 21, 23, 78, 80, 149, 154, 176, and 180.)
- [64] Mani, R. (1971). Noise due to interaction of inlet turbulence with isolated stators and rotors. *Journal of Sound and Vibration*, volume 17, number 2, pp. 251–260. (Cited on page 16.)
- [65] Marié, S., Ricot, D. and Sagaut, P. (2009). Comparison between lattice Boltzmann method and Navier–Stokes high order schemes for computational aeroacoustics. *Journal of Computational Physics*, volume 228, number 4, pp. 1056–1070. (Cited on page 43.)
- [66] Marsan, A., Lallier-Daniels, D., Sanjosé, M., Moreau, S. and Mann, A. (2018). Tip leakage flow and its implication on the acoustic signature of a low-speed fan. *Fan 2018 - International Conference on Fan Noise, Aerodynamics, Applications and Systems*. (Cited on page 20.)
- [67] McAlpine, A., Nash, E. C. and Lawson, M. V. (1999). On the Generation of Discrete Frequency Tones by the Flow around an Aerofoil. *Journal of Sound and Vibration*, volume 222, number 5, pp. 753–779. (Cited on pages xiii and 12.)
- [68] McNulty, G. S., Decker, J. J., Beacher, B. F. and Khalid, S. A. (2003). The Impact of Forward Swept Rotors on Tip-Limited Low-Speed Axial Compressors, pp. 613–624. (Cited on page 26.)
- [69] Mohammed, K. P. and Raj, D. P. (1977). Investigations on Axial Flow Fan Impellers With Forward Swept Blades. *Journal of Fluids Engineering*, volume 99, number 3, pp. 543–547. (Cited on pages 26 and 87.)
- [70] Moreau, S. (2017). Cours : Aéroacoustique, University of Sherbrooke, Canada. (Cited on page 44.)
- [71] Moreau, S. (2019). Direct noise computation of low-speed ring fans. *Acta Acustica united with Acustica*, volume 105, number 1. (Cited on page 43.)
- [72] Moreau, S. and Casalino, D. (2005). Aeroacoustic Design of Automotive Engine Cooling Fan Systems. In *11th AIAA/CEAS Aeroacoustics Conference*. Aeroacoustics Conferences, American Institute of Aeronautics and Astronautics. (Cited on page 78.)
- [73] Moreau, S. and Roger, M. (2005). Effect of Angle of Attack and Airfoil Shape on Turbulence-Interaction Noise. In *11th AIAA/CEAS Aeroacoustics Conference*. Aeroacoustics Conferences, American Institute of Aeronautics and Astronautics. (Cited on pages xiii, 11, 12, 13, and 14.)
-

-
- [74] Moreau, S. and Roger, M. (2007). Competing Broadband Noise Mechanisms in Low-Speed Axial Fans. *AIAA Journal*, volume 45, number 1, pp. 48–57. (Cited on page 23.)
- [75] Moreau, S., Roger, M. and Christophe, J. (2009). Flow Features and Self-Noise of Airfoils Near Stall or in Stall. In *15th AIAA/CEAS Aeroacoustics Conference (30th AIAA Aeroacoustics Conference)*. Aeroacoustics Conferences, American Institute of Aeronautics and Astronautics. (Cited on page 13.)
- [76] Paterson, R. and Amiet, R. (1976). Acoustic radiation and surface pressure characteristics of an airfoil due to incident turbulence. In *3rd Aeroacoustics Conference*. Aeroacoustics Conferences, American Institute of Aeronautics and Astronautics. (Cited on pages 14 and 15.)
- [77] Paterson, R. W., Amiet, R. K. and Munch, C. L. (1975). Isolated Airfoil-Tip Vortex Interaction Noise. *Journal of Aircraft*, volume 12, number 1, pp. 34–40. (Cited on page 13.)
- [78] Paterson, R. W., Vogt, P. G., Fink, M. R. and Munch, C. L. (1973). Vortex Noise of Isolated Airfoils. *Journal of Aircraft*, volume 10, number 5, pp. 296–302. (Cited on page 12.)
- [79] Perot, F., Moreau, S., Kim, M.-S., Henner, M. and Neal, D. (2010). Direct aeroacoustics predictions of a low speed axial fan. In *16th AIAA/CEAS Aeroacoustics Conference*. American Institute of Aeronautics and Astronautics. (Cited on page 35.)
- [80] Pestana, M., Perira, A., Salze, E., Thisse, J., Sanjose, M., Jondeau, E., Souchotte, P., Roger, M., Moreau, S., Regnard, J. and M., G. (2017). Aeroacoustics of an axial ducted low mach-number stage: numerical and experimental investigation. *23rd AIAA/CEAS Aeroacoustics Conference, Denver, CO, June 2017*. (Cited on page 61.)
- [81] Piellard, M., Coutty, B. B., Goff, V. L., Vidal, V. and Perot, F. (2014). Direct aeroacoustics simulation of automotive engine cooling fan system: effect of upstream geometry on broadband noise. In *20th AIAA/CEAS Aeroacoustics Conference*. American Institute of Aeronautics and Astronautics. (Cited on pages 23, 154, 176, and 180.)
- [82] Pope, S. B. (2000). Turbulent flows. Cambridge University Press, Cambridge, UK, doi:10.1017/CBO9780511840531. (Cited on page 160.)
- [83] Powell, A. (1959). On the Aerodynamic Noise of a Rigid Flat Plate Moving at Zero Incidence. *The Journal of the Acoustical Society of America*, volume 31, number 12, pp. 1649–1653. (Cited on page 9.)
- [84] Pröbsting, S. and Yarusevych, S. (2015). Laminar separation bubble development on an airfoil emitting tonal noise. *Journal of Fluid Mechanics*, volume 780, pp. 167–191. (Cited on page 12.)
-

-
- [85] Preidel, W. (1907). *Screw-propeller*. Google Patents. (Cited on page 22.)
- [86] Rabinowitz, P. M. (2005). Is noise bad for your health? *The Lancet*, volume 365, number 9475, pp. 1908–1909. (Cited on page 1.)
- [87] Rajoo, S. and Martinez-Botas, R. (2008). Mixed Flow Turbine Research: A Review. *Journal of Turbomachinery*, volume 130, number 4, pp. 044001–044001–12. (Cited on page 5.)
- [88] Reed, H. L. and Saric, W. S. (1989). Stability of Three-Dimensional Boundary Layers. *Annual Review of Fluid Mechanics*, volume 21, number 1, pp. 235–284. (Cited on pages 87 and 112.)
- [89] Roger, M. and Moreau, S. (2005). Back-scattering correction and further extensions of Amiet’s trailing-edge noise model. Part 1: theory. *Journal of Sound and Vibration*, volume 286, number 3, pp. 477–506. (Cited on pages 15 and 162.)
- [90] Sanjosé, M. and Moreau, S. (2018). Fast and accurate analytical modeling of broadband noise for a low-speed fan. *The Journal of the Acoustical Society of America*, volume 143, number 5, pp. 3103–3113. (Cited on pages 24, 47, 80, 81, 82, 88, and 167.)
- [91] Sanjose, M., Lallier-Daniels, D. and Moreau, S. (2015). Aeroacoustic Analysis of a Low-Subsonic Axial Fan. American Society of Mechanical Engineers Digital Collection. (Cited on pages 80 and 82.)
- [92] Sanjose, M. and Moreau, S. (2017). RANS based analytical modeling of broadband noise for a low speed fan. In *International Symposium on Transport Phenomena and Dynamics of Rotating Machinery Maui, Hawaii, December 16-21, 2017*. (Cited on page 162.)
- [93] Sanjose, M., Moreau, S., Perot, F. and Kim, M.-S. (2011). Direct self-noise simulation of the installed controlled diffusion airfoil. In *17th AIAA/CEAS Aeroacoustics Conference (32nd AIAA Aeroacoustics Conference)*. American Institute of Aeronautics and Astronautics. (Cited on page 40.)
- [94] Saucci, S. (2012). Course in lattice boltzmann methods for simulation of complex phenomena across scales. Nordic Institute for Theoretical Physics. (Cited on pages xiii and 33.)
- [95] Schlinker, R. H. A. (1981). *Helicopter rotor trailing edge noise. [noise prediction]* (Technical report). (Cited on page 8.)
- [96] Schoder, S., Junger, C. and Kaltenbacher, M. (2020). Computational aeroacoustics of the EAA benchmark case of an axial fan. *Acta Acustica*, volume 4, number 5, p. 22. (Cited on page 139.)
-

-
- [97] Seong, J. C., Park, T. H., Ko, J. H., Chang, S. I., Kim, M., Holt, J. B. and Mehdi, M. R. (2011). Modeling of road traffic noise and estimated human exposure in Fulton County, Georgia, USA. *Environment International*, volume 37, number 8, pp. 1336–1341. (Cited on page 1.)
- [98] Sharland, I. J. (1964). Sources of noise in axial flow fans. *Journal of Sound and Vibration*, volume 1, number 3, pp. 302–322. (Cited on pages 7, 9, 10, 14, 15, and 29.)
- [99] Shumway, R. H. and Stoffer, D. S. (2017). Time series analysis and its applications. Springer International Publishing. (Cited on page 72.)
- [100] Signor, D. B., Yamauchi, G. K., Mosher, M., Hagen, M. J. and George, A. R. (1996). Effects of Ingested Atmospheric Turbulence on Measured Tail Rotor Acoustics. *Journal of the American Helicopter Society*, volume 41, number 1, pp. 77–90. (Cited on pages 14 and 16.)
- [101] Sinayoko, S., Kingan, M. and Agarwal, A. (????). Trailing edge noise prediction for rotating blades: analysis and comparison of two classical approaches. In *18th AIAA/CEAS Aeroacoustics Conference (33rd AIAA Aeroacoustics Conference)*. American Institute of Aeronautics and Astronautics. (Cited on page 8.)
- [102] Smith, Leroy H., J. and Yeh, H. (1963). Sweep and Dihedral Effects in Axial-Flow Turbomachinery. *Journal of Basic Engineering*, volume 85, number 3, pp. 401–414. (Cited on pages 25, 27, 83, and 94.)
- [103] Sturm, M. and Carolus, T. (2012). Tonal fan noise of an isolated axial fan rotor due to inhomogeneous coherent structures at the intake. *Noise Control Engineering Journal*, volume 60, number 6, pp. 699–706. (Cited on pages xiii and 17.)
- [104] Sturm, M. and Carolus, T. (2013). Impact of the large-scale environment on the tonal noise of axial fans. *Proceedings of the Institution of Mechanical Engineers, Part A: Journal of Power and Energy*, volume 227, number 6, pp. 703–710. (Cited on page 16.)
- [105] Sturm, M., Sanjose, M., Moreau, S. and Carolus, T. (2015). Aeroacoustic simulation of an axial fan including the full test rig by using lattice boltzmann method. Fan 2015. (Cited on pages 61, 66, and 137.)
- [106] Tyler, J. M. and Sofrin, T. G. (1962). *Axial Flow Compressor Noise Studies* (Technical Report 620532). SAE International, Warrendale, PA. (Cited on page 16.)
- [107] US EPA, O. (2015). Clean Air Act Title IV - Noise Pollution. (Cited on page 1.)
- [108] Vad, J. (2008). Aerodynamic effects of blade sweep and skew in low-speed axial flow rotors at the design flow rate: An overview:. *Proceedings of the Institution of Mechanical Engineers, Part A: Journal of Power and Energy*. (Cited on pages xiii, 26, 27, and 29.)
-

-
- [109] Vad, J. (2012). Forward Blade Sweep Applied to Low-Speed Axial Fan Rotors of Controlled Vortex Design: An Overview, pp. 803–812. (Cited on pages 26 and 87.)
- [110] Vad, J., Halász, G. and Benedek, T. (2015). Efficiency gain of low-speed axial flow rotors due to forward sweep. *Proceedings of the Institution of Mechanical Engineers, Part A: Journal of Power and Energy*, volume 229, number 1, pp. 16–23. (Cited on page 27.)
- [111] Vad, J., Kwedikha, A. R. A. and Jaberg, H. (2006). Effects of blade sweep on the performance characteristics of axial flow turbomachinery rotors. *Proceedings of the Institution of Mechanical Engineers, Part A: Journal of Power and Energy*, volume 220, number 7, pp. 737–749. (Cited on pages 26, 175, 176, 179, and 180.)
- [112] van Schalkwyk, M. C. I. and Mindell, J. S. (2018). Current issues in the impacts of transport on health. *British Medical Bulletin*. (Cited on page 1.)
- [113] Versteeg, H. and Malalasekara, W. (2007). An introduction to computational fluid dynamics: The finite volume method. (Cited on page 41.)
- [114] Wallis, R. A. (1961). *Axial flow fans: design and practice*. Academic Press. (Cited on page 9.)
- [115] Williams, J. E. F. and Hawkings, D. L. (1969). Sound generation by turbulence and surfaces in arbitrary motion. *Phil. Trans. R. Soc. Lond. A*, volume 264, number 1151, pp. 321–342. (Cited on page 44.)
- [116] Wright, T. and Simmons, W. E. (1990). Blade Sweep for Low-Speed Axial Fans. *Journal of Turbomachinery*, volume 112, number 1, pp. 151–158. (Cited on pages 26, 27, 28, 29, and 30.)
- [117] Wu, H., Moreau, S. and Sandberg, R. D. (2020). On the noise generated by a controlled-diffusion aerofoil at $Re=1.5\times 10^5$. *Journal of Sound and Vibration*, volume 487, p. 115620. (Cited on page 150.)
- [118] Y, R. (2007). *Modelisation analytique du bruit aerodynamique a large bande des machines tournantes : utilisation de calculs moyennes de mecanique des fluides*. Ph.D. thesis, LECOLE CENTRALE DE LYON, Lyon, France. (Cited on page 46.)
- [119] Yakhina, G., Roger, M., Moreau, S., Nguyen, L. and Golubev, V. (2020). Experimental and Analytical Investigation of the Tonal Trailing-Edge Noise Radiated by Low Reynolds Number Aerofoils. *Acoustics*, volume 2, number 2, pp. 293–329. (Cited on page 12.)
- [120] You, D., Wang, M., Moin, P. and Mittal, R. (2007). Large-eddy simulation analysis of mechanisms for viscous losses in a turbomachinery tip-clearance flow. *Journal of Fluid Mechanics*, volume 586, pp. 177–204. (Cited on page 20.)
- [121] YU, J. and JOSHI, M. (1979). On sound radiation from the trailing edge of an isolated airfoil in a uniform flow. In *5th Aeroacoustics Conference*. American Institute of Aeronautics and Astronautics. (Cited on page 91.)
-

-
- [122] Yu, J. C. and Tam, C. K. W. (1978). Experimental Investigation of the Trailing Edge Noise Mechanism. *AIAA Journal*, volume 16, number 10, pp. 1046–1052. (Cited on page 9.)
- [123] Zenger, F. (2012). *Semi-Analytical Prediction of Wake-Interaction Noise in Counter-Rotation Open Rotors*. Ph.D. thesis, ECOLE CENTRALE DE LYON, Lyon, France. (Cited on page 46.)
- [124] Zenger, F. (2017). *Sound emission of low-pressure axial fans under distorted inflow conditions*. Ph.D. thesis, Friedrich-Alexander University Erlangen-Nürnberg, Erlangen, Germany. (Cited on pages xiii, xiv, xviii, 3, 9, 26, 28, 29, 30, 31, 58, 60, 61, 63, 77, 161, 164, and 166.)
- [125] Zenger, F. J., Renz, A., Becher, M. and Becker, S. (2016). Experimental investigation of the noise emission of axial fans under distorted inflow conditions. *Journal of Sound and Vibration*, volume 383, pp. 124–145. (Cited on pages xiii and 27.)
- [126] Zhou, J., Adrian, R. J., Balachandar, S. and Kendall, T. M. (1999). Mechanisms for generating coherent packets of hairpin vortices in channel flow. *Journal of Fluid Mechanics*, volume 387, pp. 353–396. (Cited on page 109.)
- [127] Zhu, T., Lallier-Daniels, D., Sanjosé, M., Moreau, S. and Carolus, T. (2018). Rotating coherent flow structures as a source for narrowband tip clearance noise from axial fans. *Journal of Sound and Vibration*, volume 417, pp. 198–215. (Cited on pages xiii, 17, 18, 19, 20, 23, 176, and 180.)
-

